Effet de la symétrie des lacunes d'oxigène dans MgO sur le transport électronique polarisé en spin

Beata Taudul

▶ **To cite this version:**

Beata Taudul. Effet de la symétrie des lacunes d'oxigène dans MgO sur le transport électronique polarisé en spin. Physique [physics]. Université de Strasbourg, 2017. Français. NNT : 2017STRAE042 . tel-01820642

HAL Id: tel-01820642
https://theses.hal.science/tel-01820642

Submitted on 22 Jun 2018

HAL is a multi-disciplinary open access archive for the deposit and dissemination of scientific research documents, whether they are published or not. The documents may come from teaching and research institutions in France or abroad, or from public or private research centers.

L'archive ouverte pluridisciplinaire **HAL**, est destinée au dépôt et à la diffusion de documents scientifiques de niveau recherche, publiés ou non, émanant des établissements d'enseignement et de recherche français ou étrangers, des laboratoires publics ou privés.

THÈSE de DOCTORAT

pour obtenir le titre de
Docteur de l'université de Strasbourg
Discipline/Spécialité: Physique

Impact of symmetry of oxygen vacancies on electronic transport in MgO-based magnetic tunnel junctions

Université de Strasbourg
École Doctorale de Physique et Chimie-Physique
Institut de Physique et Chimie des Matériaux de Strasbourg

présentée par
Beata Taudul
soutenue le 12 décembre 2017

Jury :

Rapporteurs :	S. Biermann
	A. Smogunov
Examinateur :	J.-F. Dayen
Directeur de thèse :	M. Alouani
Invité :	M. Bowen

Acknowledgments

This manuscript is a culmination of the last three years of my PhD thesis which was performed in the Institut de Physique et Chimie des Matériaux de Strasbourg (IPCMS) in the Département Magnétisme des Objets NanoStructurés (DMONS). During this period I had a pleasure to meet and work with amazing people to whom I would like to thank now.

First and foremost I would like to express my gratitude to my supervisor Prof. Mébarek Alouani. Thank you for all your advices and guidance which allow me to complete this PhD. I am mostly grateful for your patience and effort in explaining me the scientific issues I had problems with and your encouragement, especially during writing this manuscript. I have learned a lot under your supervision and I developed as a scientist and also as a person.

I would like thank Dr Martin Bowen who was in charge of experimental part of this work. Your enthusiasm and ideas were the driving wheel and motivation for performing new calculations to understand experiments better. Thank you for that passion to science you have and these fruitful discussions we had.

Furthermore, I want to thank members of the jury Prof. Silke Bierman, Dr Alexander Smogunov and Dr Jean-Francois Dayes to agree review this manuscript.

A huge thanks to IT department in the IPCMS and ones in charge of computational clusters (HPC and CINES) I was using. You were always ready to help me in solving software issues I encountered.

I would like to also acknowledge direction and members of DMONS group with whom I had pleasure to cooperate and discussed. Special thanks go to Veronique Verner who is just amazing person and like no one else can manage, sometimes confusing, administration. I have to also mention here Jacek Arabski and Guy Schmerber. Thank you for these talks not necessarily about science and your humour which was nice distraction in everyday work.

These years are also unforgettable experience thanks to friendship of other students working as me and who understand ups and downs of a young researcher life. A big thanks to Michał Studniarek who during these years we spent in one office became my friend and trustee and changed my point of view on many aspects. I would like to thank Filip Schleicher and Wojciech Szewc for these amazing trips you took me to and for showing me the charm of Alsace. My special thanks go also to Ufuk Halisdemir, Kostia Katcko and Etienne Urbain for this time spent together outside the institute and also your involvement in explaining me how the experiment actually works. I am also grateful to Nicolas Bachelier for helping me to discover my passion to climbing. Thank you! Many thanks to my former office mates Anant Dixit, Dimitra Xenioti and Saber

Gueddida who helped me a lot at the beginning of my thesis and guide me thorough complexities of computer science. I cannot forget here also about new people in my office, Garen Avedissian, Olivier Ngassam Nyakam and Gladice Magnifouest Tchinda and Khaled Rassoul. Thank you for your company, help and encouragement especially during the last weeks of my thesis. And good luck in you future work! There are many other current and previous PhD students and in general people from Strasbourg I would like to mention and who made this time incredible: Adam Brandstteter-Kunc, Michał Ochapski, Jarosław Kirdoda, Marek Twardoch, Zyiad Chaker, Mathias Dolci, Lalit M. Kandpal, Sambit Mohapatra, Ousmane Ly, Donald Mouafo, Guillaume Urbain, Ola Czmiel, Justyna Skuza, Staz Macharchuk, Jérôme Hurst, Burak Ozdymar, Mathilde Menadrd.

I would also like mention people outside Strasbourg. Here, my special thanks I dedicate to Edyta Pietruszka who is my friend since the beginning of our studies. Thank you for staying with me that long, pushing me to try new things and always be there to provide advice and support. I want also to thank Krzysztof Herman and Stanisław Binkiewicz who also know me since first days of my studies. Guys, thank you so much for your faith in me and this awesome time we had, and hopefully we will still have, together. A big thanks to Marta Brzezińska for your friendship despite the miles that separate us.

Last but not least I am really grateful to my family. They are always there for me, trying to understand my choices and giving me unconditional support despite everything.

It's not possible to mention all the people I have met during these years and their impact on my life, so let me just say thank You all!

Contents

General introduction 1

I Introduction and background 5

1 Introduction to the physics of magnetic tunnel junctions 7
1.1 Origins of tunnel magnetoresistance . . . 7
1.1.1 Julliere's model . . . 9
1.1.2 Stern's approach . . . 11
1.1.3 Slonczewski's model . . . 11
1.2 Spin and symmetry filtering in crystalline Fe/MgO/Fe junction . . . 12
1.2.1 Crystal structure of Fe/MgO interface . . . 13
1.2.2 Bloch states and wave function symmetries . . . 14
1.2.3 Symmetry states in Fe leads . . . 15
1.2.4 Symmetry filtering in the MgO barrier . . . 20
1.2.5 Importance of symmetry . . . 23
1.3 Transmission calculations of Fe/MgO/Fe junction . . . 24
1.3.1 Transmission and TDOS for parallel configuration . . . 24
1.3.2 Transmission and TDOS for antiparallel configuration . . . 29
1.3.3 Other types of electrodes . . . 30
1.4 Experimental realization . . . 31

2 Role of defects in MTJs 33
2.1 Interface oxidation . . . 33
2.2 Grain boundaries in MgO thin films . . . 35
2.3 Boron diffusion . . . 37
2.4 Point defects within MgO . . . 39
2.4.1 Single oxygen vacancy - F center . . . 40
2.4.2 Double oxygen vacancies - M center . . . 46
2.5 Scientific motivations of this thesis . . . 50

II Methodology 53

3 Method of calculation 55
3.1 Many-body electron problem . . . 56
3.2 Density functional theory . . . 59

3.2.1 Hohenberg-Kohn Theory . . . 59
3.2.2 Kohn-Sham equations . . . 60
3.2.3 Local density approximation . . . 62
3.2.4 General gradient approximations . . . 63
3.2.5 Hybrid functionals . . . 66
3.3 Solving Kohn-Sham equations . . . 70
3.3.1 Periodicity and plane waves . . . 72
3.3.2 Choice of convergence parameters . . . 78
3.3.3 Pseudopotential method . . . 79
3.3.4 Projector augmented wave method . . . 84
3.3.5 Numerical atomic orbitals . . . 89
3.3.6 Summary . . . 94

4 Ballistic transport 95
4.1 Landauer-Büttiker formalism . . . 95
4.2 Ballistic transport calculations in PWCOND . . . 100
4.3 Ballistic transport calculation in TranSIESTA . . . 108
4.3.1 Single particle Green function . . . 108
4.3.2 System with interactions . . . 110

III Results and discussion 117

5 Electronic properties of oxygen vacancies in magnetic Fe(FeCo)/MgO junctions 119
5.1 F/M-MgO structural properties . . . 119
5.2 Defect formation energy . . . 121
5.3 Electronic properties of M-MgO . . . 123
5.3.1 Band unfolding . . . 125
5.3.2 Hybrid calculations . . . 126
5.4 Thin films of MgO . . . 127
5.5 Fe/MgO junctions . . . 130
5.5.1 Ideal Fe/MgO junction . . . 131
5.5.2 M-MgO/Fe junction . . . 135
5.6 FeCo/MgO junction . . . 137
5.6.1 Ideal FeCo/MgO junction . . . 137
5.6.2 M-MgO/FeCo junction . . . 139
5.7 Chain of vacancies . . . 140
5.8 Complex band structure of defects in MgO . . . 141
5.9 Summary . . . 143

6 Transmission through the Fe/MgO/Fe junction 145
6.1 Ideal MgO-based junctions . . . 145
6.2 F/M center in the middle layer of MgO . . . 147
6.3 Effect of shifting the vacancy on the transmission . . . 149
6.4 Rotating the M center . . . 152

6.5 Summary of PWCOND results 155
6.6 Calculated conductance with TranSIESTA 157

7 Probing a device's active atoms using synchrotron radiation 163
7.1 X-ray absorption spectroscopy 163
7.2 Combined XAS and magnetotransport measurement 164
7.3 Theoretical investigations 168
7.4 Summary 171

8 General conclusions and perspectives 173

Appendices 177

A Generation of USPP 179

B FeCo/MgO ideal junction 181

Bibliography 183

Bibliography 183

Résumé en français

La spintronique est un exemple de la recherche multidisciplinaire qui se développe ces dernières années, son principal champ d'intérêt est de contrôler activement les degrés de liberté de spin dans les systèmes à l'état solide.[1–4] Le contrôle de spin concerne le contrôle du courant de spin et/ou de manipuler le spin de manière cohérente un seul ou quelques systèmes de spin.[1] La question principale à répondre est de savoir comment le spin de la particule interagit avec son environnement à l'état solide et comment on peut utiliser cette information pour mettre en œuvre des dispositifs opérationnels. Par conséquent, la recherche fondamentale de la spintronique se consacre au transport de spin, sa dynamique et sa relaxation en combinaison avec des moyens effectifs pour générer et détercter une polarisation de spin dans les systèmes.

Parmi les différents domaines de la spintronique, l'étude des hétérostructures multicouches constitue actuellement un sujet d'intérêt majeur. Cet engouement repose sur la découverte de Fert *et al.*[5] et de Grünberg *et al.*,[6] d'un effet de magnétorésistance géante (GMR) dans certaines structures multicouches. Dans le cas d'une structure sandwich F/N/F, où F est un métal ferromagnétique et N un métal ou isolant non magnétique, on observe une forte variation de résistance électrique en fonction de l'orientation relative de l'aimantation des couches magnétiques. Il est à présent établi que le mécanisme de magnétorésistance provient de la différence de probabilité de diffusion des électrons pour les deux directions de spin. Cette asymétrie intervient dans les différentes couches ainsi qu'à l'interface entre les couches magnétiques et non magnétiques. Ainsi, la transmission d'un électron dépend du spin de l'électron considéré et de l'orientation relative de l'aimantation des couches magnétiques, conduisant à une diffusion sélective et dépendante du spin. L'amplitude de cet effet est caractérisée par le rapport GMR qui traduit la variation relative de résistance (ou de conductance) entre les configurations ferromagnétique et antiferromagnétique de l'aimantation.

Parmi les hétérostructures, les jonctions tunnel magnétiques (JTM) à base de Fe/MgO se révèlent particulièrement attractives. En effet, ces jonctions de type Fe/MgO/Fe présentent une magnétorésistance très importante à température ambiante faisant de ces jonctions un matériau privilégié pour des capteurs magnétorésistifs ou des mémoires d'ordinateur de prochaine génération (MRAM). L'origine de ces magnétorésistances élevées provient de la polarisation en spin, mais également de la sélection en symétrie (de type Δ_1) des états électroniques transmis au travers de la barrière tunnel de MgO.

Pour exploiter les applications offertes par cet effet GMR pour ces systèmes, des études fondamentales sont indispensables en vue de comprendre la stabilité des différentes structures, ainsi que l'origine de la polarisation de spin et la symétrie des états éle-

ctroniques. Ainsi, une compréhension précise des phénomènes de transport à l'échelle nanoscopique, mis en jeu dans ces matériaux, nécessite la connaissance réaliste de la structure électronique des matériaux ferromagnétiques, des semiconducteurs et des oxydes isolants, et plus spécifiquement des interfaces qui les séparent. Des approches de type *ab initio* se révèlent par conséquent indispensables afin de comprendre les mécanismes de la magnétorésistance.

Le modèle le plus simple a été proposé par Jullière en 1975,[7] mais sa réalisation pratique avec un ratio de magnétorésistance tunnel élevée (TMR) a dû attendre le développement de nouvelles méthodes de dépôt au milieu des années 90. Les premiers JMT étaient basés sur une couche isolante de Al_2O_3 entre les électrodes ferromagnétiques. Les résultats de ces JMT, bien que prometteurs, étaient encore limités. La TMR la plus élevée est obtenue en utilisant comme espaceur Al_2O_3 et est au maximum 70%, à température ambiante. Les calculs effectués par MacLaren et. *al.*[8] ont montré que la TMR était beaucoup plus élevée pour des barrières cristallines que pour des amorphes. Mathon et Umerski[9] ont commencé à explorer les JMT avec le MgO comme barrière et ont montré que le MgO peut donner des valeurs de TMR supérieures à 10000 %. Depuis l'an 2000, les jonctions avec les barrières de MgO ont été en constante évolution. Les plus grandes valeurs de TMR dans les jonctions cristallines résultent de la conservation du spin et de la symétrie de la fonction d'onde lors du transport par effet tunnel.[8,10–13] Cela signifie que lorsque les électrons se propagent dans un cristal, ils ressentent le potentiel périodique généré par les ions et leur fonction d'onde est décrite par la fonction d'onde de Bloch avec le vecteur d'onde k parallèle à la direction du mouvement. En outre, le les électrons peuvent être classés selon leur composants des fonctions d'onde de Bloch le long de la direction de mouvement: *spd*-, *pd*- et *d*- qui correspondent aux symétries suivantes Δ_1, Δ_5, $\Delta_{2/2'}$, respectivement (le long de la direction Γ-H de forte symétrie). Cette classification est basée sur des orbitales atomiques qui sont impliquées dans la création de bandes du système Fe/MgO/Fe. En conséquence, des canaux de conduction spécifiques, selon les symétries apparaissant dans la structure, peuvent être distingués. Il faut noter que les électrons peuvent se propager uniquement dans le canal d'une symétrie donnée. Ce phénomène porte le nom de transport cohérent.

Malgré l'importance incontestable des technologies JTM, la compréhension de tous les aspects d'un dispositif opérationnel n'est toujours pas complète. La magnétorésistance tunnel est un phénomène complexe et dépend fortement de la structure électronique des électrodes, les propriétés de la barrière isolante et la liaison chimique à l'interface entre les deux types de matériaux. Toute cette complexité se reflète dans la réalisation expérimentale où actuellement les plus hautes valeurs de la TMR atteignent 600% à température ambiante[14] et sont considérablement inferieurs aux prédictions théoriques. Pourtant, rien n'est toujours parfait dans la réalité et toute imperfection structurelle dans les MTJs devraient être un facteur limitant de la TMR mesurée. Par conséquent, un intérêt particulier est orienté vers le contrôle et l'explication l'impact des défauts afin de créer des dispositifs avec les propriétés souhaitées. Pour comprendre l'origine et l'impact des imperfections structurelles sur l'effet tunnel des études fondamentales du phénomène sont nécessaires. Les approches pour déterminer la structure électronique ab initio sont indispensables pour comprendre le mécanisme de la

magnétorésistance et les modifications dues à des défauts.

Dans nos études, nous nous concentrons sur les jonctions nominales à base de MgO avec des propriétés de filtrage de symétrie. Néanmoins, les principes connus s'appliquent aux jonctions avec une structure cristalline idéale. Les études expérimentales révèlent cependant souvent une oxydation à l'interface[15] qui modifie la nature de la liaison chimique à l'interface entre l'électrode ferromagnétique et un espaceur MgO et qui à son tour provoque une diminution de la TMR. La combinaison des études théoriques[16] et expérimentales[17] a prouvé que même si on inclut le désordre d'interface ou l'oxydation de la couche interfaciale de Fe la chute drastique de la TMR expérimentale ne peut pas être entièrement justifiée. Bien qu'une amélioration constante des procèdes technologique de fabrication des hétérojonctions évite l'oxydation et permet d'obtenir des interfaces de meilleure qualité, les valeurs de TMR dans la meilleure jonction ne dépassent pas quelques centaines pour cent.

Une autre question que l'on peut considérer est l'effet des joint de grains qui apparaissant dans l'espaceur MgO sur le transport électronique. Ce type de défauts structurels sont difficiles à comprendre de point de vue expérimentale et théorique. Néanmoins, la littérature montre[18,19] que les joint de grains peuvent provoquer une diminution de la barrière effective de MgO, mais cette diminution ne correspond pas aux valeurs expérimentales et les hauteurs de barrières observées ne peuvent être expliquées. Une autre possibilité était due à la désintégration atomique au cours de la préparation de l'échantillon et recuit. En particulier, la principale préoccupation concernait les jonctions CoB/MgO/FeCoB puisque ces types de MTJ sont supposées avoir de plus hautes TMR. Dans la littérature,[20–23] on peut trouver une variété de paysages possibles concernant la présence de bore, par exemple, le dioxyde de bore dans la barrière MgO (formant des oxydes BO_x) ou la ségrégation à l'interface CoFe/MgO. Cependant, de nouvelles investigations expérimentales semblent prouver que le bore ne se trouve pas dans la barrière MgO[24–26] et avec une température de recuit appropriée, le bore ne s'insère pas dans le MgO mais plutôt se trouve plus loin des interfaces. Ces études nous motivent à nous intéresser dans cette thèse aux défauts créés dans l'espaceur MgO, tels que les lacunes d'oxygène. Ce type de défaut crée des niveaux d'énergie supplémentaires dans la bande interdite nominale de MgO.[27–30] Par conséquent, la hauteur de barrière rencontrée par les électrons en propagation est localement réduite. Les électrons peuvent ensuite passer à travers la barrière via ces états avec des taux de diffusion qui diffèrent de la barrière idéale. De plus, ces niveaux pourraient être électriquement mesurés et en effet plusieurs groupes expérimentaux ont rapportés des hauteurs de barrières dans les MTJ à base de MgO beaucoup plus petites que la valeur nominale de 3.9 eV de MgO. Par exemple les barrières de hauteur 0.39/0.82 eV[31] et 0.39 eV[32] ont été mesurées dans les jonctions Fe/MgO/Fe ou 1.1-1.7 eV dans les jonctions FeCo/MgO/FeCo.[33] L'identification exacte du type de défaut responsable d'une hauteur de barrière particulière n'est toujours pas élucidé. La hauteur de barrière la plus intéressante est celle de 0.4 eV car elle est favorable à un transport cohérent.[30,34] Il a été suggéré par Schleicher *et al.*[30] qui est peut être le résultat d'appariements d'oxygène appelés "M-centre". En effet, de point de vue théorique les recherches de McKenna et Blumberg[34] montrent que le transport cohérent peut être conservé si les lacunes individuelles d'oxygène sont séparées par moins de 6 Å. Cela indique que des

lacunes d'oxygène appariées, ou centres M, peuvent préserver le transport tunnel et les symétries des électrons qui participent au transport électronique. Puisque les propriétés des centres M ne sont pas bien comprises, surtout lorsqu'ils sont incorporés dans des MTJ, ils ont besoin d'études plus approfondies. Des recherches expérimentales intensives sur les MTJ à base de MgO et sur les propriétés des lacunes appariées d'oxygène dans MgO sont également menées à IPCMS. Ces efforts expérimentaux ont besoin d'un fort support théorique pour expliquer les niveaux d'énergies mesurés et les associer avec un type particulier de lacune d'oxygène. L'objectif principal de cette thèse est par conséquent de calculer les propriétés électroniques des lacunes d'oxygène dans le MgO et révéler leur impact sur le transport polarisé de spin et de symétrie dans les jonctions Fe/MgO/Fe par des calculs ab initio fondés sur la théorie de la fonctionnelle de la densité.

Méthodologie

Théorie de la fonctionnelle de la densité

Les bases mathématiques de la théorie de la fonctionnelle de la densité (DFT) ont été établies par les théorèmes de Hohenberg-Kohn[35] et leur implémentation est réalisée grace aux équations de Kohn-Sham.[36]
Lorsqu'on définit les équations de Kohn-Sham, il est crucial d'admettre qu'un système en interaction peut être représenté pour un autre système "inerte" avec la même densité électronique. Ainsi, l'équation à résoudre est une équation de Schrödinger à un électron comme celle comportant un potentiel effectif qui tient compte de toutes les interactions dans le système. Cependant, le formalisme de la DFT nécessite encore des approximations et des choix à faire avant de résoudre les équations de Kohn-Sham. Ces approximations sont résumées sur le schéma ci-dessous où V_{ext} est le potentiel externe dû au noyaux, V_H le champ interaction coulombien électron-électron et V_{xc} le potentiel d'échange corrélation.

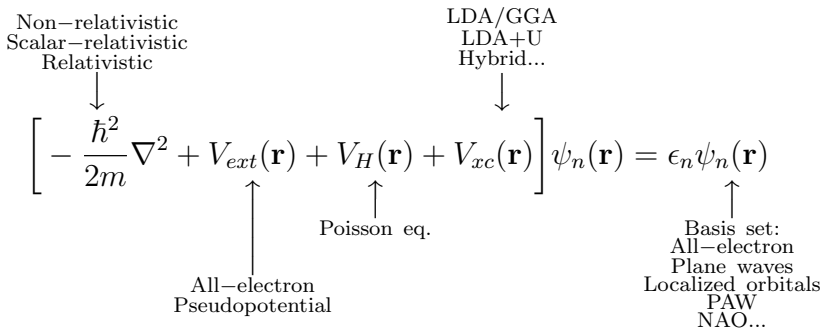

De plus, la base des fonctions d'onde doit être tronquée et le nombre d'ondes planes inclus dépend de l'énergie de coupure ("cutoff energy") fixée par l'utilisateur. Ensuite, il faut définir le maillage de points k dans la zone de Brillouin (BZ) et choisir la méthode d'approximation de l'échantillonnage de BZ. Le nombre des points k dépend de la précision requise et du type de matériau, c'est-à-dire que les métaux nécessitent un nombre de points k plus grand que les matériaux semi-conducteurs ou isolants. Lors de l'utilisation des grandes super cellules, le nombre de points k peut être réduit

de façon significative par rapport à ceux requis pour un calcul de cellule primitive car l'espaces réel et l'espace réciproques sont inversement proportionnels. Enfin, les critères de convergence pour l'énergie totale et les forces exercées sur les atomes au cours du cycle d'auto-cohérence devraient également être définis.

Dans la pratique, la solution d'un problème à plusieurs corps même après une série d'approximations est assez complexe. Néanmoins, grâce à des algorithmes efficaces, à la parallélisations massive et à l'utilisation des supercalculateurs; les calculs DFT peuvent être effectués avec une grande précision pour des systèmes comportant des centaines d'atomes. Dans cette thèse, les résultats ont été obtenus en utilisant trois codes différents, VASP[37,38] qui met en œuvre la méthode des ondes planes projetées (PAW), Quantum-Espresso (QE)[39,40] qui utilise une base d'ondes planes avec un pseudo potentiel avec concervation de norme ou ultra-doux (NCPP, USPP) ou la méthode PAW et le code SIESTA[41–43] qui combine la base d'orbitales atomiques numériques (NAO) et les NCPP.

Les calculs de l'état fondamental sont d'abord effectués en considérant un MgO massif sans défauts et puis des structures avec des défauts d'oxygène F et M. Les centres F/M ont été créés en supprimant un ou deux atomes d'oxygène neutres de la super cellule qui contient 64 atomes dans une forme cubique simple. Ces calculs ont été effectués en utilisant le code VASP et la fonctionnelle GGA-PBE. Une valeur de 500 eV d'énergie de coupure a été utilisée et le critère de convergence fixé pour une énergie de 1 μeV. Les structures présentant des défauts ont été relaxées en exigeant que les forces agissant sur les atomes soient inférieures à -0.001 eV/a.u.. En raison de la grande taille de la super cellule, nous avons trouvé qu'un maillage de points k dans la zone de Brillouin de 4×4×4 un élargissement τ gaussien de 0.2 eV est largement suffisant pour la convergence des niveaux de défauts. Les mêmes paramètres de convergences ont été utilisés pour les calculs utilisant les potentiels hybrides HSE03. Dans le cas des films minces de MgO et des jonctions complètes avec des électrodes ferromagnétiques, l'énergie de coupure ainsi que le critère de convergence étaient les mêmes à l'exception de la valeur de τ qui a été réduite à 0.1 eV.

Transport balistique

Classiquement, les phénomènes de transport obéissent à la loi d'Ohm où un courant est une fonction linéaire de la tension appliquée. Cependant, lorsque la taille de l'échantillon devient comparable à la longueur d'onde électronique, les effets quantiques commencent dès lors à se manifester. Le facteur le plus crucial qui définit la conductance électrique est lié aux propriétés de diffusion d'un dispositif. Landauer a été le premier à développer un formalisme reliant les ropriétés de diffusion à la conductance et à donner une description du transport électronique dans le régime quantique balistique.[44,45] Il a relié la conductance d'un nano contact à la probabilité de transmission d'un électron au niveau de Fermi pour traverser un dispositif. Dans cette approche, un nano contact est modélisé sous la forme d'une région de diffusion avec des fils métalliques connectés de chaque côté à des électrodes infinies qui servent de réservoirs d'électrons. Chacune des électrodes a un potentiel chimique bien défini désigné par μ_L et μ_R respectivement pour les électrodes gauche et droite. À l'intérieur des con-

ducteurs, les électrons peuvent être décrits comme des ondes de Bloch se propageant dans la direction longitudinale, tandis que dans les directions perpendiculaires causées par un confinement latéral, leur impulsion est quantifiée. Par conséquent, lorsqu'un faible biais est appliqué entre les réservoirs, le courant est entraîné par un certain nombre de modes de déplacement gauche et droit. Le nombre de modes permis par le confinement latéral dépend de la taille des conducteurs métalliques dans les directions transversales, c'est-à-dire dans la limite d'une section transversale infinie, un seul mode transversal serait autorisé et il n'y aurait qu'un canal disponible pour le transport de charge. Due au fait que les électrons de la région centrale peuvent être diffusés, nous pouvons introduire une probabilité T (E) pour un électron d'énergie E pour être transmis dans le conducteur du côté opposé et une probabilité R (E) celle de son rejet, telle que T(E) + R(E) = 1. Par conséquent, la formule pour le courant peut être écrite comme[46]

$$I = \frac{2e}{h} \int T(E) \left(f_L(E - \mu_L) - f_R(E - \mu_R) \right) dE. \tag{0.1}$$

La différence μ_L-μ_R entre les potentiels chimiques gauche et droit a été supposée suffisamment faible pour que la dépendance énergétique de T et R dans cette plage d'énergie puisse être négligée et que la conductance soit évaluée uniquement à l'énergie de Fermi:

$$G = \frac{2e^2}{h} T(E_F). \tag{0.2}$$

La formule ci-dessus montre que dans le régime linéaire, la conductance peut être obtenue en évaluant le coefficient de transmission à l'énergie de Fermi. Dans le cas limite, pour un seul mode conducteur idéal, le mode est parfaitement transmis et $T(E_F) = 1$ qui donne le quantum de la conductance G_0.

Un formalisme plus général, étendu à la transmission en mode multiple a été proposé par Büttkier.[47] Ici, chaque mode peut être partiellement rejeté et partiellement transmis à lui-même ou dans d'autres modes. Supposons que pour une énergie donnée, nous avons des modes actifs M_L dans le conducteur gauche et des modes actifs M_R dans le conducteur droit. Une onde incidente provenant du nième canal gauche a une probabilité T_{mn} d'être transmise dans le mième canal de l'autre côté du diffuseur et R_{mn} d'être rejetée vers le mième canal du même côté du diffuseur. Les grandeurs analogiques pour les états provenant de la bonne électrode peuvent également être définies et sont désignées par des nombres premiers. Les amplitudes des modes entrants et sortants sont connectées par la matrice dite de diffusion S. De la gauche vers la droite, la conductance totale de l'électrode généralisée à la situation multicanal, est maintenant écrite comme:

$$G = \frac{2e^2}{h} \sum_m T_{mn} = \frac{2e^2}{h} \sum_m |t_{mn}|^2 = \frac{2e^2}{h} Tr[tt^\dagger]. \tag{0.3}$$

Ces formules sont encore implémentées dans deux codes qui sont utilisés dans cette thèse: PWcond et TranSIESTA. Dans ces deux codes, le courant à travers le dispositif est évalué selon le formalisme de Landauer- Büttiker en utilisant différentes techniques pour calculer la transmission. Dans PWcond, un flux d'électrons est injecté sur la zone

de diffusion d'un dispositif, et une probabilité pour que chaque état soit transmis ou rejeté est évaluée. Dans TranSIESTA, une approche différente est adaptée, à savoir qu'on peut considérer explicitement le système avec des conditions aux limites ouvertes, et traiter les conditions hors-équilibre provoquées par la tension appliquée en utilisant le formalisme de Keldysh avec la fonction de Green hors-équilibre.

Résumé des calculs du matériau massif

Dans la première étape, nous avons considéré l'influence des lacunes d'oxygène sur la structure électronique de MgO massif. Le MgO est un cristal ionique avec une structure cubique à faces centrées (FCC) dans laquelle chaque atome de Mg ou d'oxygéne est six fois coordonné.[27] Par conséquent pour le calcul de la structure électronique de MgO avec les lacunes d'oxygéne, ces lacunes ont été générées dans des supercellules ayant une structure cubique simple avec 64 ou 216 atomes en enlevant simplement un centre F ou deux atomes d'oxygène neutres voisins (M-center). Pour tous les calculs, nous avons utilisé le paramètre de réseau expérimental du MgO.

L'élimination d'un atome d'oxygène produit une cavité (dans l'environnement octaédrique) avec deux électrons confinés. En conséquence, un état localisé est créé dans la densité d'états du MgO autour de 1.1 eV en dessous du niveau de Fermi (E_{F}).[28,30,48] C'est un état fondamental avec une symétrie des orbitales s. L'état excité correspondant est placé près du minimum de la bande de conduction (CB) et possède une symétrie p.[28,29]

Le centre M est formé en supprimant deux atomes d'oxygène voisins (distance 3 Å), créant ainsi une double lacune. Dans l'état fondamental du centre M, il reste quatre électrons qui forment deux niveaux occupés dans la structure de bande du MgO. Cette situation est présentée dans la Fig. 1 ou la lacune double d'oxygène entraîne la création de deux niveaux d'énergie occupés au-dessous de E_{F}. Les électrons qui restent, après élimination de l'oxygène, sont localisés sur les sites de lacune, et interagissent, ce qui entraîne la création de deux niveaux d'énergie occupés distincts qui ressemblent à la création de niveaux liants et antiliants (basés sur la distribution d'électrons présentée dans les encadrés de la Fig. 1).

Pour comprendre la nature des niveaux du centre M, nous avons calculé la structure de bande d'orbitale projectée, appelée "fat bands", et la densité d'états électroniques projetée sur les orbitales (PDOS) pour le M-MgO comme indiqué sur la figure 1. Les états de valence de MgO sont principalement de caractère O p tandis que les bandes de conduction sont faites de Mg mélange des états s et des états p. Les niveaux de défauts montrent principalement des contributions d'orbitales sous forme p avec une plus petite partie provenant des états s. En projetant séparément la DOS sur des sites de Mg et O, nous avons trouvé que pour la plupart, les niveaux M sont créés par des orbitales Op s'hybridant avec des états s et p provenant du Mg. La contribution des états de type d est beaucoup plus petite et peut être négligée.

Des résultats similaires ont été obtenus lorsque nous avons étudié la distribution électronique autour des sites vacants ou lacune pour une gamme d'énergie contenant les niveaux d'état fondamental du centre M et les états excités correspondants dans la région de la bande de conduction. La figure 2 présente une distribution spatiale de la

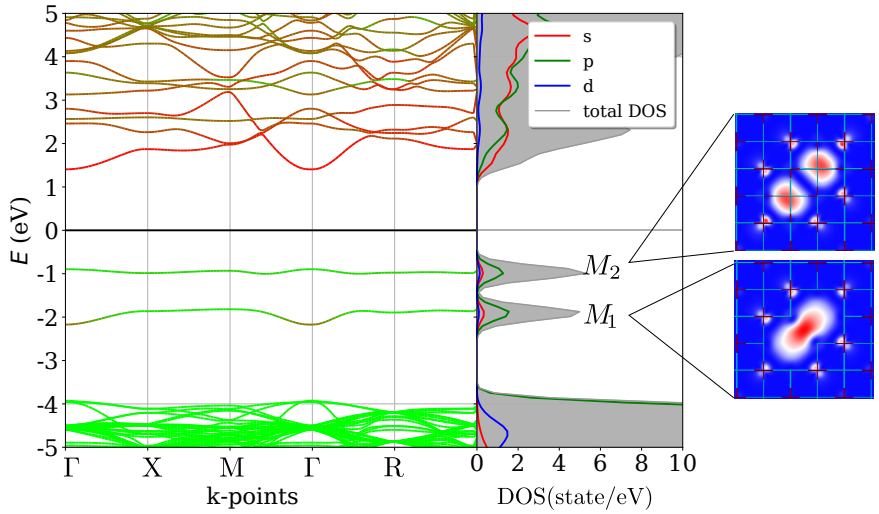

Figure 1: Structure de bandes et DOS projetéé par orbitale pour M-MgO. Les encarts montrent la distribution des électrons pour chacun des niveaux d'énergie de l'état fondamental du centre M.

densité électronique à la fois pour l'état fondamental (panneaux a/c) et états excités (panneaux b/d) de M-MgO. Dans les panneaux a/b (c/d), une supercellule de 214 atomes (62 atomes) a été utilisée. Les électrons restant après l'élimination de l'oxygène sont localisés sur les sites vaccants ou les lacune. Puisque l'état excité du centre M se trouve dans les états de la bande de conduction, une densité électronique non nulle est présente sur les atomes loin du défaut. Les diagrammes de densité électronique révèlent également une hybridation entre les états fondamenaux et les états excités du centre M et les ions d'oxygène les plus proches qu'en effet le niveau de déviation devrait être principalement dû aux orbitales Op.

De plus, le centre M affecte aussi les atomes d'oxygène les plus proches qui conduit à sa taille effective de 4 ML dans le plan de défaut et 3 ML dans la direction perpendiculaire. Ce fait restreint la taille de l'espaceur MgO qui peut être utilisé pour préserver les propriétés des centres M à au moins 5 ML. La distribution d'électrons indique aussi que les états fondamentaux du centre reflètent principalement la distribution de type s, alors que les états excités sont de type p. De plus, nous traçons sous forme d'encart dans la Fig. 1 séparement la distribution des électrons pour chacun des centres centre M. Il est clair que la distribution d'électrons pour l'état M_1 ressemble à un état liant et M_2 a un comportement d'état antiliant. Comme dans le cas de la formation de liaison entre les atomes, le couplage entre deux centres F provoque la création d'état liant avec une énergie plus faible et un état anti-liant avec une énergie plus élevée par rapport à l'état F d'origine. Par conséquent, la hauteur de la barrière créée par le centre F sera toujours supérieure à celle associée à l'état M_2.

Comme prévu, la bande interdite du MgO calculée avec la GGA est de 4.73 eV et est inférieure à la valeur expérimentale de 7.8 eV. Afin de corriger cette bande interdite, nous avons utilisé une fonctionnelle hybride (HSE03) qui mélange l'échange de Fock non local avec l'échange DFT dans une certaine proportion. En ajustant la proportion d'échange de Fock dans la fonctionnelle HSE03, nous avons reproduit la

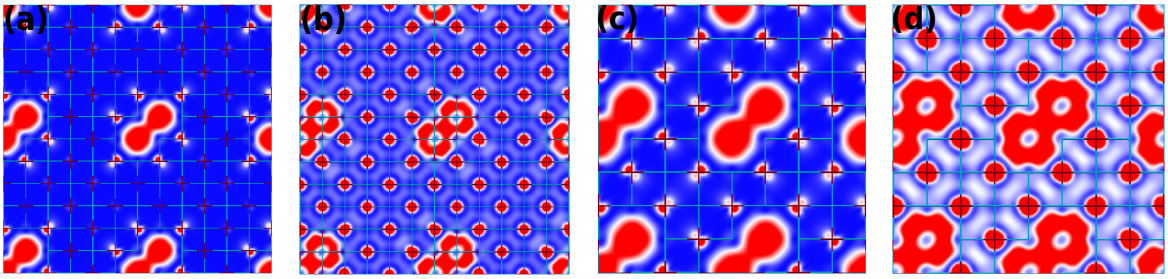

Figure 2: Une distribution spatiale de la densité électronique à la fois pour l'état fondamental (panneaux a/c) et états excités (panneaux b/d) de M-MgO. Dans les panneaux a/b (c/d), une supercellule de 214 atomes (62 atomes) a été utilisée. Des images périodiques sont également montrées.

bande interdite expérimentale de 7.8 eV. Comme les calculs avec des fonctionnelles hybrides nécessitent beaucoup de temps CPU et de mémoire, nous avons limité ces calculs à la supercellule de 64 atomes. Pour les F-MgO et M-MgO, par rapport aux résultats GGA, la fonctionnelle hybride provoque un déplacement des bandes de valence et de conduction vers les basses et hautes énergies, respectivement. Mais en dehors d'un léger changement dans la position énergétique de M_1, nous obtenons une dépendance énergétique similaire de la DOS. Il convient de noter que les niveaux de défauts sont placés près du milieu de la bande interdite de MgO indépendamment de la fonctionnelle utilisée. Cela démontre que des calculs moins intensifs, fondés sur la GGA, produisent déjà semi- quantitativement les propriétés électroniques des lacunes d'oxygène dans le MgO. La GGA peut par conséquent être utilisée pour étudier les structures plus compliquées, telles que les jonctions Fe/MgO/Fe.

Jonctions Fe(FeCo)/M-MgO

Nous avons ensuite considéré, le cas des hétérostructures à base de Fe ou FeCo et MgO. Nous avons fixé le paramètre de réseau du MgO ($a_{\mathrm{MgO}} = 4.21$ Å) et réglé le réseau des électrodes ($a_{\mathrm{Fe/FeCo}} = \sqrt{2}a_{\mathrm{MgO}}$). Ce choix reflète la preuve expérimentale[49] que le recuit des JMT de FeCoB/MgO conduit à une recristallisation des interfaces afin que l'électrode adopte la constante de réseau du MgO. La distance entre Fe(Co) et O à l'interface a été fixée à 2.17 Å. De plus le niveau de Fermi est déplacé en énergie pour chaque type d'interface.

Dans la figure 3, nous présentons la densité d'états (DOS) projetée pour les couches des systèmes Fe(7ML)/M(F)-MgO(7ML) et FeCo(7ML)/M(F)-MgO (7ML) où E_F est au zéro d'énergie. Comme on peut le voir, les deux premières couches de la barrière MgO produisent certains états dans la bande d'énergie interdite. De plus, la bande interdite diminue pour les couches MgO proche de l'interface. Les troisième et quatrième couches ont la même DOS et la même bande interdite que le MgO massif. Comme on l'a mentionné précédemment, le changement des électrodes déplace également le niveau de Fermi (E_F): les positions des états de défauts par rapport à E_F sont légèrement modifiées. Nous avons ainsi pu constater que le niveau du centre F apparaît entre -1.2 eV et -0.7 eV pour les électrodes Fe et FeCo, respectivement, en accord avec la

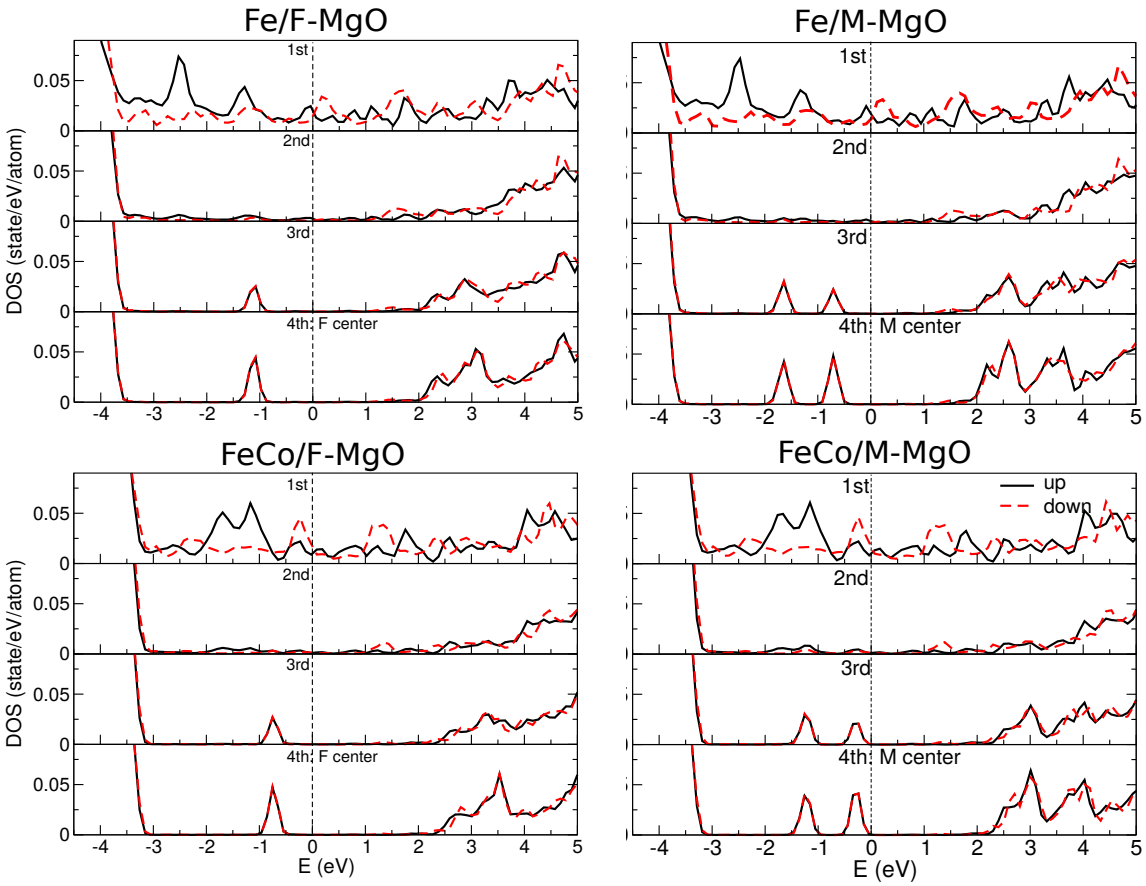

Figure 3: DOS projetée sur les couches pour les jonctions Fe/F-(M-)MgO (hauts panneaux) et FeCo/F-(M-)MgO (bas panneaux).

valeur expérimentale de -1.1 eV. L'état M_2 obtenu à -0.7 eV (électrode Fe) et à -0.2 eV (électrode FeCo) correspond à la valeur expérimentale de la barrière de -0.4 eV. Il est important de noter que si nous déplaçons le centre M dans l'espaceur MgO ou si nous changeons son orientation, les positions des pics restent pratiquement identiques. Ce qui nous permet d'associer les barrières expérimentales de 0.4 eV à l'existence de centres M dans le MgO.

Transmission par F(M)-MgO/Fe MTJs

Nous avons commencé avec les calculs de jonctions avec la structure idéale de MgO pour avoir un point de référence lorsque les défauts sont introduits. Le nombre de couches de MgO a été varié et nous nous sommes d'abord concentrés sur les structures avec 5 Mono-couches (MC) d'espaceur. Les résultats trouvés pour 7 ML d'espaceur sont similaires et ne seront discutés que brièvement. Toutes les données présentées concernent la conductance calculée au niveau de Fermi.

La figure Fig. 4 présente la transmission dans la zone de Brillouin bidimensionnelle (2D BZ) pour l'aimantation de l'électrode parallèle pour les canaux d'électrons spin up et spin down (les panneaux de gauche et du milieu) et la transmission correspon-

dante pour la configuration antiparallèle (le panneau de droite). En accord avec les prédictions théoriques précédentes, nous avons trouvé que la transmission d'électrons majoritaire était centrée autour du point Γ et est dominée par la symétrie Δ_1. La transmission pour le canal minoritaire se produit essentiellement sur les bords de la BZ 2D et est beaucoup plus petite que pour le canal majoritaire. La transmission dans la configuration AP est un mélange de caractéristiques observées dans les deux canaux de spin. En additionnant la transmission sur la BZ et en multipliant par G_0 pour chaque canal, nous avons obtenu la conductance et la TMR résultante.

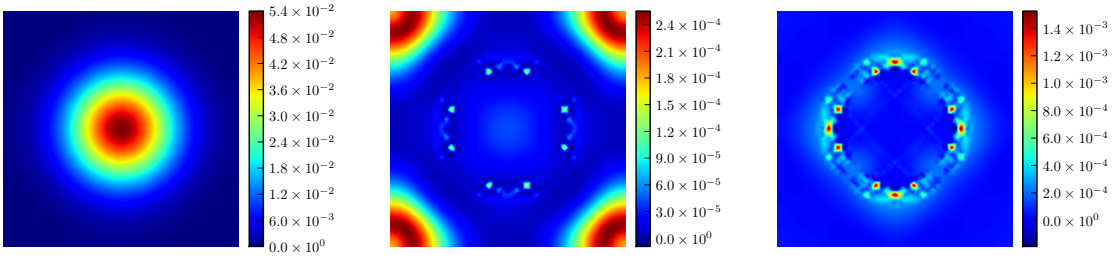

Figure 4: La transmission dans la zone de Brillouin bidimensionnelle (2D BZ) pour le Fe/MgO(5MC)/Fe ideal jonction pour l'aimantation de l'électrode parallèle pour les canaux d'électrons spin up et spin down (les panneaux de gauche et du milieu) et la transmission correspondante pour la configuration antiparallèle (le panneau de droite). Toutes les autres figures de transmission sont disposées de la même manière.

Dans Tab. 1 nous avons résumé les résultats pour les jonctions avec 5 et 7 MC de MgO. Comme prévu, la valeur de la transmission décroît exponentiellement avec l'épaisseur de l'espaceur MgO et diminue donc d'au moins un ordre de grandeur lorsque nous passons de 5 à 7 MC de MgO. En même temps, la TMR augmente avec le nombre de couches de MgO. Cela reflète l'effet de filtrage de spin. En particulier, le long de la direction de transport au niveau de Fermi du Fer, des états avec des symétries différentes pour les électrons spin-up et spin-down existent et donnent lieu à des valeurs TMR élevées pour les jonctions cristallines Fe/ MgO/Fe. Les canaux de symétrie Δ_5 et Δ_2 apparaissent pour les deux populations de spin et contribuent à la conductance dans les configurations P et AP. La symétrie Δ_1 n'est présente que pour la population électronique majoritaire et domine la transmission dans la configuration P. Chacun de ces canaux de symétrie a un taux d'atténuation différent dans la région de barrière, tel que $\kappa_{\Delta_1} < \kappa_{\Delta_5} < \kappa_{\Delta_{2/2'}}$. Lorsque l'épaisseur de MgO est augmentée, les contributions à la conductance des canaux Δ_5 et Δ_2 fortement atténués deviennent plus faibles. Ceci conduit à une plus grande différence globale dans la transmission entre les configurations P et AP et provoque l'augmentation de la TMR. D'après la littérature,[50] la valeur de la TMR devrait continuer à croître jusqu'à 13 MC de MgO où l'on s'attend à ce que le Δ_1 domine la transmission. Après avoir dépassé cette épaisseur, la TMR commencera également à diminuer en raison de la décroissance exponentielle du courant tunnel.

Table 1: La transmission totale calculée et la TMR résultante pour le Fe/MgO/Fe idéal jonction avec 5 et 7 MC de MgO.

	P-UP	P-DOWN	AP	TMR [%]
5 MC	$7.90{\cdot}10^{-3}$	$4.57{\cdot}10^{-5}$	$9.99{\cdot}10^{-5}$	7850
7 MC	$5.33{\cdot}10^{-4}$	$2.93{\cdot}10^{-7}$	$4.26{\cdot}10^{-6}$	12402

Centre F/M dans la couche intermédiaire de MgO

Dans la prochaine étape de nos études, nous avons généré des lacunes d'oxygène dans la couche intermédiaire de l'espaceur MgO. Le centre M a été placé dans un plan parallèle aux interfaces. Les figures 5(c) et 6(c) montrent la transmission ZB 2D correspondante pour les centres F et M, respectivement. La distribution de transmission pour les électrons spin-down (spin minoritaire) est presque inchangée par la présence des lacunes. Nous avons observé seulement une augmentation de l'amplitude de transmission par rapport au cas idéal. Des changements plus importants sont notés dans le canal d'accélération où une distinction claire entre les défauts F et M peut être faite. Il semble que le centre F diffuse les électrons en propagation dans les états avec des valeurs de vecteur **k** plus élevées. En conséquence, la transmission a un minimum au point Γ et se produit principalement le long des lignes k_x et k_y ayant un maximum sur les bords de la ZB 2D. Les électrons sont dispersés symétriquement dans chaque direction en raison de la symétrie sphérique d'une seule lacune d'oxygène. Cependant, pour la transmission des centres M, elle devient élargie dans la ZB 2D et a des valeurs maximales principalement centrées autour du point Γ. Ceci suggère clairement que, contrairement au centre F, le transport cohérent peut encore être possible lorsque les centres M existent dans l'espaceur MgO. La transmission totale est cependant réduite par rapport à la jonction idéale (tableau 2). En outre, la distribution de transmission dans la configuration AP change de manière significative par rapport à la figure 1. La baisse de la TMR lorsque les défauts sont présents est évidente mais atteint des valeurs plus élevées pour le centre M plutôt que pour le centre F. Nous avons trouvé des tendances similaires pour l'espaceur de 7 MC pour lequel la transmission totale est indiquée dans le Tab. 1. Encore une fois, si nous augmentons le nombre de couches de MgO, la TMR augmente également quel que soit le type de défauts. Les résultats de transmission obtenus pour les structures avec des lacunes d'oxygène peuvent expliquer les résultats expérimentaux d'une TMR élevée dans les jonctions avec la hauteur de barrière de 0.4 eV due à des lacunes d'oxygène appariées. Ils confirment également l'hypothèse initiale qu'un transport cohérent peut être préservé lorsqu'un centre M est présent.

Table 2: La transmission totale calculée et la TMR résultante pour les Fe/F-MgO/Fe et Fe/M-MgO/Fe jonctions avec 5 et 7 MC de MgO. Les centres F et M sont toujours dans la couche intermédiaire de MgO.

	P-UP	P-DOWN	AP	TMR [%]
F (5ML)	$7.21{\cdot}10^{-4}$	$6.31{\cdot}10^{-5}$	$3.20{\cdot}10^{-4}$	145
M (5ML)	$1.71{\cdot}10^{-3}$	$1.47{\cdot}10^{-4}$	$4.48{\cdot}10^{-4}$	315
F (7ML)	$1.19{\cdot}10^{-5}$	$6.21{\cdot}10^{-7}$	$3.08{\cdot}10^{-6}$	304
M (7ML)	$6.19{\cdot}10^{-5}$	$6.87{\cdot}10^{-7}$	$3.63{\cdot}10^{-6}$	1624

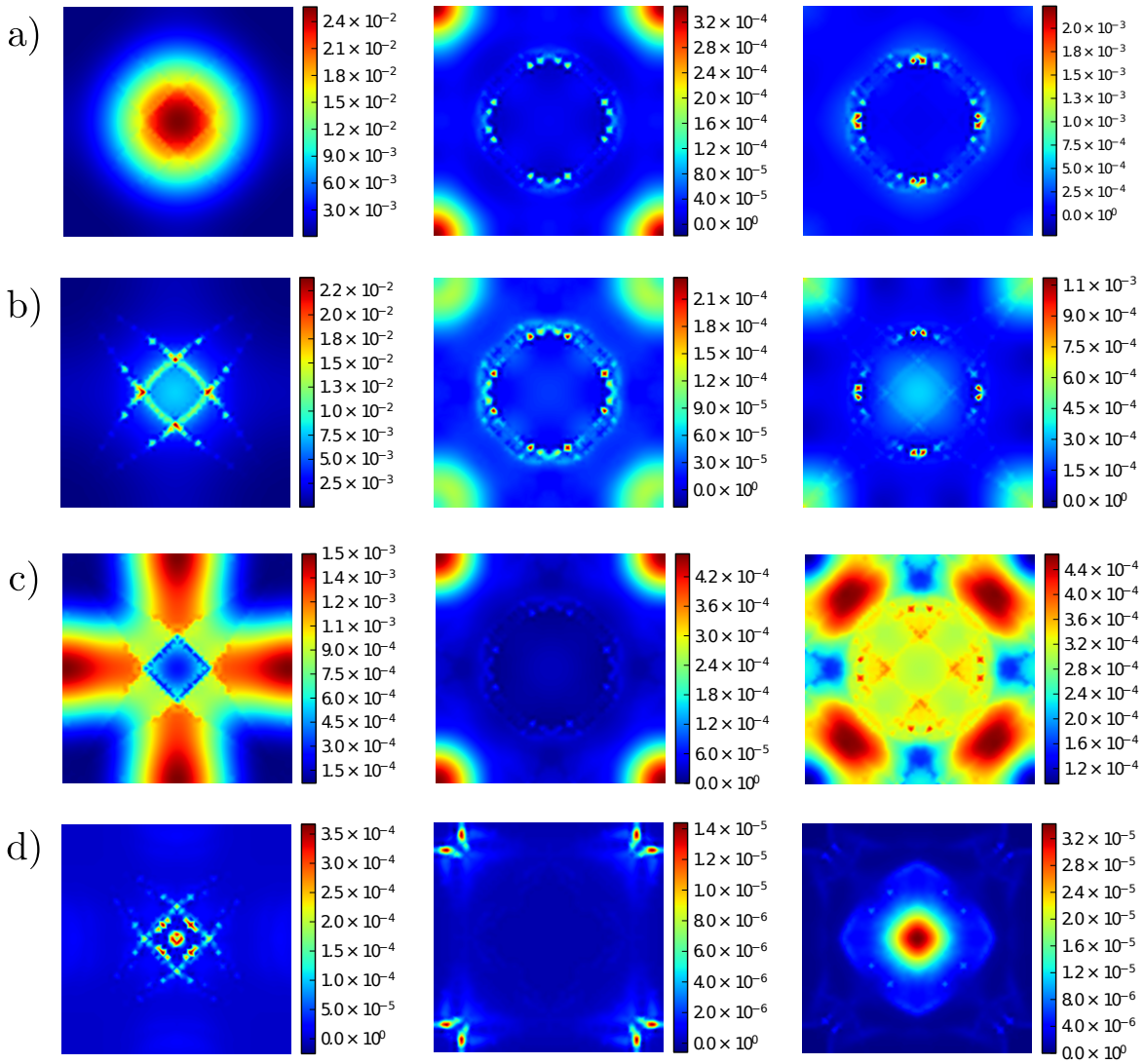

Figure 5: La transmission dans la 2D BZ pour le Fe/F-MgO/Fe avec le centre F dans la a) premier MC, b) deuxième MC, c) troisième MC et d) quatrième MC. Notez que les panneaux a-c sont pour F-MgO avec 5 MC espaceur alors que le panneau d est pour 7 MC.

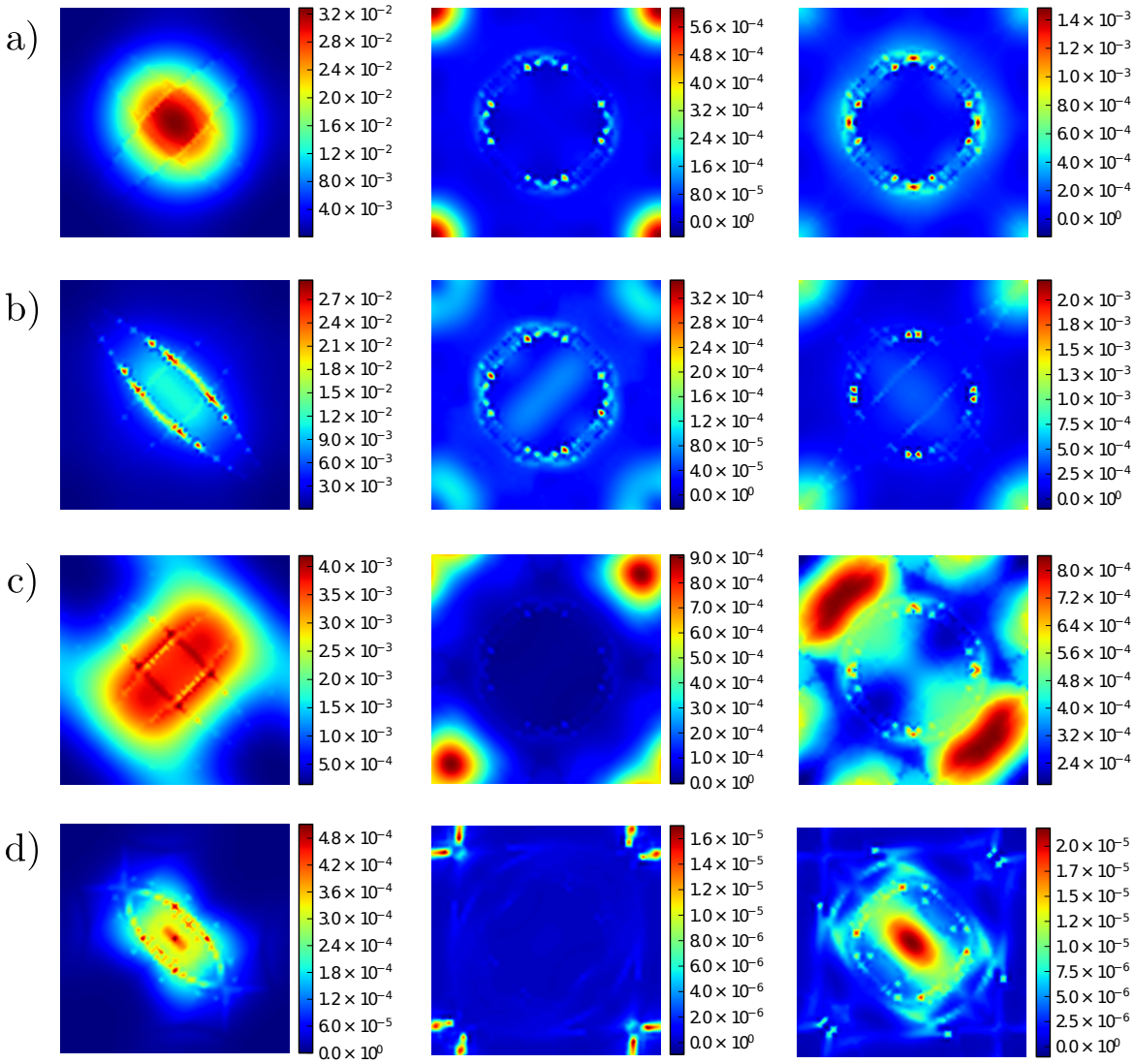

Figure 6: La transmission dans la 2D BZ pour le Fe/M-MgO/Fe avec le centre M dans la a) premier MC, b) deuxième MC, c) troisième MC et d) quatrième MC. Notez que les panneaux a-c sont pour M-MgO avec 5 MC espaceur alors que le panneau d est pour 7 MC.

Effet du décalage de la lacune sur la transmission

Nous avons voulu vérifier si les modifications de la transmission induites par les centres F et M sont sensibles à leur position dans la jonction et donc au milieu environnant. Pour ce faire, nous avons modifié la position et l'orientation des lacunes F/M dans le MgO. Bien que, nous n'avons pas observé de changement significatif dans la couche projetée DOS lorsque la lucune s'approche de l'interface, le calcul montre que la transmission dépend significativement de la position du défaut.

Les figures 5(a) et 6(a) montrent la transmission 2D BZ avec des lacunes générées dans la couche interfaciale MgO. Notez que le centre M est toujours dans le plan parallèle aux interfaces. Nous avons constaté que la distribution de la transmission est presque la même que pour la jonction idéale avec l'amplitude des pics très proche du cas idéal (voir la figure 0.4). La TMR calculée atteint environ 4261% et 3911% pour le centre F et M respectivement, et elles sont du même ordre de grandeur que celles de la jonction idéale.

Lorsque nous avons placé des lacunes sur la deuxième couche à partir de l'interface, nos calculs montrent que la transmission diminue (figures 5(b) et 6(b)) alors que les distributions de diffusion et de transmission AP ne sont que légèrement affectées. Encore une fois, il n'y a pas de distinction claire entre l'influence du centre F et M.

Pour comprendre ce comportement, nous avons comparé ces résultats avec le cas de l'espaceur MgO de 7 MC où la lacune est dans la couche intermédiaire et écrantée symétriquement des électrodes ferromagnétiques par trois couches de MgO de chaque côté. La transmission résultante pour le centre F et M est représentée sur les Fig. 5(d) et 6(d), respectivement. Une fois de plus, nous assistons à l'apparition de caractéristiques supplémentaires provenant de pics pointus entourant le pic du milieu. Certains changements sont également perceptibles dans le spin-down et la transmission AP, mais ces changements sont dus aux effets de filtrage de symétrie discutés précédemment. Nous pourrions essayer d'expliquer ce comportement de type oscillatoire en considérant la position géométrique de la lacune par rapport aux atomes de Fe. Nous pouvons distinguer deux situations: (i) les atomes d'oxygène/lacunes sont directement au-dessus des atomes de Fe, (ii) la distance entre Fe et O/lacune est augmentée et l'interaction Fe-lacune est écrantée par des atomes de Mg. Nous obtenons des caractéristiques plus nettes que celles observées lorsque la lacune est dans la même ligne que l'atome de Fe interfacial. L'alternance des couches provoque également la rotation du centre M dans le plan xy lorsque l'on passe d'une couche à la suivante et explique la rotation observée dans l'amplitude de transmission dans la ZB 2D (comparer par exemple les panneaux (c) et (d) Fig. 6).

Rotation du centre M

Un autre scénario intéressant que nous avons pris en compte la rotation dans le plan du centre M. Les résultats dont nous avons discuté jusqu'ici concernaient le centre M placé dans un plan MgO parallèle aux interfaces. Puisque le centre M s'étend sur plusieurs couches, il peut être tourné par rapport à la direction de transport. Les calculs de structure de bandes complexes (CBS) ont indiqué que si le centre M est partiellement dans la direction de transport, le coefficient d'atténuation pour le Δ_1 peut être encore

plus petit ou comparable au cas idéal. Par conséquent, nous avons voulu vérifier si cela a un impact sur la valeur de la transmission. Pour être cohérent, nous avons étudié une structure symétrique de la jonction avec un nombre pair de couches de MgO avec le centre M généré dans les deux couches intermédiaires. Nous avons commencé avec un espaceur MgO de 4 MC mais cela n'était pas suffisant pour filtrer correctement le centre M de l'influence des électrodes Par conséquent, nous avons augmenté l'épaisseur de MgO à 6 MC avec le centre M réparti entre la troisième et la quatrième couche. Nous avons également augmenté le nombre de couches des électrodes pour assurer une adaptation géométrique correcte aux interfaces.

La figure 7 présente la transmission pour les deux canaux de spins dans la configurations P et AP. Les transmissions par ralentissement P et AP ne sont pratiquement pas affectées par le défaut. La transmission est encore plus concentrée autour du point Γ. La valeur de TMR atteint 1423%, aussi élevée que le centre F/M dans la couche interfaciale. En fait, si nous comparons la transmission par spin up de la figure 7 et 6(c), nous concluons que la forme de la transmission reflète dans un certain sens la symétrie/orientation du centre M. Lorsque le centre M est généré dans le même plan xy, c'est-à-dire parallèle aux interfaces, la fonction d'onde électronique rencontre simultanément les deux lacunes d'oxygène. Cela explique également l'augmentation du pic de transmission le long de la diagonale du plan de la figure 6(c). D'autre part, lorsque le centre M est partiellement dans la direction de transport, c'est-à-dire dans le plan yz où les deux lacunes d'oxygène sont dans des plans xy consécutifs, l'électron se propage d'abord la première lacune d'oxygène puis dans l'autre. En conséquence, la transmission est maintenant plus improrante suivant la direction k_y de la ZB (figure 7).

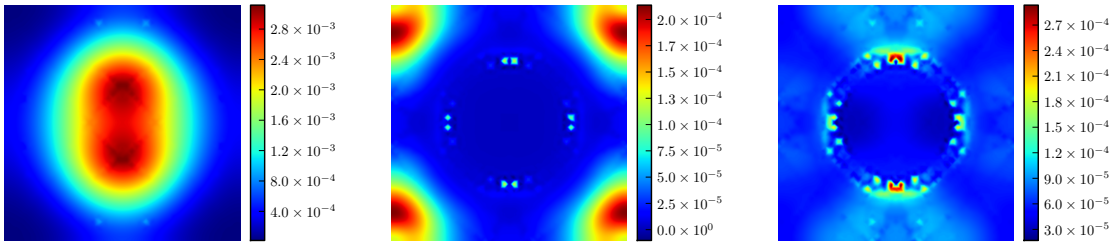

Figure 7: La transmission dans la 2D BZ pour le Fe/M-MgO/Fe avec 6 MC de MgO avec le centre M réparti entre la troisième et la quatrième couche.

Mesures In operando

Les techniques expérimentales en science des matériaux se concentrent usuellement soit sur des investigations des ropriétés physiques, ou soit sur la réponse d'un dispositif soumis à un stimulus extérieur. Ces dernières années, les études dites *in operando* se sont multipliées combinant études des matériaux et études des dispositifs. L'objectif est de corréler les performances des dispositifs avec leurs propriétés physiques.[51–54] Cette nouvelle approche a été utilisée pour des jonctions magnétiques tunnel à base de MgO où les jonctions, durant les mesures de magnéto-transport, ont été

éclairées par des rayons X mous. Cette procédure permet d'évaluer les contributions des photoélectrons émanant de l'état 1s de l'oxygène sur le transport électronique. Ces nouvelles expériences ont été effectuées au synchrotron SOLEIL par des expérimentateurs de l'IPCMS et ont été interprétées à l'aide de nos calculs théoriques.[55]

Les dites jonctions étaient composées de FeCoB(4)/MgO(2.5)FeCoB avec du SiO_2 utilisé pour isoler l'électrode supérieure de l'électrode inférieure du dispositif. Le rôle clé des performances des MTJ est joué par le spin et la densité d'état polarisée en symétrie des états électroniques créés à l'interface entre le ferromagnétique de l'électrode et la barrière tunnel. Ici, un des facteurs cruciaux est la présence de liaisons Fe-O. En conséquence, l'étude s'est concentrée sur le seuil K de l'oxygène.

Comparons les spectres XAS avec les mesures de magnétorésistance, comme présenté dans la Fig. 8. Le transport électronique à travers la MTJ a été mesuré en faisant varier l'énergie des photons. En raison des mécanismes de filtrages en symétries à travers les jonctions de Fe/MgO/Fe, la résistance R change lorsque que l'on passe de l'alignement parallèle à un alignement antiparallèle de l'aimantation des électrodes. C'est ceci qui définit la TMR du dispositif. La transmission dominante dans les canaux P et AP est gouvernée par les électrons de symétrie Δ_1 et Δ_5 respectivement. Les panneaux (b) et (c) correspondent à la dépendance $R(E)$ à T= 20 K lorsque l'on atteint le seuil O K et lorsqu'un voltage de 10 mV est appliqué dans les configurations parallèle (R_{P}) et antiparallèle (R_{AP}) de l'aimantation des électrodes.

La région pré-seuil d'énergie $537 < E(eV) < 541$, R_{P} montre clairement un petit minimum à 539.3 eV quand les états $\Delta_1^{\downarrow}$ de l'oxyde de fer interfacial est adressé. Ceci montre que les liaisons Fe-O sont présentes et jouent un rôle dans le transport, bien que les mesures XAS aient montré une réduction de ces liaisons avec le recuit. On peut expliquer ce minimum dans R_{P} en considérant un électron supplémentaire dans un état "excité" qui apparaît en raison de l'absorption des rayons X et qui augmente le transport électrique à travers le Fe-O supposé autrement isolant et diminuant ainsi la résistance. Cet effet est présent seulement dans R_{P} puisque le canal de transmission Δ_1 domine l'effet tunnel à travers le MgO dans l'état P. D'un autre côté, R_{AP} n'est pas affecté par la photo-excitation des états $\Delta_5^{\downarrow}$ de l'oxyde de fer, car les états de spin up correspondant sont totalement occupés. De ce fait, il n'y a pas d'état disponible dans la contre électrode (nous supposons ici que les deux interfaces sont oxydées). Nous n'observons pas de fortes corrélations entre le XAS de la couche d'encapsulation de SiO_2 et le magnéto-transport pour R_{P} et R_{AP}. Ceci indique que l'excitation des états Si-O n'influence pas les performances du dispositif. En conséquence, la périphérie des piliers des MTJ joue un rôle secondaire dans les performances du dispositif.

Pour comprendre ce comportement, nous avons fait des calculs théoriques en utilisant une approche dite $Z+1$.[56–58] Cette approximation peut être utilisée pour simuler la structure électronique d'un atome lorsque celui-ci absorbe des photons X et dans lequel un électron additionnel est placé dans la bande de conduction. En pratique, ceci veut dire que nous avons remplacé l'oxygène dans le MgO par du fluor qui possède un électron de plus que l'oxygène. De ce fait, nous obtenons un électron "excité" dans la bande de conduction. Pour valider cette approche, nous avons calculé l'XAS du MgO et du MgF avec le code VASP en utilisant la fonctionnelle PBE. L'XAS est calculé en se reposant sur l'approximation du dipôle électrique. La simulation de la cellule des deux

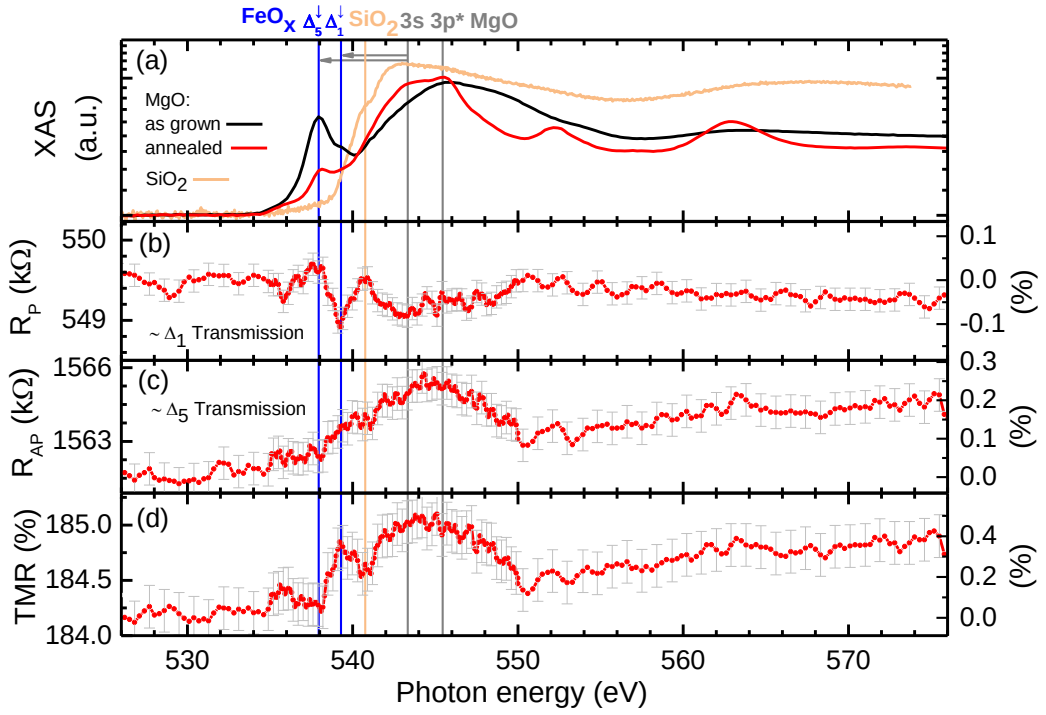

Figure 8: Mesures combinées de XAS et de magnétorésistance de MTJ à base de MgO. (a) Les spectres XAS acquis avec des photons polarisés verticaux linéaires sur les piles de référence du MgO recuit et non recuit, et encapsulant SiO $_2$. Noter une intensité décroissante des pics d'oxyde de Fe lors du recuit. La dépendance en énergie photonique de la résistance MTJ dans les états P (b) et AP (c) avec le rapport TMR résultant (d) a été enregistrée à $T = 20\,\mathrm{K}$ et basse tension de polarisation $V{=}{\pm}10\,\mathrm{mV}$. L'échelle de la main droite reflète l'écart par rapport à la ligne de base établie dans la région antérieure au bord. Extrait de la Réf. 55.

matériaux possède une structure bcc avec deux atomes par cellule unitaire. Pour faire coïncider les spectres expérimentaux avec les spectres théoriques, les courbes théoriques ont été déplacées en énergie et unefonction saut a été incluse. Nous trouvons une bonne concordance en ce qui concerne la séparation en énergie entre spectres théoriques et expérimentaux. La forme du seuil implique que même lorsque l'on remplace les sites d'oxygène avec du fluor, on conserve un nombre équivalent de transitions autorisées dans l'approximation dipolaire, ce qui suggère que le choix de l'approximation Z+1 donne un résultat raisonnable.

En conséquence, pour simuler des scénarii de façon plus réaliste, nous avons considéré la transmission à travers les jonctions Fe/MgO(5MC)/Fe avec un atome de fluor qui remplace l'oxygène dans la couche du milieu de MgO. La transmission résultante résolue en k est tracée dans la Fig. 9. En effet, nous avons remarqué une augmentation dans le canal de transmission de spin up par rapport au MgO non excité (voir Fig. 4). De plus, la transmission est plus large dans la BZ, mais toujours centrée autour du point Γ. La transmission totale sommée sur tous les points de la BZ, pour le canal de spin up augmente de $7.5 \cdot 10^{-3}$ à $1.85 \cdot 10^{-1}$. Le changement dans la transmission va de $4.63 \cdot 10^{-5}$ pour le MgO normal à $4.842 \cdot 10^{-4}$ pour le MgO "excité". Il apparaît clairement que le canal de spin up dominé par les contributions Δ_1 est plus affecté que

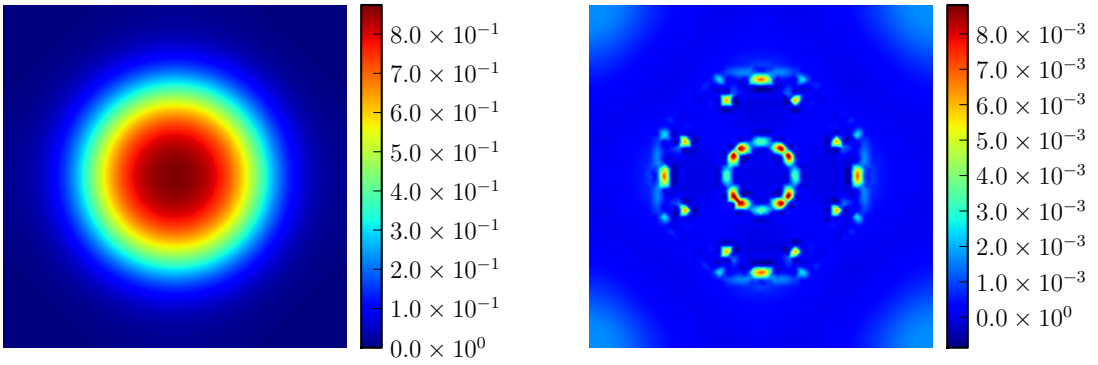

Figure 9: La transmission dans la 2D BZ pour le jonction Fe/MgO(5MC)/Fe avec un atome de fluor qui remplace l'oxygène dans la couche du milieu de MgO. Le panneau de gauche correspondre au canal d'électrons spin up et le panneau de droite au canal d'électrons spin down pour l'aimantation de l'électrode parallèle.

le canal de spin down où la symétrie Δ_5 domine. Ceci est en accord avec les prédictions CBS pour le MgO "excité" et l'expérience.

Conclusions

Cette thèse a été dédiée aux investigations théoriques en ce qui concerne les lacunes d'oxygène se trouvant dans un espaceur de MgO des jonctions tunnel magnétiques et leur impact sur le transport électronique. Puisque les procédés technologiques sont nécessairement liés à la création de défauts variés dans les MTJ à base de MgO, nous pouvons tenter de les utiliser et comme nous l'avons montré, les doubles lacunes d'oxygène peuvent donner lieu à des perspectives prometteuses pour les applications en spintronique. Comme nous l'avons trouvé, les hauteurs de barrière correspondant aux centres M sont toujours plus petites que les barrières associées aux centres F. Ceci est dû au processus de création des centres M durant lequel deux centres F s'hybridisent et donnent lieu à deux niveaux d'énergie de centre M, lesquels localisés dans la bande interdite du MgO, miment les états de liaisons/antiliaisons. Le niveau des anti-liaisons d'un centre M est toujours plus haut en énergie que le niveau en énergie d'un centre F et de ce fait, crée une hauteur de barrière plus basse pour les électrons qui tunnellent par rapport aux centres F. Quand nous avons incorporé les centres F et M dans les jonctions Fe(FeCo)/MgO, nous avons trouvé une diminution de la TMR d'un ordre de magnitude par rapport à une jonction idéale qui peut expliquer les différences mentionnées précédemment entre les TMR prédites théoriquement et les valeurs expérimentales. De plus, nous avons observé que les défauts avaient un impact plus important sur le canal de transmission de spin up où le rôle dominant est joué par les électrons de symétrie Δ_1 et laissent pratiquement inchangé le canal de spin down correspondant dominé par les électrons Δ_5 . Le centre F cause une forte dispersion de la fonction de propagation d'onde vers les états avec un vecteur $\mathbf{k}$ de valeur plus haute, ce qui fait décroître la conductance dans le canal de spin up pour la configuration P. Au contraire, en présence de centres M, les spectres de transmission ont été élargis dans la 2D BZ mais tou-

jours centrés autour du point Γ et de ce fait, préservent partiellement la transmission cohérente. Par Conséquent, nous obtenons toujours des valeurs plus hautes de la TMR en présence de centres M qu'en présence de centres F. Le facteur le plus crucial qui affecte les propriétés des centres F et M est leurs positions par rapport à l'interface. Placer des lacunes sur la couche interfaciale du MgO donne des formes de la distribution de transmission et de son amplitude pratiquement de même forme que pour une jonction idéale. Dans cette situation, il n'y a pas de distinction claire entre les centres F et M. Ceci peut être interprété comme une diminution effective de l'épaisseur de la barrière pour les électrons. Lorsque l'on a déplacé les lacunes plus loin de l'interface, la transmission a chuté drastiquement mais était plus importante en présence de centres M qu'en présence de centres F. Dans l'ensemble, s'il est impossible d'éviter les lacunes d'oxygène dans l'espaceur de MgO, il est mieux d'avoir des centres M que des centres F. Nos calculs ont aussi démontré que la formation d'une double lacune d'oxygène est énergétiquement préférable à deux lacunes séparées dans la même structure. De plus, les résultats expérimentaux ont montré que l'on est capable de contrôler le type de lacune d'oxygène dans l'échantillon en choisissent judicieusement les conditions de préparation. Par exemple, l'augmentation de la température de recuit jusqu'à 300°C peut déclencher le regroupement de lacunes d'oxygène dans des amas plus gros. Bien que nous n'allons pas éliminer totalement les lacunes de type F, nous pourrons diminuer leur population relative par rapport à ceux des centres M dans l'échantillon. Nous pensons que notre étude théorique nous donne un meilleur aperçu sur la transmission induite par les défauts au travers de jonctions tunnel magnétiques à base de MgO et aide à résoudre l'origine des hauteurs de barrières basses qui peuvent être maintenant associées aux doubles lacunes d'oxygène. Nous avons également expliqué comme il est possible de contrôler le type de lacune d'oxygène dans l'échantillon et déterminer les facteurs cruciaux qui définissent leurs propriétés. Nous espérons que ce travail contribuera dans le futur à faire avancer davantage la théorie et les expériences vers de possibles applications technologiques.

General introduction

Spintronics, or spin electronics, is a fast growing multidisciplinary field[1–4] of research concerned with the role played by electron spin in solid state physics. Its main scope of investigation concerns with the detection and manipulation of the spin degrees of freedom in solid-state systems.[1] The main question to answer is how the particle's spin interacts with its solid state environment and how one can use this knowledge to produce working devices. Therefore, the fundamental research on spintronics is about spin transport, its dynamics and relaxation in combination with effective ways of generating spin polarization in systems and their detection.

Spintronics research was developed thanks to the discovery of the giant magnetoresitance (GMR) phenomenon by Grunberg[6] and Fert[5] in 1988. In heterostructures composed of ferromagnetic electrodes separated by a thin metallic layer, they observed variations of the resistance as a function of the relative alignment of the magnetization of the ferromagnetic electrodes. The difference in the resistance for the parallel (P) and the antiparralel (AP) electrode magnetic alignments was the basis to define the magnitude of the GMR. It is well established now that the observed difference in the resistance was due to the different diffusion probability for the electron spin up and down populations to be transmitted from one ferromagnetic electrode to another. Since then, the GMR effect found applications in many fields, including hard disk read heads[59,60] or magnetic field sensors,[61,62] and offered an alternative to the semiconductor-based electronics.[63]

Another step forward was made by replacing the metallic layer by a thin non-magnetic insulating layer, thus creating the so called magnetic tunnel junction (MTJ). This was proposed by Julliere[7] in 1975 but its practical realization with a high tunnel magnetoresistance (TMR) ratio had to wait until the development of new deposition methods in the mid 90s. The first MTJs were based on Al_2O_3 as an insulating layer sandwiched between ferromagnetic electrodes.[64,65] The results of these MTJ, although promising, were still limited. The highest measured TMR with Al_2O_3 was at most 70% at room temperature. The theoretical studies by MacLaren *et al.*[8] concerning Fe/ZnSe/Fe MTJ revealed that the TMR can be greatly increased if the amorphous barrier is replaced by a crystalline one. Shortly after Mathon and Umerski[9] explored MTJs with MgO as an insulating spacer and showed that the resulting TMR exceed 10000%. Since the year 2000, MTJs with tunnel barriers of crystalline MgO have been under constant development due to their promising properties for applications from data read-out and storage to processing, magnetic sensors or novel logic devices.[66–68] Such a high TMR is indeed possible due to spin and symmetry preserving transport in the class of crystalline MTJs[8,10–13]

Despite the undeniable importance of MTJ technologies, the understanding of all physical aspects of operating devices is still not complete. The tunnelling magnetoresistance effect is a complex phenomenon and depends strongly on the electronic structure of the electrodes, the properties of the insulating barrier and on the chemical bonding at the interface between the two types of materials. All these complexities are reflected in the experimental realization where presently the highest values of the TMR reach 600% at room temperature[14] and are still much lower than the theoretical predictions. Yet, nothing is ever perfect in reality and any structural imperfections in the MTJs are expected to be a limiting factor of the measured TMR. Therefore, a special interest is directed towards controlling and explaining the impact of defects to create devices with desired properties. To understand the origin and the impact of structural imperfections on tunnelling process fundamental studies are necessary. The approaches, like *ab initio* electronic structure, are indispensable in understanding the mechanism of the magnetoresistance and modifications due to defects.

In our studies we focus on nominal MgO-based junctions with well established symmetry filtering properties. Nonetheless, the known principles apply to junctions with ideal crystal structure. The experimental studies often reveal an occurrence of interface oxidation[15] which affects the nature of chemical bonding at the interface between the ferromagnetic electrodes and the MgO spacer which in turn causes the TMR decrease. The combination of theoretical[16] and experimental[17] studies proved that even if one includes the interface disorder or the oxidation of the interfacial Fe layer the drastic drop of TMR cannot be fully explained. Although, a constant improvement of technological process of heterojunction preparation avoids oxidation at the interface and makes them of better quality, the values of TMR in the best junctions do not exceed few hundred percent.

Another type of defect to consider are grain boundaries in MgO. This kind of structural defect and its impact on transport is difficult to understand from both experimental and theoretical point of view. Nonetheless, it was shown in the literature[18,19] that grain boundaries can cause a decrease of the effective barrier of MgO, but this decrease can not explain the observed low barrier heights.

One more possible defect is due to atomic diffusion during the sample preparation and annealing. In particular, the main concern was about boron diffusion within FeCoB/MgO/FeCoB junctions since these type of MTJ are reported to have the highest TMR. In the literature[20–23] one can find a variety of possible sceneries concerning the faith of boron, for instance boron diffusion into MgO spacer (forming BO_x oxides) or the segregation at the CoFe/MgO interface. However, resent experimental investigations seem to prove that boron is not found within the MgO spacer[24–26] and with a proper annealing temperature, boron does not diffuse into the MgO but rather goes further away from the interfaces.

This motivates us to focus on defects created in the MgO spacer and especially on oxygen vacancies which are the most common type of possible imperfections. This kind of defect creates additional energy levels within the nominal band gap of MgO.[27–30] As a result, the barrier heights encountered by the propagating electrons are locally reduced. The electrons can then tunnel through the barrier via these additional states with different scattering rates than for an ideal barrier. Moreover, these additional lev-

els might be electrically probed and indeed several experimental groups have reported barrier heights for MTJs with an MgO spacer much lower than the nominal value of 3.9 eV, for instance barriers of heights 0.39/0.82 eV[31] and 0.39 eV[32] were found for Fe/MgO/Fe junctions or 1.1-1.7 eV for FeCo/MgO/FeCo junctions.[33] Yet, the exact identification of the type of defect responsible for a particular barrier height is still lacking. The most interesting barrier height is the one at 0.4 eV because it is favourable to coherent transport.[30,34] It was suggested by Schleicher *et al.*[30] that it can be the result of paired oxygen vacancies called "M-centers". Indeed, theoretical investigations of McKenna and Blumberg[34] predict that coherent transport can be preserved if the single oxygen vacancies are separated by less than 6 Å. It indicates that paired oxygen vacancies, or M centers, can preserve coherent tunnelling and symmetries of the incoming electrons. Since the properties of the M centers are not well understood, especially when incorporated in MTJs, they need more thorough studies. Intensive experimental investigations of MgO-based MTJs and the properties of single and paired oxygen vacancies in MgO are also conducted at IPCMS. This experimental effort needs a theoretical support to be able to correlate the measured device response with a particular type of oxygen vacancy. The main objective of this thesis is therefore to compute the electronic properties of oxygen vacancies in MgO and reveal their impact on spin and symmetry polarized transport in Fe/MgO/Fe junctions employing density functional theory.

This thesis is organized as follows:
The aim of the first part is to give a general introduction to the physics of the magnetic tunnel junctions. In chapter 1 we explain the basic concepts of the tunnelling magnetoresitance process and the models proposed to describe this phenomenon. We focus especially on crystalline junctions to emphasize the importance of the symmetry filtering effect. In chapter 2 we review the experimental and the theoretical studies of different kinds of structural imperfections in MTJs and their impact on the tunnelling current.

In the second part of this thesis we introduce our method of calculation. In chapter 3 we present the basics of the density functional theory (DFT), and we focus mostly on aspects that were of special importance to our work, especially the codes we use (VASP, Quantum Espresso and SIESTA). We present various convergence tests that were conducted to ensure the reliability of our results. In chapter 4 we extend the ground state formalism to the transport calculations. We first make an introduction to the electronic transport in nanoscale devices and derive the Landauer-Büttiker formula for the conductance. We then explain a practical implementation of this formalism in the PWcond and TranSIESTA codes used in this thesis.

The last part is devoted to the presentation of our results and their discussion. In chapter 5 we begin with a general discussion of the electronic properties of oxygen vacancies in MgO bulk material. Then, we switch to the case of Fe(Co)/MgO junctions where we examine the position of the defect level with respect to Fermi energy and explain the factors that might affect the defect level position. In chapter 6 we present the results of transmission evaluated at the Fermi level using the PWcond code. We discuss the changes in the transmission induced by oxygen vacancies and emphasize

the difference between the properties of a single (F) and double (M) oxygen vacancies. We then show how the geometrical position of oxygen vacancies with respect to the ferromagnetic electrodes can affect the transmission. In the last part of the chapter we present the results including the application of bias voltage between the electrodes. These latter results are however preliminary and not yet completely conclusive. In the last chapter we present a joint experimental and theoretical studies of MgO based junctions where the magnetotransport measurements are performed during a continuous illumination of the sample by soft x-rays. We discuss the way we used ground state DFT and the assumptions we made to support such a complex experimental study and try to understand the processes taking place during the experimental setup.

In the last part we give a general conclusions of this study and discuss some of the perspectives of this thesis.

Part I

Introduction and background

1

Introduction to the physics of magnetic tunnel junctions

The discovery of tunnelling magnetoresistance effect has triggered intensive studies to understand this novel physics and develop devices based on this phenomenon. Special interest is directed towards magnetic tunnel junctions (MTJs), where the canonical example is Fe/MgO/Fe system, composed of a MgO spacer sandwiched between Fe electrodes. Because of the high values of tunnelling magnetoresistnce ratio (TMR) predicted for such junctions,[9] they become promising candidates for applications from data read-out and storage to processing, magnetic sensors or novel logic devices.[66] The experimental values of TMR presently reach 600% at room temperature[14] while according to theory even higher values, reaching few thousand percent, are possible. These high values are due to conservation of both the electron's spin and the wave function symmetry during tunnelling through the structurally ordered barrier. In this chapter the basic physical concepts necessary for the understanding of the tunnelling magnetoresistance in crystalline junctions will be presented.

1.1 Origins of tunnel magnetoresistance

Here we consider two metallic electrodes separated by an insulator or a vacuum spacer. If we apply a bias between the electrodes in such junction according to lows of a classical physics we won't measure any current. The incoming electrons will encounter a potential barrier of the insulator and will be reflected at the interface. If however the insulating layer is made thin enough there is a non-zero probability for the electron to cross the potential barrier even though it does not have enough kinetic energy. This is known as a *tunnelling effect*[69] and is a purely quantum mechanical phenomenon. A simple illustration of the tunnelling process is presented in Fig. 1.1. An electron incoming from the left with energy E and wave function e^{ikz}, where $\mathbf{k}$ is the wave

vector, encounters a potential barrier of height V_B, where $V_B > E$. At the interface the electron wave function is partly reflected (re^{-ikz}) and partly transmitted through the barrier and reappears on the other side of the barrier (te^{ikz}). The amplitude of the electron wave function is exponentially attenuated within the barrier as $e^{-\kappa z}$ with $\kappa^2 = (2m/\hbar^2)(V_B - E)$. This simple model can be solved analytically by dividing the space into three regions and considering the form of the wave function in each of them separately. At the interfaces the wave function and its first derivative are required to be continuous. The derivation of this model can be found in quantum mechanics text books, will not be repeated here.

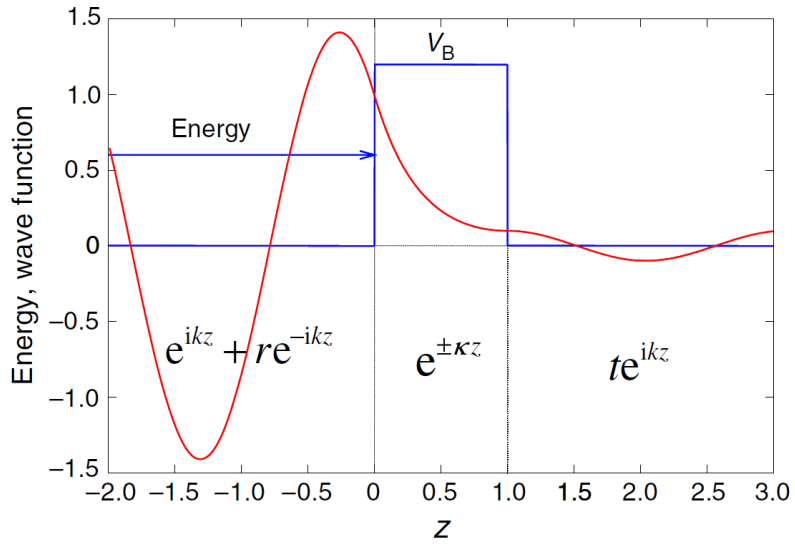

Figure 1.1: Simple barrier model for electron tunnelling. An incoming electron from the left with wave function e^{ikz} encounters a potential barrier of high $V_B > E$. At the interface the electron wave function is partly reflected, re^{-ikz} and partly transmitted through the barrier, te^{ikz}. Within the barrier the electron wave function decays exponentially as $e^{-\kappa z}$. Taken from Ref. 11.

Let's consider now a situation where the metallic electrodes are ferromagnetic. The basic feature of a ferromagnetic material is its *spin polarization*, i.e. the electron density of states (DOS) for spin up and down at the Fermi level (E_F) are different due to an exchange splitting mechanism.[70] A device, composed of two ferromagnetic electrodes and an insulating barrier placed between them is called a *magnetic tunnel junction* (MTJ). The inequality of the two spin populations and the fact that the electrons close to E_F are involved in the transport make the current across the tunnel barrier spin-polarized. The barrier hight seen by the electrons with different spins will be different. As a consequence, the resistance of a MTJ depends on the relative magnetization of the electrodes, which can be the same for the two electrodes (*parallel* configuration - P) or opposite (*antiparallel* configuration - AP). The magnetization of each ferromagnetic electrode can be reversed by an applied external magnetic field. Moreover, if the coercive fields of the ferromagnets are different the magnetization of each electrode can be reversed separately as schematically shown in Fig. 1.2.

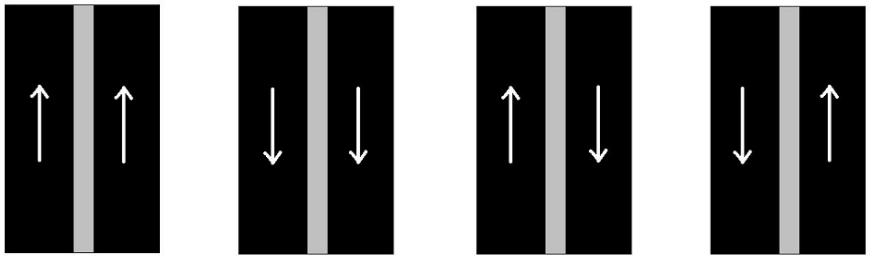

Figure 1.2: Four different magnetization configurations of the ferromagnetic electrodes in a magnetic tunnel junction.

This change in the resistance with the electrode's magnetization is called the *tunnel magnetoresistance* ratio and can be written as

$$TMR = \frac{R_{\mathrm{AP}} - R_{\mathrm{P}}}{R_{\mathrm{P}}} = \frac{G_{\mathrm{P}} - G_{\mathrm{AP}}}{G_{\mathrm{AP}}}, \tag{1.1}$$

where R_{P} is the resistance for the parallel configuration, R_{AP} for the antiparallel one and $G_{\mathrm{P}}, G_{\mathrm{AP}}$ are the corresponding conductances ($G = 1/R$).

In a ferromagnet, one spin population is greater than the other and is called the *majority* spin population and the other the *minority* one. Usually, the majority population spins are oriented parallel to the magnetization axis, and those of the minority one antipatrallel to it. In the following chapters the majority/minority spin populations and spin up/down electrons will be used interchangeably and treated as equivalent.

Although, the concept of the tunnelling magnetoresistance presented above seems simple, the quantitative theoretical explanation is not. Even today, not all the details are well understood since one has to determine accurately the electronic properties of both the electrodes and the insulating barrier. One has also to consider imperfections in the MTJs and the influence of external factors such as the voltage bias and/or the temperature. In the following subsections various approaches for describing the phenomenon of tunnel magnetoresistance will be discussed.

1.1.1 Julliere's model

One of the first explanation of the magnetoresistance phenomenon was proposed by Julliere in his famous paper published in 1975.[7] He considered the electron conductance between ferromagnetic electrodes as occurring within two separated spin sub-channels which do not mix. Thus, the total conductance for the parallel and the antiparallel configurations are the sum of the corresponding spin channels, i.e. $G_{\mathrm{P}} = G^{\uparrow\uparrow} + G^{\downarrow\downarrow}$ and $G_{\mathrm{AP}} = G^{\uparrow\downarrow} + G^{\downarrow\uparrow}$, respectively. Furthermore, it is assumed that the tunnelling current for each spin channel is proportional to the corresponding spin polarized DOS at the Fermi level of each electrode. Hence, the conductance in terms of DOS can be expressed as:

$$G_{\mathrm{P}} \propto \rho_1^{\uparrow}\rho_2^{\uparrow} + \rho_1^{\downarrow}\rho_2^{\downarrow}, \tag{1.2a}$$

$$G_{\mathrm{AP}} \propto \rho_1^{\uparrow}\rho_2^{\downarrow} + \rho_1^{\downarrow}\rho_2^{\uparrow}, \tag{1.2b}$$

where $\rho_i^{\uparrow}$ and $\rho_i^{\downarrow}$ stand for the spin up and down of the DOS density of states of each electrode, $i = 1, 2$ at the Fermi level.

The mechanism of two channel conductance is presented schematically in Fig. 1.3. In the parallel alignment case, the electrons with spin up from the emitting electrode tunnel to the collecting one only if at E_F there are states available for spin up electrons. The same rule also applies to the spin down population. Because at E_F there are less spin down states in the both electrodes, the parallel conductance G_P will be dominated by the majority spin channel. In the antiparallel case we basically switch the spin populations in one of the two electrodes such that the majority population becomes minority and minority becomes majority (Fig. 1.3(b)). As a consequence, the majority electrons from the emitting electrode have less available states in the collecting electrode to tunnel to and vice verse. Thus, the overall conductance in the AP configuration will be smaller than the P one, $G_{AP} < G_P$.

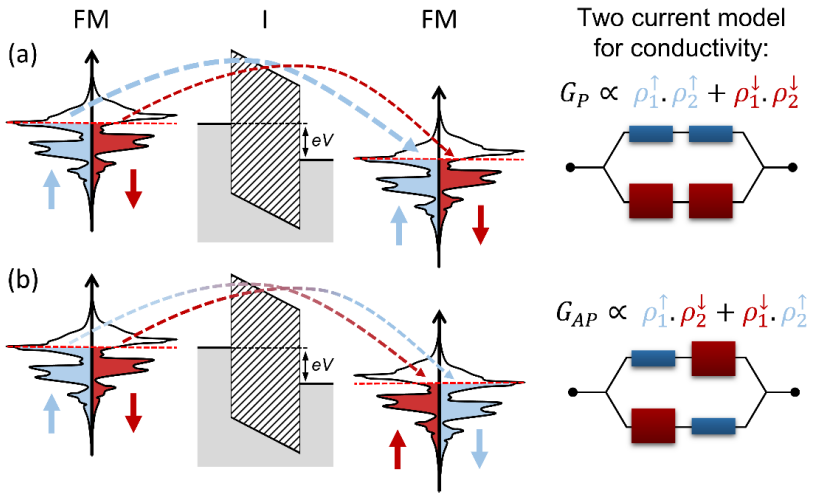

Figure 1.3: Two current model for the TMR. The electrons tunnel between the ferromagnetic (FM) electrodes through a potential barrier (I) when a bias V is applied. a) Parallel and b) antiparallel configurations are shown. Note that in the AP case the spin populations in the collecting electrode is switched with respect to that of the emitting electrode. On the right, the schematic application of two current model is shown to explain the resulting conductivity in both magnetic configurations.

Defining the spin polarization P_i of each electrode as the relative difference between spin up and down DOS at E_F:

$$P_i = \frac{\rho_i^{\uparrow} - \rho_i^{\downarrow}}{\rho_i^{\uparrow} + \rho_i^{\downarrow}}, \tag{1.3}$$

the TMR can be rewritten as

$$TMR = \frac{(\rho_1^{\uparrow}\rho_2^{\uparrow} + \rho_1^{\downarrow}\rho_2^{\downarrow}) - (\rho_1^{\uparrow}\rho_2^{\downarrow} + \rho_1^{\downarrow}\rho_2^{\uparrow})}{\rho_1^{\uparrow}\rho_2^{\downarrow} + \rho_1^{\downarrow}\rho_2^{\uparrow}} = \frac{2P_1P_2}{1 - P_1P_2} \tag{1.4}$$

In this model the spin polarization is an intrinsic property of the electrode material so if the electrode is non-magnetic, $P = 0$ and when the DOS of the electrode is fully spin-polarized at E_F, $|P| = 1$.

However simple in nature, the definition of the polarization in the Julliere model is not that straightforward. Experimentally the polarization can be measured using

ferromagnet/Al-O/superconductor tunnel junction[71] and for Fe, Ni and Co as electrodes it always gives positive values.[71,72] The TMR calculated with Julliere fomrula, eq. 1.4, based on the measured values of the polarization agrees quite well with the TMR observed experimentally. On the other hand, theoretical predictions based on ab inition electronic structure calculations for the polarization itself do not agree with the measured spin polarizations and resulting TMRs. In some cases even the sign of the calculated polarization is opposite to that obtained experimentally. This happens for example in the case of Co and Ni where the theory predicts negative spin polarizations, but the polarizations measured experimentally for these metals are positives.

The discrepancies between theory and experiment can be explained by considering what is actually missing in the Julliere model. Julliere described the TMR only using the DOS of the two spin populations of the two ferromagnetic electrodes. Yet, there is no distinction between bands with different electronic character (i.e. s, p or d-like states) or changes in electronic structure induced at the ferromagnet/insulator interface. Thus, further extensions of the model has to be made.

1.1.2 Stern's approach

In a $3d$ ferromagnets the electrical conductivity can be associated with s and d-like electrons.[73] The s-like electrons are more delocalized than the d electrons which is a consequence of different effective masses (bigger for d electrons). Therefore, the decay rate in the potential barrier is not the same for all incident electrons. This kind of reasoning was first proposed by Stern in 1977[74] to explain the observed spin-polarization of Fe, Co and Ni. Indeed, if one considers different character of the energy bands, the measured polarization will not correspond to the bulk value but rather to the polarization of band with the slowest decay rate within the barrier. Thus, Stern has redefined the polarization in terms of the electron wave vector:

$$P = \frac{k^{\uparrow} - k^{\downarrow}}{k^{\uparrow} - k^{\downarrow}}. \tag{1.5}$$

In the case of Co and Ni this implies that the s-electrons are mostly responsible for the tunnelling. These states are polarized due to a hybridization with d-like orbitals, which results in a positive spin polarization (opposite to the bulk value). This in turn explains the measured positive spin polarization.

The above considerations clearly show that the understanding of spin dependent tunnelling (SDT) requires more detailed knowledge of the electronic structure of the whole heterostructure.

1.1.3 Slonczewski's model

An improved model for describing the TMR was introduced by Slonczewski in 1989[75] who carried out calculations of a plane wave propagating through a complete FM/I/FM junction. He assumed tunnelling between two identical ferromagnetic leads separated by a rectangular potential step. The exchange-splitting of the spin bands in the ferromagnet was described by two parabolic bands shifted rigidly with respect to each

other. By applying periodicity along the layers in the x and y directions and matching the electron wave function at the interfaces, he solved the Schrödinger equation and obtained expression for the conductance in terms of the relative magnetization alignments of the two ferromagnetic electrodes as:

$$G(\Theta) = G_0(1 + P^2 \cos\Theta), \tag{1.6}$$

where Θ is the angle between the magnetization direction of the electrodes. The effective spin polarization of the ferromagnetic-barrier couple is given by

$$P = \frac{k^{\uparrow} - k^{\downarrow}}{k^{\uparrow} + k^{\downarrow}} \frac{\kappa^2 k^{\uparrow} k^{\downarrow}}{\kappa^2 k^{\uparrow} k^{\downarrow}}, \tag{1.7}$$

where κ is the decay rate of the electron wave function within the barrier determined by the potential barrier height V, $\kappa = \sqrt{(2m/\hbar^2)(V - E_{\mathrm{F}})}$. A detailed derivation of the polarization value can be found in the refereed article. The most important difference with respect to the polarization defined in Julliere model is the addition of the factor which depends on the barrier height. In the limit of a high barrier this factor goes to unity reducing Slonczewski formula for TMR to that of Julliere. On the other hand, if the barrier is not very high and κ is comparable or smaller to the wave vector of the electron, the value of TMR will decrease with decreasing V and even can change sign for sufficiently low barriers.[75,76]

The main message from the Slonczewski formula is that it shows the role played by the tunnel barrier on the polarization of the electrode and on the resulting TMR. Although this approach is more accurate yet it only considers the band structure of the electrodes and neglects the band structure effects of the barrier. It is equivalent to the tunnelling between electrodes separated by a vacuum. As it will be shown hereafter the band structure of the insulating barrier in a crystalline junction plays a crucial role in defining the TMR.

1.2 Spin and symmetry filtering in crystalline Fe/MgO/Fe junction

The Julliere approach and the free-electron based models can explain quite well the magnetoresistive properties of junctions containing amorphous barriers. However, in the case of a fully crystalline junctions the situation is more complicated. Crystalline structure enforces modification to the electron wave function due to a periodic potential created by the ions which in turn influences the tunnelling process. As we will show later, due to the periodic potential the electron wave functions in the electrodes can be grouped based on their symmetry properties. Each of these symmetries is coupled differently to the states in the crystalline barrier. As a consequence also the attenuation coefficient for each wave function is symmetry dependent. Thus, along with the spin conservation, the symmetry of the electron wave function is also conserved during the transport through the junction which gives rise to high TMR values in crystalline MTJs.

All the necessary aspects of the spin and symmetry dependent tunnelling will be described in the case of the canonical Fe/MgO/Fe junction which is the best understood example and which we choose to study in this thesis. We assume here ideal crystalline structure of the heterojunction and the interfaces. The modifications to tunnelling processes caused by structural imperfections are the subject of the next chapter.

1.2.1 Crystal structure of Fe/MgO interface

In order to obtain structurally ordered heterojunction, the lattice constants of the used materials should match or be almost the same (lattice mismatch less than few percent). This is the case for Fe electrodes and MgO insulating barrier. In this subsection the structure of Fe/MgO junction and its epitaxial growth will be briefly discussed.

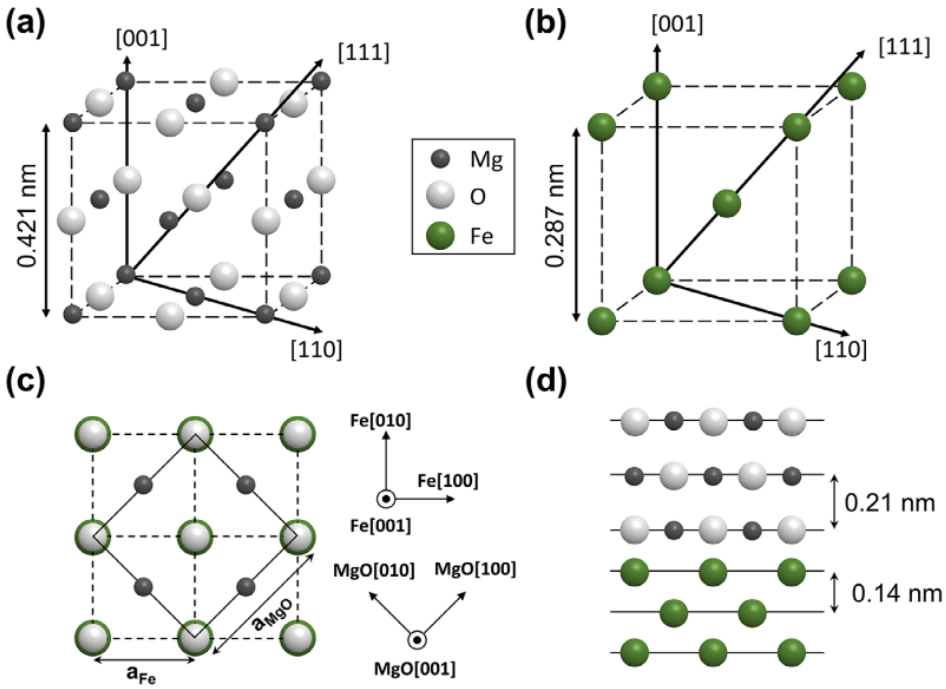

Figure 1.4: Structure of the Fe/MgO(001) interface. Panels (a) and (b) show the crystal structure of MgO and Fe respectively. The epitaxial relation between the two materials is schematically presented in panels (c) top view and (d) cross section of the Fe/MgO interface. MgO deposited on top of Fe crystal is rotated by 45° with respect to the substrate. The lattice mismatch is small and does not affect significantly the structure of MgO. Taken from Ref. 77.

MgO is an ionic material created by charge transfer between magnesium and oxygen atoms. It crystallizes in *fcc* structure (rock salt), with lattice constant $a_{\mathrm{MgO}} = 4.21$ Å, where each Mg and O atom are six-fold coordinated. The electronic structure of MgO consists of a filled valence band (VB), of mainly oxygen character, and empty conduction bands (CB) build mainly from magnesium states.[27] This is a consequence of the electronic configuration of both atoms, O: $1s^2\ 2s^2\ 2p^4$ and Mg: $1s^2\ 2s^2\ 2p^6\ 3s^2$, and a charge transfer from $3s^2$ orbital of Mg to $2p^4$ orbital of O when the crystal is formed.

This charge transfer produces an insulating MgO with direct band gap of 7.8 eV. Iron is a metal which crystallizes in a *bcc* structure with a lattice constant $a_{\mathrm{Fe}} = 2.87$ Å.

When MgO is deposited atop of a perfect Fe monocrystal it grows crystalline, however it is rotated by a 45° to match the lattice constants of both materials and avoid strains in the structure, thus $a_{\mathrm{MgO}} = \sqrt{2}a_{\mathrm{Fe}}$. This is schematically shown in Fig. 1.4. The lattice mismatch is about few percent (∼3%). During Fe/MgO growth, it was shown experimentally that O atoms are placed on top of Fe atoms.[15,17]

1.2.2 Bloch states and wave function symmetries

At the beginning of this chapter the tunnelling of an electron was described in terms of a free electron encountering a potential barrier. The potential felt by the electron, before reaching the barrier, was constant and we could use simply an incoming plane wave for defining the electron motion. Consequently, the model predicted a single decay rate for a given electron wave function within the barrier, which should decay exponentially within the barrier as $\exp(-2\kappa d)$ and $\kappa = \sqrt{(2m/\hbar^2)(V-E) + k_{\parallel}^2}$.

In a real crystal however this approach is not quite correct. First of all, one has to include the atomistic nature of the electrodes and the barrier and the potential generated by the ions creating the structure. Thus, during its propagation through the crystalline junction, the electron feels the periodic potential and the electron wave function is described by a Bloch wave function.[69,73] Moreover, the wave functions have to be matched at each interface, where the matching conditions depend on the properties of the incoming wave, i.e. the spin state and the symmetry of the wave function. As a consequence, the electron can propagate only within the spin channel with corresponding symmetry, where each of such channels undergoes its respective decaying rate. The physical explanation of symmetry dependent decay coefficient lies in the fact that these symmetry states have different amounts of curvature in the plane parallel to the interfaces.[10–13] These oscillations are responsible for increasing the decay rate perpendicular to the interfaces, i.e. the bigger the curvature the faster the decay of the wave function. The lateral variations of the wave function were not actually included in the free-electron model (except for the variations associated with the lateral component of the wave vector, $\mathbf{k}_{\parallel}$). Nonetheless, in a real systems the wave function can still have lateral oscillations even when $\mathbf{k}_{\parallel} = 0$.

Following Butler *et al.*[13] one can assume that the boundary conditions at the edge of the barrier can be matched with a separable form of the wave function, $\Psi(x,y,z) = \phi(x,y)\exp(-\kappa z)$. Then, the decay parameter is given by

$$\kappa^2 = \frac{2m}{\hbar^2}(V-E) - \frac{\langle\phi|\left(\frac{\partial^2}{\partial x^2} + \frac{\partial^2}{\partial y^2}\right)|\phi\rangle}{\langle\phi|\phi\rangle} \tag{1.8}$$

where $\phi(x,y)$ is the planar component of the wave function and the variation of ϕ is assumed to be oscillatory. The second term in the above equation is positive and depends on the number of nodes of $\phi(x,y)$. The higher the number of nodes the more important this term is. By using symmetries in this approach one can determine the number of nodes of the wave function in the plane of the interface. This translates into

curvature in the plane and affects the ensuing decay rate. As a result, states which are primarily of s-character will have little of this curvature, p-like states will have more and d-like states even more of the curvature.[12,13] Thus, one can conclude that the nature of the states in the electrode will influence its attenuation rate in the barrier and this is a general physical phenomenon.

1.2.3 Symmetry states in Fe leads

The electronic configuration of Fe is [Ar] $3d^6$ $4s^2$, so the states in Fe are created by atomic orbitals of s, p and d character. As we will show, by using symmetry properties, one can group these orbitals with respect to the common symmetries, for example the orbitals p_z and d_{z^2} are invariant under rotations about the z axis.

Brillouin zone and band structure of Fe

Iron has a *bcc* structure and its Brillouin zone is presented in Fig. 1.5 for its bulk and (001) surface.

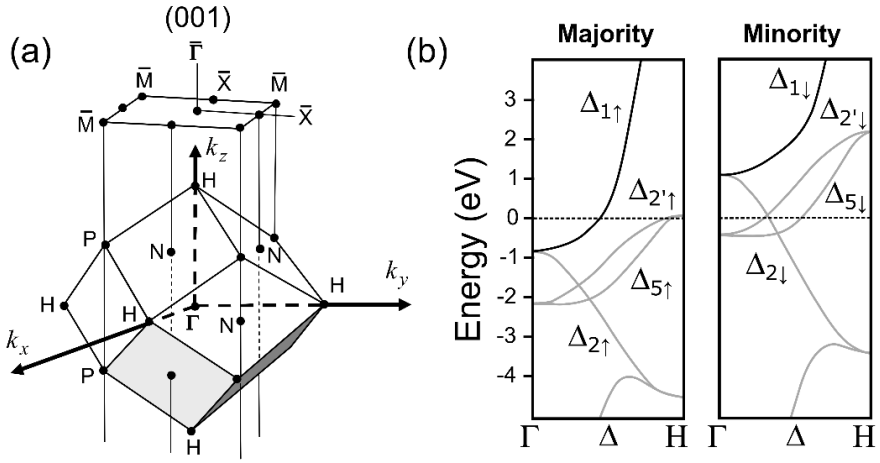

Figure 1.5: Brillouin zone and band structure of *bcc* Fe. a) Brillouin zone corresponding to its bulk and (001) surface. The electron propagates along [001] axis in a real space which corresponds to Γ-H direction in a reciprocal space. b) Related spin and symmetry resolved band structure along Γ-H line. The states available for the majority channel at the E_F are Δ_1, Δ_5 and $\Delta_{2'}$ while for the minority spin channel these are Δ_2, Δ_5 and $\Delta_{2'}$. Figure adapted from Ref. 78.

The tunnelling of the electrons is preferential in the direction perpendicular to the (001) plane of Fe thus for the electrons with $\mathbf{k}_{\parallel} = 0$. This direction in a real space corresponds to Γ-H line in a reciprocal space of a 3-dimensional bulk material and to the $\overline{\Gamma}$ point in the Brillouin zone for the (001) surface. Hence, the band structure in this direction, also denoted as Δ, is the most important one. Group theory classifies these bands with respect to the symmetry properties of the orbitals involved in creating the states. Without going into details, Fig. 1.6 and Tab. 1.1 summarize the Bloch states existing in the Γ-H direction with their respective symmetries.[11,13]

Only electrons in the vicinity of the Fermi level take part in the transport so one has to distinguish symmetry states crossing the E_F. Fig. 1.5(b) presents spin and symmetry resolved band structure of Fe along the transport direction, the Δ line. As it can be seen from Fig. 1.5 states with Δ_1, Δ_5 and $\Delta_{2'}$ exist for the majority spin electrons while the states of minority electrons have Δ_2, Δ_5 and $\Delta_{2'}$ symmetries. The most important consequence of the wave function symmetries at the Fermi level is the fact that electrons can tunnel between electrodes only within subchannels with the same spin and symmetry. Thus, the measured conductance is a sum of each spin channel which in turn is composed of all available symmetries. The Δ_1 and Δ_2 symmetries exist only for the majority and minority electrons respectively. The $\Delta_{2'}$ and Δ_5 appear for both spin populations at E_F and hence they give only little contribution to spin polarization of the current (they provide an almost similar current flow in any configuration of the electrode's magnetization). In the AP case, the majority (minority) electrons from the first electrode tunnel into the minority (majority) states in the second one and thus only the electrons with $\Delta_{2'}$ and Δ_5 are important in this process. The lack of Δ_1 and Δ_2 symmetry channels in the AP state results in a significant difference of the conductance between the P and AP configurations and hence leads to a strong increase of the TMR.

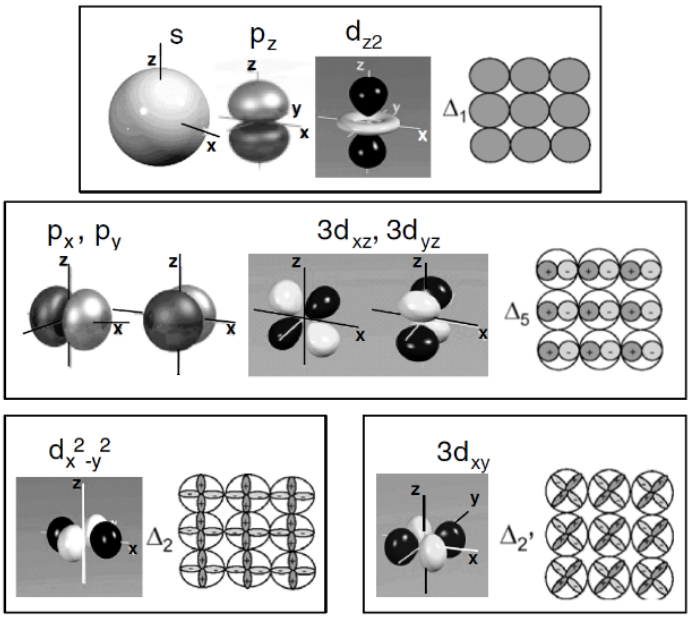

Figure 1.6: The atomic-like orbitals grouped according to their symmetry properties in the direction of propagation [001] (z axis). The corresponding transverse nodes are schematically drawn on the right of each symmetry group. Taken from Ref. 78.

Table 1.1: Bloch states in Γ-H direction with the corresponding symmetries. States available in Fe can be grouped with respect to their orbital symmetries. The electron propagation is always assumed along the z direction.

Bloch state	Corresponding orbitals	Symmetry
Δ_1	s, p_z, d_{z^2}	$z; x^2+y^2; z^2$
Δ_5	p_x, p_y, d_{xy}, d_{yz}	$(R_x, R_y); (xz, yz); (x, y)$
Δ_2	$d_{x^2-y^2}$	x^2-y^2
$\Delta_{2'}$	d_{xy}	xy

Effect of lateral variations of a wave function

As stated at the beginning of this subsection, the decay rate for each symmetry channel depends on the lateral variations of the electron wave function in the plane parallel to the interfaces. Here we will examine in more detail these results. Two cases can be distinguished, one with $\mathbf{k}_\parallel = 0$ and the other with $\mathbf{k}_\parallel \neq 0$, and they will be discussed separately. All the presented analysis is based on the work of Butler and co-workers.[10–13]

Case for $\mathbf{k}_\parallel = 0$

For $\mathbf{k}_\parallel = 0$, we consider only states with wave vector perpendicular to the interfaces and the decay parameter can be written as

$$\kappa = \sqrt{\frac{2m}{\hbar^2}(V-E) + g^2} \tag{1.9}$$

with $\phi(x,y) = \exp(i\mathbf{g}\cdot\boldsymbol{\rho})$, $\boldsymbol{\rho}$ being a vector in xy plane and $\mathbf{g}$ a vector of the corresponding reciprocal space. The $\Delta_1(s, p_z, d_{z^2})$ states do not have any nodes in the xy plane which correspond to $g = 0$ and a decay parameter $\kappa = \sqrt{\frac{2m}{\hbar^2}(V-E)}$ (as in a simple barrier model). The other states, however, decay faster. If we denote the lattice parameter as a, the states $\Delta_2(d_{x^2-y^2})$ and $\Delta_5(p_x, p_y, d_{xz}, d_{yz})$ will correspond to vectors $\mathbf{g_1} = (2\pi/a, 0), (0, 2\pi/a), (-2\pi/a, 0), (0, -2\pi/a)$. These states thus decay with $\kappa = \sqrt{\frac{2m}{\hbar^2}(V-E) + g_1^2}$ where $g_1 = 2\pi/a$ and have one node in the xy plane. The states $\Delta_{2'}$ are of d character with a xy symmetry, Hence, they decay as $\kappa = \sqrt{\frac{2m}{\hbar^2}(V-E) + g_2^2}$, where the corresponding vectors are $\mathbf{g_2} = (2\pi/a, 2\pi/a)$, $(2\pi/a, -2\pi/a)$, $(-2\pi/a, 2\pi/a)$, $(-2\pi/a, -2\pi/a)$ with norm $g_2 = \sqrt{2}(2\pi/a)$. Table 1.2 summarizes the decay rates corresponding to each symmetry channel.

Table 1.2: Decay rates of the wave function corresponding to each symmetry channel along Γ-H direction. The decay rate depends on the lateral variations of wave function in the plane perpendicular to the transport direction. See the text for more details.

Bloch state	**Decay rate**
Δ_1	$\kappa = \sqrt{\frac{2m}{\hbar^2}(V-E)}$
Δ_5	$\kappa = \sqrt{\frac{2m}{\hbar^2}(V-E) + g_1^2}$
Δ_2	$\kappa = \sqrt{\frac{2m}{\hbar^2}(V-E) + g_1^2}$
$\Delta_{2'}$	$\kappa = \sqrt{\frac{2m}{\hbar^2}(V-E) + g_2^2}$

To construct the $\phi(x,y)$ functions one has to remember that they should obey symmetries of the corresponding states. For example, in case of Δ_1 state we stated that it has no nodes in the xy plane so $g = 0$ and simply $\phi(x,y) = \exp(i\mathbf{g}\cdot\boldsymbol{\rho}) = 1$ is allowed. For Δ_5 states with one node in the xy plane we can use linear combinations of four plane waves associated with different $\mathbf{g_1}$ vectors, $\phi(x,y) = \exp(\pm i2\pi x/a)$ and $\exp(\pm i2\pi y/a)$ to construct the states with Δ_5 symmetry as $\sin(2\pi x/a)$ and $\sin(2\pi y/a)$. This is because of the symmetry of these functions in the xy plane, they have to change sign under the operations that change $x \to -x$ or $y \to -y$. The symmetry Δ_2 is characterized by the following operations in the xy plane: $\phi(-x,y) = \phi(x,-y) = \phi(-x,-y) = \phi(x,y)$ and $\phi(y,x) = -\phi(x,y)$. With the same $\mathbf{g_1}$ vectors, we obtain the function $\cos(2\pi x/a) - \cos(2\pi y/a)$ which respects the Δ_2 symmetry. In similar manner the $\phi(x,y)$ functions with vectors $\mathbf{g_2}$ are of the form $\phi(x,y) = \exp(\pm i2\pi x/a \pm i2\pi y/a)$ giving a wave function which respects the $\Delta_{2'}$ symmetry as $\cos(2\pi x/a + 2\pi y/a) - \cos(2\pi x/a - 2\pi y/a)$.

To prove the influence of the number of nodes and the symmetry of a state on attenuation rate Butler *et al.*[13] have calculated the decay of the tunnelling DOS as a function of number of layers between the Fe(100) electrodes separated by a vacuum. As a method of calculation they employed the layer Korringa, Kohn, and Rostoker (LKKR) technique. The DOS was calculated by applying the scattering boundary conditions, thus assuming that there is a unit flux of incident electrons on the left side of the barrier plus reflected electrons on the same side and transmitted electrons on the right side. Such boundary conditions give a tunnelling DOS which decays within the barrier from left to right. More details about the calculation method can be found in their paper and references therein.

Fig. 1.7 shows the decay of the tunnelling DOS corresponding to the electrons at the Fermi level with $\mathbf{k}_\parallel = 0$ which are the most significant for tunnelling across the vacuum. This is referred afterwords as a *tunnelling density of states*, TDOS. It is evident that electronic states with different symmetries have distinct decay rates in the barrier. This also proves the relation between the number of nodes and the attenuation rate: decay of Δ_1 states (nodeless) is smaller than these of Δ_2, Δ_5 and $\Delta_{2'}$ states. It is worth noticing that in the presented case the potential barrier is simply a vacuum which does not actually affect the electronic symmetries in the electrode. However,

when one considers an insulator like MgO placed as a barrier, the situation is more complex and the decay rate will be also dependent on the electronic structure of the barrier material. This point will be discussed in the following sections.

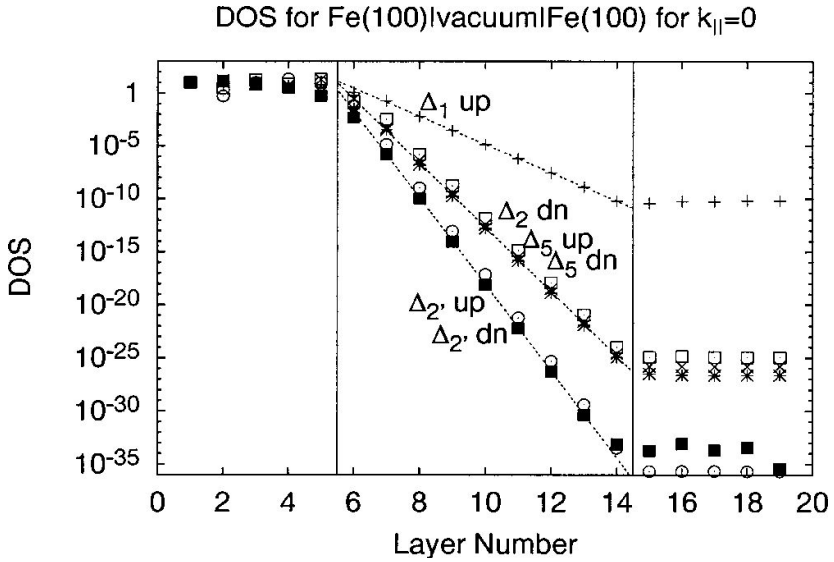

Figure 1.7: Calculated tunnelling DOS for the states at the E_F with $\mathbf{k}_\parallel = 0$ for Fe(100)/vacuum/Fe(100) system. The electrodes are in the parallel configuration. The total (+) and the s (×) and d (∗) partial DOSs are plotted. The decay rate increases with the increasing number of nodes in the xy plane of the wave function (see text for details). Taken from Ref. 13.

Case for $\mathbf{k}_\parallel \neq 0$

For the situation where $\mathbf{k}_\parallel \neq 0$ the picture of Bloch wave function symmetries and their coupling to the corresponding evanescent states becomes more complex. The detailed description can be found in the works of MacLaren *et al.*[8] and Butler *et al.*,[13] here only the basic points will be presented. After MacLaren, the wave function in the barrier can be expanded in terms of reciprocal lattice vectors as

$$\Psi(\boldsymbol{\rho}, z) = \sum_{\boldsymbol{g}} c_{\mathbf{g}} e^{i(\mathbf{k}_\parallel + \mathbf{g})\cdot\boldsymbol{\rho} - \sqrt{\frac{2m}{\hbar^2}(V-E) + (\mathbf{k}_\parallel + \mathbf{g})^2} z}, \tag{1.10}$$

where $\boldsymbol{\rho}$ is a vector in the xy plane as before, but the limit of thick barrier is assumed to exclude growing evanescent states. Thus, for $\mathbf{k}_\parallel \neq 0$ the states in the barrier contain a linear combination of different reciprocal lattice vectors decaying at different rates.

Fig. 1.8 shows the angular momentum decomposition of the tunnelling density of states (TDOS) for $\mathbf{k}_\parallel = (0.036, 0.018)$. The left panel presents the case where the decaying state has Δ_1 symmetry at $\overline{\Gamma}$ point. We can see that the total TDOS (+) as well as the one corresponding to s (×)and d (∗) states have the same decay rate. Thus, these states are affected in the same manner by the vacuum. Next, we can consider again the state at $\mathbf{k}_\parallel = (0.036, 0.018)$ but this time for a band without the Δ_1 symmetry at $\overline{\Gamma}$ point, hence with oscillations in the xy plane (right panel of Fig. 1.8). In this case the TDOS is mainly composed of d states which generate no contribution

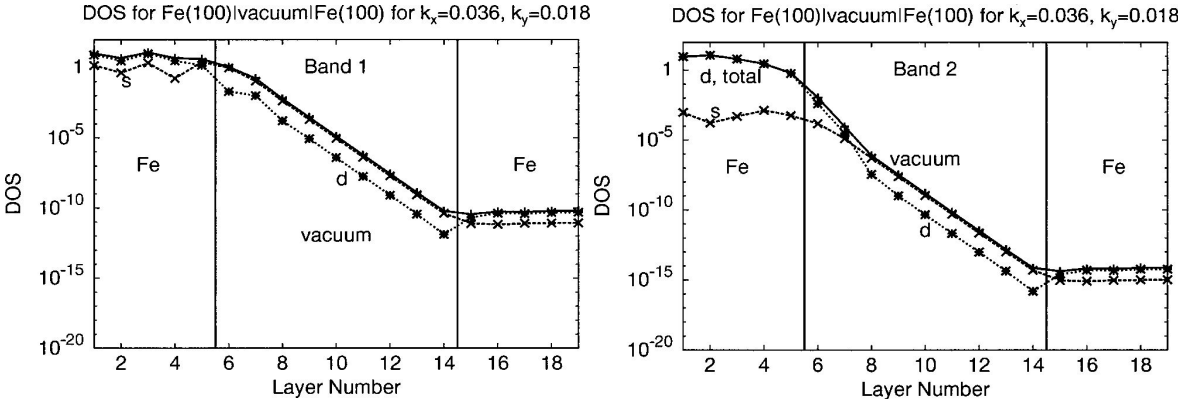

Figure 1.8: Calculated tunnelling DOS for the states at E_F with $\mathbf{k}_{||}$ almost at the Γ point for Fe(100)/vacuum/Fe(100) system. The electrodes are in the parallel configuration. Panel a) corresponds to Bloch state of Δ_1 symmetry; b) Bloch state that has no $g = 0$ component. The total (+) and the s ($\times$) and d ($*$) partial TDOSs are plotted. Taken from Ref. 13.

with the $g = 0$ and hence should decay very rapidly in the first few layers of the barrier. Indeed, this kind of behaviour is seen at Fig. 1.8 (b) where the TDOS shows initially rapid decay since wave functions with in plane oscillations obey eq. 1.10 with $g \neq 0$. After these term are gone there is small residual component that decays at the rate given by eq. 1.10 with $g = 0$. This result indicates that for sufficiently thick barriers only states associated with $g = 0$ will sustain and determine the attenuation of the TDOS.

1.2.4 Symmetry filtering in the MgO barrier

As we saw in the previous subsections, the electronic states in Fe have different symmetries and consequently distinct decay rates. The question to answer now is what will happen if instead of a vacuum spacer we use an insulator like MgO with a well defined crystal structure? How this will affect the decay of the electron wave functions? This issue will be addressed in the following subsections.

MIGS and complex bad structure

A behaviour of an electron in a metal approaching a surface was first described by Heine in 1965.[79] He showed that one can evaluate the electron wave function close to the surface by matching the solutions at both sides of the interface. An assumption to make is that within the volume of the metal the electron wave function has a wave vector $\mathbf{k}$ with real values while next to the surface $\mathbf{k}$ can be complex. The real bands in a metal are then matched with the decaying wave functions outside a metal. These metal states extending into the vacuum (or insulator) are called *Metal-Induced Gap States* (MIGS).

The role of MIGS in tunnelling processes was pointed out by Mavropoulos *et al.*[80] The basic idea was that the electron tunnelling through the junction is largely determined by the electronic properties of the insulator within the band gap. These properties can be evaluated by examining the *complex band structure* (CBS) of the

insulator, i. e. the dispersion relation of the form $E = E(k_z)$, where k_z is a complex number, to determine the decay of the evanescent electronic states. These evanescent electronic states exist due to the fact that an insulator surface can host interface states (MIGS) with their energy lying in the band gap. Despite that MIGS exist only at surfaces of insulators their properties can be obtained form these of bulk by extending the solutions of the Schrödinger equation to complex $\mathbf{k}$ vectors. This approach is justified by noticing that the interface induced changes in the charge density and in the potential are confined generally to the first few monolayers of the material, and hence they do not modify the potential drastically. Evanescent wave functions on the other hand extend over many layers into the crystal and correspond to solutions of the bulk Schrödinger equation but for imaginary $\mathbf{k}$ vectors. Therefore, for perfect epitaxial growth which preserves the two-dimensional periodicity, the electron wave function can be described by a $\mathbf{k}$ vector of the form $\mathbf{k} = (\mathbf{k}_\parallel, k_z)$ where $\mathbf{k}_\parallel$ is a vector parallel to the interface and is conserved during transport, while k_z is in part perpendicular to the interface with complex values $k_z = q + i\kappa$. Then, for each real value of $\mathbf{k}_\parallel$ the evanescent states can be described in terms of the dispersion relation $E = E(k_z)$, which produces a complex band structure. The imaginary part, κ, is an attenuation parameter and the corresponding wave function decays as $\sim e^{-\kappa z}$.

If one chooses a certain $\mathbf{k}_\parallel$ vector and an arbitrary complex k_z, the solutions of the Schrödinger equation associated with a real energy value will form the so-called *real lines* or complex bands in a three-dimensional (q, κ, E) space. Real lines, starting at real q axis at points corresponding to a local maximum or a minimum of the real band structure, can either extend in energy to $-\infty$ (free-electron like parabolic solutions) or connect back to other extrema of the real band structure, creating a closed loop. By analogy to real bands, complex bands can be also characterized by the corresponding orbital symmetries. Moreover, complex bands inherit the symmetry properties of the real bands to which they are connected. This implies that in the case of closed complex loops, the connected real bands and the complex ones have the same symmetry. More detail studies considering complex band structure can be found in papers of Heine,[79] Chang,[81] Mavropoulos *et al.*[80] and Dederichs *et al.*[82]

Going back to the case of a metal/insulator interface and keeping in mind that the electron wave function and its first derivative have to be continuous at the interface, it is evident that electronic states available at E_F in the electrode with well defined symmetries have to couple to the insulator evanescent states with exactly the same symmetry. The decay rate is again symmetry dependent and can be evaluated based on the complex band structure of the insulator. In the following, this point will be discussed with more details by considering Fe/MgO tunnel junction.

Analysis of complex band structure of MgO

Fe/MgO/Fe system has a crystalline structure hence we can assume that the transverse $\mathbf{k}_\parallel$ component of the wave vector is conserved during ballistic transport. Due to epitaxial growth of Fe/MgO interface (see sec. 1.2.1) and assuming the transport along the z direction, the electronic structure of MgO along [001] line is of major importance for further considerations. This corresponds to the Γ-X line in the reciprocal space. The Brillouin zone for bulk and surface of MgO as well as band structure associated

with Γ-X line are presented in Fig. 1.9.

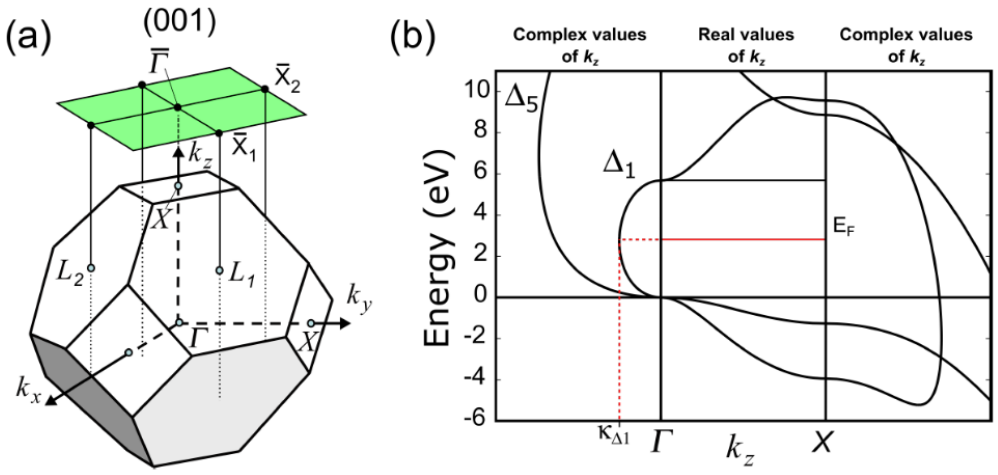

Figure 1.9: Brillouin zone of MgO with the corresponding complex band structure along Γ-X line. For each Bloch state with symmetry Δ_i at the E_F the value of κ is determined as the intersection point of the Fermi energy and a complex loop (panel (b)). Taken from Ref. 80.

As already mentioned, only states at the vicinity of the Fermi level in Fe are taking part in the tunnelling process. These states will couple to MgO gap states defined by complex k_z values and create MIGS. MIGS inherit symmetry properties of propagating Bloch wave functions from Fe and are attenuated with different rates within the MgO barrier. The decay coefficients κ for each Bloch state with symmetry Δ_i at the E_F can be evaluated based on a complex band structure of MgO along the transport direction Γ-X as the intersection point of the Fermi energy and a complex loop (Fig. 1.9 (b)). Therefore, the value of κ in the MgO band gap depends strongly on the position of the Fermi level of the junction. In the case of Fe/MgO heterostructure the Fermi level is imposed by the ferromagnetic leads and it is positioned in the middle of MgO band gap, which in MgO is defined by states with Δ_1 symmetry; the band gap for Δ_5 between the valence and conduction states is much higher.

By examining the complex band structure of MgO shown in Fig. 1.9(b) and pinning E_F to the midgap, it is evident that $\kappa_{\Delta_1} << \kappa_{\Delta_5} << \kappa_{\Delta_{2'}}$. The complex $\Delta_{2'}$ is not shown because it is much larger then the other ones. Hence, the states compatible with Δ_1 symmetry have the smallest attenuation rate in the barrier and have the biggest impact on the tunnelling current. Since the Δ_1 symmetry appears only for the majority electrons, it dominates the conductance in the parallel configuration. In the AP case the conductance is governed by states with a decay rate much bigger than κ_{Δ_1}. The big difference between G_P and G_{AP} generates high values of TMR predicted for crystalline Fe/MgO junctions.

It is worth noticing that the above analysis is valid for the case with $\mathbf{k}_{\parallel} = 0$. The situation with $\mathbf{k}_{\parallel} \neq 0$ is not considered here since the values of κ are increasing even more and consequently give less contribution to the tunnelling current.[80]

1.2.5 Importance of symmetry

The simple Juliere model for describing the magnetoresistance is successful in the case of amorphous barriers, but does not capture the essential physics for crystalline junctions. Amorphous barriers, due to the disorder in the structure, mix all the conduction channels and as a result all of them decay with the same rate. Crystalline barriers on the other hand preserve the symmetries of incoming Bloch states and electrons can propagate only within the channel with the same symmetry across the junction. Consequently, if the collecting electrode does not have states available for the incoming electron with a particular spin and symmetry, the electron will not pass through the barrier. The total conductance therefore is a sum of spin and symmetry channels available in the electrodes for the energy of the incoming electrons.

Another consequence of crystalline symmetry is the lateral variation of the wave function in the plane perpendicular to the transport direction. This is actually the origin of the different attenuation rate of each wave function within the barrier. The greater the lateral curvature of the wave function the larger the decay parameter and different contribution to the total transmission.

However, to ensure these effects to occur, we have to choose suitable ferromagnetic electrodes and barrier material. First, the electronic band structure of a ferromagnet should present different symmetry states for the majority and minority spin channels. This can be different depending on the direction in the reciprocal space along the transport direction. Second, the incoming wave should be effectively coupled to the evanescent sates within the insulating barrier thus, also the band structure of the insulator has to be taken into account. Finally, we need a good epitaxial growth of the electrode and the barrier, with a good lattice match, which will establish a good symmetry matching of the wave function at the interfaces.

These conditions are fulfilled in the case of Fe/MgO/Fe(001) (see subsec. 1.2.1) along the (001) direction corresponding to Γ-H line in the reciprocal space of *bcc* Fe. The electronic structure of Fe exhibits different symmetry states for the two spin populations along the (001) direction. It is not the case for example along (110) or (111) directions where both spin populations have exactly the same symmetries thus the barrier filtering is occurring in the same manner for P and AP configurations. To match the lattices of MgO and Fe during the epitaxial growth process, they have to be rotated with respect to each other by 45°. Therefore, state having $x'y'$ symmetry in the Fe corresponds to state with $x^2 - y^2$ symmetry in the MgO where coordinate system x', y' and x, y are rotated with respect to each other by 45°. Combination of spin and symmetry filtering effects in the epitaxial tunnel junctions leads to high values of TMR which is demanded for practical applications of devices based on tunnel magnetoresistance. This is also the greatest advantage of epitaxial junctions over these with amorphous barriers.

1.3 Transmission calculations of Fe/MgO/Fe junction

The advantage of crystalline Fe/MgO/Fe junctions over amorphous ones is that the conductance is computationally less involved. Butler *et al.*[83] calculated the transmission for Fe/Mg/Fe system and explained the tunnelling processes for separate conduction channels. They used the layer-Korringa-Kohn-Rostoker method (LKKR)[8,83] for the electronic structure calculations of the Fe/MgO/Fe junction and evaluated conductance using the Landauer-Büttiker formula. The Landauer-Büttiker approach connects the conductance to the transmission probability for each propagating Bloch state assuming that $\mathbf{k}_{\parallel}$ is conserved

$$G = \frac{e^2}{h} \sum_{\mathbf{k}_{\parallel},j} T(\mathbf{k}_{\parallel}, j), \tag{1.11}$$

where e is the electron charge, h the Planck constant and $T(\mathbf{k}_{\parallel}, j)$ is the tunnelling probability for the wave function with a given transverse momentum and with symmetry j. In other words this formula states that conductance is a sum of the transmission probabilities of all independent conduction channels. More detail analysis concerning the Landauer-Büttiker formalism will be presented during the discussion of the transport properties of nanoscale devices in Chapter 4. Here, only the state of the art results will be presented.

1.3.1 Transmission and TDOS for parallel configuration

Majority spin channel: Figure 1.10 shows the calculated $\mathbf{k}_{\parallel}$ resolved transmission probability in the parallel configuration for majority (left panels) and minority (right panels) spin channels for 4, 8 and 12 layers of MgO. In the case of the majority spin channel, the transmission has a rather broad peak centered at $\mathbf{k}_{\parallel} = 0$. An important feature is, as the insulating barrier becomes thicker, the transmission is exponentially reduced and concentrated around $\mathbf{k}_{\parallel} = 0$. A similar behaviour is predicted also for the free electron tunnelling through a simple square barrier.

Minority spin channel: In the case of the minority spin channel (Fig. 1.10 right panels) the transmission is far from the one predicted for the majority spin channel or simple barrier model. One observes sharp peaks which are not at $\mathbf{k}_{\parallel} = 0$ but mostly along the lines $k_x = 0$ and $k_y = 0$. Moreover, the conductance is practically zero a the Γ point. With the increase of the barrier thickness the amplitude of the peaks is exponentially reduced with a rate κ much bigger than that for the majority spin electrons. It was shown that the structure of the transmission for the minority spin channel arises from the interplay of the interfacial resonance states, the $\mathbf{k}_{\parallel}$ dependence of the wave function decay in MgO (including interference effects), and the symmetry of the minority Fe Bloch states relative to that of the complex energy bands of MgO.[9,13,83]

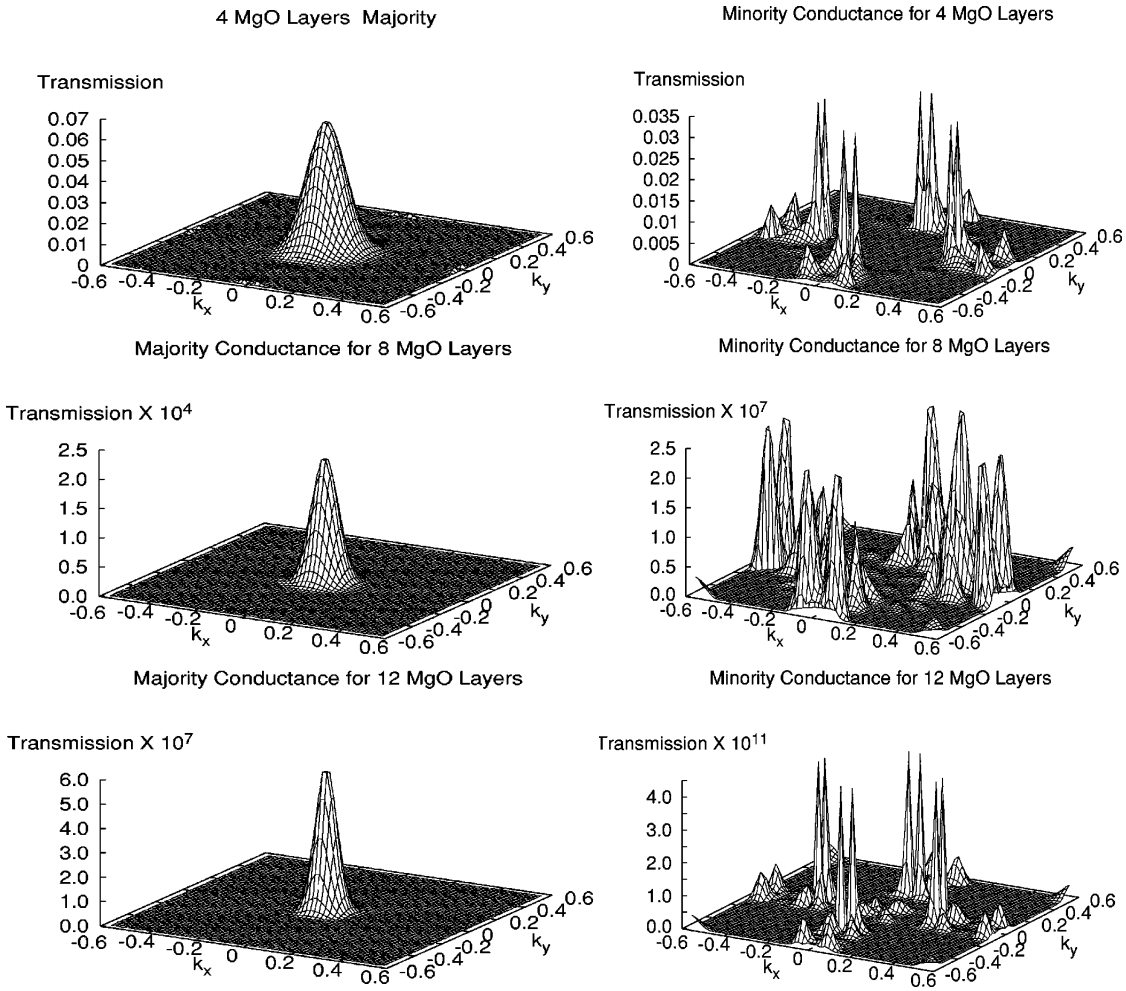

Figure 1.10: $\mathbf{k}_{\parallel}$ resolved conductance for Fe/MgO/Fe junction for the parallel magnetization of the electrodes. The majority (left) and minority (right) spin channels are presented for 4, 8 and 12 layers of MgO. Taken from Ref. 83.

Tunnelling density of states

To better understand the conductance one can study the tunnelling density of states (TDOS) for $\mathbf{k}_{\parallel} = 0$ for the individual energy bands and their changes with the number of MgO layers. The TDOS reflects the probability of propagation of a particular state through the barrier. It is defined as a density of electronic states with the following boundary conditions: on the left from the interface there is an incoming Bloch state with unit flux and the corresponding reflected Bloch state; on the right are the corresponding transmitted Bloch states. This TDOS represents hence the number of states which are found in each layer of the junction, and this is therefore directly related to the transmission probability and its attenuation rate.

The TDOS corresponding to each of the Fe(100) Bloch states with $\mathbf{k}_{\parallel} = 0$ is presented in Fig. 1.11. In the left emitting electrode at the Fermi level one can find states with symmetry $\Delta_1, \Delta_{2'}$ and Δ_5 for the majority spin channel and $\Delta_2, \Delta_{2'}, \Delta_5$ for the minority one. The incoming Δ_1 and Δ_5 states will decay as evanescent states with the same symmetry in MgO. However, Δ_2 states from Fe will couple to $\Delta_{2'}$ states in

MgO as was mentioned before. Similarly $\Delta_{2'}$ states from Fe will decay as Δ_2 states in MgO. Based on Fig. 1.11, we can see that only the Δ_1 states are decaying slowly within the barrier and dominate the transport in the parallel configuration ($G^{\uparrow\uparrow}$). The states Δ_5 and $\Delta_{2'}$ decay much faster with the number of MgO layers. This agrees with the predictions of the complex band structure of MgO and the discussion on the connection between lateral symmetry of the wave function and the resulting decay rate. In the right panel the results for the minority spin channel can be seen ($G^{\downarrow\downarrow}$). The main difference is the luck of the Δ_1 states in the minority population and appearance of Δ_2 states. However, for both channels they are coupled to the available states in the collecting electrode.

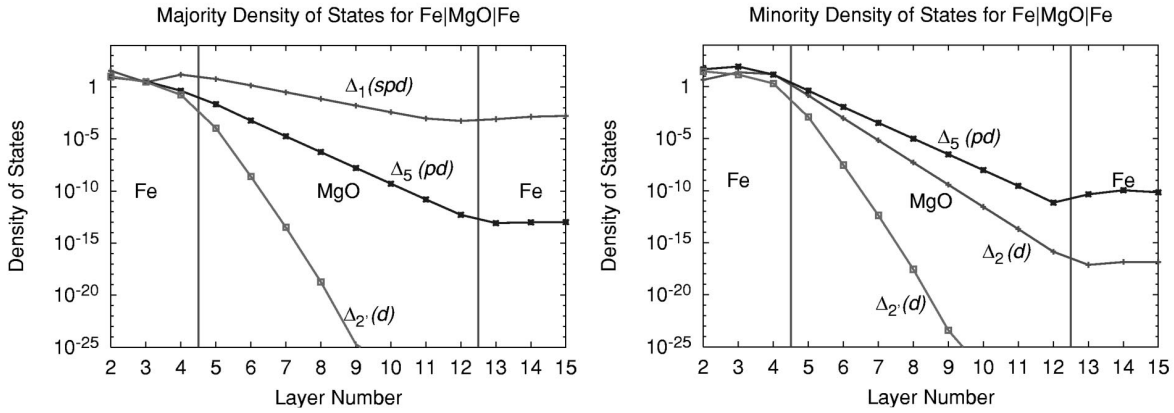

Figure 1.11: Tunnelling DOS (TDOS) for $\mathbf{k}_{\parallel} = 0$ in the parallel configuration. The TDOS is plotted as a function of the atomic layer for majority (left) and minority (right) spin channels. Taken from Ref. 83.

As it was already mentioned, the total conductance is a sum of all individual spin and symmetry channels and as such can be written in the following form for the parallel alignment of the electrodes:

$$G_{\mathrm{P}} = G^{\uparrow\uparrow}_{\Delta_1} + G^{\uparrow\uparrow}_{\Delta_5} + G^{\downarrow\downarrow}_{\Delta_5} + G^{\downarrow\downarrow}_{\Delta_2}. \tag{1.12}$$

The contribution from $\Delta_{2'}$ is neglected here since it is decaying the fastest and will have minor impact on the conductance.

Transmission oscillations as a function of $\mathbf{k}_{\parallel}$

Additional feature of the majority spin channel transmission can be seen if the transmission is represented using a logarithmic scale. This is shown in the left panel of Fig. 1.12. Clearly the transmission dependence on $\mathbf{k}_{\parallel}$ is more complicated and shows an oscillatory behaviour. The comparison between the predictions of a simple barrier model (dashed line) and a LKKR calculations (solid line) for 4 and 8 layers of MgO is shown. As it can be seen the initial decrease is much faster than what would be expected from a simple barrier theory. On the other hand, for larger values of k_x the calculated decrease is much smaller than what is predicted by a standard theory. These oscillations in the transmission result from the interference of complex bands of MgO in the energy gap.[83]

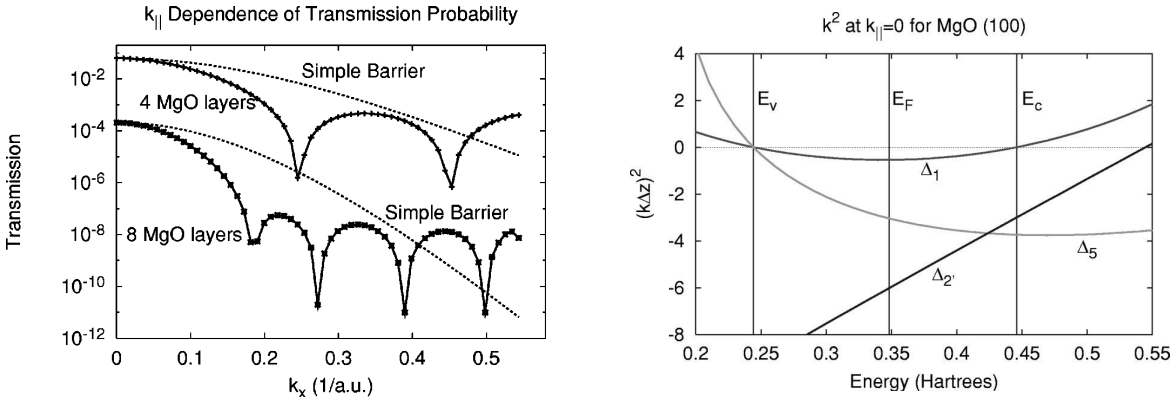

Figure 1.12: Left: Majority transmission probability as a function of k_x and for $k_y = 0$ for 4 and 8 layers of MgO. Right: Complex values of k_z at the Fermi energy. Taken from Ref. 83.

Interfacial resonant states

We mentioned before that the complicated k-dependence of the transmission in the minority spin channel can be related to the *interface resonant states* (IRS). Here, the concept of IRS and their influence on the conductance will be discussed in more details.

As a word of reminder, surface states are formed at the surface or at the interface of materials. They originate from the change of the electronic band structure of a material with finite size when one goes from a bulk material to the vacuum (or other material). The weakened potential at the surface allows for creation of new electronic states, within the local energy gaps, which correspond to solutions of Schrödinger equation with imaginary $\mathbf{k}$ wave vector and the exponential decay of those states on both sides of the interface. Those states are normally localized close to the material surface. Nevertheless, it is possible that a surface state can hybridize with with the bulk one forming the so called *interface resonant states*. These IRS extend away from the interface and thus can participate to the tunnelling current (see Fig. 1.13).

In the equilibrium conditions (no voltage applied) IRS are present away from the Γ point and can be neglected in the asymptotic limit since the contributions coming from $\mathbf{k} \neq (0, 0)$ are suppressed for large barrier thicknesses. However, for the intermediate and thin barriers IRS can dominate the transport mechanism. The appearance of IRS can be explained based on the layer projected density of states for iron electrode. The interfacial Fe layer is modified due to the presence of the barrier. For the minority electrons a big narrow peak is present slightly above the Fermi level (plot not shown here, see Butler *et al.*[83]). This peak indicates the presence of the the interface/surface state. More direct relation between the transmission in the minority spin channel and IRS can be understood by comparing the k-dependent transmission with the k-resolved interfacial density of states (Fig. 1.14). The maximum values of DOS appear along the lines with $k_x = 0$ and $k_y = 0$ as well as the maximum values of the transmission. However, the maximum peaks in the DOS and in the transmission do not exactly overlap. Moreover, the transmission is quite low for the value of $\mathbf{k}_{\|}$ for which the DOS of the interfacial resonance is the highest. Thus, IRS are not the only factor defining transmission in the minority channel. The other major element is the wave function symmetry. By analyzing a character of the Bloch states it becomes clear that the state

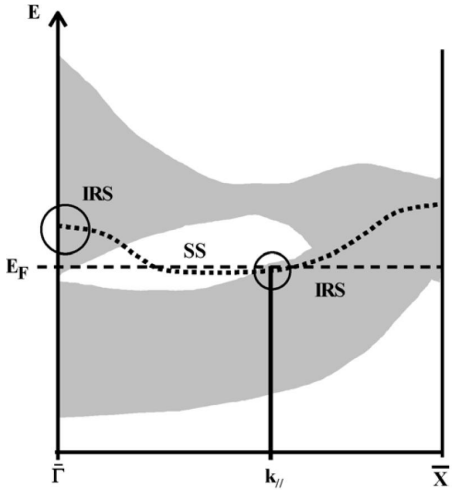

Figure 1.13: Schematic band structure for bulk and surface states in Fe (001). The gray zone indicates the bulk bands while dashed line a surface state. When the two overlap, they form interfacial resonant states (IRS) and contribute to the minority spin transmission. Taken from Ref. 78.

at $k_x = 0.299, k_y = 0$ has no s-character thus it can couple only to an evanescent state in the MgO that decays rapidly. Just a little bit out of $k_y = 0$ plane, however, the wave function has significant s-character and can couple to evanescent states with slow decay rate.[83] Belashchenko *et al.*[84] have performed first-principles calculations of

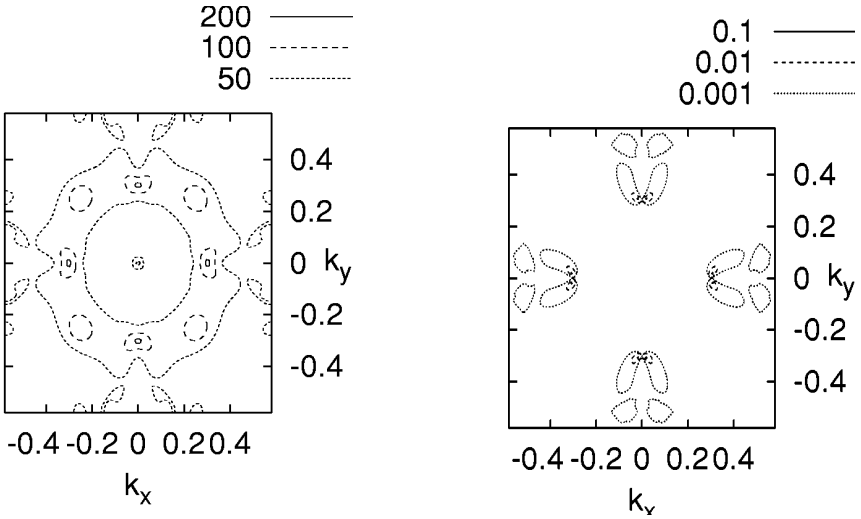

Figure 1.14: Minority k-resolved DOS and transmission. The left panel shows k-dependent DOS (states/hartree) on the interfacial Fe layer. The right panel is the corresponding transmission in the minority spin channel. units of k_x and k_y are inverse bohr radii. Taken from Ref. 83.

Fe/MgO/Fe (001) tunnel junctions to determine the effect of the interface states on the spin-dependent tunnelling. They found that in the case of a small MgO thickness the minority-spin resonant bands at the two interfaces make a significant contribution for the antiparallel alignment of the electrode's magnetizations. In the case of parallel

alignment these bands are mismatched by disorder and/or small applied bias. This in turn explains the observed decrease in the TMR for thin MgO barriers.

1.3.2 Transmission and TDOS for antiparallel configuration

The $\mathbf{k}_{\parallel}$ resolved transmission for the antiparallel alignment of the electrodes shows features appearing in both spin channels (Fig. 1.15).

Fig. 1.16 represents the TDOS in the AP alignment for both majority to minority ($G^{\uparrow\downarrow}$) and minority to majority ($G^{\downarrow\uparrow}$) spin channels respectively. For the $G^{\uparrow\downarrow}$ at the E_{F} we have states with Δ_1, Δ_5 and $\Delta_{2'}$ in the emitting electrode which are coupled to the evanescent states within the MgO and decay similarly as in the $G^{\uparrow\uparrow}$ case. However, in the collecting electrode with minority states at the E_{F}, there are no states available for the Δ_1 electrons, thus Δ_1 will continue to decay in the collecting electrode resulting in a strong reduction of the tunnelling current for the $G^{\uparrow\downarrow}$. Similar situation concerns $G^{\downarrow\uparrow}$ tunnelling, there are no Δ_1 states in the emitting electrode. The overall conductance for the antiparallel case can be written as

$$G_{\mathrm{AP}} = G^{\uparrow\downarrow}_{\Delta_5} + G^{\downarrow\uparrow}_{\Delta_5}. \tag{1.13}$$

The tunnelling magnetoresistance ratio in terms of the P an AP conductances is given by

$$TMR = \frac{G_{\mathrm{P}} - G_{\mathrm{AP}}}{G_{\mathrm{AP}}}. \tag{1.14}$$

Based on the above symmetry considerations, one would expect large values of TMR since the conductance G_{P} is predicted to be much larger than G_{AP}.

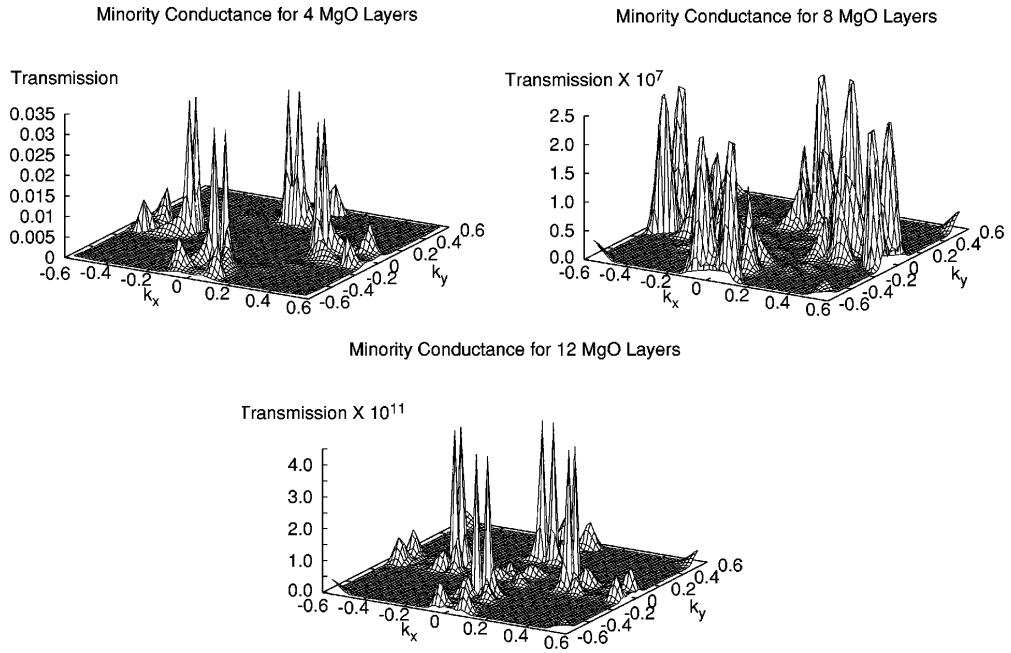

Figure 1.15: Transmission probability in the antiparallel configuration as a function of $\mathbf{k}_{\parallel}$ for 4 and 8 layers of MgO. The transmission shows features appearing in both majority an minority spin channels. Taken from Ref. 83.

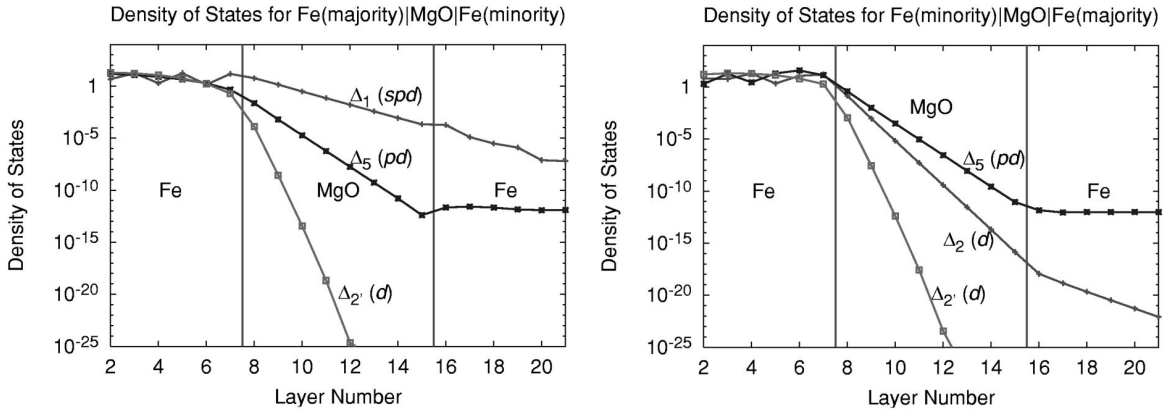

Figure 1.16: Tunnelling DOS (TDOS) for $\mathbf{k}_{\parallel} = 0$ in the antiparallel configuration. The TDOS is plotted as a function of the atomic layer for majority and minority spin channels. The states with Δ_1 symmetry have the smallest attenuation rate in the barrier. Taken from Ref. 83.

1.3.3 Other types of electrodes

All above discussions were based on Fe/MgO/Fe model system because both materials have well understood band structure and symmetry filtering properties. However, as pointed out before, the spin-filtering phenomenon depends on the electronic structure of the whole junction, and as such a proper choice of the electrodes might enhance the TMR.

Zhang and Butler,[85] in analogy to Fe/MgO/Fe junctions, studied theoretically the transport properties of MTJs with *bcc* Co and CoFe electrodes. They predicted that the magnetoresistance for such electrodes can be several times larger than in the case of Fe/MgO/Fe systems. The origin of this difference can be explained by comparing the bands crossing the Fermi level for Fe and Co electrodes. The band structure for both materials along the transport direction, Γ-H, is schematically presented in Fig. 1.17.

The main difference between the two is that for Co all states at the Fermi level are totally spin polarized. For Fe, the Δ_1 symmetry appears only for the majority electrons while Δ_5 and $\Delta_{2'}$ states are present for both majority and minority spin channels giving contributions to a electron current in both magnetic configurations. For Co, Δ_1 exists only in the majority spin electron population while Δ_5 and $\Delta_{2'}$ symmetries appear only for the minority one. As a consequence the TMR is dominated by the parallel majority spin conductance, which in turn is dominated by the Δ_1 states with the slowest decay rate. This is valid for both the Co/MgO/Co and FeCo/MgO/FeCo junctions and produce results similar to these for Fe/MgO/Fe. However, in contrast to latter, for Co(FeCo)/MgO/Co(FeCo) junctions in the antiparallel magnetic alignment all the states at $\mathbf{k}_{\parallel} = 0$ are reflected (Fig. 1.18). This results in a further reduction of the G_{AP} conductance and hence a strong increase of the TMR.

The theoretically predicted TMR is about 5000 %, 13000% and 34000 % the Fe/MgO, Co/MgO and FeCo/MgO junctions respectively.[85] These values do not include contributions from the minority spin channel since for the minority conductance the presence of sharp peaks for $\mathbf{k}_{\parallel} \neq 0$ are hard to calculate accurately. According to

the authors these contributions would not change the TMR significantly.

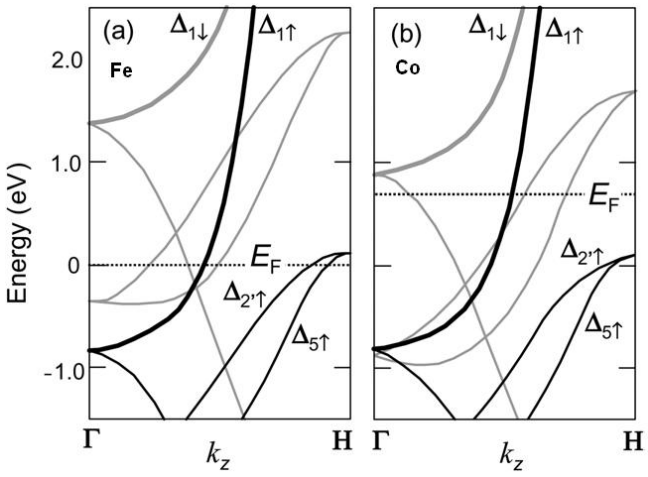

Figure 1.17: Spin- and symmetry resolved band structure of bcc Fe (left) and Co (right). In bcc Fe Δ_5 and $\Delta_{2'}$ states are present in both, majority and minority channels giving contributions in P and AP configurations. In the case of Co all the states are totally spin polarized at the E_F. Taken from Ref. 86.

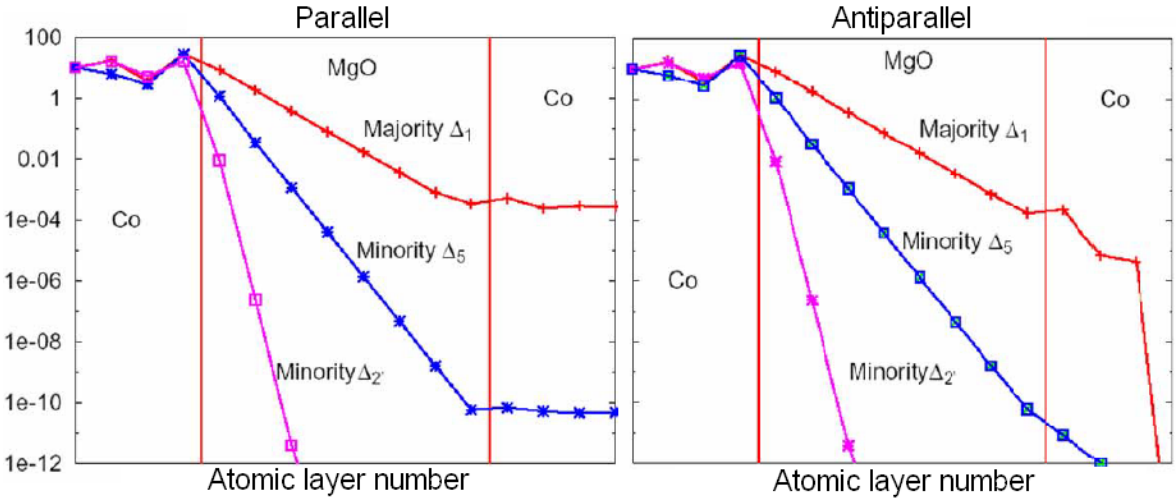

Figure 1.18: TDOS at $\mathbf{k}_{\|} = 0$ for majority and minority spin channels in parallel and antiparallel magnetic configurations for Co/MgO(8ML)/Co MTJ. Taken from Ref. 85.

1.4 Experimental realization

Indeed, experimental works seem to confirm the theoretical predictions. The first reported sizable TMR values, in junctions using Fe electrodes, were published by Bowen *et al.*[87] in 2001 and reached 27% at room temperature (RT). In 2003, this value was increased to 67% at RT in MTJ made by molecular beam epitaxy (MBE) technique by

Faure-Vincent *et al.*[88] Soon after, TMR of 180% was measured in the Fe/MgO/Fe junctions made epitaxially by ensuring clean interfaces.[32] The group of Parkin fabricated textured MTJs and obtain a TMR up to 220% at RT.[33]

In the case of Co electrodes, fully epitaxial Co/MgO/Co MTJ were produced with metastable *bcc* Co(001) electrodes, where the value of the TMR at RT reached up to 410%[86] confirming the theoretical predictions. Recently, Bonell *et al.*[89] have performed detailed experimental and theoretical studies of $Fe_{1-x}Co_x$/MgO/$Fe_{1-x}Co_x$ junctions and showed that the TMR value depends on the content of Co. They have found a maximum TMR value of about 300% at RT for a Co concentration of x=25%.

However, if we want to use MTJ with high TMR in practical devices they need to have specific stacking structure, that is a seed layer, an antiferomagnetic (AF) layer, a synthetic ferrimagnetic structure (SyF), a tunnel barrier and a ferromagnetic free layer.[77] The fundamental problem in using MgO is that the AF/SyF layers have a *fcc*(111) structure on top of which MgO(001) cannot be grown because of a mismatch in the structural symmetry. It was soon realized that the best solution is to used CeFeB electrodes with MgO spacer.[90] Djayaprawira *et al.*[90] fabricated heterojunctions based on CoFeB electrodes that exhibit 230% TMR at RT. In contrast to FeCo electrodes the CoFeB has an amorphous structure, but surprisingly, the MgO barrier with (001) rock-salt texture can grow on top of such an amorphous electrode. The annealing step is then necessary to trigger recristallization from MgO barrier which propagates towards CoFeB electrodes. Due to the fact that FeCoB electrode is amorphous, it can be grown on any kind of underlayers and that makes it compatible with mass production techniques. Moreover, adding boron stabilizes the structure of the electrode. In the case of pure FeCo electrode one has to pay attention to the Co concentration (as was pointed out by Bonell *et al.*[17]) because to much percentage of Co can change the stabilized crystal structure after annealing, increase the lattice mismatch between the electrode and the barrier and consequently reduce the TMR. Boron concentration above 10% helps the layers to grow amorphously and ensures a *bcc* structure after recristalization. Lee *et al.*[91] studied the effect of the electrode composition and thickness on the TMR of $(Co_x/Fe_{100-x})_{80}B_{20}$/MgO/$(Co_x/Fe_{100-x})_{80}B_{20}$ MTJs. They obtained a TMR of 500% at RT for MTJ having 4-nm-thick$(Co_{25}Fe_{75})_{80}B_{20}$ electrodes with a 2.1-nm-thick MgO barrier annealed at 475°C. Another step forward was made by Ikeda *et al.*[14] by showing that the suppression of Ta diffusion into the CoFeB electrode can increase TMR up to 604% at RT. This is the highest TMR value measured experimentally in crystalline junctions, based on MgO barriers.

2 Role of defects in MTJs

The magnetoresistance effect, occurring in magnetic tunnel junctions, is a quite complex physical phenomenon as was described in the previous chapter. It depends on the type and electronic structure of the ferromagnetic electrode, the properties of the insulating barrier, and the chemical bonding at the interface between the two types of materials. These rules can be successfully applied to MTJs with perfect crystalline ordering. Yet, nothing is ever perfect and the resulting TMR strongly depends on the quality of the junction. As it was shown experimentally, the values of the TMR are much smaller than the theoretical predictions even when the highest measured value reaches 604% at RT.[14] The disagreement between theory and experiment was assigned to defects and structure imperfections present in real junctions. Therefore, defect control and characterization are crucial factors for making devices with desired properties and it is essential to determine the origin of these imperfections and compute their properties. Thus, to explain the discrepancy between theory and experiment more realistic models for MTJs are needed, which can handle also intrinsic issues appearing within the heterostucture like interface imperfections.

In this chapter several possible defect types in nominal Fe/MgO/Fe system and FeCoB/MgO/FeCoB for which the highest TMR has been measured and their influence on tunnelling current will be discussed. The main focus will be put on point oxygen vacancies within the MgO barrier since the understanding of the properties of these type of defects are the main goal of this thesis.

2.1 Interface oxidation

One of the crucial factors determining the value of the TMR is the bonding at the interface between the ferromagnet and the insulating barrier. The chemical nature of the interfacial bonds will define the spin polarized tunnelling and the resulting TMR. In the perfect situation oxygen atoms are located on top of iron atoms and ensure

effective coupling of the incoming wave function from the electrode to the evanescent states within the barrier. Even though a big effort is put on making devices with better crystalline quality it remains difficult to control the interfaces between materials.

Meyerheim *et al.*[15] showed that a FeO layer often forms at the interface between Fe and MgO when MgO is deposited onto a Fe(001) surface. The modification of the interface can significantly influence the spin dependent tunnelling as compared to the ideal interface. Based on the experimental work, Zhang *et al.*[16] studied the impact of the interface oxidation from first principles. They considered a structure of Fe-FeO_x-MgO-Fe stack with 8 monolayers of MgO using the experimental intralayer distances and atomic configuration.[15] The conductance was calculated using LKKR method as a function of the oxygen concentration (x), and it is summarized in Fig. 2.1.

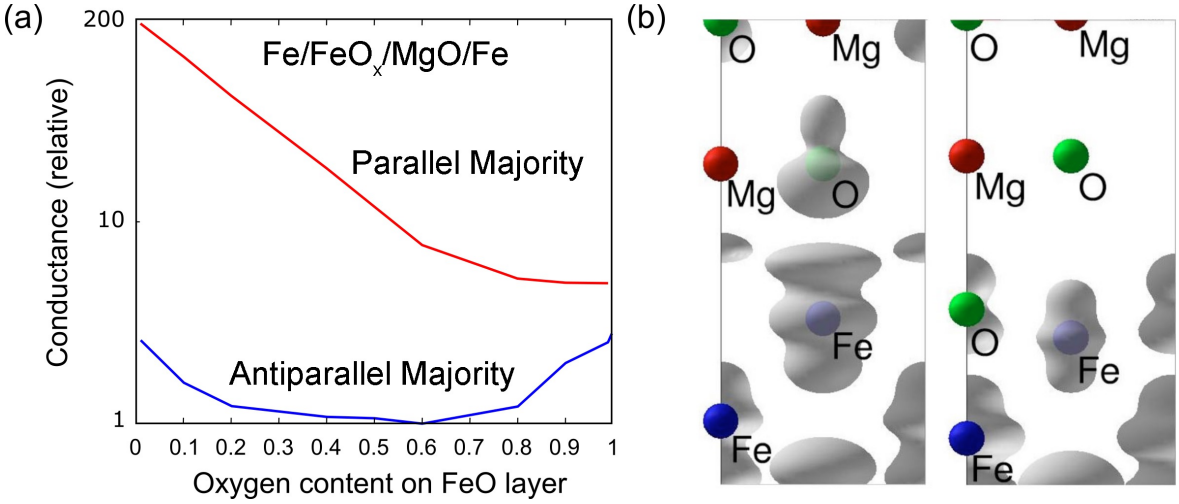

Figure 2.1: Oxidation of the Fe/MgO interface. a) Conductance evaluated as a function of oxygen concentration within the interfacial FeO layer. b) Partial DOS at the Fermi energy for Δ_1 majority states near the oxidized (right) and ideal (left) interface. Taken from Ref. 16.

Fig. 2.1(a) shows the relative conductance of the majority spin channel for the parallel magnetic configuration, and the majority-minority channel for the antiparallel alignment as a function of oxygen concentration in the FeO_x layer. It is evident that the main effect of iron oxidation is a reduction of the conductance in the parallel channel. The antiparallel one is only slightly affected by the additional FeO layer. This can be explained by the change of the electron density at the Fermi energy corresponding to the Δ_1 majority state when FeO layer is introduced. Fig. 2.1(b) presents the partial density of states at the E_F for the Δ_1 channel near the ideal (left panel) and the oxidized (right panel) interface. As it can be seen, the introduction of the FeO layer greatly reduces the density of states in the interlayer region compared to the clean interface. In contrast to weak interaction between Fe and MgO at the interface in Fe/FeO/MgO the charge transfer between Fe and O in the oxidized layer changes drastically the electronic structure of the interface.[16] Moreover, a significant magnetic moment was found on the O sites in the FeO layer which implies a strong hybridization between the O atoms and neighbouring Fe atoms. As a consequence, the Δ_1 electron density is essentially concentrated within the Fe-O plane and the coupling of the Δ_1 states becomes less effective, resulting in a strong reduction of the tunnelling current in the majority spin

channel. Since the Fe-O bonds are mainly composed of s and p-like electrons, the d-like electrons are not significantly affected by the presence of the O atoms of the FeO layer. Thus, the impact of the Fe-O bonds on the majority spin channel is much larger than on the minority one. Because the current in the antiparallel configuration is carried out mostly by the Δ_5 electrons and is hardly modified by the additional FeO layer, it results in a drop of the TMR value.

More recent experimental studies of Bonell *et al.*[17] showed that the TMR decreases when the interface oxygen concentration increases, and it is caused by a reduction of the conductance for the parallel magnetization, while the antiparallel one is barely altered, in agreement with the theory.[16] However, in contrast to the theory, the measured drop of the TMR caused by the interface oxidation was not that drastic as expected. They noted a change of the TMR from 140% for a ideal Fe/MgO/Fe system to 120% in FeO_x/MgO/Fe junctions and still reaches 85% with a disordered 2 ML of FeO at the interface. They suggested that although the interface oxidation and the structural disorder have a negative impact on the resulting TMR, they are not the main source of the discrepancies between theory and experiment and additional factors have to be included.

2.2 Grain boundaries in MgO thin films

In almost all practical devices metal oxide films are polycrystalline, i.e. there exist crystal grains and grain boundaries (GB). This is also the case for the textured MgO(001) barrier in the CoFeB/MgO/CoFeB MTJs. However, very little is know about the influence of the grain boundaries on the tunnelling conductance in such junctions.

One might expect that this kind of imperfections would lead to leakage current reducing both the tunnelling resistance and the TMR ratio. Nonetheless, the R·A (Resistance · Area) products and TMR values reported for CoFeB/MgO/CoFeB junctions with textured MgO barriers are similar to these of epitaxial MTJs with a single-crystal MgO barrier.[32,86,90,91] To clarify the role of the GB, Mizuguchi *et al.*[18] used STM technique to measure the local tunnelling conductance in a polycrystalline MgO(001) barrier grown on an amorphous CoFeB electrode. The main conclusion of their work is that the tunnelling current flows uniformly despite the existence of grain boundaries and thus GBs cannot affect considerably the overall device performance.

Some more light was recently shaded by Bean *et al.*[19] where they examined the structure and the role played by the grain boundaries from experimental and theoretical point of view. They used the annular bright-field (ABF) scanning TEM (STEM) imagining to determine the granular structure of the MgO barrier in FeCoB/MgO/FeCoB MTJs with policrystalline MgO barriers. Their analysis identified the most commonly occurring GB structural units allowing them to construct model systems for first principles calculations. These structures are presented in Fig. 2.2.

The calculations were carried out using DFT methodology as implemented in the VASP package and PBE and HSE06 functionals to describe the exchange-correlation term (see the next chapter for details). Since HSE06 gives better estimation of the MgO band gap (7.2 eV comparing to the experimental value of 7.8 eV) than PBE functional (4 eV), only the results obtained with the former functional will be presented. It is

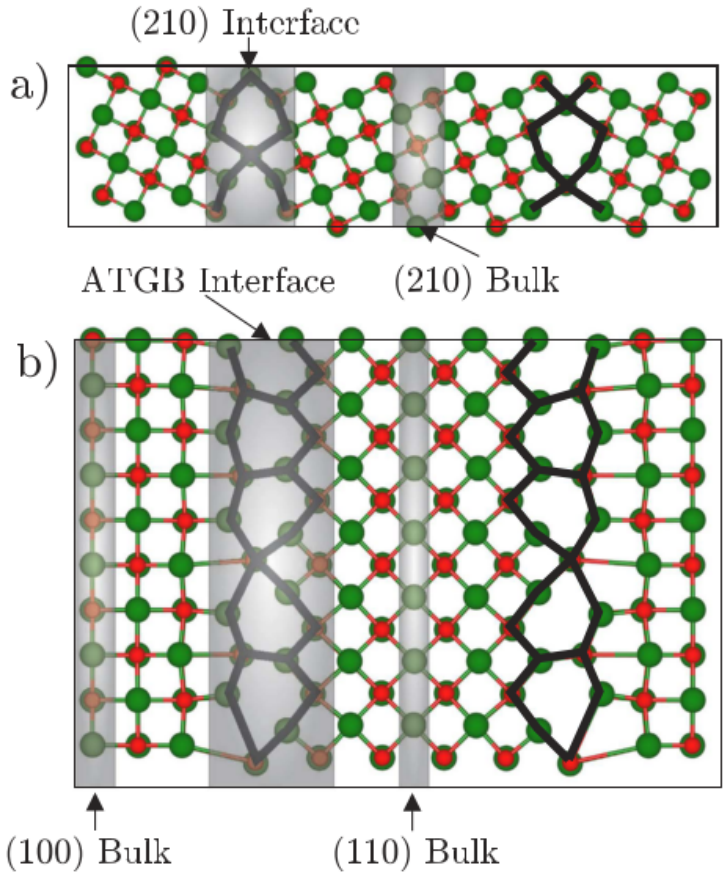

Figure 2.2: Supercells used to model common grain boundary structures occurring in MgO films. a) $\sum$(210)[001] symmetric tilt grain boundary and b) (100)/(110)[001] asymetric tilt grain boundary. Red and green atoms represent O and Mg respectively. The shaded areas indicate atoms used to evaluated the projected density of states. Taken from Ref. 19.

worth noticing that despite the PBE underestimation of the band gap both functionals gave similar qualitative results and predicted similar changes in the electronic structure of MgO.

Bean *et al.* evaluated the electronic structure for each GB supercell and analyzed a density of states projected onto the bulk and the interface regions of the supercell (shaded areas indicated in Fig. 2.2) to isolate the electronic states associated with GB defects. In both cases GB reduce locally the MgO band gap up to 3 eV.

For the $\sum$(210)[001] symmetric tilt GB (Fig. 2.3 (a)) the associated electronic states are the highest occupied levels (about 0.05 eV higher than the bulk valence band maximum) and more prominent wide band of states in a 2 eV window below the conduction band minimum. This effectively reduces the band gap at the GB to 5 eV.

For the (100)/(110)[001] asymmetric tilt GB the changes in electronic structure are even more pronounced (Fig. 2.3(b)). In this case the DOS is projected onto the bulk regions of each grain separately since these may be slightly different due to small unphysical strain in the supercell. Nevertheless, as seen in Fig. 2.3 (b), the difference is very small proving that the strain has a negligible effect on electronic properties. Here, also the highest occupied states correspond to the (100)/(110)[001] GB (about 0.2 eV

above the valence band maximum). Again the most prominent feature is a wide band of states below the conduction band minimum but this time spanning energy window of 3 eV. This reduces the band gap at the GB to 4 eV.

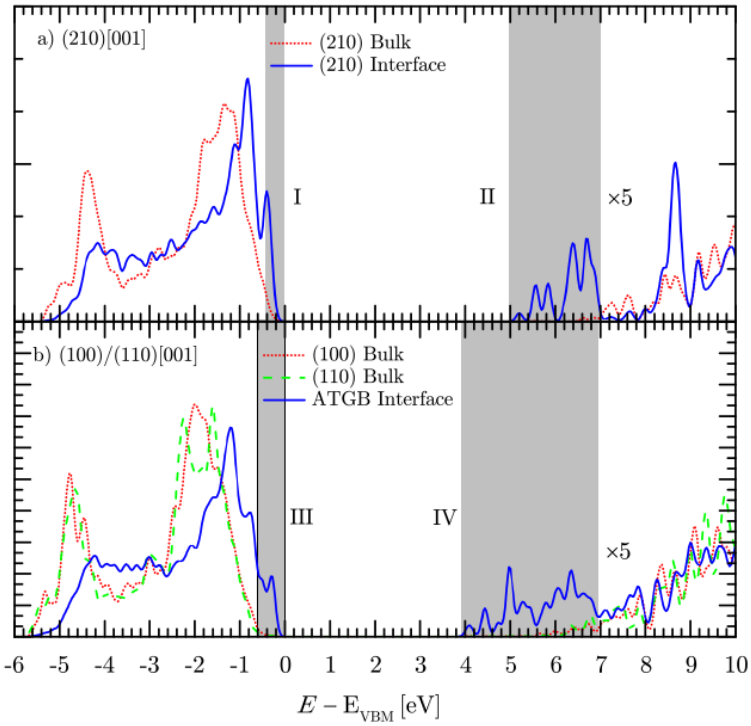

Figure 2.3: DOS for grain boundary (GB) in MgO within HSE06 functional. a) $\sum$(210)[001] symmetric tilt GB and b) (100)/(110)[001] asymetric tilt GB. Taken from Ref. 19.

To better understand the effect of GB on magnetoresistance, the authors developed a simple phenomenological model where they relate the resistance of the bulk and the GB regions to their respective cross-section areas and the transmission coefficients using Landauer formula. The transmission coefficients are evaluated based on a simple square barrier model. They predicted that, due to the band gap reduction at the GB and the associated barrier for tunnelling, a high proportion of the tunnelling current is shunted through GBs, rather than through the bulk-like regions, even for relatively large grain sizes. However, due to lower symmetry at the GB the symmetry filtering effect is not that effective as for the ideal MgO structure which leads to lowering of the overall TMR effect. Nonetheless, this model is very simple and does not include details of MgO and Fe band structures and gives only qualitative estimations. More advance analysis and transport calculations would certainly improve the actual effect of the GB on transport properties.

2.3 Boron diffusion

The highest TMR values were obtained for junctions of type CoFeB/MgO/CoFeB which are also more preferable for commercial usage (see subsection 1.4). During the junction deposition the CoFeB electrode grows amorphously and the sample has to

be afterwords annealed to trigger the crystallization process. However, during the annealing process some atoms might diffuse between the layers and create unpredicted structural defects which effectively worsen the device performance. As was shown by Ikeada *et al.*,[14] by suppressing the diffusion of Ta into the upper electrode layers, the TMR can be increased up to 600% at RT.

The diffusion of boron is more controversial and there have been many contradictory results on the fate of boron following the annealing process. The possible scenarios include boron diffusion towards the Ta layer (used as a capping layer),[20,21] the segregation at the CoFe/MgO interface[22,23] and the diffusion into MgO barrier (forming BO_x oxides).[23,92–94] However, resent experimental investigations seem to prove that boron is not found within the MgO barrier.[24–26] Generally, the composition and the quality of the junction depends strongly on the preparation method and controlling the growth condition can help avoiding undesired boron diffusion towards the interfaces and the barrier. This diffusion can be partially controlled/suppressed by a good choice of the material serving as a capping layer[20] and by adjusting the annealing temperature.[25]

There are also several theoretical papers which estimated the effect of boron on the tunnelling magnetoresitance.[93,95,96] For example, Burton *et al.*[95] included boron at the CoFe/MgO interface and found that for crystalline CoFeB/MgO/CoFeB(001) MTJs it is more favourable energetically for B to remain at the CoFeB/MgO interface rather than in the electrode. The presence of B at the interface reduces the conductance through the Δ_1 channel due to weakening of the bonding between CoFe and MgO. However, the attenuation coefficient of the Δ_1 remains the same since it is defined by the complex band structure of MgO. The overall effect of boron at the interface is to reduce the TMR, and hence one should prevent this situation from happening. While, Han *et al.*,[93] also using ab initio calculations, reached the opposite conclusion by considering the scenario where boron impurities appear within the MgO barrier in Fe/MgO(5ML)/Fe MTJ. They considered two cases: a) a B^{3+} ion substituting a Mg^{2+} ion at the central layer of MgO $[(MgO)_{39}_B^{3+}O^{2-}]$; b) a pair of B^{1+} ions replacing a Mg^{2+} $[(MgO)_{39}(B^{1+})_2O^{2-}]$. The first situation considers +3 oxidation state of boron in B_2O_3, and the second that each B in B_2O_3 has three oxygen neighbours. They concluded that the main effect of boron is to reduce the MgO band gap with the increase of boron concentration, which will lead to a gradual increase of the tunnelling current. A different situation was considered by Bai *et al.*[96] They proposed that in the case of thin MgO films sandwiched between CoFeB electrodes a $Mg_3B_2O_6$ phase can be created after annealing. Their calculated values of TMR for such CoFeB/MgOB/CoFeB structures are found to be in good agreement with experiment. The new MgOB phase has a lower symmetry than the cubic MgO which leads to a strong scattering of the $\mathbf{k}_\parallel$ transmission.

The above calculations are interesting however they did not compute the energy barrier for the migration of boron across the interface. Therefore it is not clear whether the results reached are realistic. It is also important to notice that none of these calculations has shown additional midgap states inside the MgO band gap induced by boron.

2.4 Point defects within MgO

Another common type of defects within MgO, except of grain boundaries, are point vacancies. The presence of vacancies in MgO give rise to a variety of interesting optical,[97] catalytic and transport properties which are absent in the ideal crystalline material. Since MgO is an ionic crystal, several possibilities of lattice vacancies might occur, in which the ground states of cationic or anionic vacancies are either in neutral or charged form. The most plausible are oxygen and magnesium vacancies, denoted F and V respectively. They can appear in a neutral as well as charged or doubly charged states, denoted as F^+, F^{2+}, V^- and V^{2-}. Moreover, defects can show up a single F and V centers or paired vacancies like oxygen divacancies, F_2 or M, and neighboring oxygen-magnesium vacancies, P centers, as shown schematically in Fig. 2.4.

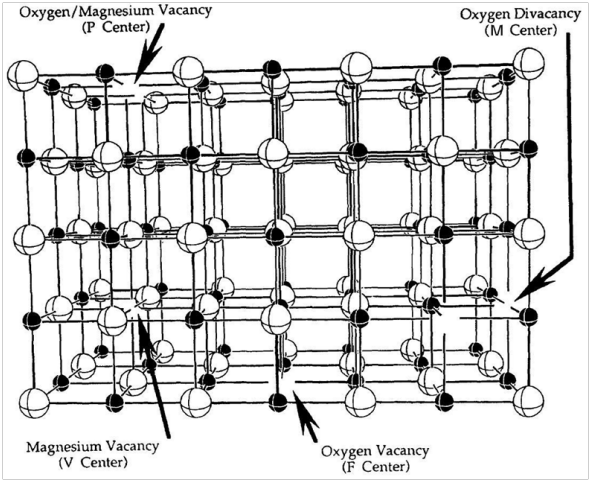

Figure 2.4: Various defects in MgO. Taken from Ref. 27.

In addition, Tab. 2.1 presents the formation energies for possible vacancies species within MgO.[27] As it can be seen, the formation energy for the oxygen vacancies is the lowest and implies that such defects are more likely to occur.

Table 2.1: Calculated formation energies for defects in MgO. Values taken from Ref. 27.

Defect	F	F^+	F^{2+}	F_2/M	V	V^-	V^{2-}	P
Formation energy [eV]	1.82	3.67	5.47	3.23	13.82	14.83	16.35	3.48

Such imperfections in crystalline MgO can lead to the creation of additional energy levels within the nominal band gap of MgO and thus to a local reduction of the effective tunnelling barrier height. Electrons can tunnel through the barrier via these additional states with different scattering rates than for an ideal barrier. Moreover, these defect states can mix symmetries of the electron wave function and might have a negative impact on TMR.

Additional energy levels within the insulating barrier might act as new paths for electrical transport through the barrier and as such they can be electrically probed.

Indeed, several experimental groups have reported measured barrier heights for MTJs with MgO spacer much lower than the nominal value of 3.9 eV and these are summarized in Tab. 2.2.

Table 2.2: Experimentally reported barrier heights for MTJ based on MgO.

MTJ	TMR [%]	Barrier height [eV]	t_{MgO} [nm]	Ref.
Fe/MgO/Fe	130 (190_{1K})	0.38/0.82*	2.5	31
Fe/MgO/Fe	180 (247_{20K})	0.39	2.3	32
FeCo/MgO/FeCo	120-220	1.1-1.7	2-3	33
FeCoB/MgO/FeCoB	100	0.62/0.5**	2.5	30
Fe/MgO/FeCo	$23_{4.2K}$/ 20_{70K}	0.9	2.6	98

* Barrier heights estimated for the symmetry coherent tunnelling process and the normal spin-coherent tunnelling process respectively.
** Barrier heights evaluated for parallel and antiparallel magnetic configurations.

These barrier heights were associated with different kinds of oxygen vacancies within MgO in their neutral as well as charge states, i.e. F/F^+ centers are responsible for barriers at 1.1 eV. However, the exact identification of defect types responsible for all kinds of barrier heights is not an easy task. The most interesting defects are these whose barriers are at 0.4 eV because they might influence the TMR and their origin is not known. Indeed Schleicher *et al.*[30] suggested that they can be the result of paired oxygen vacancies and have strong effect on transport. Since the main focus of this thesis is to study the effect of single and double oxygen vacancies on tunnelling transport, these defects will be described in the following subsections.

2.4.1 Single oxygen vacancy - F center

As it was explained in subsection 1.2.1, the valence bands of MgO are mainly of oxygen character and thus they contain mostly oxygen $2p$ orbitals. As for the lowest conduction bands, they are essentially of $3s$ states of magnesium. When a neutral oxygen atom is removed from MgO a doubly occupied electronic state is created in its energy band gap. This is a consequence of the ionic nature of the electronic structure of MgO.[27,73,99] After the removal of one oxygen atom, the remaining two electrons of O^{2-} are essentially localized in the vacancy site to preserve the ionicity of $Mg^{2+}O^{2-}$.

Velev *et al.*[28] reported ab initio study on the effect of the F center on the spin-dependent tunnelling in a Fe/MgO/Fe MTJ. Vacancies were introduced simply by a removal of one oxygen atom from supercells containing 32, 64 or 216 atoms. Atomic relaxations showed that the MgO lattice is only slightly distorted in the vicinity of the vacancy. To study the impact of the vacancy on the MgO electronic structure they compared the resulting DOS of the F-MgO to that of bulk MgO (see Fig. 2.5). It was shown that, due to the oxygen removal, a localized state laying close to the middle of the energy band gap of MgO is produced (denoted Fs). As discussed at the beginning of this section, this state is doubly occupied. Moreover, there appears also an unoccupied state close to the bottom of the conduction band (marked as Fp state). The examination of the electron density on the vacancy site revealed that the

occupied state below the Fermi level shows a spherical distribution of its charge and is thus of s character (Fig. 2.5 (a)). Based on Fig. 2.5(a) it is also clear that the Fs state hybridizes with the p states of the nearest neighbour oxygen atoms. Similar analysis for the unoccupied F state shows that it is of p character (Fig. 2.5 (b)). Here, also the hybridization with the nearest oxygen atoms is seen. Since the Fp state lays in the continuum of the conduction bands, a nonzero electron density is present on the atoms far away from the vacancy site.

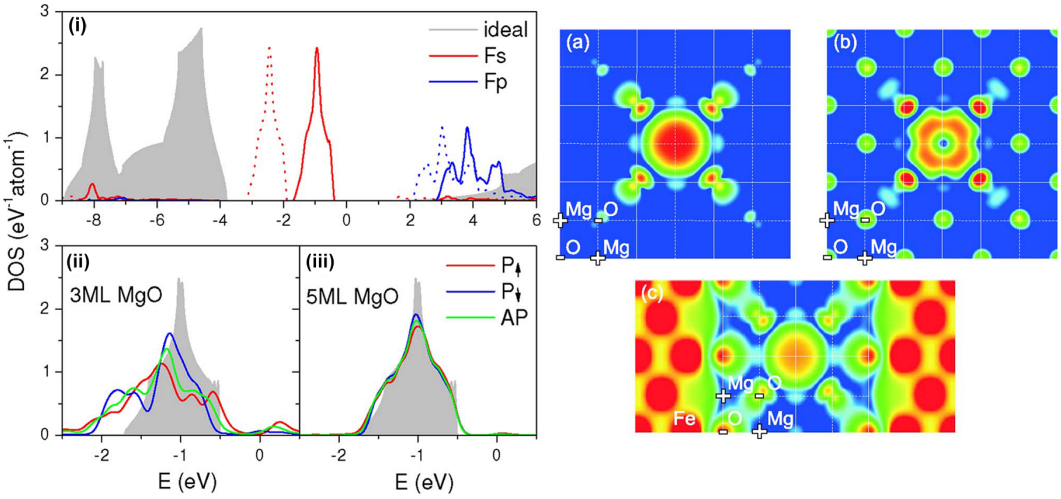

Figure 2.5: Electronic properties of F center within MgO. (i) The DOS of F center superimposed on the DOS for bulk MgO - shaded area. (a/b) Electron distribution on vacancy site for occupied and unoccupied defect levels respectively. (ii/iii) The DOS for F state within Fe/MgO/Fe stuck with 3 (left) and 5 ML (right) of MgO. (c) Electron distribution on vacancy site placed in Fe/MgO(5ML)/Fe junction. Take from Refs. 28, 29.

The above discussion concerns the properties of the F center within the MgO crystal. However, for a proper estimation of the defect level position within the band gap and resulting barrier high for the electron tunnelling the ferromagnetic electrodes have to be included in the calculations. The results of Velev *et al.*[29] for the F center within MgO integrated in Fe/MgO/Fe junction are presented in the panels (ii), (iii) and (c) of Fig. 2.5. The vacancy is generated in the middle layer of the MgO spacer. The resulting DOSs for Fs state within 3 and 5 ML thick MgO barrier are shown in panels (ii) and (iii), respectively; the shaded area represents the DOS for the Fs state within the MgO bulk. As it can be seen, the width of the localized state depends on its coupling to the Fe electrodes as well as on the magnetic configuration of the electrodes. For small thickness of MgO, when the interaction between the Fs state and the electrodes is strong, the peak broadens due to a large escape rate between the localized state and the electrodes. When the MgO thickness is increased to 5 ML (panel (iii)) the properties of the Fs state are recovered, thus the minimum separation between Fe and the vacancy site should be at least 2ML. Similar results were also obtained in our calculations as it will be presented afterwords. Panel (c) depicts the electron density of the defect in the Fe/MgO/Fe heterostucture with 5 ML of MgO. By analogy to the Fs in bulk MgO, a localized defect interacts mostly with the nearest neighbours and the interface oxygen atom are practically not affected.[29] It is important to notice that

when the electrodes are included the position of Fs state with respect to the Fermi level can be estimated. Thus, the Fs level is located around 1 eV below the Fermi energy. This is in agreement with the experimental studies showing barrier heights of 1.1-1.7 eV and associating them with single oxygen vacancies.[33]

Impact on the conductance

In the next step Velev *et al.*[28,29] studied the tunnelling conductance in Fe/MgO/Fe(001) MTJ with 5 ML of MgO. For the self-consistent electronic structure calculations they used the tight-binding linear muffin-tin orbital (TB-LMTO) method in the atomic sphere approximation. The transmission probability as a function of energy was obtained based on the principal layer Green function technique. The oxygen vacancy was simulated by an empty sphere with this same atomic radius as an oxygen atom placed in the middle layer of MgO.

Fig. 2.6 (a-c) plots the transmission as a function of energy for the majority and the minority spin channels in the parallel and the antiparallel configurations, respectively. The resulting TMR is presented in panel (d). All the results are confronted with calculations for ideal junctions without any defect.

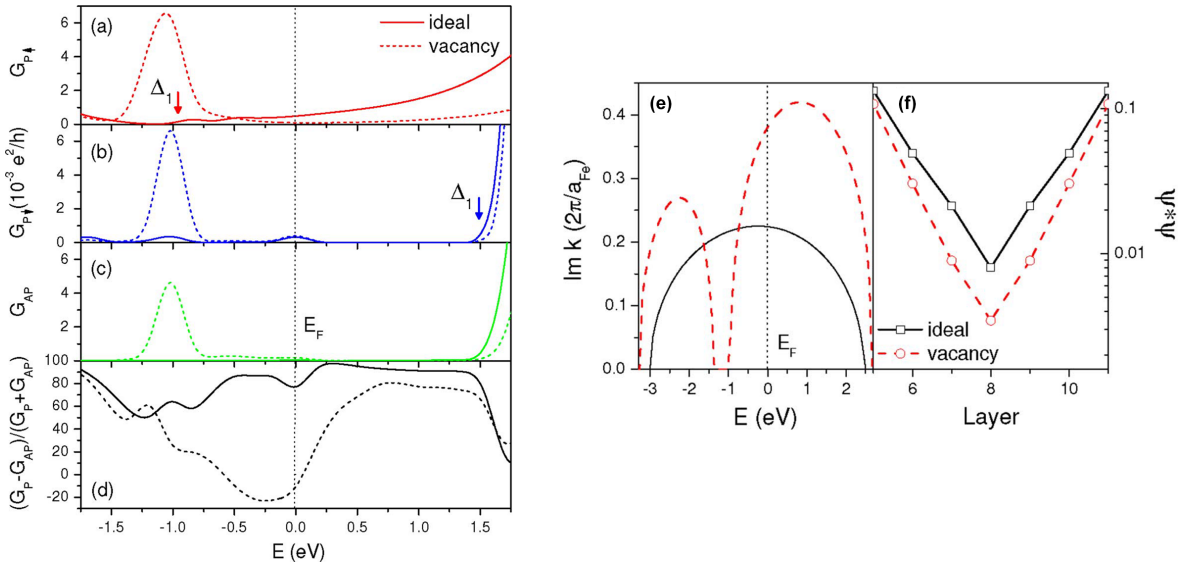

Figure 2.6: Impact of the F center on the transmission through Fe/MgO/Fe junction. The conductance as a function of energy for (a) the majority and (b) the minority spin channels in the parallel and (c) the antiparallel alignment of the electrode's magnetizations. The decay rate for the Δ_1 channel evaluated based on (e) complex band structure for ideal (solid line) and defective (dashed line) MgO crystal and (f) from the probability density $|\Psi|^2$ in the Fe/MgO/Fe at the E_F. Take from Ref. 29.

Evidently, the existence of an F center results in a large peak in the conductance when the energy of the tunnelling electrons is in a resonance with the energy of the localized state, namely around 1 eV below E_F (panels a-c). Similar peak appears around 3.5 eV above the E_F and corresponds to the F center p state near the conduction band (not shown). In the resonance conditions the conductance is enhanced for both spin channels in the parallel and antiparallel spin configurations (G_P, G_{AP}). As a result

the difference between G_{P} and G_{AP} decreases as well as the value of the TMR around the resonance (panel d). Moreover, the O vacancy affects the majority Δ_1 channel also away from the resonance; the corresponding minority channel and conductance in the AP configuration are practically unchanged with respect to the ideal structure away from the resonance. From panel (a) one can see that $G_{\mathrm{P}}^{\uparrow}$ is reduced by a factor of 5-7 off the resonance. This reduces the differences between G_{P} and G_{AP} as well as the ensuing TMR. The reduction of the conductance in the majority channel is explained by the scattering of tunnelling electrons between states with different transverse wave vectors $\mathbf{k}_{\parallel}$. As was presented in the previous chapter, the states with $\mathbf{k}_{\parallel} \neq 0$ are attenuated much faster within the barrier than those of $\mathbf{k}_{\parallel} = 0$ states.[29]

This interpretation can be also verified by studying the decay rate of the Δ_1 state within an ideal and a defective MgO crystal. Figure 2.6(e) presents the complex band structure for MgO with (dashed line) and without (solid line) O vacancy. The Fermi level is the one corresponding to the Fe/MgO/Fe junction. The existence of the defect state at 1 eV below E_{F} splits the gap into two parts. At the resonance the attenuation coefficient (proportional to Im(k) value) is strongly reduced which explains the large peak in the conductance at this energy. On the other hand, out off the resonance the decay parameter is increased and becomes larger than the one for bulk MgO. This confirms that the presence of F center effectively increases the decay rate. In addition, the decay rate of MIGS can be evaluated based on the slope of the probability density $|\Psi|^2$ as a function of MgO thickness, t_{MgO}. Figure 2.6(f) presents $|\Psi|^2$ for the Δ_1 state at the E_{F}, showing that the decay rate is about 24% larger than for the ideal case.[29] This implies a decrease of the transmission as seen before.

In the case of the minority electrons the influence of the F state is not that pronounced since the minority transmission is mostly due to the states with $\mathbf{k}_{\parallel} \neq (0,0)$. Consequently, out off resonance scattering can contribute to both spin channels, constructively and destructively, and is not expected to change significantly the minority transmission.

More oxygen vacancies in MgO barrier

The work of Velev *et al.* described above considered only a single oxygen vacancy in the middle layer of MgO. However, the situation in a real junction can be much more complicated and can involve different number and types of O vacancies (OV). In this respect, Ke *et al.*[50] studied a system composed of semi-infinite Fe electrodes and 13 ML of MgO with oxygen vacancies distributed within the MgO layers. Their calculations were based on DFT in conjunction with Keldysh nonequilibrium Green function formalism. In order to average over many disordered configurations the theory of nonequlibrium vertex corrections was used. An oxygen vacancy was created by randomly replacing an oxygen atom with a vacuum sphere (VA) of the same size and the lattice distortion around the defect was neglected. The substitutional disorder is realized by the alloy model $\mathrm{O}_{1-\mathrm{X}}\mathrm{VA}_{\mathrm{X}}$ where X denotes the percentage of oxygen vacancy. Finally, the conductance is calculated as a function of oxygen vacancies concentration X. Figures 2.7(a) and 2.7(b) show the conductance as a function of X for P and AP configurations where the concentration of OV on layer 1 of MgO (first interface) is fixed to 3% and varies as X% on layer 13 (second interface), leaving the rest

of MgO layers unchanged. As it is clearly seen, the vertex corrections which are related to diffusive scattering dominate all conduction channels. The $G_{\mathrm{P}}^{\downarrow}$, $G_{\mathrm{AP}}^{\uparrow}$ and $G_{\mathrm{AP}}^{\downarrow}$ are almost entirely due to diffusive scattering. This is explained by the fact that interface oxygen vacancies promote interchannel scattering. As a consequence, the minority Fe electrons can couple to the slowly decaying Δ_1 band of MgO. In the ideal case these minority states would be filtered out by the MgO barrier. The ensuing increase of G_{AP} strongly reduces the resulting TMR from the ideal limit of 10 000% to about 250 %, as shown in Fig. 2.7 (c) for several junctions. Moreover, to emphasize the role of the interfacial oxygen vacancies, additional OV were added in layer 7 of MgO. As it can be seen in the inset of Fig. 2.7 (d) the TMR stays at 350% practically independent of the OV in layer 7.

In further analysis, the OV were located in layers 2 and 12, leaving all other layers of MgO clean. It was found that the effects on the TMR are qualitatively the same as for the interfacial OV. The TMR decreases up to 250% and additional OV in the middle layers of MgO do not have any significant impact on the TMR value. The main difference between the junction with interfacial OV and that with next-neighbour OV is the behaviour of G_{P}. In the case of interfacial OV (Fig. 2.7 a) the conductance increases with X% while for next-neighbour OV the conductance decreases. The G_{AP} conductance follows the same trend as in Fig. 2.7 (b). An interfacial OV reduces the effective width of the MgO tunnel barrier, thus enhancing the tunnelling probability. In contrast, the OVs (especially the interior ones) create scattering centers for electrons that reduce tunnelling.

Next, the OV were placed in the interior MgO layers leaving the interface and the next-neighbour MgO layers clean. By systematically putting the same OV concentration at one layer at a time, it was found that the further away from the interface it is, the lesser is the decrease of the TMR caused by OVs. As mentioned, the interfacial OV causes interchannel scattering and thus increases the coupling between minority states in Fe to the slowly decaying states within MgO which effectively increases G_{AP}. But, as the oxygen vacancy is shifted into the interior of MgO layers, the wave function of spin-down electrons has more difficulty to reach the localized state and the impact of interchannel scattering is reduced. The $G_{\mathrm{P}}^{\uparrow}$ conductance for all interior OV (layers 3-11) was found to decrease with increasing of OV concentrations. Finally, when we compare the impact of oxygen vacancies[50] with interface disorder,[100] it was shown that the interface oxygen vacancies are more efficient in reducing the TMR than the interface disorder.

The general conclusion of the studies presented by Ke *et al.*[50] is that a small amount of OVs at or near the interface triggers diffusive scattering, causing the spin-down minority electrons in Fe to couple with Δ_1 states within MgO, leading to a reduction of the TMR ratio from the ideal theoretical limit to the experimentally observed values. The effects of the interior OV are much less pronounced, but breaks the symmetry of Δ_1 states which significantly increases the junction resistance.

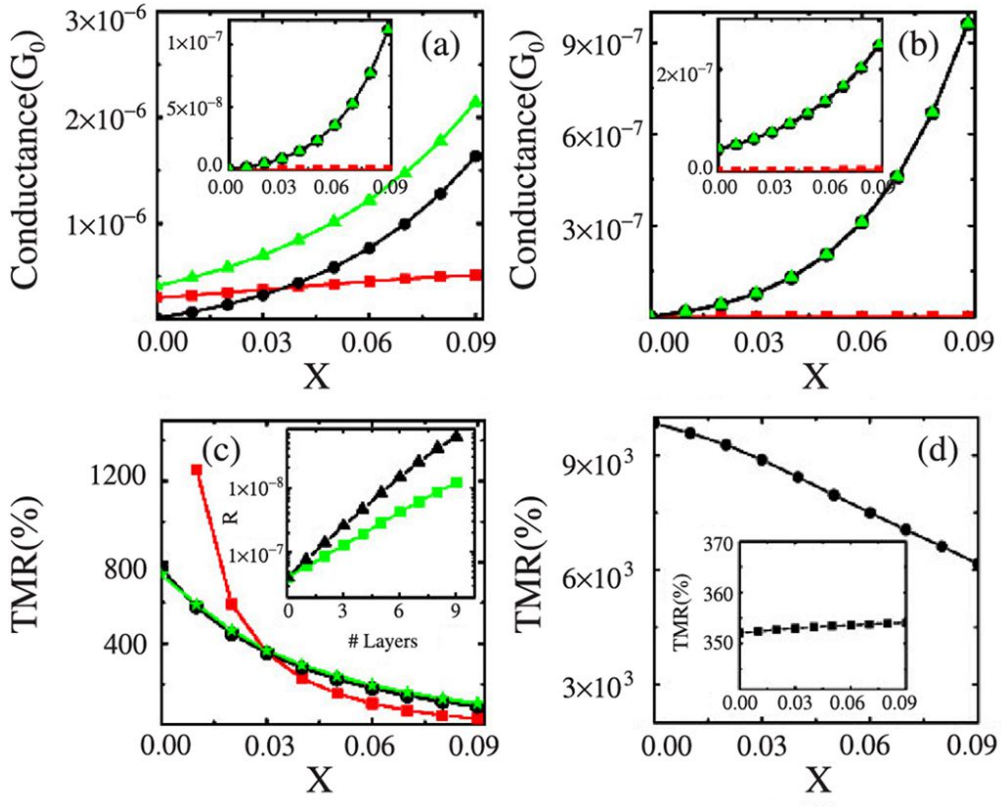

Figure 2.7: Conductance of Fe/MgO(13ML)/Fe junction as a function of oxygen vacancy concentration. a,b) conductance for spin up and -down (insets) channels in P and AP configurations respectively. O vacancies are placed at the interfaces, first one with fixed 3% of vacancy concentration and the second interface with varied concentration $X\%$. The total conductance is marked by green up-triangles, the coherent part by red squares, and the vertex correction part by black circles. c) The resulting TMR for symmetric junctions (red squares) with the same number $X\%$ of OV at both 1 and 13 layers; and asymmetric junctions (black circles) with 3% of OV on layer 1 and $X\%$ on layer 13. The green stars stand for junctions with the same disorder as black circles but with only 7 ML of MgO. d) TMR value for structures where OV are replaced by nitrogen atoms Take from Ref. 50.

Optical activity of the F center

Point vacancies can be also a source of interesting optical properties of ionic crystals and be responsible for their colors.[73,99] As it was already stated, the F centers are negatively charged ion vacancies, where the remaining electrons are localized around the vacancy to maintain charge neutrality of the crystal. These electrons create additional energy levels within the MgO band gap and can be involved in optical spectra produced by various excitations between defect levels giving rise to the color of MgO.[73,97,99,101–103] Here, only the main points in optical characterization of F/F^+ centers will be presented

since optical activity is not the main focus of this thesis.

Several works have investigated optical activity of oxygen vacancies within pristine MgO crystals and with varying defect concentration.[48,97,104–108] The F and F^+ centers present broad photoluminescence (PL) bands centered at ∼2.3 eV[106] (∼ 500 nm) and ∼3.2 eV[103,106] (∼ 400 nm), respectively. The absorption band associated with the F and F^+ states is about 5 eV. It was further found by Kappers *et al.*[103] that this band is actually the convolution of two distinct absorption bands at 4.96 eV and 5.03 eV, due to F^+ and F states, respectively. More detailed time- and temperature-resolved PL measurement have shown that the optical activity of F/F^+ centers is a more complicated phenomenon.[48,97] The PL spectra of F^+ shows a strong temperature dependence which suggest the possibility of involving temperature activated processes.[48] The PL of the F center on the other hand shows almost no change with temperature. Moreover, time resolved PL experiment revealed that the F^+ luminescence has a fast decay component, in the $ns - \mu s$ timescale, while the F center emission is detected only at longer detection delays.[48] To explain these unconventional results Rosenblatt *et al.*[97] have proposed a model where trap states and lattice relaxation influence the PL spectra. This model was further modified by Uchio and Uenaka[48] to include the temperature dependence and the fast decay component of the F^+ band. These models will not be discussed here in more detail, all the information can be found in the literature.[48,97]

It is worth however mentioning the recent work by Rinke *et al.*[109] and Ertekin *et al.*[110] concerning the optical activity of F and F^+ centers from a theoretical point of view. In these works the absorption and emission spectra for these vacancy sites have been calculated using different methodologies. The calculation of Rinke *et al.* is based on many-body perturbation theory with the G_0W_0 approximation while that of Ertekin *et al.* on Quantum Monte-Carlo (QMC) approach. In both calculations, quantitative values were obtained for the absorption and emission spectra of F and F^+ states and were found to compare well with experiment except for the F center emission. The latter is found at 3.4 eV (Rinke *et al.*) and at 3.5 eV (Ertekin *et al.*) compared to the experimental value of 2.3 eV. To explain this difference Rinke *et al.* proposed a modification of Rosenblatt model to attribute the 3.2 eV luminescence to both F and F^+ centers. The emission peak at 2.3 eV was rather associated to the electron relaxation from F/F^+ levels to the hole states existing within the valence band.

2.4.2 Double oxygen vacancies - M center

As seen in the previous subsection F centers can appear in different concentrations and in various configurations within MgO spacer affecting differently the processes of electron tunnelling. When the concentration of oxygen vacancies increases they can interact to create more complicated clusters of vacancies. The simplest one is a double oxygen vacancy called M center. Similar to the F center, paired oxygen vacancies can appear in charged (M^+) and/or excited states (denoted by *). Although M centers were mentioned in several experimental[30,32,101,104] and theoretical[27,34,101,111,112] papers they did not attract as much attention as F centers. Here, we will summarize what is known about the M centers.

Optical activity of M center

As for the F centers, they can also take part in the optical activity of MgO crystals. Chen *et al.*[104] studied the effect of defect clusters in neutron-irradiated, electron-irradiated, and Mg-additively colored samples of MgO single crystals. They found broad absorption bands at 3.47 eV (352 nm), 2.16 eV (573 nm) and 1.27 eV (975 nm) in neutron irradiated samples which were ascribed initially to the F-aggregates centers. However, these bands were not observed in electron-irradiated and additively colored samples and hence it was not clear if these peaks can be associated with oxygen vacancy aggregates because they were not present in all types of samples.

Further experiments on additively coloured MgO modified PL spectra due to uniaxial stress[113] and polarized luminescence.[114] The authors were able to measure absorption peaks at 3.31 eV (375 nm)[113] and 2.8 eV (441 nm)[114] which were ascribed to M and M^{+2} centers respectively.

More recent experiments of Monge *et al.*[115] considered thermochemically reduced MgO crystals to produce anion vacancies. In the absorption measurement, in addition to the F center peak at 4.95 eV (250 nm), the authors observed also bands at 3.5 eV (355 nm), 3.05 eV (406 nm), 2.82 eV (440 nm), 2.58 eV (480 nm) and 1.27 eV (975 nm) tentatively associated with vacancy clusters. Indeed, the bands at 3.5 eV and 1.27 eV had been identified as due to different transitions within M centers.

Domingez and Ariza[111] performed theoretical calculations to resolve the origin of the additional peaks in the optical spectra of MgO. They studied M centers in neutral and charged states within the bulk and at the surface of MgO. It was found that the M center produces two doubly occupied states within the band gap of MgO and associated two excited states close to the conduction band minimum. This is because the M states are a result of hybridization between the states of neighbouring F centers. The simple diagram in Fig. 2.8 represents the relative level positions of M and F centers. In the ground state the optical transition is expected to occur between the highest occupied M center level and the lowest unoccupied state laying at 4.4 eV higher in energy. This is about 1 eV larger than a band reported in a neutron irradiated samples and attributed to aggregates of F centers.[104] However, the origin of this band is not really clear as was also stated before, in some samples its not even present.[104] When the M center is in its excited state, denoted as M^{+}, such that one electron from higher M level is removed, an additional absorption peak is expected. The transition involves the lowest doubly occupied M state and the partially filled state 1.3 eV above.

To summarize, resolving the origin of the optical spectra of MgO crystals is a quite complicated task. As was briefly discussed for the F and M centers not all models and interpretations fully agree with each other. Moreover, additional peaks in MgO PL have been also reported. The PL spectra is generally very sensitive to possible defects within MgO and thus depends also on the method of sample preparation. Besides, in the case of nanocrystalline MgO powders one has to include also the influence of the surface and possible emission from surface states.

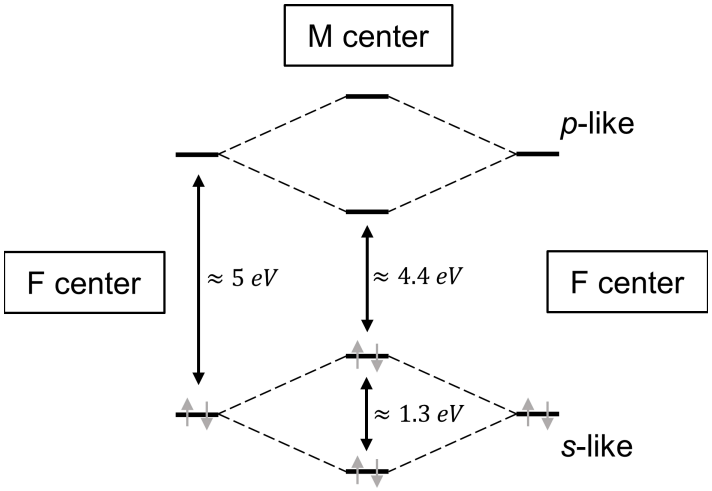

Figure 2.8: Relative positions of F and M center electronic levels and possible optical transitions between the levels are also shown. Taken from Ref. 111.

Coherent tunnelling between vacancies in MgO

McKenna and Blumberg[34] theoretically investigated the electron transfer between two F centers in MgO. The calculations were based on constrained density functional theory (CDFT) method implemented with periodic boundary conditions. For accurate description of the MgO electronic structure a hybrid functional for approximating the exchange-correlation energy and a supercell included many atoms to properly described the ionic polarization were used. The authors were particularly interested in the electron tunnelling between a neutral F^0 center and a charged F^+ center separated by a distance d. The process can be written schematically as

$$F_i^0 + F_{ii}^+ \rightarrow F_i^+ + F_{ii}^0. \tag{2.1}$$

Generally the initial and final states should have the same energy (but the lattice configuration is different) and the electron should spend most of its time trapped either on defect i or ii. As such, the electron transfer rate can be estimated within the semiclassical Marcus theory where the key parameters are the electronic coupling matrix element (H_{ab}) and the reorganization energy (λ). Both of the parameters are computed using the CDFT approach.

The most important results are plotted in Fig. 2.9. The panels (a, b) and (c) show respectively the electronic coupling (H_{ab}), the reconfiguration energy (λ) and a transfer rate as a function of defect separation along different crystallographic directions. The electronic coupling should decay exponentially as a function of the distance d, as represented by the red line in Fig. 2.9(a). However, as it can be seen, the values of H_{ab} deviate significantly from the expected behaviour. The authors claim that this deviation is a result of an intrinsic anisotropy in the separation dependence of the electronic coupling elements. Especially, if the defects are along the [110] direction the coupling is larger than along other crystallographic directions, as indicated in panel (a). This is explained by the fact that the p orbitals of oxygen atoms in MgO, next to the vacancies, mix with the s-like defect electron wave function, resulting in an augmentation of the

electron density along the [110] direction. Consequently, the wave function and the electronic coupling decay more slowly along lines with this particular symmetry.[34]

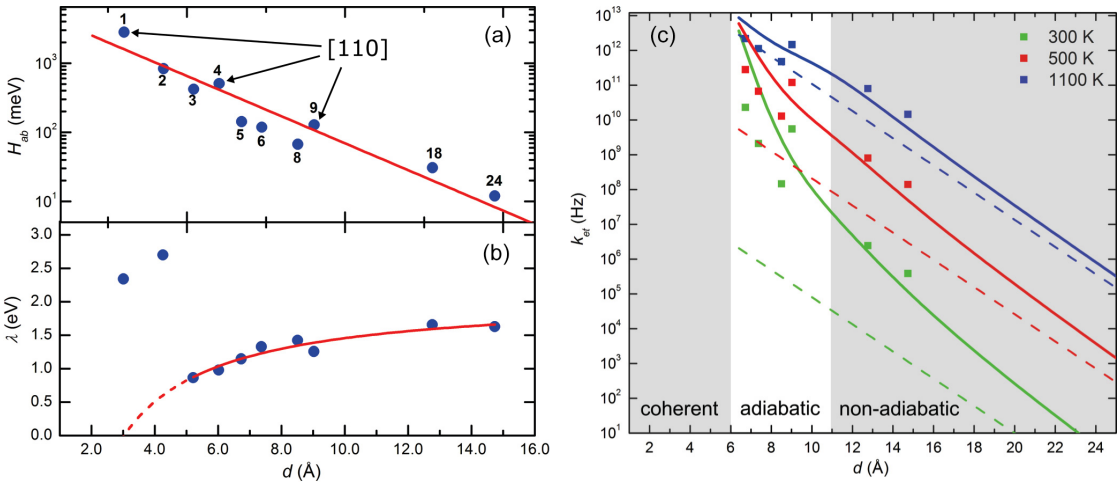

Figure 2.9: Electron transfer rate between oxygen vacancies in MgO. (a) The electronic coupling matrix elements(H_{ab}), (b) the reconfiguration energy (λ) and (c) electron transfer rate for the different temperatures as a function of the distance between two F centers along different crystallographic directions. The solid lines are analytical functions evaluated for the electron transfer rate and the dashed lines indicate the rates obtained assuming nonadiabatic electron transfer and a constant activation energy. Taken from Ref. 34.

The reorganization energy, as shown in panel (b), is large when the defects are separated by less than 5 Å. This is caused by overlapping and opposing ionic distortion fields. When the distance increases above 5 Å, the value of λ becomes smaller and decreases further with distance.

The calculated electronic transfer rate as a function of defect separation for different temperatures, using Marcus theory[34] (panel (c)) shows three transfer regimes. The *non-adiabatic* one with defects are separated by more than 11 Å where the electron transfer rate decays exponentially due to the reduction of the electronic coupling between defects; the *adiabatic* one with defect separation between 6 Å and 11 Å where the transfer behaviour deviates from mono-exponential decrease because it depends both on the electronic coupling and the strong increase in the reorganization energy which in turn defines the electron transfer activation energy; and finally there is a crossover to a *coherent* regime when the defect separation is smaller than 6 Å. The most interesting for us is the coherent regime where the activation energy is negative, which indicates that the localization of an electron on one of the vacancy sites is unstable and so the electronic ground state has to involve delocalization of the electron between defects in a bonding orbital.

The paper of McKenna and Blumberg[34] for the first time showed that defects can promote coherent tunnelling. Despite their calculations are limited to defects in bulk MgO, not really applied to MTJs, these results provide a clue that defects created within the dielectric of MTJs can be actually advantageous in preserving electron's spin and symmetry, in contrast to what is generally believed. This is also a motivation for further investigation of paired oxygen vacancies and their influence on MTJs performance.

2.5 Scientific motivations of this thesis

This chapter was devoted to explaining the crucial role of defects in MTJs and their influence on the device performance. The structural imperfections are the most important factor determining the TMR value and also a way to understand the discrepancies between the predicted high theoretical TMR values for crystalline junctions and the experimental ones.

Even if one includes the interface disorder or oxidation of interfacial Fe layer the drastic drop of TMR cannot be fully justified. Moreover, a constant improvement of technological process of heterojunction preparation avoids the oxidation and makes interfaces with better quality. Still, the values of TMR in the best junction did not exceed few hundred percent. In addition the impact of grain boundaries, which is a challenging task from both experimental and theoretical point of view, cannot explain the measured low barrier heights. Although, grain boundaries can cause a decrease of the effective barrier of MgO, this decrease doesn't match the experimental values. One more issue was raised by the possibility of atomic diffusion during the sample preparation and annealing. In particular, the main concern was about boron diffusion within FeCoB/MgO/FeCoB junctions (these type of MTJ are reported to have the highest TMR). However, as was shown theoretically boron diffusion should not create additional states within the MgO band gap. Moreover, recent experimental studies prove that with a proper annealing temperature, boron does not diffuse into the MgO but rather goes further away from the interfaces. It was noted also that barriers of height around 0.4 eV, initially associated to the M center states, were measured even for samples without boron in the electrodes, hence boron diffusion cannot explain these barrier heights.

This motivates our interest on understanding the electronic structure of various types of oxygen vacancies in MgO and their effect in quantum transport in MTJs. As was discussed, oxygen vacancies result in a variety of localized states in the band gap of MgO and can affect the optical and the electrical properties of the dielectric. Despite the clear importance of the role played by point vacancies, their precise identification and impact on the tunnelling current is not well understood. As it was shown by theoretical considerations[28,29,50] single oxygen vacancies should create barrier heights of about 1.1 eV for the tunnelling electrons and decrease the resulting TMR. Even if we consider more F-type vacancies within MgO, the general conclusion is that these vacancies should have a negative impact on the TMR. Nonetheless, the barrier heights of 0.4 eV cannot be associated with F/F^+ centers since these create barriers of 1.1 eV. Furthermore, the barrier height reported for parallel configuration, ϕ_P, are equal or higher than that for the antiparallel ϕ_{AP}[30] one, which seems to be in contradiction with expectations. Since $G_P > G_{AP}$, we expect that $\phi_P < \phi_{AP}$.

McKenna and Blumberg[34] theoretically predicted that coherent transport can be preserved if the F centers are separated by less than 6 Å. It indicates that paired oxygen vacancies, or M centers, can preserve coherent tunnelling and symmetries of the incoming electrons. Also, as suggested by experimentalists, M center can be responsible of the 0.4 eV barriers. Since the properties of the M canters are not well understood, especially when incorporated in the MTJs, they need further studies. The main goal of

this thesis is therefore to evaluate electronic properties of paired oxygen vacancies and reveal their impact on the tunnelling conductance in nominal Fe/MgO/Fe junctions. The presented work is based on density functional theory calculations and Landauer-Büttiker formalism for the transport calculations. The methodology and ensuing results are described in detail in the next chapters.

Part II

Methodology

3
Method of calculation

The basic understanding of material properties requires insight into the nature of chemical bonds and the resulting electronic structure. To describe complex condensed matter systems one can start from what is known, i.e. they are made of atoms, composed of electrons and nuclei, which interact to create chemical bonds. All of the essential physics arises ultimately from these basic interactions. The behaviour of the particles involved is governed by quantum mechanics principles which state that all the necessary information is contained in the wave function of the system under study. Then, by solving the many-body Schrödinger equation one can determine the eigenfunctions of the Hamiltonian which are used to obtain the corresponding observables of the system. This approach is at the hart of the so called first-principles or *ab-initio* methods, which rely completely on information gathered form atoms constituting the system without the need of empirical data[1]. One of the methods based on ab initio approach is the *density functional theory* (DFT) which is the method of choice used throughout this thesis. To tackle the many body problem and complexity of a condensed matter systems, DFT promotes the electron density from one of the observables to the main quantity describing the system form which all other observables are evaluated. DFT produces ground state properties like total energy, bond lengths and angles, electron distribution, band structure and so on. However, as DFT is a ground state theory, electronic transport which us the subject of this thesis is clearly a non-equilibrium phenomenon. Therefore, to treat electronic transport either one should use the linear response theory or extend the formalism beyond DFT.

This chapter will discuss problems arising due to many-body interactions and how to treat them using DFT. The practical aspects of the various DFT implementations and the manner of evaluating the observables will be also presented. We will explain then how to evaluate electronic transport based on input produced by various DFT calculations.

[1] Apart form the approximations used in the exchange-correlation functionals.

3.1 Many-body electron problem

In quantum mechanics if we know the full wave function of a system and we solve the Schrödinger equation, we can compute systems observables. This seems to be a simple eigenvalue problem to handle using basic algebra. However, for real physical systems, the analytical solution can be only derived for a two-body problem like for example the hydrogen atom. In the case of a material, which contains $\sim 10^{23}$ particles, it is an impossible task even numerically. The Hamiltonian $\hat{H}$ for a system of N electrons, with masses m_e, interacting with M nuclei, with masses M_I and charges $Z_\mathrm{I}e^2$, and with other electrons by Coulomb interactions is written as

$$\begin{aligned}\hat{H} = &-\frac{\hbar^2}{2m_e}\sum_{i=1}^{\mathrm{N}}\nabla_i^2 - \sum_{\mathrm{I}=1}^{\mathrm{M}}\frac{\hbar^2}{2M_\mathrm{I}}\nabla_\mathrm{I}^2 + \frac{1}{2}\sum_{i\neq j}^{\mathrm{N}}\frac{e^2}{|\mathbf{r}_i-\mathbf{r}_j|} \\ &-\sum_{i=1}^{\mathrm{N}}\sum_{\mathrm{I}=1}^{\mathrm{M}}\frac{Z_\mathrm{I}e^2}{|\mathbf{r}_i-\mathbf{R}_\mathrm{I}|} + \frac{1}{2}\sum_{\mathrm{I}\neq\mathrm{J}}^{\mathrm{M}}\frac{Z_\mathrm{I}Z_\mathrm{J}e^2}{|\mathbf{R}_\mathrm{I}-\mathbf{R}_\mathrm{J}|},\end{aligned} \tag{3.1}$$

where the terms represent respectively the kinetic energy of the electrons and the nuclei, the potential energy due to electron-electron and electron-nucleus interactions and the potential energy due to the interaction between nucleus. Moreover, there is no obvious prescription of how to construct the corresponding many-body wave function which would include all the electrons and the nucleus in the system. Therefore, because of the complexity of the many-body interacting problem the analytical solution of the corresponding Schrödinger equation is impossible in practice and some approximations have to be made.

The complexity of the many-body problem can be reduced following the Born-Oppenheimer approach,[116] where the motion of the electrons and nuclei is separated and the system's wave function is decoupled into electronic and nuclei part. This procedure can be justified based on the observation that the time-scale associated with the motion of nuclei is usually much slower than that associated with the motion of electrons. As a consequence, electrons can follow any changes in the nuclei positions by rapidly relaxing to their instantaneous ground state. In fact, in this picture, nuclei can be considered as a stationary and their kinetic energy can be taken to be zero. This approach is also know as the *adiabatic approximation*, and it can be explained by the huge difference between the mass of the atomic nucleus and that of an electron. For example, in the case of hydrogen the nucleus mass is approximately 1836 times larger than that of an electron. In the adiabatic approximation the Coulomb interaction between nuclei contributes to the eigenvalues by only a constant and will not be discussed. The impact of ionic degrees of freedom is included only in the remaining nucleus-electron interaction operator, denoted also as an external potential acting on the electrons, and the resulting wave function depends only on the electronic coordinates. In other words, the many-body Schrödinger equation is reduced to the problem of interacting electrons moving in the external potential V_{ext} created by the nuclei. In the Born-Oppenheimer approximation the Hamiltonian is then given by

$$\hat{H} = -\frac{\hbar^2}{2m_e}\sum_{i=1}^{\mathrm{N}}\nabla_i^2 + \frac{1}{2}\sum_{i\neq j}^{\mathrm{N}}\frac{e^2}{|\mathbf{r}_i-\mathbf{r}_j|} - \sum_{i=1}^{\mathrm{N}}\sum_{\mathrm{I}=1}^{\mathrm{M}}\frac{Z_\mathrm{I}e^2}{|\mathbf{r}_i-\mathbf{R}_\mathrm{I}|}, \tag{3.2}$$

where the first term is again the kinetic energy operator of electrons ($\hat{T}$), the second describes the interactions between electrons ($\hat{U}$) and the third the external potential acting on the electrons by the nuclei ($\hat{V}_{ext}$). The operators $\hat{T}$ and $\hat{U}$ are the same for any system interacting via the Coulomb interaction and depend only on the number of electrons. It is only the external potential $\hat{V}_{ext}$ that depends on the spatial arrangement of the nuclei, $\mathbf{R}_{\mathrm{I}}$, that distinguishes a molecule from a solid. Therefore $\hat{T}$ and $\hat{U}$ are universal operators, the same for any system, while $\hat{V}_{ext}$ is system-dependent.

As a result of applying the Born-Oppenheimer approximation, the initial complexity of the many-body problem was reduced to the interacting electron system in the external potential. There are two kinds of electron–electron interactions which have to be represented. One is the exchange interaction due to the Pauli exclusion principle accounting for the fact that each electron has a spin. The other one, more complicated in nature, is a correlation interaction, where each electron is affected by the motion of the rest of the electrons in the system. One of the first attempts to describe the electron-electron interactions was proposed by Hartree.[117] He stated that the many-electron wave function can be written as a product of one electron states, i.e.

$$\Psi(\mathbf{r}_1, \mathbf{r}_2, ..., \mathbf{r}_{\mathrm{N}}) = \psi_1(\mathbf{r}_1)\psi_2(\mathbf{r}_2)...\psi_{\mathrm{N}}(\mathbf{r}_{\mathrm{N}}). \tag{3.3}$$

In other words, the electrons are treated as independent particles which interact with each other only via the mean-field Coulomb potential. The variational principle yields the one-electron Schrödinger equations where the Hamiltonian for electron i is in the form

$$\hat{H} = -\frac{\hbar^2}{2m}\nabla_i^2 - \sum_{\mathrm{I}=1}^{\mathrm{M}} \frac{Z_{\mathrm{I}}e^2}{|\mathbf{r}_i - \mathbf{R}_{\mathrm{I}}|} + e^2 \sum_{\substack{j=1 \\ j\neq i}}^{\mathrm{N}} \int \frac{|\psi_j(\mathbf{r}')|^2}{|\mathbf{r}_i - \mathbf{r}'|} d\mathbf{r}', \tag{3.4}$$

where N is the number of electrons and the mean field is generated by $N-1$ other electrons in the system. The last term in the Hamiltonian is called the Hartree potential arising due to other electrons and denoted V_{H}. Despite that the Hartree theory includes the interaction between electrons it does not capture all the essential physics of the many-body problem namely electrons are treated as indistinguishable fermions. The Pauli exclusion principle states that two fermions cannot occupy the same quantum state and hence requires that the many-body wave function is antisymmetric with respect to the interchange of any two electrons which cannot be satisfied by the form of the wave function proposed by Hartree. The exchange condition can be satisfied if the full wave function is constructed as an antisymmetric product of a single particle wave functions i.e. as a Slater determinant[118] of single-particle orbitals of the form

$$\Psi(\mathbf{x}_1, \mathbf{x}_2, ..., \mathbf{x}_{\mathrm{N}}) = \frac{1}{\sqrt{N!}} \begin{vmatrix} \psi_1(\mathbf{x}_1) & \psi_2(\mathbf{x}_1) & \dots & \psi_{\mathrm{N}}(\mathbf{x}_1) \\ \psi_1(\mathbf{x}_2) & \psi_2(\mathbf{x}_2) & \dots & \psi_{\mathrm{N}}(\mathbf{x}_2) \\ \vdots & \vdots & \ddots & \vdots \\ \psi_1(\mathbf{x}_{\mathrm{N}}) & \psi_2(\mathbf{x}_{\mathrm{N}}) & \dots & \psi_{\mathrm{N}}(\mathbf{x}_{\mathrm{N}}) \end{vmatrix},$$

where $\psi_i(\mathbf{x}_j)$ refers to the ith one-electron state defined by spatial and spin components included in a single variable $\mathbf{x}_j = (\mathbf{r}_j, \sigma_j)$. The extension of the method to

include the Pauli principle was done by Fock[119] and is now known as the Hartree-Fock approximation. The resulting Hamiltonian operator in this approximation is given by

$$\begin{aligned}\hat{H}\psi_i(\mathbf{r}) = &-\frac{\hbar}{2m}\nabla_i^2\psi_i(\mathbf{r}) - \sum_{\mathrm{I}=1}^{\mathrm{M}}\frac{Z_{\mathrm{I}}e^2}{|\mathbf{r}-\mathbf{R}_{\mathrm{I}}|}\psi_i(\mathbf{r}) + e^2\sum_{\substack{j=1\\j\neq i}}^{\mathrm{N}}\int\frac{|\psi_j(\mathbf{r}')|^2}{|\mathbf{r}-\mathbf{r}'|}\psi_i(\mathbf{r})d\mathbf{r}' \\ &- e^2\sum_{\substack{j=1\\j\neq i}}^{\mathrm{N}}\int\frac{\psi_j^*(\mathbf{r}')\psi_i(\mathbf{r}')}{|\mathbf{r}-\mathbf{r}'|}\psi_j(\mathbf{r})d\mathbf{r}'.\end{aligned} \tag{3.5}$$

For simplicity we have omitted the spin coordinates in the above equation, however if these are included additional sum over spin component should be performed. By comparing the above equation with the form of the Hamiltonian defined in the Hartree approximation, eq. 3.4, we can see an additional term which represents the *exchange interaction*, and which arises due to the antisymmetric nature of the many-electron wave function. This term is non-local and accounts for the fact that an electron has a spin, i.e. Pauli exclusion principle will not allow two electrons with the same spin to be close to each other. An electron with spin σ_i at position $\mathbf{r}_i$ will push away an electron with the same spin at position $\mathbf{r}_j$. The resulting Hartree-Fock formula is an integro-differential equation which has to be solved to calculate the wave function which in turn will define the potential standing in the Hamiltonian operator. This kind of equation has to be solved self-consistently.

Despite the proper description of the exchange interaction between the electrons the Hartree-Fock approximation does not include any correlation in the system. As a result the theory breaks down for a metals and insulators in general, producing overestimated band gaps and underestimated binding energies. Moreover, the problem with solving the Hartree-Fock equation is the great demand of the computational resources, which in practice restricts the sizes of simulated systems. These obstacles gave a need to develop new theories which would capture the basic electronic interactions in materials and make the calculations computationally feasible. There are many Post-Hartree-Fock methods trying to improve deficiencies inpinned in this approach, like the configuration interaction (CI) method, coupled cluster (CC) method or perturbative methods. Another philosophy of treating N-electron interacting system was initiated by Thomas and Fermi who proposed that the wave function of the system can be replaced with its electron density. In his picture, the total energy of the system can be obtained from the electronic density by expressing the kinetic, the exchange and the correlation parts in terms of density corresponding to the homogenous electron gas solution. However, in most of the atoms and materials the electron density is far from being homogenous and the Thomas-Fermi theory failed to produce correct quantitative results. Nonetheless, their idea of replacing the wave function by the electron density triggered development of the *density functional theory* (DFT) which is the method used throughout this thesis and is described in the subsequent sections.

3.2 Density functional theory

The birth of DFT is attributed to the work of Hohenberg and Kohn[35] who gave in 1964 a solid mathematical foundations required for the method. They adopted the Born-Oppenheimer approximation and followed Thomas-Fermi idea by assuming that any property of the system can be evaluated from the system's ground-state density instead of its full wave function. Therefore, the electron density $n(r)$ was promoted from just one among observables to the key variable, which can be used to evaluate the physical properties of the system under study. In the following, the fundamental theorems of DFT will be presented. The Kohn-Sham ansatz which allows for practical DFT implementations is also described.

3.2.1 Hohenberg-Kohn Theory

DFT is based on two Hohenberg-Kohn[35] theorems which state that

Theorem I. *The ground state density of the interacting particles uniquely determines the external potential acting on them and thus all properties of the system.*

Theorem II. *For any particular external potential, the ground state of the system is the global minimum value of the $E[n]$, and the density n that minimizes the functional is the exact ground state density n_0.* In other words, the energy of a many-body system can be written as a *functional* of the ground-state density:

$$E[n(\mathbf{r})] = T[n(\mathbf{r})] + U[n(\mathbf{r})] + \int d\mathbf{r} V_{ext}(\mathbf{r}) n(\mathbf{r}) \equiv F[n(\mathbf{r})] + V_{ext}[n(\mathbf{r})], \tag{3.6}$$

where $n(\mathbf{r})$ is the electron density, $T[n(\mathbf{r})]$ the kinetic energy, $U[n(\mathbf{r})]$ the electron-electron interaction energy, $V_{ext}[n(\mathbf{r})]$ the external potential and $F[n(\mathbf{r})] = T[n(\mathbf{r})] + U[n(\mathbf{r})]$ is an universal functional independent of the system.

The importance of the Hohenberg-Kohn theorems is that they define the mathematical basis of the density functional theory by showing that a simple quantity like the electron density can give access to all ground-state electronic properties of any system. As the authors stated in their article from 1990:[120] *" We felt - and still feel - that the main significance of our work was that it resulted in a clear and formally rigorous reformulation - now called density functional theory - for quantum mechanical ground states in terms of the density, a vantage point from which existing approximations could be more clearly understood and appraised and from which new and better approximations could be derived."*

The total energy of the electron system is now a variational quantity and if we know the $E[n]$ functional the ground-state energy for a given external potential can be found by minimizing $E[n]$ with respect to the electron density $n(\mathbf{r})$. The energy functional minimization can be performed in different ways. One of the methods is a direct minimization of the energy with respect to the basis set coefficients. However, if one chooses the basis set other than plane waves, the problem becomes rather complicated (many parameters to minimize). An alternative way is to refine the density iteratively.

This is performed by means of a self-consistent cycle in DFT based calculations. One needs to guess the initial electron density for the system at hand. When the eigenvectors are found a new electron density is calculated and then mixed with initial one to generate the input density for the next iteration. The major difficulty remains in the determination of the universal functional $F[n]$ which is not known in terms of the electron density. A cleaver approximation proposed by Kohn and Sham[36] in 1965 gave a way for practical implementation of DFT as it will be discussed in the next subsection.

3.2.2 Kohn-Sham equations

Kohn and Sham devised an *ansatz*, where the many-body problem of the interacting electrons in an external potential is mapped onto a non-interacting electron system with the same electron density moving in some effective potential.[36] This leads to independent-particle equations, the so called *Kohn-Sham* equations, for non-interacting system which can be solved. All many-body terms are incorporated into an exchange-correlation functional of the density.

In the Kohn-Sham approach the energy functional for the many-electron interacting system, defined by eq. 3.6, can be rewritten as

$$E[n(\mathbf{r})] = T_s[n(\mathbf{r})] + U_{\mathrm{H}}[n(\mathbf{r})] + \int d\mathbf{r} V_{ext}(\mathbf{r}) n(\mathbf{r}) + E_{xc}[n(\mathbf{r})], \tag{3.7}$$

where $T_s[n(\mathbf{r})]$ is the free electron kinetic energy, $U_{\mathrm{H}}[n(\mathbf{r})]$ is the electron-electron Coulomb like interaction (Hartree term) and $E_{xc}[n(\mathbf{r})]$ denotes the exchange-correlation energy. The E_{xc} term incorporates the differences in the energy of the interacting and the noninteracting systems, $T - T_s$ and $U - U_{\mathrm{H}}$, hence all the unknown interactions that can not be described analytically. The second Hohenberg-Kohn theorem guarantees that the minimum of this functional will correspond to the ground state density, $n(\mathbf{r})$ and the problem is reduced to minimization of the energy functional with respect to the density as

$$\mu = \frac{\delta E[n]}{\delta n(\mathbf{r})} = \frac{\delta T_s[n]}{\delta n(\mathbf{r})} + V_{ext}(\mathbf{r}) + V_{\mathrm{H}}(\mathbf{r}) + V_{xc}(\mathbf{r}), \tag{3.8}$$

where μ is Lagrange multiplier corresponding to the requirement that number of particles is conserved. The particular terms denote respectively: $V_{ext}(\mathbf{r}) = \delta v_{ext}/\delta n$ the external potential; $V_{\mathrm{H}}(\mathbf{r}) = \delta U_{\mathrm{H}}/\delta n$ the Hartree potential and $V_{xc} = \delta E_{xc}/\delta n$ the exchange-correlation potential. The V_{xc} can be explicitly calculated once an approximation for E_{xc} has been chosen.

If we consider now a noninteracting system of density $n_s(\mathbf{r})$, which is supposed to be the same as the ground state density of the interacting one, and having an effective potential $V_{eff}(\mathbf{r})$ the energy functional is

$$E[n(\mathbf{r})] = T_s[n(\mathbf{r})] + \int d\mathbf{r} V_{eff}(\mathbf{r}) n(\mathbf{r}), \tag{3.9}$$

and the minimization condition becomes

$$\mu = \frac{\delta E_s[n]}{\delta n(\mathbf{r})} = \frac{\delta T_s[n]}{\delta n(\mathbf{r})} + V_{eff}(\mathbf{r}), \tag{3.10}$$

there are no Hartree and exchange-correlation terms in the absence of interactions. The two solutions, for the interacting and the noninteracting systems, will give the same densities, $n_s(r) = n(r)$, only if V_{eff} is chosen to be

$$V_{eff}(\mathbf{r}) = V_{ext}(\mathbf{r}) + V_{\mathrm{H}}(\mathbf{r}) + V_{xc}(\mathbf{r}). \tag{3.11}$$

Therefore, the density of the interacting many–body system in the external potential can be evaluated by solving equations of noniteracting electrons in the effective potential $V_{eff}(\mathbf{r})$. This leads to a set of Schrödinger-like equations, also called the Kohn-Sham equations of the auxiliary system of noninteracting particles given by

$$\left[-\frac{\hbar^2}{2m}\nabla^2 + V_{eff}(\mathbf{r})\right]\psi_i(\mathbf{r}) = \epsilon_i\psi_i(\mathbf{r}), \tag{3.12}$$

where $\psi_i(\mathbf{r})$ are one-electron orbitals that reproduce the density $n(\mathbf{r})$ of the original system evaluated as

$$n(\mathbf{r}) = \sum_{i=1}^{\mathrm{N}} f_i|\psi_i(\mathbf{r})|^2, \tag{3.13}$$

where f_i denotes the occupation of the i'th orbital. The total kinetic energy operator T_s can be expressed simply in terms of single-particle orbitals $\psi_i(\mathbf{r})$, by analogy to the Hartree-Fock approach, as

$$T_s[n(\mathbf{r})] = -\frac{\hbar^2}{2m}\sum_{i}^{\mathrm{N}}\int d\mathbf{r}\psi_i^*(\mathbf{r})\nabla^2\psi_i(\mathbf{r}). \tag{3.14}$$

The Hartree term describing the Coulomb interactions between electrons is given by

$$V_{\mathrm{H}}[n(\mathbf{r})] = \frac{1}{2}\int\int d\mathbf{r}d\mathbf{r}'\frac{n(\mathbf{r})n(\mathbf{r}')}{|\mathbf{r}-\mathbf{r}'|}. \tag{3.15}$$

The Kohn-Sham equations (3.11-3.13) replace the problem of the functional minimization, $E[n(\mathbf{r})]$, by that of solving the noninteracting Schrödinger equation for the effective potential V_{eff}. In order to describe spin-polarized systems it is sufficient to consider the total electron density as a sum of the two independent spin densities, $n = n^{\uparrow} + n^{\downarrow}$. The interaction beetween the two spin components can be included in the exchange-correlation part $E_{xc}[n^{\uparrow}, n^{\downarrow}]$.

The total ground-state energy E_0 in the Kohn-Sham approach is

$$E_0 = \sum_{i=1}^{\mathrm{N}}\epsilon_i - \frac{1}{2}\int d\mathbf{r}\int d\mathbf{r}'\frac{n(\mathbf{r})n(\mathbf{r}')}{|\mathbf{r}-\mathbf{r}'|} - \int d\mathbf{r}V_{ext}[n(\mathbf{r})]n(\mathbf{r}) + E_{xc}[n(\mathbf{r})], \tag{3.16}$$

and it is not simply the sum of the Kohn-Sham energies ϵ_i as one might expect. The evaluated eigenvalues, ϵ_i, are these of an auxiliary single-body system whose eigenfunctions (orbitals) give the ground state electron density. In fact, only the density has a physical meaning in the Kohn-Sham equations and the obtained eigenvalues should not be trusted quantitatively.[121,122]

Although the Kohn-Sham method gives a prescription for treating the many-body electron problem it does not define explicitly the exchange-correlation energy E_{xc}. The E_{xc} can be decomposed as $E_{xc} = E_x + E_c$, where E_x is the exchange term due to the Pauli exclusion principle and E_c the energy due to the electronic correlations. The exchange energy can be expressed in terms of single particle orbitals as defined by Fock (last term in eq. 3.5), but no general expression in terms of the density is known. In the case of the correlation energy no explicit expression is known in terms of orbitals or the density. The Hohenberg-Kohn theorems guarantee that E_{xc} is a functional of density, but since its exact form is not known it has to be approximated. Even though, the energy contribution due to the E_{xc} term is small, it plays an important role in defining the mechanism of chemical bonding and it is necessary to describe expressions for the exchange-correlation potential used in this work.

3.2.3 Local density approximation

The first, and the simplest, approximation to the exchange-correlation energy was proposed by Kohn and Sham.[36] They stated that electrons in solids can be considered locally as a homogeneous electron gas and the exchange-correlation effects can be treated as local. This approach is known as the *local density approximation* (LDA) and the exchange-correlation energy functional $E_{xc}^{\mathrm{LDA}}[n(\mathbf{r})]$ in the LDA formulation is simply given by

$$E_{xc}^{\mathrm{LDA}}[n(\mathbf{r})] = \int d\mathbf{r} n(\mathbf{r}) \epsilon_{xc}^{hom}[n(\mathbf{r})], \tag{3.17}$$

where $\epsilon_{xc}^{hom}[n(\mathbf{r})]$ is the exchange-correlation energy density in a homogeneous electron gas that depends only upon the density $n(\mathbf{r})$ at point $\mathbf{r}$ and it can be separated in two parts: exchange ϵ_x^{hom} and correlation ϵ_c^{hom} as

$$\epsilon_{xc}^{hom}[n(\mathbf{r})] = \epsilon_x^{hom}[n(\mathbf{r})] + \epsilon_c^{hom}[n(\mathbf{r})]. \tag{3.18}$$

Exchange-correlation potential V_{xc}, which is inserted into Kohn-Sham equations is evaluated as

$$V_{xc}(\mathbf{r}) = \frac{\delta E_{xc}^{\mathrm{LDA}}[n(\mathbf{r})]}{\delta n(\mathbf{r})} = \epsilon_{xc}^{hom}[n(\mathbf{r})] + n(\mathbf{r}) \frac{\partial \epsilon_{xc}^{hom}[n(\mathbf{r})]}{\partial n(\mathbf{r})}. \tag{3.19}$$

The exchange energy density $\epsilon_x^{hom}[n]$ per volume for a homogenous electron gas is known exactly from the Thomas-Fermi theory and it is given by

$$\epsilon_x^{hom}[n(\mathbf{r})] = -\frac{3}{4} \left(\frac{3}{\pi} \right)^{1/3} n(\mathbf{r})^{1/3}, \tag{3.20}$$

so that

$$E_x^{\mathrm{LDA}}[n(\mathbf{r})] = -\frac{3}{4} \left(\frac{3}{\pi} \right)^{1/3} \int d\mathbf{r} n(\mathbf{r})^{4/3}. \tag{3.21}$$

The correlation energy $E_c[n(\mathbf{r})]$, however, is not known exactly even for a homogeneous electron gas. Highly accurate data for the correlation energy were found by

Ceperley and Alder[123] using Quantum Monte Carlo method. Recent expressions for the $\epsilon_c^{hom}[n(\mathbf{r})]$ are actually different parametrizations of these data.[124,125]

The results obtained with the LDA are proved to be successful, even when applied to systems that are quite different from the homogeneous electron gas. A partial justification for this success lies in the systematic error cancellation, namely the LDA underestimates the E_c but overestimates E_x, resulting in good values of E_{xc}.[122] Consequently the LDA can predict with high accuracy the geometries of systems with strong chemical and ionic bonds. It also gives good predictions of the electronic structure, e.g. density of states and band structure of many systems. Because the LDA is computationally relatively cheap, the electronic structure of systems with hundreds of atoms per unit cell can be computed.

Nonetheless, the LDA completely neglects any inhomogeneities of the electron distribution. Therefore, the LDA tends to overestimate the binding energies and the cohesive energies in solids. Also the predicted band-gap values are strongly underestimated. The failures of the LDA have stimulated many attempts to construct better functionals, some of which will be presented in the next subsections.

3.2.4 General gradient approximations

An improvement to the LDA can be made by including the gradient of the electron density. A first try was to systematically calculate the gradient-corrections of the form $|\nabla n(\mathbf{r})|, |\nabla n(\mathbf{r})|^2, |\nabla^2 n(\mathbf{r})|$, etc., to the LDA. This was known as the *gradient-expansion approximations* (GEA). In practice, however, low-order gradient corrections almost never improve results obtained with the LDA and the higher-order corrections are difficult to calculate.[122,126]

Therefore, it was realized that more general functionals of $n(\mathbf{r})$ and $\nabla n(\mathbf{r})$ have to be constructed instead of the power-series-like expansion. Such functionals, with the general form $f[n(\mathbf{r}), \nabla n(\mathbf{r})]$, are known as the *general gradient approximations* (GGAs). By including the gradient dependency, the non-homogeneity of the electron density at any local point in space is taken into account.

In the nonpolarized case, the GGA exchange-correlation functional can be expressed in a general form as

$$E_{xc}^{\mathrm{GGA}}[(n(\mathbf{r})] = \int d\mathbf{r}\ n(\mathbf{r})\ \epsilon_x^{hom}[n(\mathbf{r})] F_{xc}[r_s(\mathbf{r}), s(\mathbf{r})], \tag{3.22}$$

where $F_{xc}[r_s, s]$ is an enhancement factor over the local exchange, expressed as a function of the reduced density gradient

$$s = \frac{|\nabla n(\mathbf{r})|}{2k_{\mathrm{F}} n(\mathbf{r})}, \tag{3.23}$$

and an average distance between electrons,

$$r_s = (4\pi n(\mathbf{r})/3)^{-1/3}, \tag{3.24}$$

with k_F being the Fermi wavelength. In principle, $F_{xc}(r_s, s)$ should be constrained in the ranges of r_s and s that dominate the system and its physical properties. Typically,

$r_s \leq 1$ and $s \leq 1$ in the core of the atom where the largest values of s occur in the outermost orbitals.[127] In the case of valence electrons in metals these parameters are $1 \leq r_s \leq 6$ and $s \leq 2$, with $s = 0$ at the boundary of a unit cell. For a uniform system LDA is exact and $F_{xc}[r_s, s = 0] = \epsilon_{xc}(n)/\epsilon_x(n)$. The GGAs differ in the choice of the function F_{xc} and thus one can obtain very different expressions. The most widely used forms of F_{xc} have been proposed by Becke,[128] Lee-Yang-Parr (LYP),[129] Perdew-Wang (PW91)[130] and Pedrew-Burke-Enzerhof (PBE).[131]

Analogically to the LDA, the exchange and the correlation part of the energy can be calculated separately and different enhancement factors can be defined for each part, denoted F_x and F_c, respectively. Figure 3.1 compares F_x factors for three chosen GGA formulations. Two regions can be distinguished: (i) with small s ($0 < s \leq 3$) and (ii) with large s ($s \geq 3$). In the first region, which is the most relevant for the majority of the physical applications, different F_x have practically identical shapes, which explains why different GGAs give similar improvement for many systems with small density gradient contributions. Moreover, in this region $F_x \geq 1$ which leads to an exchange energy lower for all GGAs than that of the LDA. This results in reduced values of binding energies and corrects the LDA overbinding. In the second region (ii), the different behaviours of F_x result from choosing different physical conditions which has to be fulfilled by the form of F_x when $s \to \infty$, e.g. F_x can be required to give correct exchange energy density such that $\epsilon_x \to -1/2r$. These differences between various GGAs in the large density gradient regions reflect an inherent difficulty in understanding and describing such regions and also shows that even if one form of GGA gives the correct result for a certain physical property others will fail. Therefore, it does not guarantee that it will always produce correct results especially when different physical conditions are explored.

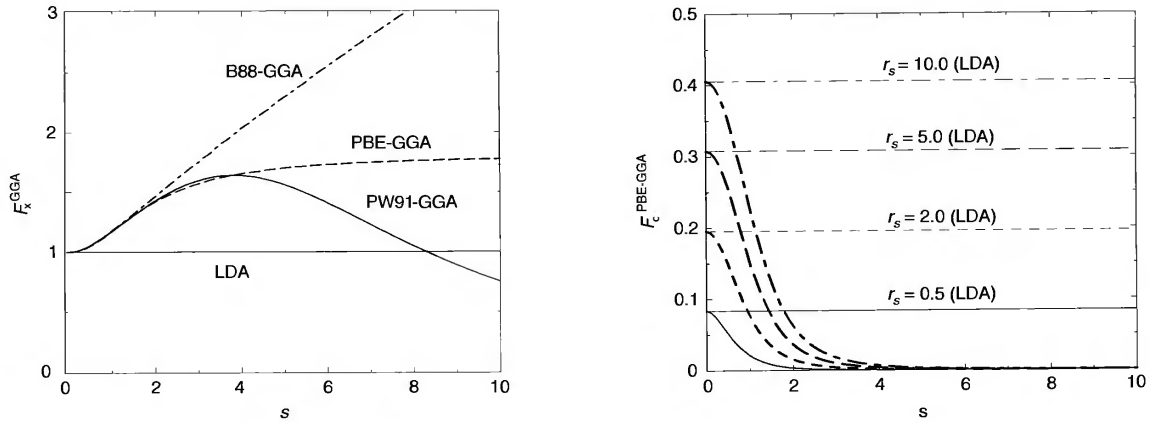

Figure 3.1: Left: Exchange enhancement factor F_x as a function of dimensionless density gradient s for various GGAs. In the range relevant for most materials, $0 < s \leq 3$ all functionals have similar shapes. Right: Correlation enhancement factor F_c as a function of s for the PBE-GGA. Taken from Ref. 126.

The correlation part is more difficult to write as a functional, however its contribution to the total energy is typically much smaller than that of the exchange. Besides,

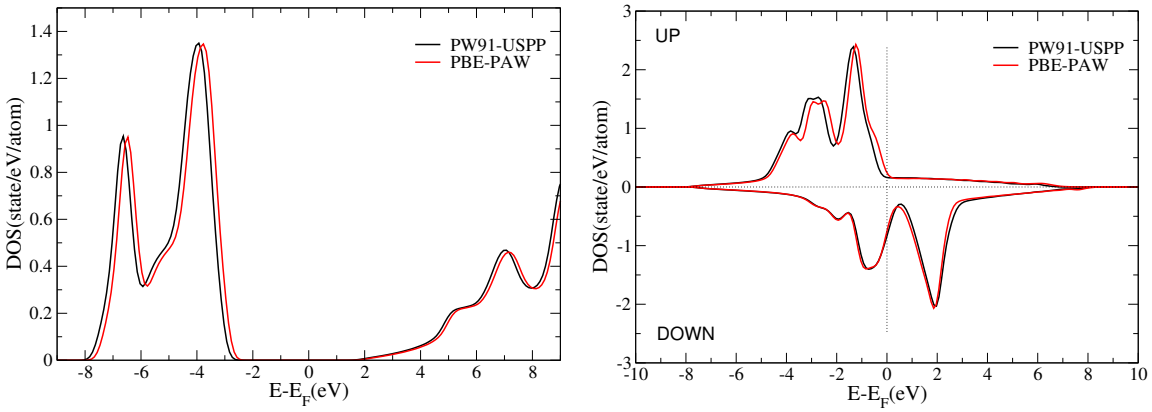

Figure 3.2: Comparison of DOSs for MgO (left) and Fe (right) calculated with different GGA functionals, GGA-PW91 + USPP and GGA-PBE+PAW. The calculations were done with QE, with $20 \times 20 \times 20$ k-point mesh and a cutoff energy of 40 Ry.

for large density gradients the magnitude of the correlation energy decreases and vanishes when $s \to \infty$. To understand this behaviour one can imagine strong confining potential which generates large density gradients and increases level spacings which in turn reduces the effect of the interaction between electrons. Fig. 3.1 shows an example of correlation enhancement factor $F_c^{\mathrm{GGA-PBE}}$ for the PBE functional which is almost identical to that for PW91-GGA.[126]

In this thesis, two GGAs were used in the calculations. A ground state calculations of bulk MgO and Fe/MgO junctions were done with VASP and used the GGA-PBE functional. The same functional is also used in our SIESTA calculations. The transmission calculations performed with Quantum Espresso (QE) + PWCOND module use GGA-PW91 functional form. The choice of the GGAs were dictated by some of the technical details. For example, the transmission calculations in PWCOND module are implemented with ultrasoft pseudopotentials and we needed to use the same form of the pseudopotential and corresponding exchange-correlation functional for all atoms in the junction. Since we have used the pseudopotentials already generated and available in the QE library, the GGA-PW91 was the best choice for all different atom types included in the junction. Nonetheless, as explained above the PBE and PW91 give similar results even though the form of the functional differ. To confirm the validity of this statement, we have compared the density of states for MgO and Fe electrodes before going to a more extensive transmission calculations. The density of states, especially at the vicinity of Fermi level, is the most important quantity when electronic transport is considered. The comparison of the results obtained with GGA-PBE (+PAW) and GGA-PW91 (+USPP) are show in the Fig. 3.2 (the pseudopotential approach and the PAW method will be described in the following sections). As it can be seen, the shape of the DOS are practically independent of the choice of the GGA functional.

What is important to keep in mind is that both LDA and any GGA fail to describe materials with localized and strongly correlated electrons as in transition-metal oxides. These systems contain elements with localized d or f orbitals and delocalized band-like states originating from s and p orbitals. The failure of the LDA and the GGA functionals for these types of materials is due to the fact that those functionals provide

orbital-independent potentials with unphysical self interaction. The self interaction produces incorrect description of their electronic properties. The performance of the LDA/GGA can be improved by adding so called Hubbard term either in the so called LDA+U approach[132,133] or dynamical mean field theory (DMFT),[134,135] however, this was not included in our calculations.

Moreover, GGA also greatly understimates the band gap of materials. The band gaps are better than these calculated with the LDA but still too small compared to experiment. In the case of MgO our calculated band gaps were 4.65 and 4.76 eV within LDA and GGA, respectively, while the experimental gap is 7.8 eV. This fact is of great importance since we want to describe the position of the vacancy levels within the MgO band gap. This is the reason we used *hybrid functionals* which give more realistic estimation of the band gaps, but are more computationally demanding. We restrict ourselves therefore to the smallest supercell possible of 64 atoms. The description of hybrid functionals is presented in the next subsection.

3.2.5 Hybrid functionals

Hybrid functionals[136–140] are constructed by mixing the Fock exchange and the local DFT exchange in a certain proportion. This kind of construction can be motivated by the fact that the deficiencies of DFT and Hartree-Fock (HF) method are in some sense complementary, i.e. band gaps calculated by DFT are too small while these predicted by HF are too large. Thus, mixing of the two exchange potentials may produce more accurate energy gaps, total energies and geometries. As in the case of the LDA/GGA, there are also few schemes for mixing the two potentials. Here, the so called PBE0[136] and HSE[137] hybrid functionals will be briefly presented since these two functionals were used in our calculations.

The PBE0 functional is constructed by mixing 25% of HF exchange with 75% PBE exchange.[136] The correlation energy is fully described by the PBE density functional. This can be written as

$$E_{xc}^{\mathrm{PBE0}} = 0.25E_x^{\mathrm{HF}} + 0.75E_x^{\mathrm{PBE}} + E_c^{\mathrm{PBE}}. \tag{3.25}$$

The nonlocal HF exchange energy in a real space can be written in terms of the one-electron Bloch states $\psi_{\mathbf{k}n}(\mathbf{r})$ and the corresponding occupational numbers $f_{\mathbf{k}n}$ as[138]

$$E_x^{\mathrm{HF}} = -\frac{e^2}{2}\sum_{\mathbf{k}n,\mathbf{q}m} 2w_{\mathbf{k}}f_{\mathbf{k}n} \times 2w_{\mathbf{q}}f_{\mathbf{q}m} \times \int\int d\mathbf{r}d\mathbf{r}' \frac{\psi^*_{\mathbf{k}n}(\mathbf{r})\psi_{\mathbf{q}m}(\mathbf{r})\psi^*_{\mathbf{q}m}(\mathbf{r}')\psi_{\mathbf{k}n}(\mathbf{r}')}{|\mathbf{r}-\mathbf{r}'|}, \tag{3.26}$$

where the sums over $\mathbf{k}$ and $\mathbf{q}$ are performed over all k points sampling of the irreducible Brillouin zone (BZ) whereas the sums over n and m are performed over all energy bands. The $w_{\mathbf{k}}$ denotes weights of each k point which sum up to one and the factor 2 account double occupancy of each one-electron states. The k-point sampling will be described in more detail later. The corresponding exchange potential is then given by

$$\begin{aligned} V_x(\mathbf{r},\mathbf{r}') &= -e^2\sum_{\mathbf{q}m} 2w_{\mathbf{q}}f_{\mathbf{q}m}\frac{\psi^*_{\mathbf{q}m}(\mathbf{r}')\psi_{\mathbf{q}m}(\mathbf{r})}{|\mathbf{r}-\mathbf{r}'|} \\ &= -e^2\sum_{\mathbf{q}m} 2w_{\mathbf{q}}f_{\mathbf{q}m}e^{-i\mathbf{q}\cdot\mathbf{r}'}\frac{u*_{\mathbf{q}m}(\mathbf{r}')u_{\mathbf{q}m}(\mathbf{r})}{|\mathbf{r}-\mathbf{r}'|}e^{i\mathbf{q}\cdot\mathbf{r}}, \end{aligned} \tag{3.27}$$

where $u_{\mathbf{q}m}(\mathbf{r})$ is the periodic part of the Bloch state at the $\mathbf{q}$ point with band index m. The $\psi_{\mathbf{q}m}(\mathbf{r})$ states can be decomposed using plane waves

$$\psi_{\mathbf{q}m}(\mathbf{r}) = \frac{1}{\sqrt{\Omega}} \sum_{\mathbf{G}} c_{\mathbf{q}m}(\mathbf{G}) e^{i(\mathbf{q}+\mathbf{G})\cdot\mathbf{r}}, \tag{3.28}$$

and the Fock potential rewritten as

$$V_x(\mathbf{r},\mathbf{r}') = \sum_{\mathbf{k}} \sum_{\mathbf{G}\mathbf{G}'} e^{i(\mathbf{k}+\mathbf{G})\cdot\mathbf{r}} V_{\mathbf{k}}(\mathbf{G},\mathbf{G}') e^{-i(\mathbf{k}+\mathbf{G}')\cdot\mathbf{r}'}, \tag{3.29}$$

where

$$\begin{aligned} V_{\mathbf{k}}(\mathbf{G},\mathbf{G}') &= \langle \mathbf{k}+\mathbf{G}| \hat{V}_x |\mathbf{k}+\mathbf{G}'\rangle \\ &= -\frac{4\pi e^2}{\Omega} \sum_{m\mathbf{q}} 2 w_{\mathbf{q}} f_{\mathbf{q}m} \\ &\times \sum_{\mathbf{G}''} \frac{c^*_{\mathbf{q}m}(\mathbf{G}'-\mathbf{G}'') c_{\mathbf{q}m}(\mathbf{G}-\mathbf{G}'')}{|\mathbf{k}-\mathbf{q}+\mathbf{G}''|^2}, \end{aligned} \tag{3.30}$$

represents the Fock exchange potential in reciprocal space.

The PBE0 functional has shown significant improvement over the PBE.[139] This can be attributed to the fact that a portion of the exact exchange reduces the self-interaction error of the density functional. However, in the case of infinite systems with periodic boundary conditions the calculation of the HF exchange is very time consuming due to slow reduction of the exchange interaction with distance. To overcome this difficulty, Heyd *et. al*[137] proposed to separate the exchange term in a short-range and a long-range part

$$\frac{1}{r} = S_\mu(r) + L_\mu(r) = \underbrace{\frac{erfc(\mu r)}{r}}_{sr} + \underbrace{\frac{erf(\mu r)}{r}}_{lr}, \tag{3.31}$$

where $erfc(\mu r) = 1 - erf(\mu r)$ and μ is an adjustable parameter determining the distance beyond which the short-range interaction becomes negligiable. In the HSE03 functional, the mixing of HF and DFT exchange is applied only to short-range interaction, i.e.,

$$E_{xc}^{\mathrm{HSE03}} = 0.25 E_x^{\mathrm{sr,HF}} + 0.75 E_X^{\mathrm{sr,PBE}} + E_x^{\mathrm{lr,PBE}} + E_c^{\mathrm{PBE}}, \tag{3.32}$$

where sr denotes short-range and lr long-range interaction.

It has been determined empirically that the value of $\mu \approx 0.2$-0.3 is a good universal choice of the range-separation parameter.[140] The short range part of the exchange energy $E_x^{\mathrm{sr,HF}}$ and the corresponding potential $V_x^{\mathrm{sr,HF}}$ can be written now as

$$E_x^{\mathrm{sr,HF}} = -\frac{e^2}{2} \sum_{\mathbf{k}n,\mathbf{q}m} 2 w_{\mathbf{k}} f_{\mathbf{k}n} 2 w_{\mathbf{q}} f_{\mathbf{q}m} \times \int\int d\mathbf{r} d\mathbf{r}' \frac{\mathrm{ercf}(\mu)}{|\mathbf{r}-\mathbf{r}'|} \times \psi^*_{\mathbf{k}n}(\mathbf{r}) \psi_{\mathbf{q}m}(\mathbf{r}) \psi^*_{\mathbf{q}m}(\mathbf{r}') \psi_{\mathbf{k}n}(\mathbf{r}'), \tag{3.33}$$

and

$$\begin{aligned} V_{\mathbf{k}}^{\mathrm{sr,HF}}(\mathbf{G},\mathbf{G}') &= \langle \mathbf{k}+\mathbf{G}| \hat{V_x^{sr}} |\mathbf{k}+\mathbf{G}'\rangle \\ &= -\frac{4\pi e^2}{\Omega}\sum_{m\mathbf{q}} 2w_{\mathbf{q}} f_{\mathbf{q}m} \\ &\times \sum_{\mathbf{G}''} \frac{c^*_{\mathbf{q}m}(\mathbf{G}'-\mathbf{G}'')c_{\mathbf{q}m}(\mathbf{G}-\mathbf{G}'')}{|\mathbf{k}-\mathbf{q}+\mathbf{G}''|^2} \\ &\times (1-e^{-|\mathbf{k}-\mathbf{q}+\mathbf{G}''|^2/4\mu^2}). \end{aligned} \tag{3.34}$$

The only difference with respect to the expression for complete HF exchange potential in eq. 3.30 is the last term representing the complementary error function in reciprocal space.[138] The short and long-range part of the PBE exchange energy and potential can be found using analogical decomposition.[137,138] As it can be noted from eq. 3.31 the long-range term becomes zero for $\mu = 0$ and the short-range part equals then the full Coulomb operator, while for $\mu \to \infty$ it is the opposite. Consequently two limiting cases for the HSE03 functional are the PBE0 for $\mu = 0$ and a pure PBE for $\mu \to \infty$.

The hybrid functionals show a great improvement of structural parameters and atomization energies in the case of molecules with respect to the LDA/GGA calculations.[136,140] However, for solids the performance of hybrid functionals is more ambiguous. For example, PBE0 and HSE03 predict more accurate lattice constants and bulk moduli for most solids than standard GGA, but the atomization energies are less accurate than the PBE values. The main advantage of hybrid functionals is that they improve significantly the band gaps of narrow and medium gap semiconductors, but to a lesser degree for large-gap insulators (see Fig. 3.3). Nonetheless, the values found by HSE03 functional are much closer to the experiment than for standard DFT functionals which is important to our work.

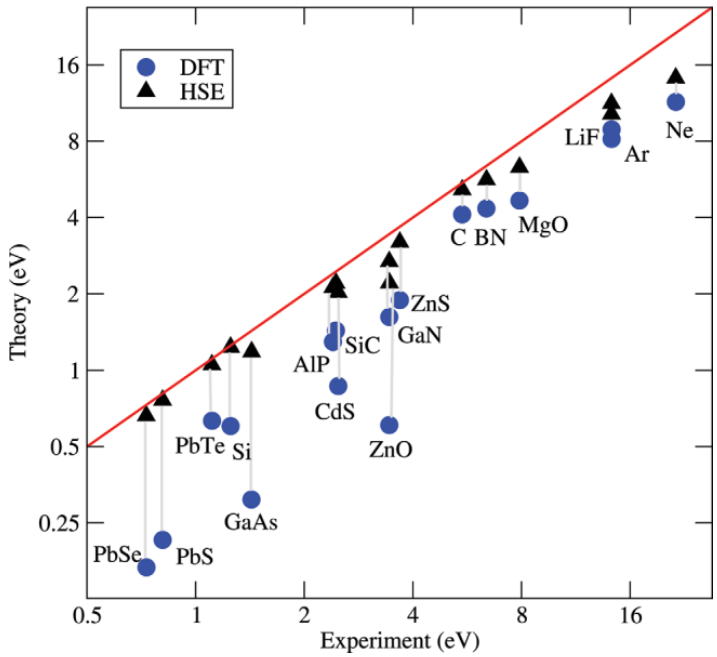

Figure 3.3: Band gaps for various semiconductors and insulators calculated using PBE and HSE03 functionals. Taken from 140.

The two hybrid functionals described above are implemented in the VASP code. For details about how the exchange and correlation interaction is dealt within the PAW formalism see sec. 3.3.4. VASP allows for an adjustment of the range separation parameter μ when using the HSE functional, i.e. it distinguishes HSE03 with $\mu = 0.3$ and HSE06 with $\mu = 0.2$. Moreover, it is possible to change the proportion of the exact Fock exchange and the type of GGA used in the calculation. This is actually useful in our work since MgO is a large-band gap insulator. The HSE03 functional fails with large band gaps materials because in these materials the non-local exchange should approach the unscreened Fock exchange. Indeed, if we compare the band gap values obtained for MgO in our work (Tab. 3.1), the PBE0 functional gives the value closest to the experimental one. On the other hand, a full HF calculation greatly overestimates the band gap.

Table 3.1: Band gap energy for bulk MgO calculated with different exchange-correlation functionals.

Functional	LDA	GGA	PBE0	HSE03	HF	Expt.
Band gap [eV]	4.65	4.76	7.17	6.18	15.46	7.8

It is evident that the resulting value of the band gap depends on the interplay between exact exchange and density functional proportion used in the calculations. By changing this ratio in PBE0 or HSE03 one can reproduce the experimental band gap value. Since PBE0 gives the best result so far it would be natural to use this functional in this thesis. However, one has to remember that hybrid functional calculations are time- and memory-intensive in general and PBE0 functional includes unscreened long-range exchange interaction which is difficult to calculate. Moreover, with plane-wave basis the Fock exchange requires a fine k-point mesh to ensure convergence.[138,140] In this respect HSE03 functional offers a significant computational advantage since it restricts the range at which the exact exchange is calculated and allows coarser grids. This is referred as "downsampling".[138] The difference in performance of both functionals in the case of an ideal MgO with only two atoms per unit cell is not large, but not for supercells needed for defect calculations. This is main reason we have chosen to work with HSE03 functional. The adjusting of the parameters was done for ideal fcc MgO with $9 \times 9 \times 9$ k-point mesh and 500 eV cutoff energy for the plane wave basis set. We have found that by increasing the Fock exchange up to 43% in HSE03 we reproduced the experimental band gap of MgO. This portion of HF was further used in calculations of MgO with defects where we limited the size of the supercell to 64-atoms and we reduced the k point grid to $4 \times 4 \times 4$ points.

In Fig. 3.4 we compare the MgO total DOS obtained using LDA and PBE0 functionals. Clearly, the main effect of adding the Fock exchange is a rigid shift of the conduction band towards higher energies.

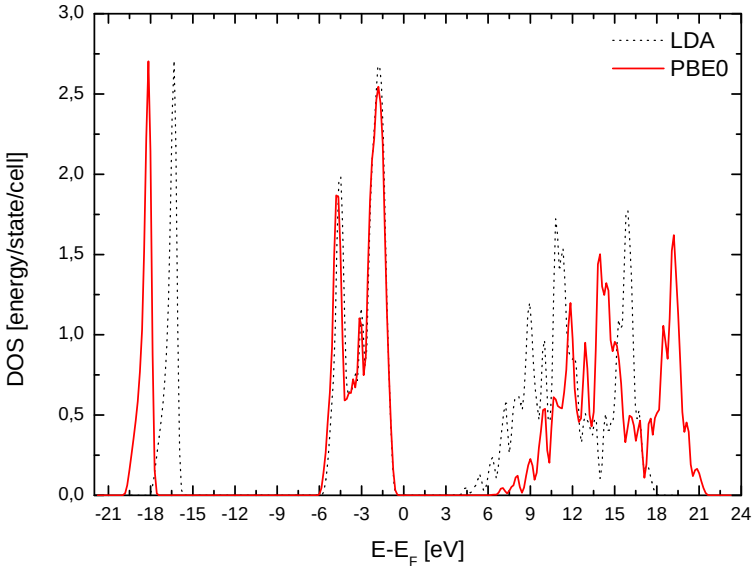

Figure 3.4: Comparison of LDA and PBE0 DOS for bulk MgO.

3.3 Solving Kohn-Sham equations

Having defined all elements in the effective potential $V_{eff}(\mathbf{r})$ one can proceed with solving the Kohn-Sham equations. These equations have to be solved in a self-consistent manner because the potential V_{eff} depends on the density $n(\mathbf{r})$, which is itself evaluated from the one-electron orbitals $\psi_n(\mathbf{r})$, and the latter depends on $V_{eff}(\mathbf{r})$. The starting point is an initial guess for $n(\mathbf{r})$. The next step is the calculation of the corresponding potential $V_{eff}(\mathbf{r})$, and solving the Kohn-Sham equations (3.12) to determine ϵ_n and ψ_n. A new density (3.13) is calculated, and is usually mixed with the old one to improve the convergence, and then the cycle starts again. The process is repeated until the electron density is converged (Fig. 3.5). To ensure that the system is in its optimal state the relaxation of atoms should also be performed. The relaxation procedure is repeated until the forces acting on the atoms cancel. In the the self-consistent cycle, when the total energy is evaluated, the forces on the atoms are calculated according to Hellmann-Feynman theorem as

$$\mathbf{F}_\mathrm{I} = -\frac{\partial E_0}{\partial \mathbf{R}_\mathrm{I}}. \tag{3.35}$$

Next, the atoms are shifted along the directions of the forces and a new self-consistent cycle begins. The relaxation stops when the forces are smaller than a specified threshold value. VASP implements few algorithms for updating the atomic positions: (i) the Verlet algorithm, (ii) the quasi-Newtonian RMM-DIIS scheme and (iii) the conjugate gradient method. In our work we have used the conjugate gradient algorithm to relax the MgO structure after the generation of vacancies.

One more important point to mention when solving Kohn-Sham equations is the choice of the basis set for one-electron wave functions expansion. The basis functions should be analytical with well known properties and the choice should be made

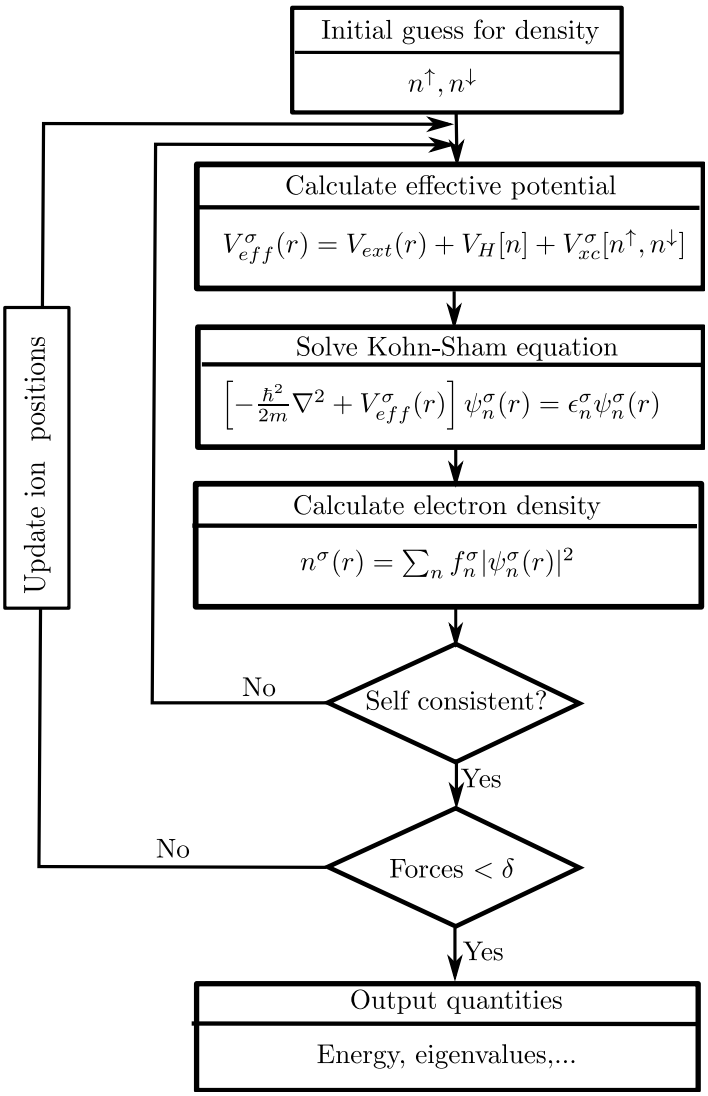

Figure 3.5: Self-consistent cycle chart. The starting point is an initial guess for the electron density. Next, the effective potential is evaluated and inserted into the Kohn-Sham equations. The Kohn-Sham equations are solved to get the eigenvalues and eigenfunctions and to evaluate the new electron density and the total energy. When the convergence criterion is fulfilled other observables can be calculated. If the forces on atoms are bigger than a required threshold value δ the ion positions are updated and the cycle is repeated. Here, σ denotes the spin of the electron.

to minimize the computational cost of calculations but still maintain sufficient accuracy. There exist a variety of basis sets that can be constructed. The most widely used are: (i) plane waves which create easily controllable complete basis set, (ii) the localized-atomic orbitals like Gaussian and Wannier functions or numerical atomic orbitals (NAOs), (iii) atomic sphere methods where the space is divided in two regions and atomic-like wave functions are used near the nucleus while smoothly varying functions are used between atoms. The VASP and the QE codes implement Kohn-Sham

equations with plane wave basis set in conjunction with PAW method or pseudopotential approach (see next subsections). Plane waves are not system dependent and so are convenient for any type of material under study. To increase the accuracy of the calculation one needs simply to increase the number of plane waves used. The SIESTA code is based on different philosophy and takes advantage of localized basis set of numerical atomic orbitals (NAOs). For convenience NAOs are implemented with norm conserving pseudopotential replacing the core electrons. More details and consequences of using such basis sets are described in the next subsections.

3.3.1 Periodicity and plane waves

Due to the crystalline structure of most of bulk materials, the potential felt by an electron is periodic with respect to translations involving Bravais lattice vectors. In the Kohn-Sham equations it means that $V_{eff}(\mathbf{r}) = V_{eff}(\mathbf{r} + \mathbf{a}_i)$, where $\mathbf{a}_i$ is a Bravais lattice vector. It is therefore convenient to apply Born–von Karman periodic boundary conditions where $\psi_{n\mathbf{k}}(\mathbf{r} + N\mathbf{a}_i) = \psi_{n\mathbf{k}}(\mathbf{r})$. In practical implementations of Kohn-Sham equations with Born–von Karman boundary conditions this makes all of the studied system periodic in some sense, i.e. even molecules which do not have periodic structure are now replicated in all three directions and gain some kind of artificial periodicity. It is then straightforward to include Bloch's theorem and plane wave expansion and write the electron wave function as

$$\psi_{n\mathbf{k}}(\mathbf{r}) = e^{i\mathbf{k}\cdot\mathbf{r}} u_{n\mathbf{k}}(\mathbf{r}), \tag{3.36}$$

with an arbitrary function $u_{n\mathbf{k}}(\mathbf{r}) = u_{n\mathbf{k}}(\mathbf{r} + \mathbf{a}_i)$ having the periodicity of a lattice, n denoting the band index and $\mathbf{k}$ a wave vector. It is easy to see that the wave function translated by a vector $\mathbf{a}_i$ takes the form

$$\psi_{n\mathbf{k}}(\mathbf{r} + \mathbf{a}_i) = e^{i\mathbf{k}\cdot\mathbf{a}_i} \psi_{n\mathbf{k}}(\mathbf{r}), \tag{3.37}$$

so that the probability density $|\psi_{\mathbf{k}}(\mathbf{r})|^2$ does not change from cell to cell. Since $u_{n\mathbf{k}}(\mathbf{r})$ is also periodic it can be expanded in terms of plane waves

$$u_{n\mathbf{k}}(\mathbf{r}) = \sum_{\mathbf{G}} c_{n,\mathbf{k}+\mathbf{G}} e^{i\mathbf{G}\cdot\mathbf{r}}. \tag{3.38}$$

Combining above equations yields electron wave function expanded in the form

$$\psi_{n\mathbf{k}}(\mathbf{r}) = \sum_{\mathbf{G}} c_{n,\mathbf{k}+\mathbf{G}} e^{i(\mathbf{k}+\mathbf{G})\cdot\mathbf{r}}, \tag{3.39}$$

where $c_{n,\mathbf{k}+\mathbf{G}}$ are Fourier coefficients and $\mathbf{G}$ a general vector in reciprocal space. If we insert now the wave function $\psi_{n\mathbf{k}}(\mathbf{r})$ expressed using Bloch waves into Kohn-Sham equations 3.12 we obtain the following eigenvalue problem

$$\sum_{\mathbf{G}'} \Big[|\mathbf{k}+\mathbf{G}|^2 \delta_{\mathbf{G}\mathbf{G}'} + V_{\mathrm{H}}(\mathbf{G}-\mathbf{G}') + V_{xc}(\mathbf{G}-\mathbf{G}') + \\ + V_{ext}(\mathbf{k}+\mathbf{G}, \mathbf{k}+\mathbf{G}') \Big] c_{n,\mathbf{k}+\mathbf{G}} = \epsilon_{n\mathbf{k}} c_{n,\mathbf{k}+\mathbf{G}}. \tag{3.40}$$

The Hartree potential in represented in reciprocal space as

$$V_{\mathrm{H}}(\mathbf{G}) = 4\pi \frac{n(\mathbf{G})}{|\mathbf{G}|^2}, \tag{3.41}$$

where $n(\mathbf{G})$ is the Fourier transform of the electronic density

$$n(\mathbf{G}) = \frac{1}{\Omega_a} \int_{\Omega_a} d\mathbf{r} n(\mathbf{r}) e^{i\mathbf{G}\cdot\mathbf{r}}, \tag{3.42}$$

where Ω_a is the volume of the cell in real space. The V_{xc} is analogically obtained by Fourier transforming the exchange-correlation potential. The matrix elements of the external potential are

$$V_{ext}(\mathbf{k}+\mathbf{G}, \mathbf{k}+\mathbf{G}') = \frac{1}{\Omega_a} \int_{\Omega_a} d\mathbf{r} e^{-i(\mathbf{k}+\mathbf{G})\cdot\mathbf{r}} V_{ext} e^{-i(\mathbf{k}+\mathbf{G}')\cdot\mathbf{r}}. \tag{3.43}$$

In principle, infinite number of $\mathbf{G}$ vectors are required to represent the wave functions with infinite accuracy, but in practice this is an impossible task. Sine the Fourier coefficients $c_{n,\mathbf{k}+\mathbf{G}}$ decrease with increasing $|\mathbf{k}+\mathbf{G}|$, the plane wave expansion can be effectively truncated. The plane wave expansion is therefore limited to describe wave functions with kinetic energy lower than some cutoff value E_{cut}

$$\frac{\hbar^2}{2m} |\mathbf{k}+\mathbf{G}|^2 \leq E_{cut}. \tag{3.44}$$

Such truncation can lead to errors in the computed physical quantities, but can be easily handled by increasing the cutoff energy. This is why it is important to converge the value of total energy, or other physical quantity of interest, with respect to the basis set size before producing meaningful predictions.

Folding and unfolding the band structure

Another important element in using plane wave basis set is connected with k-points for which the wave function is evaluated. To ensure cancellation of the phase factor it is required that $e^{i\mathbf{k}\cdot\mathbf{a}_i} = 1$, meaning that the wave function is in phase in all the periodic replicas of the unit cell. Such condition distinguishes particular class of $\mathbf{k}$ vectors which can be used in plane wave expansion and are determined by

$$\mathbf{k} = \frac{2\pi n}{a_i}, \quad \text{for } n \in \mathbb{Z}. \tag{3.45}$$

One can construct now the corresponding reciprocal space where $\mathbf{k}$ vectors are defined. For each lattice vector $\mathbf{a}_i$ of a unit cell in a real space there exist a corresponding reciprocal lattice vector $\mathbf{b}_j$ such that $\mathbf{a}_i\mathbf{b}_j = 2\pi\delta_{ij}$. The $\mathbf{b}_j$ vectors define also a unit cell but in a reciprocal space which contains the allowed $\mathbf{k}$ wave vectors and is referred as a *first Brillouin zone* (BZ). The two unit cells are connected by the following relation

$$\Omega_a = \frac{(2\pi)^3}{\Omega_b}, \tag{3.46}$$

where Ω_a and Ω_b are the volumes of cells in the real and in the reciprocal spaces, respectively. Consequently, if the volume of a unit cell in the real space is enlarged the corresponding cell in the reciprocal space becomes smaller and in the limit $\Omega_a \to \infty$ we get $\Omega_b \to 0$. In this limit there is no need to describe periodicity since the system under study can be adequately sampled using a single $\mathbf{k} = 0$ point which is the Γ point.

To understand the consequences of such a construction we can consider the dispersion relation of free electron model $\epsilon(k) = \hbar^2 k^2/2m$ schematically shown in Fig. 3.6. The values of k are not necessarily confined to the first BZ defined by $|k| \leq \pi/a$. However, for practical reasons it is customary to shift the wave vectors back to the first BZ by subtracting a reciprocal lattice vector. For example, a wave vector k' in the second BZ folds onto the vector $k = k' - 2\pi/a$, and a wave vector k'' in the third BZ on the vector $k = k'' - 4\pi/a$ as shown in Fig. 3.6. Then, the folded bands correspond to momentum values $k_n = k + G_n$ with k in the first BZ, $G = 2\pi n/a$ and n integer. This scenario is valid also for electron moving in an effective Kohn-Sham potential and can be generalized to three dimensional lattice as $\mathbf{k}' = \mathbf{k} + \mathbf{G}$. In the presented example

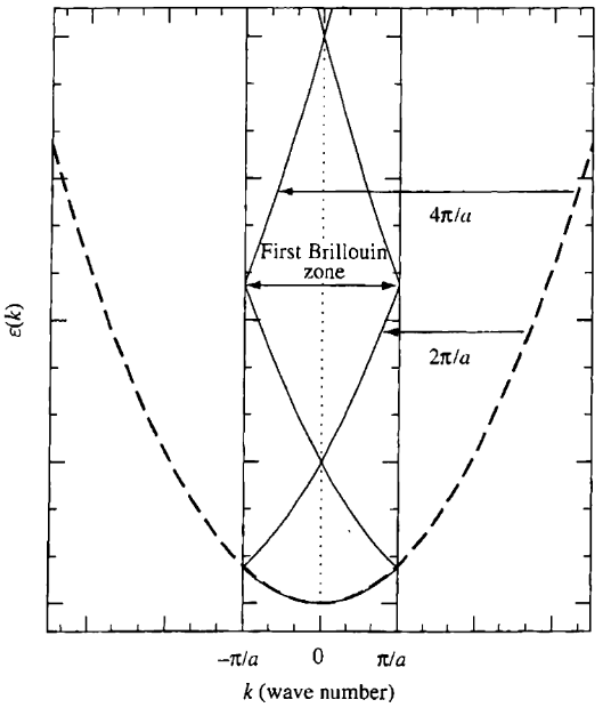

Figure 3.6: Dispersion relation for a one-dimensional system in a free electron model. Taken from Ref. 141.

the band folding is just a simple trick to simplify a visualization of the electronic band structure. It also works well for structures where primitive cells with only few atoms can be used. However, if we consider a bigger simulation cell with increased number of atoms so that primitive cell is replicated, the corresponding BZ becomes smaller since these two lattices are inversely proportional. Consequently, more and more bands are folded back to the first BZ and the band structure picture gets more complicated and difficult to interpret.

In our case, to investigate the influence of the oxygen vacancies onto MgO electronic

structure the size of the simulation cell had to be increased to properly model vacancies and prevent artificial interactions between defects due to periodic boundary conditions. As a result we doubled the MgO lattice parameter and ended up with supercell of 64 atoms in a simple cubic structure. As one can imagine the corresponding band structure, folded to the first BZ, become really complicated and it was practically impossible to verified how the nominal MgO band structure is affected by the presence of vacancies. Nonetheless, if folding is possible one can also do the opposite by unfolding the bands. This can be done using the BandUP code developed by Medeiros *et al.*[142,143] BandUP is a post-processing tool compatible with output data generated by VASP, QE, ABINIT or CASTEP which allows to obtain a primitive cell representation of the band structure of system calculated using supercell. In principle, no explicit calculations involving the reference primitive cell are required. Only the primitive cell vectors have to be know in order to determine geometric unfolding relations.

The procedure of the band unfolding performed by BandUP is the following. Lets define first Ω_{PCBZ} and Ω_{SCBZ} as the volumes of the primitive cell BZ and supercell BZ, respectively. Then, for each wave vector $\mathbf{K}$ of the SCBZ, there are $N_{unfold} = \Omega_{PCBZ}/\Omega_{SCBZ}$ corresponding wave vectors $\mathbf{k}_i$ of the PCBZ such that

$$\mathbf{k}_i = \mathbf{K} + \mathbf{G}_{\mathbf{k}_i \leftarrow \mathbf{K}}, \tag{3.47}$$

where $i = 1, 2, ..., N_{unfold}$ is the number of the wave vectors $\mathbf{k}_i$ and $\mathbf{G}_{\mathbf{k}_i \leftarrow \mathbf{K}}$ are vector belonging to the SC reciprocal lattice. The wave vector $\mathbf{K}$ is unfolded onto $\mathbf{k}_i$ with the unfolding vector $\mathbf{G}_{\mathbf{k}_i \leftarrow \mathbf{K}}$.

If we now assume that $|\psi^{\mathrm{SC}}_{m\mathbf{K}}\rangle$ is the eigenstate of the Hamiltonian corresponding to the SC and $|\psi^{\mathrm{PC}}_{n\mathbf{k_i}}\rangle$ is the eigenstate in the PC then

$$|\psi^{\mathrm{SC}}_{m\mathbf{K}}\rangle = \sum_{n,\mathbf{k}_i \in \{\tilde{\mathbf{k}}_i\}} \alpha(\mathbf{k}_i, n; \mathbf{K}, m)\, |\psi^{\mathrm{PC}}_{n\mathbf{k}_i}\rangle\,, \tag{3.48}$$

where $\{\tilde{\mathbf{k}}_i\}$ is the set of wave vectors $\mathbf{k}_i$ in the PCBZ which satisfies the relation 3.47 and correspond to PS eigenstates with the same eigenvalues as the SC.

Now, the probability for the $|\psi^{\mathrm{SC}}_{m\mathbf{K}}\rangle$ to have the same character as a PC Bloch state with wave vector $\mathbf{k}$ is defined by the spectral weight $P_{m\mathbf{K}}(\mathbf{k})$ is

$$P_{m\mathbf{K}}(\mathbf{k}) = \sum_n |\,\langle \psi^{\mathrm{SC}}_{m\mathbf{K}} | \psi^{\mathrm{PC}}_{n\mathbf{k}} \rangle\,|^2 = \sum_{\mathbf{g} \in \mathrm{PCRL}} |C^{\mathrm{SC}}_{m\mathbf{K}}(\mathbf{g} + \mathbf{k} - \mathbf{K})|^2, \tag{3.49}$$

where $\mathbf{g}$ are the wave vectors belonging to PC reciprocal lattice (PCRL), and $C^{\mathrm{SC}}_{m\mathbf{K}}$ are the coefficients of the plane waves that span the eigenstates of the SC. Consequently, the values of $P_{m\mathbf{K}}(\mathbf{k})$ can be obtained entirely from the coefficients $C^{\mathrm{SC}}_{m\mathbf{K}}$ which means that the knowledge of the PC eigenstates is not required. The spectral function $A(\mathbf{k}; \epsilon)$ is then defined

$$A(\mathbf{k}; \epsilon) = \sum_m P_{m\mathbf{K}}(\mathbf{k}) \delta(\epsilon - \epsilon_m(\mathbf{K})), \tag{3.50}$$

and the pairs $(\mathbf{k}, \mathbf{K})$ which need to be included are these in which $\mathbf{K}$ unfolds onto $\mathbf{k}$. The unfolding procedure described up till now is strictly exact only for perfect SC but can still provide a meaningful physical representation, in terms of an effective PC band

structure (EBS), if the perturbations from the perfect cell are small. To obtain EBS the authors define infinitesimal version $dS_{\mathbf{k}}(\epsilon) = A(\mathbf{k};\epsilon)d\epsilon$ of the cumulative probability function $S_{\mathbf{k}}(\epsilon)$. Then, $dS_{\mathbf{k}}(\epsilon)$ represents the number of PC bands, at the PC wave vector $\mathbf{k}$, that crosses the energy interval $(\epsilon, \epsilon + d\epsilon)$. Hence, the region of interest in the $(\mathbf{k};\epsilon)$ space is mapped onto a $(\mathbf{k}_i, \epsilon_j)$ grid with energy intervals $\delta\epsilon$ and a weight $\delta N(\mathbf{k}_i;\epsilon_j)$ assign to each point and given by

$$\delta N(\mathbf{k}_i;\epsilon_j) = \int_{\epsilon_j-\delta\epsilon/2}^{\epsilon_j+\delta\epsilon/2} dS_{\mathbf{k}_i}(\epsilon) = \sum_m P_{m\mathbf{K}}(\mathbf{k}_i) \int_{\epsilon_j-\delta\epsilon/2}^{\epsilon_j+\delta\epsilon/2} \delta(\epsilon - \epsilon_m(\mathbf{K}))d\epsilon. \tag{3.51}$$

In other words, the above expression gives the number of PC bands crossing $(\mathbf{k}_i, \epsilon_j)$. Finally, the $\delta N(\mathbf{k}_i;\epsilon_j)$ is averaged over wave vectors $\mathbf{k}_i$ related by symmetry operations of the PCBZ.

An example of the unfolded EBS for the Stone-Wales (SW) defect in graphene is shown in Fig. 3.7. As it can be seen, the main appreciable feature of EBS is the smearing of the PC eigenvalues $\epsilon_n^{\mathrm{PC}}(\mathbf{k})$: a set of energy levels $\epsilon_m^{(i)}(\mathbf{k})$ apears smeared around band centers $\tilde{\epsilon}_n(\mathbf{k}) \approx \epsilon_n^{\mathrm{PC}}(\mathbf{k})$ with smearing widths $\Delta\epsilon_n(\mathbf{k})$. Then, the summation of δN for these energy levels gives approximately the number of PC bands crossing $(\mathbf{k};\epsilon)$ for pristine graphene.

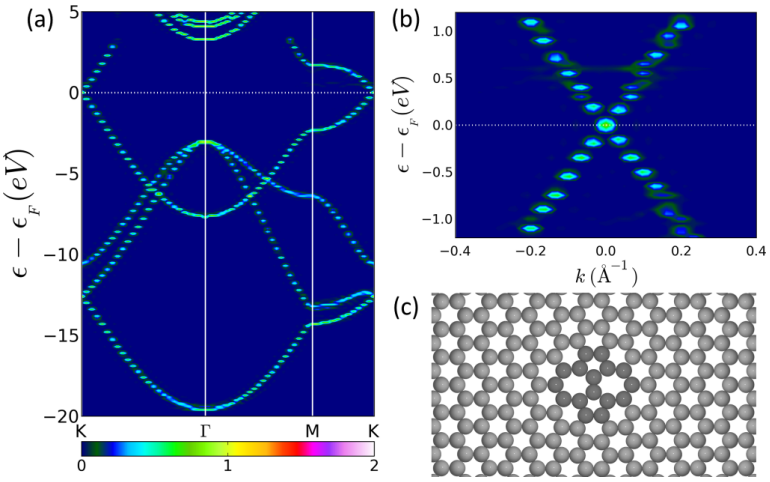

Figure 3.7: SW defect in graphene. (a) and (b) are EBS, and (c) shows the geometry of the SW structure. In (b), the k axis is perpendicular to he K-Γ direction and the point K is at $k = 0$. The color scale represents δN. Taken from 142.

Sampling Brillouin zone

By applying periodic boundary conditions and defining a set of allowed $\mathbf{k}$ vectors in the BZ we arrive to Kohn-Sham equations in the form

$$\begin{aligned} \left[-\frac{\hbar^2}{2m}\nabla^2 + V_{eff}\right]\psi_{n\mathbf{k}} &= \epsilon_{\mathbf{k}}\psi_{n\mathbf{k}}, \\ n(\mathbf{r}) &= \sum_{n\mathbf{k}} f_{n\mathbf{k}}|\psi_{n\mathbf{k}}|^2, \end{aligned} \tag{3.52}$$

which has to be solved in a self-consistent manner for each independent **k** vector and band index n. For many physical properties, e.g. total energies, density of states or charge density, it is essential to integrate over **k** throughout the BZ, and such integral I is in the form

$$\overline{I} = \frac{1}{\Omega} \sum_{n}^{occ} \int_{\mathrm{BZ}} I_n(\mathbf{k}) d\mathbf{k}, \tag{3.53}$$

where the sum is over all occupied bands. This would required an infinite number of **k** points which is again impossible in practical implementations, and hence the integral in the BZ is replaced by a sum over a finite number of k-points

$$\frac{1}{\Omega} \int_{\mathrm{BZ}} I_n(\mathbf{k}) d\mathbf{k} \quad \rightarrow \quad \frac{1}{N_k} \sum_{\mathbf{k}}^{N_{\mathbf{k}}} I_n(\mathbf{k}) \tag{3.54}$$

where $N_{\mathbf{k}}$ is the number of k-points in the BZ. This is referred as *BZ sampling*. The question to answer now is how to choose the k points to achieve a fast convergence of the summation? There are few schemes proposed in the literature but the most widely used one is the Monkhorst-Pack method.[144] The k-points are distributed uniformly through space as

$$\mathbf{k} = \frac{n_1}{N_1}\mathbf{b}_1 + \frac{n_2}{N_2}\mathbf{b}_2 + \frac{n_3}{N_3}\mathbf{b}_3, \tag{3.55}$$

with $n_1 = 0..., N_1 - 1; \quad n_2 = 0..., N_2 - 1; \quad n_3 = 0..., N_3 - 1$, where the N_i is the number of subdivisions along each reciprocal lattice vector $\mathbf{b}_i$. A further computation savings may be made using the point group symmetry of the lattice and reducing the number of k-points calculated explicitly only to the irreducible wedge of the Brillouin zone (IBZ) part. The sums over BZ are can be written in modified form as

$$\overline{I} = \sum_{n}^{occ} \sum_{k \in \mathrm{IBZ}} \omega_{\mathbf{k}} I_n(\mathbf{k}), \tag{3.56}$$

where $\omega_{\mathbf{k}}$ is a weight of each **k** point in the BZ.

In addition, one can specify if the Γ point is included or not in the k-point mesh by defining a shift of the grid. If the grid is shifted out of the Γ point it can break the underlying point group symmetry and increase the number of nonequivalent k-points in the IBZ. This might be useful in some cases where the energy levels are degenerate along high symmetry directions, the shifted grid can improve the convergence.

It is important to mention that the calculations of physical quantities over the IBZ include only the occupied states. In the case of insulators or semiconductors the distinction between occupied and unoccupied levels is quite easy since these materials have a well defined band gaps. However, problems might occur when considering metals with complex Fermi surface shapes. During the self-consistent cycle, the Fermi level is adjusted to provide the number of valence electrons N_{el}. The value of N_{el} is obtained from the total density of states, here D(E), as

$$N_{el} = \int_{-\infty}^{E_F} D(E) dE, \tag{3.57}$$

where

$$D(E) = \frac{1}{\Omega}\sum_{n}\int_{\mathrm{BZ}}\delta(E-\epsilon_{n\mathbf{k}})d\mathbf{k} = \sum_{n\mathbf{k}\in\mathrm{IBZ}}\omega(\mathbf{k})\delta(E-\epsilon_{n\mathbf{k}}). \tag{3.58}$$

In the case of metals it means that for k points close to k_{F} the highest occupied bands can enter or exit the BZ sampling from one iteration to another. This introduces an instability and makes convergence more difficult to achieve. One can try to increase the BZ sampling to solve this issue but this may imply an intractable number of k points and significantly increase the time of calculations. A simpler solution is to smear the Fermi surface by introducing a distribution of occupation numbers and replace Dirac delta function $\delta(\epsilon)$ in eq. 3.58 by a regular and continuous function $\tilde{\delta}(\epsilon)$ with the same normalization as $\delta(\epsilon)$. Different methods were proposed where the sharp function defining the band occupancy can be replaced by a the Fermi-Dirac distribution function or Gaussian function, or a polynominal function as proposed by Methfessel and Paxton. In this thesis we used Gaussian method which introduces a broadening τ of energy levels with Gaussian functions of the form

$$\tilde{\delta}(\epsilon) = \frac{1}{\sqrt{2\pi}\tau}e^{-(\epsilon/2\tau)^2}. \tag{3.59}$$

τ is the so called *smearing parameter*. The τ doesn't really have here a physical meaning, it's just introduced to simplify numerical calculations. Increasing τ will improve the convergence but at the same time the results will become less accurate. In general values of τ of 0.1 - 0.3 eV should be sufficient.

Another approach, which does not use an artificial level smearing, is the tetrahedron method,[145] where the BZ is divided in equal tetrahedrons. The energy values between the corners of tetrahedron are obtained by a linear interpolation. This method is more accurate, but it requires denser k-point meshes to built the tetrahedrons and obtain converged density of states.

3.3.2 Choice of convergence parameters

As discussed, a solution of Kohn-Sham equations requires a set of simplifications to be made in order to solve these equations numerically. First, the basis set has to be truncated and the number of plane waves included depends on the cutoff energy specified by the user. Next, one has to define the the k-point mesh and choose the method for approximating the BZ sampling. The number of k-points depends on the required precision and on the type of material, i.e. metals require more k-points than semiconducting or insulating materials. The number of k-points also depends on the smearing method. As it was mentioned, the tetrahedron method needs denser k-point grid than Gaussian or Fermi smearing methods. Moreover, when using large supercells the number of k-points can be significantly reduced compared to these required for a primitive cell calculation since the real and reciprocal spaces are inversionally proportional to each other. Last, the convergence criterion for for the total energy and forces calculated in the self-consistent cycle, should be also defined.

We have started with ground state calculations of ideal MgO and structure with defects denoted as F(M)-MgO. The F/M centers were created simply by removing

one/two neutral oxygen atoms from the supercell containing 64 atoms in a simple cubic form. These calculations were performed using VASP and GGA-PBE functional. The cutoff value of 500 eV was used and the convergence criterion for energy of 1μeV. The structures with defects were relaxed with requiring that the forces acting on atoms be less than -0.001. Due to the large size of supercell we found that a k-point mesh of 4×4×4 with the Gaussian smearing of $\tau = 0.2$ eV is good enough for the convergence of the defect levels. The same convergence parameters were used for HSE03 calculations.

In the case of thin MgO films and full junction with ferromagnetic electrodes the cutoff energy as well as the convergence criterion were the same. Only the value of τ was decreased to 0.1 eV. For the slab calculations, we used 7 ML of MgO in the z direction and we doubled the MgO lattice constant in the lateral directions. Periodic boundary conditions are applied in all directions. In order to drastically reduce the interaction between periodic images along the z direction, we separated the slabs by a vacuum of 15 Å.

3.3.3 Pseudopotential method

The self-consistent procedure for solving Kohn-Sham equations described in the previous section can be performed for each electron in the system, i.e. both valence and core electrons are included. However, the potential V_{ext} created by the ions has singularities at the positions of the ions. As a consequence, the valence electron wave function will develop strong oscillations in the core region to remain orthogonal to the core states. As a result a lot of plane waves are required to properly describe the valence states or a dense grid of points when using real-space representation, which is computationally very demanding. To simplify the problem, it was noticed that the chemical bonds between atoms involve only the valence electrons. The core electrons interact weakly with those of different sites and remain mostly localized around each nucleus. Thus, these states can be frozen and do not have to be included explicitly in the calculations. Instead, the nucleus and the core electrons are represented by an effective pseudopotential, smoother then the original one and the corresponding all-electron (AE) wave function is replaced by a pseudo wave (PS) function. Because the core states are removed from the calculations, the valence eigenstates corresponding to the new smooth pseudopotential, are nodeless in the core region. These pseudo-wave functions are generally smoother and easier to represent on a numerical grid than the original all-electron states. Outside the core region the pseudopotential and the pseudo wave functions have to be identical to the corresponding all-electron ones.

The pseudopotential can be constructed to satisfy a number of transferability conditions such that it may be used in a variety of different chemical environments. A good pseudopotential should fulfil few requirements:

- it should be as smooth as possible, meaning only a few plane waves are needed for the valence pseudo-wavefunctions expansion,
- it should be transferable thus, assuring reliable results for a variety of solids where the crystal potential is different from the atomic one,

- the pseudo charge density should reproduce the all-electron valence charge density as accurately as possible on the bonding region between atoms.

There are different flavours of the pseudopotentials and the ways to construct them.[146–149] Here only two will be described in more details since they were used in the some of our calculations. The pseudo-wave functions and pseudopotentials will be denoted $\tilde{\psi}$ and $\tilde{V}$ respectively.

Norm Conserving pseudopotentials

Here we will only discuss ab initio pseudopotentials. One of the first constructions of pseudopotentials was proposed by Hamann *et al.*[146] They assumed that the norm of the pseudo wave function is equal to that of all-electron wave function and thus their construction is called the norm conserving pseudopotential (NCPP). The pseudo wave functions (and potential) are assumed to be equal to the all electron valence wave function (and potential) outside some core radius r_c. Inside the r_c the pseudo wave function $\widetilde{\psi}$ is not the same as the AE wave function ψ but their norms are constrained to be equal

$$\int_0^{r_c} d\mathbf{r}|\widetilde{\psi}(\mathbf{r})|^2 = \int_0^{r_c} d\mathbf{r}|\psi(\mathbf{r})|^2. \tag{3.60}$$

For a given atomic configuration, the NCPP must also fulfil the requirement that $\widetilde{\psi}(\mathbf{r})$ is nodeless and the energy calculated from the pseudopotential is equal to that of the all-electron one, $\widetilde{\epsilon}_l = \epsilon_l$. The eigenvectors and eigenvalues are different for each angular momenta l which makes the pseudopotential l depend.

The construction of the pseudopotential and the pseudo wave functions, that satisfy the above requirements, can be accomplished using many different schemes. There are many variations with respect to the choice of the pseudo wave functions inside r_c or the cutoff radius (e.g. the method of Hamman and Schüter[146] or Troullier and Martin[148]). The general procedure for generating the NCPP can be summarized as follows:

1. Perform AE DFT calculation for an atom for a given exchange-correlation potential of a radial Schrödinger equation

$$-\frac{\hbar^2}{2m}\frac{d^2\psi_l(r)}{dr^2} + \left(\frac{\hbar^2}{2m}\frac{l(l+1)}{r^2} + V - \epsilon_l\right)\psi_l = 0, \tag{3.61}$$

   to get the atomic wave functions, eigenvalues, charge density and potential. The V is the self-consistent one electron potential which includes the ionic potential, the Hartree and the exchange-correlation potentials for the electrons.

2. Specify the cut off radius $r_{c,l}$ for each angular momentum and construct a pseudopotential for each of them.

3. Construct the pseudo wave function, $\widetilde{\psi}_l$, for the valence electrons that obey the norm conservation condition in the region $r < r_{c,l}$. Outside the $r_{c,l}$ the pseudo wave function is equal to the all-electron one.

4. Invert the Kohn-Sham equation to calculate the screened pseudopotential, $\widetilde{V}_{scr,l}(r)$,

$$\widetilde{V}_{scr,l}(r) = \epsilon_l - \frac{\hbar^2}{2m}\left[\frac{l(l+1)}{r^2} - \frac{\frac{d^2}{dr^2}\widetilde{\psi}_l(r)}{\widetilde{\psi}_l(r)}\right] = 0. \tag{3.62}$$

   Alternatively, one can generate first $\widetilde{V}_{scr,l}(r)$ in such a way that $\widetilde{\psi}_l(r)$ obeys the norm-conservation condition.

5 Unscreen the potential by removing the Coloumb and the exchange-correlation parts coming from valence electrons

$$\widetilde{V}_l(r) = \widetilde{V}_{scr,l}(r) - \widetilde{V}_{\mathrm{H}}(r) - \widetilde{V}_{xc}(r). \tag{3.63}$$

The most important consequence of the procedure described above is that each angular momentum component of the wave function will see a different potential. Therefore, before unscreening the pseudopotential, it is useful to separate the ionic potential into a local (l-independent) and a fully non-local (l-dependent) part using the construction of Kleinman-Bylander[149]

$$\widetilde{V}_l(r) = \widetilde{V}_{local}(r) + V_{\mathrm{NL}}^{\mathrm{KB}}, \tag{3.64}$$

where $\widetilde{V}_{local}(r)$ is the local part of the pseudopotential and $V_{\mathrm{NL}}^{\mathrm{KB}}$ the non-local part defined as

$$V_{\mathrm{NL}}^{\mathrm{KB}} = \sum_l \frac{|\delta V_l\ \widetilde{\psi}_{lm}\rangle\ \langle\widetilde{\psi}_{lm}\ \delta V_l|}{\langle\widetilde{\psi}_{lm}|\ \delta V_l\ |\widetilde{\psi}_{lm}\rangle}, \tag{3.65}$$

where $\delta V_l = V_l - \widetilde{V}_{local}(r)$ with V_{local} an arbitrary local function; $\widetilde{\psi}_{lm}$ is the pseudo wave function, including the angular dependence, for the reference atomic state.

The $\langle\delta V_l\ \widetilde{\psi}_{lm}|$ are the *projectors* that operate upon the wave function

$$\langle\delta V_l\ \widetilde{\psi}_{lm}|\Psi\rangle = \int d\mathbf{r}\delta V_l\ \widetilde{\psi}^*_{lm}(\mathbf{r})\Psi(\mathbf{r}). \tag{3.66}$$

The projectors are localized in space and have non-zero values only inside the pseudopotential cutoff radius where δV_l is non-zero. The biggest advantage of the separable form of the pseudopotential is that matrix elements require only the product of the projector operations

$$\langle\Psi_i|\ V_{\mathrm{NL}}^{\mathrm{KB}}\ |\Psi_j\rangle = \sum_{lm}\langle\Psi_i|\widetilde{\psi}_{lm}(\mathbf{r})\ \delta V_l\rangle\ \frac{1}{\langle\widetilde{\psi}_{lm}|\ \delta V_l\ |\widetilde{\psi}_{lm}\rangle}\ \langle\delta V_l\ \widetilde{\psi}_{lm}(\mathbf{r})|\Psi_j\rangle\,, \tag{3.67}$$

which saves computational time, especially for big systems. However, these NCPPs are labelled "hard" because they require a large number of plane-waves, especially for the first row elements and for transition metals.

In SIESTA NCPP are implemented with localized atomic orbitals as a basis set. The code reads the pseudopotential from a file in a semilocal form generated with the Troullier-Martins parametrization. Then, the semilocal form is transformed into fully nonlocal one using Kleinman-Bylander transformation. The local part of pseudopotential $\widetilde{V}_{local}(r)$ can be in principle arbitrary, but it has to be constructed in such a way that it joins smoothly to $\widetilde{V}_l(r)$, and then both match AE potential outside r_c.

Ultrasoft Pseudopotentials

A different approach for constructing "smoother" pseudopotentials, where the norm conservation is no longer required, were proposed by Vanderbilt.[147] The dropping of the norm conservation resulted in use of less plane waves in the basis set compared to NCPPs. The assumption is that the pseudo-wave function is equal to the AE wave function outside r_c as for NCPP but inside r_c it should to be as smooth as possible. This is known as the *ultrasoft psuedopotential* (USPP). However, such construction introduces also some complications.[150] First of all, because the pseudo wave functions do not have the same norm as the AE wave functions inside region defined by r_c they are necessarily not normalized. As a consequence, the pseudo-charge density cannot be any more evaluated using the pseudo-wave functions as with the NCPP since it would yield the wrong total charge. To overcome this problem an augmentation charge needs to be added in the core region. The construction of the USPP is explained in the following.

In the Vanderbilt approach the total energy functional in presence of USPP is written as

$$E = \sum_i \langle \widetilde{\psi}_i | \, T + V_{\mathrm{NL}} \, | \widetilde{\psi}_i \rangle + \int d\mathbf{r} V_{local}(\mathbf{r}) n(\mathbf{r}) + \frac{1}{2} \int \int d\mathbf{r} d\mathbf{r}' \frac{n(\mathbf{r}) n(\mathbf{r}')}{|\mathbf{r} - \mathbf{r}'|} + E_{xc}[n], \quad (3.68)$$

where the kinetic, Hartree, exchange-correlation, and local terms have the usual form. The fully non-local potential operator, V_{NL}, is redefined as

$$V_{\mathrm{NL}} = \sum_{nm} D^{(0)}_{nm} \, |\beta^{\mathrm{I}}_n\rangle \, \langle \beta^{\mathrm{I}}_m| \, , \quad (3.69)$$

where β^{I}_n are the projector functions centred on atom I, and $D^{(0)}_{nm}$ are coefficients determined during the pseudopotential generation (details can be found in Appendix A). Because the norm conservation condition is relaxed the overlap matrix, $\langle \widetilde{\psi}_i | \, S \, | \widetilde{\psi}_j \rangle$, is introduced in the form

$$S = 1 + \sum_{nmI} q_{nm} \, |\beta^{\mathrm{I}}_n\rangle \, \langle \beta^{\mathrm{I}}_m| \, , \quad (3.70)$$

where $q_{nm} = \int d\mathbf{r} Q_{nm}(\mathbf{r})$ is an augmentation charge and $Q_{nm}(\mathbf{r})$ corresponds to the augmentation functions defined as

$$Q_{nm}(\mathbf{r}) = \psi^*_n(\mathbf{r}) \psi_m(\mathbf{r}) - \widetilde{\psi}^*_n(\mathbf{r}) \widetilde{\psi}_m(\mathbf{r}). \quad (3.71)$$

As mentioned before, the pseudo charge density is evaluated based on the pseudo wave function plus an additional augmentation charge defined in the core region of atoms

$$n(\mathbf{r}) = \sum_i \left[|\widetilde{\psi}_i(\mathbf{r})|^2 + \sum_{nmI} Q^{\mathrm{I}}_{nm}(\mathbf{r}) \, \langle \widetilde{\psi}_i | \beta^{\mathrm{I}}_n \rangle \, \langle \beta^{\mathrm{I}}_m | \widetilde{\psi}_i \rangle \right] . \quad (3.72)$$

The advantage of the new form of the density is that one can increase the cutoff radii (r_c) and hence create softer pseudopotentials. This also requires a separate plane wave cutoff for the density. This is due to the fact that the pseudo-density has now a smooth part and a sharp part which needs to be expressed with plane waves with

higher frequencies. Thus, the plane wave cutoff for the density is typically several times bigger than the cutoff used tor the wave functions.

Moreover, the new form of the pseudo-density makes the Kohn-Sham equation more complex. The functional derivative of the density with respect to the orbitals is given by

$$\frac{\delta n(\mathbf{r})}{\delta \widetilde{\psi}_i^*(\mathbf{r})} = \widetilde{\psi}_i(\mathbf{r})\delta(\mathbf{r}-\mathbf{r}') + \sum_{nmI} Q^{\mathrm{I}}_{nm}(\mathbf{r})\beta^{\mathrm{I}}_n(\mathbf{r}) \left\langle \beta^{\mathrm{I}}_m | \widetilde{\psi}_i \right\rangle . \tag{3.73}$$

Combining eq. 3.68 and 3.73 one gets modified Kohn-Sham equations as

$$\begin{aligned} \frac{\delta E}{\delta \widetilde{\psi}_i^*(\mathbf{r})} &= \int d\mathbf{r}' \frac{\delta E}{\delta n(\mathbf{r}')} \frac{\delta n(\mathbf{r}')}{\delta \widetilde{\psi}_i^*(\mathbf{r})} = \\ &= \left[-\frac{1}{2}\nabla^2 + V_{eff} + \left(D^{(0)}_{nm} + \int d\mathbf{r}' V_{eff}(\mathbf{r}') Q_{nm}(\mathbf{r}') \right) |\beta^{\mathrm{I}}_n\rangle \langle \beta^{\mathrm{I}}_m| \right] |\widetilde{\psi}_i\rangle \end{aligned} \tag{3.74}$$

where $V_{eff} = V_{\mathrm{H}} + V_{loc} + V_{xc}$.
As it can be clearly seen, in the case of USPP, the coefficients of the projectors in the non-local part of the pseudopotential are updated at each iteration during the self-consistent calculation. Despite the additional complexity introduced with USPP, the gain in the plane wave expansion is significant compared to NCPP.

We used USPP with plane wave basis set as implemented in QE. This form of pseudopotential is afterwords implemented in the transport module PWcond (see next section). The ground state calculations are performed in order to generate the effective potential V_{eff} and D_{nm} coefficients which are required for calculating the transmission coefficient in PWcond. As it was described in the section 3.3, when plane waves are used as a basis set one has to define the cutoff energy to determine the number of plane waves. Moreover, in combination with USPP, an additional cutoff value has to be specified for the electron density. The recommended values for the electron density cutoff are usually 8-12 times larger than for the wave functions. We performed convergence tests to define the needed parameters for the calculations. The structure of MgO with simple cubic form and 8 atoms in a simulation cell with $a_{\mathrm{MgO}} = 4.242$ Å was used. In the case of Fe a 4 atom cubic cell was also used and whose lattice constant in lateral direction is the same as that of MgO and $a_{\mathrm{Fe}_z} = 2.980$ Å along z. The lattice parameters were adjusted to ensure proper matching at the interfaces when the two structures are connected. For all atoms the GGA-PW91 functional was used. The changes of total energy with respect to the cutoff value for the plane wave basis, denoted as '*Ecut*', for MgO and Fe and are presented in Fig. 3.8. Note that QE uses atomic units, i.e. the energy is expressed in Ry and the lattice parameters in Bohr radius. Here, the cutoff for the electron density ('*EcutRho*') is set to the default value of 4·*Ecut*. In both cases, after initial drastic drop, the total energy remains rather constant and we decided to fix *Ecut* to 40 Ry. Also the increase of the k-point mesh from 10×10×10 to 20×20×20 do not influence significantly the value of the energy and smaller grids can be used. Next, to determine proper *EcutRho* we plot changes in total energy with respect to *EcutRho* value for fixed wave function cutoff of 40 Ry (see Fig. 3.9). We choose to use a value 10 times bigger than that of the wave function cutoff as suggested in QE manual.

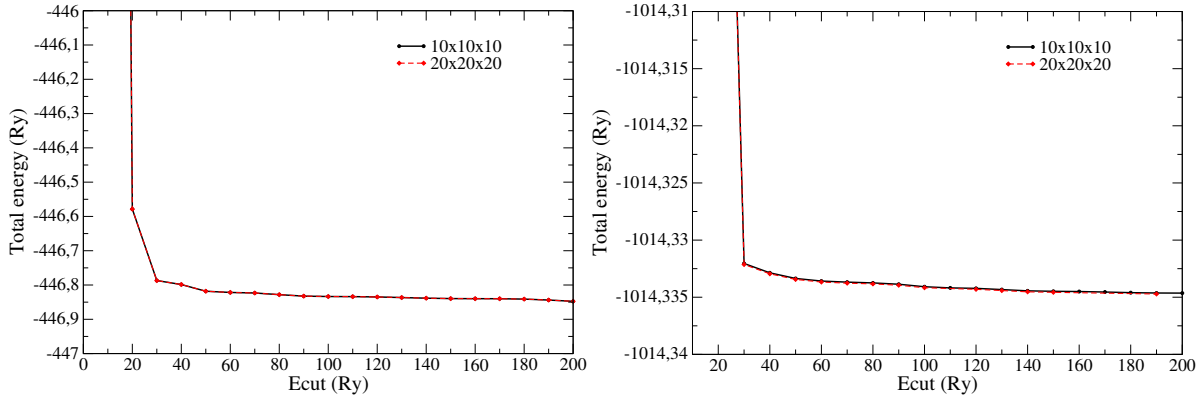

Figure 3.8: Convergence of total energy with respect to the cutoff energy (Ecut) for plane wave expansion for MgO (left) and Fe (right). The cutoff for the electron density is 4 times bigger that for the wave function. The GGA-PW91 functional with USPP was used. In both calculations the k-point mesh is converged.

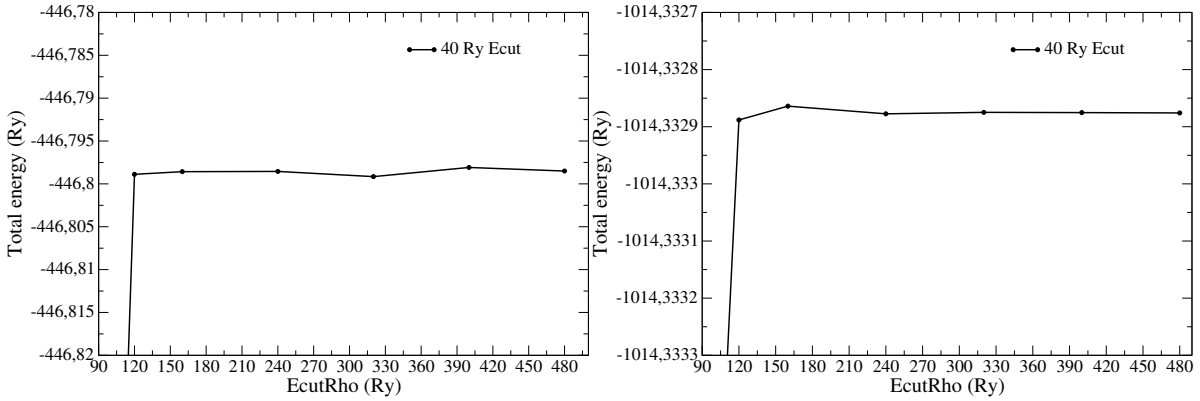

Figure 3.9: Convergence of total energy with respect to the cutoff energy (EcutRho) for electron density for MgO (left) and Fe (right). The cutoff for the wave function is fixed to 40 Ry. A mesh of 10×10×10 k-points is used.

When we switch to Fe/MgO MTJs, as mentioned, the lattice constant of MgO is doubled in the lateral plane and also increased along z with varied number of MgO layers. As a result the k-point grid can be decreased, and we used a mesh of 5×5×1. For the calculations involving the electrodes in the antiferromagnetic alignment, the k-point grid was shifted out of the Γ point to speed up the convergence. The final parameter used in QE calculations are: (1) cutoff value for energy: 40 Ry, (2) cutoff for electron density: 400 Ry, (3) Gaussian smearing with τ= 0.02 Ry, (4) energy convergence threshold: 10^{-8}, and (5) density mixing value: 0.1.

3.3.4 Projector augmented wave method

Another approach to treat electron-ion interaction, namely projected augmented wave method (PAW) is implemented in the VASP code and it is useful to describe it here. The PAW method, introduced by Blochl,[151] combines the accuracy of all-electron methods and the simplicity of the plane wave pseudopotential approach giving the most

general scheme for solving Kohn-Sham equations. The expectation values correspond to all-electron system subjected to the full all-electron potential. The PAW method makes use of the frozen core approximation where the core states are imported from the isolated atom calculations since these states are practically unaffected during the bond formation.

The idea behind the PAW method is to divide space into two types of regions, the augmentation region with non-overlaping atom-centred spheres of radius r_c^{I} for each atom I, and the interstitial region which includes the space between the augmented spheres. The wave function of the valence electron is then expanded into two different basis sets. This is justified by the fact that the valence electrons wave function vary smoothly between the atoms, and oscillates rapidly near the nuclei. Thus, a plane wave basis set can be used in the interstitial region and atomic-like partial wave basis set in the augmentation region. Each wave function and its first derivative should be continuous at the boundaries of the augmentation spheres. This matching is realized using projectors as it will be explained below. The idea behind the PAW method is schematically illustrated in Fig. 3.10.

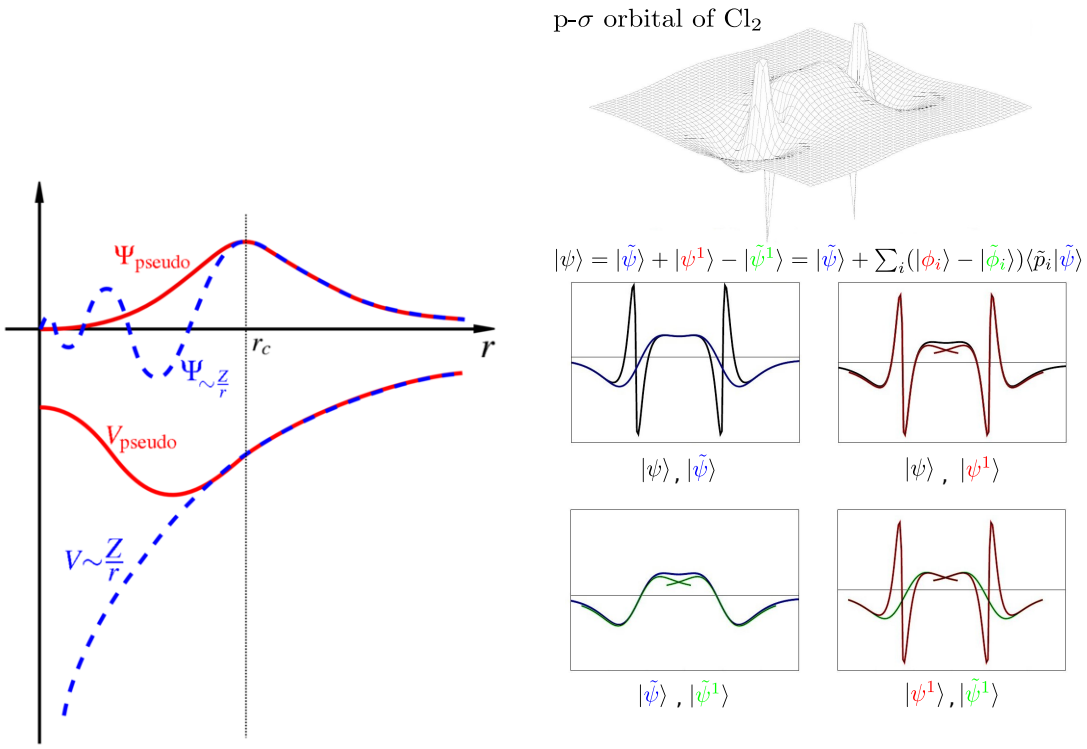

Figure 3.10: Left panel: Schematic representation of the space division into interstitial region ($r > r_c$) and augmentation region ($r < r_c$). The all-electron potential and the real wave function are in blue, the corresponding pseudo-values are in red. Right panel presents an example of the wave function decomposition in the PAW formalism for the $p\sigma$ orbital in Cl_2. The pseudo function $|\tilde{\psi}\rangle$ coincide with the true wave function $|\psi\rangle$ in the intersitial region and with $|\psi^1\rangle$ in the augmentation region. $|\psi^1\rangle$ and $|\tilde{\psi}^1\rangle$ correspond to the all electron and pseudo wave functions in the augmentation region which are expanded in atomic-like basis ($|\phi^1\rangle$ and $|\tilde{\phi}^1\rangle$), respectively.

In the PAW formalism, the all-electron wave function $|\psi_n\rangle$ is mapped onto pseudo wave function $|\tilde{\psi}_n\rangle$ by a linear transformation $\hat{T}$:

$$|\psi_n\rangle = \hat{T}\,|\tilde{\psi}_n\rangle\,, \tag{3.75}$$

where n is combined index that denotes both the band and the $\mathbf{k}$ wave vector indices. The functions $|\tilde{\psi}_n\rangle$ and $|\psi_n\rangle$ differ only in the regions around the ion cores, hence the transformation $\hat{T}$ must be different from the identity by a sum of local, atom-centred contributions $\hat{T}^{\mathrm{I}}$ such that

$$\hat{T} = 1 + \sum_I \hat{T}^{\mathrm{I}}. \tag{3.76}$$

Each local contribution $\hat{T}^{\mathrm{I}}$ acts only within some augmentation region Ω^{I} enclosing the atom. This implies that the all-electron and pseudo-wave functions coincide outside the augmentation region.

To define the local terms $\hat{T}^{\mathrm{I}}$, the all-electron wave function is expanded into the all-electron partial waves $|\phi_i^{\mathrm{I}}\rangle$ within the region Ω^{I}. For each of the $|\phi_i^{\mathrm{I}}\rangle$ partial waves corresponds a smooth pseudo partial wave $|\tilde{\phi}_i^{\mathrm{I}}\rangle$ such that

$$|\phi_i^{\mathrm{I}}\rangle = (1 + \hat{T}^{\mathrm{I}})\,|\tilde{\phi}_i^{\mathrm{I}}\rangle\,, \tag{3.77}$$

and $|\phi_i^{\mathrm{I}}\rangle = |\tilde{\phi}_i^{\mathrm{I}}\rangle$ outside the augmentation region, Ω^{I}. Moreover, these pseudo partial waves should form a complete set within the augmentation region so that every pseudo wave function can be rewritten in the form

$$|\tilde{\psi}_n\rangle = \sum_i c_{i,n}^{\mathrm{I}}\,|\tilde{\phi}_{i,n}^{\mathrm{I}}\rangle\,, \tag{3.78}$$

where $c_{i,n}^{\mathrm{I}}$ are expansion coefficients to be determined. Using equations 3.75, 3.76 and 3.78 the all-electron wave function can be expressed as

$$|\psi_n\rangle = \hat{T}\,|\tilde{\psi}_n\rangle = \sum_{I,i,n} c_{i,n}^{\mathrm{I}}\,|\phi_{i,n}^{\mathrm{I}}\rangle\,, \tag{3.79}$$

with the same expansion coefficients $c_{i,n}^{\mathrm{I}}$. Because the transformation $\hat{T}$ is required to be linear, the coefficients $c_{i,n}^{\mathrm{I}}$ should be linear functionals of the pseudo wave function $|\tilde{\psi}_n\rangle$. Hence,

$$c_{i,n}^{\mathrm{I}} = \langle \tilde{p}_i^{\mathrm{I}} | \tilde{\psi}_n \rangle\,, \tag{3.80}$$

where $|\tilde{p}_i^{\mathrm{I}}\rangle$ are fixed projector functions. In the augmentation region, the projector functions must satisfy the relation

$$\sum_i |\tilde{\phi}_i^{\mathrm{I}}\rangle\,\langle \tilde{p}_i^{\mathrm{I}}| = 1, \tag{3.81}$$

and must obey orthogonality condition

$$\langle \tilde{p}_i^{\mathrm{I}} | \tilde{\phi}_j^{\mathrm{I}} \rangle = \delta_{ij}. \tag{3.82}$$

The projector functions are also localized within the augmentation region. Therefore, the transformation $\hat{T}$ can be rewritten as

$$\hat{T} = 1 + \sum_i (|\phi_i\rangle - |\tilde{\phi}_i\rangle) \langle \tilde{p}_i| \,, \tag{3.83}$$

where the index I was omitted for simplicity. The all-electron Kohn-Sham wave function can be evaluated from the pseudo wave functions as (see Fig. 3.10 for illustration)

$$|\psi_n\rangle = |\tilde{\psi}_n\rangle + \sum_i (|\phi_i\rangle - |\tilde{\phi}_i\rangle) \langle \tilde{p}_i | \, \tilde{\psi}_n\rangle. \tag{3.84}$$

What fallows from the eq. 3.84, the transformation between all-electron and pseudo-wave functions in the PAW formalism, is specified by:

- all-electron partial waves, $|\phi_i\rangle$, defined within the augmentation region which are calculated from the radial Schrödinger equation for the isolated atom and orthogonalized to the core states,
- pseudo partial waves, $|\tilde{\phi}_i\rangle$, which are expanded into plane waves,
- projectors, $|\tilde{p}_i\rangle$, localized within the augmentation region and related with each pseudo partial wave. The projectors are calculated as a radial function multiplied by spherical harmonics but then expanded into plane waves.

Expectation value of an operator

In the PAW method it is the pseudo function that is computed and hence the all-electron observables have to be expressed as the expectation values of the pseudo wave functions. This requires transforming the operators into pseudo operators. The details of derivation can be found in the Ref. 151, here only the final form is given. The expectation value of an $\langle A \rangle$ operator is defined as

$$\langle A \rangle = \sum_n f_n \langle \psi_n | A | \psi_n \rangle, \tag{3.85}$$

where f_n denotes the occupation of the state. Using the transformation $\hat{T}$ the expectation value of $\langle A \rangle$ can be calculated as

$$\langle A \rangle = \sum_n f_n \langle \tilde{\psi}_n | \tilde{A} | \tilde{\psi}_n \rangle. \tag{3.86}$$

In the case of local operators, the pseudo operator $\tilde{A}$ is defined as

$$\tilde{A} = \hat{T}^+ A \hat{T} = A + \sum_{i,j} |\tilde{p}_i\rangle \left(\langle \phi_i | \, A \, | \phi \rangle_j - \langle \tilde{\phi}_i | \, A \, | \tilde{\phi}_j \rangle \right) \langle \tilde{p}_j | \,. \tag{3.87}$$

Hence, the expectation value of an operator A is defined as

$$\langle A \rangle = \langle \tilde{\psi}_n | \, A \, | \tilde{\psi}_n \rangle + \sum_{i,j} \langle \tilde{\psi}_n | \tilde{p}_i \rangle \left(\langle \phi_i | \, A \, | \phi_j \rangle - \langle \tilde{\phi}_i | \, A \, | \tilde{\phi}_j \rangle \right) \langle \tilde{p}_j | \tilde{\psi}_n \rangle \,. \tag{3.88}$$

For a non-local operator an additional term ΔA has to be added to the above expression:

$$\Delta A = \sum_i |\tilde{p}_i\rangle \left(\langle\phi_i| - \langle\tilde{\phi}_i|\right) A \left(1 - \sum_j |\tilde{\phi}_j\rangle \langle\tilde{p}_j|\right) + \left(1 - |\tilde{p}_j\rangle \langle\tilde{\phi}_j|\right) A \left(|\phi_i\rangle - |\tilde{\phi}_i\rangle\right) \langle\tilde{p}_i| \,. \tag{3.89}$$

The above formula can be applied to the electron density operator $|\mathbf{r}\rangle \langle\mathbf{r}|$

$$\begin{aligned} n(\mathbf{r}) &= \tilde{n}(\mathbf{r}) + n^1(\mathbf{r}) - \tilde{n}^1(\mathbf{r}) \\ &= \sum_n f_n \langle\tilde{\psi}_n|\mathbf{r}\rangle \langle\mathbf{r}|\tilde{\psi}_n\rangle \\ &+ \sum_{i,j,n} f_n \langle\tilde{\psi}_n|\tilde{p}_i\rangle \langle\phi_i|\mathbf{r}\rangle \langle\mathbf{r}|\phi_j\rangle \langle\tilde{p}_j|\tilde{\psi}_n\rangle \\ &- \sum_{i,j,n} f_n \langle\tilde{\psi}_n|\tilde{p}_i\rangle \langle\tilde{\phi}_i|\mathbf{r}\rangle \langle\mathbf{r}|\tilde{\phi}_j\rangle \langle\tilde{p}_j|\tilde{\psi}_n\rangle \end{aligned} \tag{3.90}$$

In other words, the electron density $n(\mathbf{r})$ turns into plane wave part $\tilde{n}(\mathbf{r})$ and two atom-centred components $n^1(\mathbf{r})$ and $\tilde{n}^1(\mathbf{r})$.

Analogically, the total energy can be decomposed in the PAW formalism as

$$E = \tilde{E} + E^1 - \tilde{E}^1, \tag{3.91}$$

where the $\tilde{E}$ is the smooth part evaluated on a regular grid in a real or Fourier space, while E^1 and $\tilde{E}^1$ are sum of atomic contributions evaluated on radial grids in angular momentum representation. However, when we consider a form of particular energy terms it becomes more complicated. Let us start from the kinetic energy term which is straightforwardly written as

$$\begin{aligned} E_k &= \tilde{E}_k + E_k^1 - \tilde{E}^1 \\ &= \frac{1}{2} \sum_n f_n \langle\tilde{\psi}_n| - \nabla^2 |\tilde{\psi}_n\rangle \\ &+ \frac{1}{2} \sum_{i,j,n} f_n \langle\tilde{\psi}_n|\tilde{p}_i\rangle \langle\phi_i| - \nabla^2 |\phi_j\rangle \langle\tilde{p}_j|\tilde{\psi}_n\rangle \\ &- \frac{1}{2} \sum_{i,j,n} f_n \langle\tilde{\psi}_n|\tilde{p}_i\rangle \langle\tilde{\phi}_i| - \nabla^2 |\tilde{\phi}_j\rangle \langle\tilde{p}_j|\tilde{\psi}_n\rangle \,. \end{aligned} \tag{3.92}$$

The exchange-correlation part also fallows the relation 3.88 and the mean value of the exchange-correlation energy E_{xc} is

$$\begin{aligned} E_{xc} &= \tilde{E}_{xc} + E_{xc}^1 - \tilde{E}_{xc}^1 = \\ &= \int d\mathbf{r} \tilde{n}(\mathbf{r}) \epsilon_{xc}[\tilde{n}(\mathbf{r})] + \int d\mathbf{r} n^1(\mathbf{r}) \epsilon_{xc}[n^1(\mathbf{r})] - \int d\mathbf{r} \tilde{n}^1(\mathbf{r}) \epsilon_{xc}[\tilde{n}^1(\mathbf{r})]. \end{aligned} \tag{3.93}$$

The decomposition of the Hartree term according to the PAW formalism is more complicated since the Hartree energy includes interaction between the electron density within the augmentation and interstitial regions. Consequently, in order to transform

the Hartree energy to the PAW pseudo space a compensation charge density $\hat{n}$, localized in the augmentation region, is introduced. The compensation charge permits to cancel the long range interaction of electron density enclosed within the augmentation region and the outside. The details of the derivation can be found in Ref. 151, here only final expressions will be given. Thus, Hartree energy in the PAW method is decomposed as

$$E_{\mathrm{H}} = \tilde{E}_{\mathrm{H}} + E^{1}_{\mathrm{H}} - \tilde{E}^{1}_{\mathrm{H}}, \tag{3.94}$$

with

$$\tilde{E}_{\mathrm{H}} = \frac{1}{2}\int\int d\mathbf{r}d\mathbf{r}' \frac{[\tilde{n}(\mathbf{r}) + \hat{n}(\mathbf{r})][\tilde{n}(\mathbf{r}') + \hat{n}(\mathbf{r}')]}{|\mathbf{r} - \mathbf{r}'|}, \tag{3.95}$$

$$E^{1}_{\mathrm{H}} = \frac{1}{2}\int\int d\mathbf{r}d\mathbf{r}' \frac{[n^{1}(\mathbf{r}) + n^{Z}(\mathbf{r})][n^{1}(\mathbf{r}') + n^{Z}(\mathbf{r}')]}{|\mathbf{r} - \mathbf{r}'|}, \tag{3.96}$$

$$\tilde{E}^{1}_{\mathrm{H}} = \frac{1}{2}\int\int d\mathbf{r}d\mathbf{r}' \frac{[\tilde{n}^{1}(\mathbf{r}) + \hat{n}(\mathbf{r})][\tilde{n}^{1}(\mathbf{r}') + \hat{n}(\mathbf{r}')]}{|\mathbf{r} - \mathbf{r}'|}. \tag{3.97}$$

Effective Hamiltonian operator

The effective Kohn-Sham equations in the PAW formalism are given by

$$\tilde{H}\tilde{\psi}_n(\mathbf{r}) = \epsilon_n \tilde{O}\tilde{\psi}_n(\mathbf{r}), \tag{3.98}$$

where

$$\begin{aligned} \tilde{H} &= \hat{T}^{+} H \hat{T} = -\frac{1}{2}\nabla^2 + \tilde{V}_{eff} + \sum_{i,j} |\tilde{p}_i\rangle\, h_{i,j}\, \langle\tilde{p}_j|\,, \\ \tilde{O} &= \hat{T}^{+} O \hat{T} = 1 + \sum_{i,j} |\tilde{p}_i\rangle\, o_{i,j}\, \langle\tilde{p}_j|\,, \end{aligned} \tag{3.99}$$

have the form of a separable potential. The $h_{i,j}$ and $o_{i,j}$ are respectively

$$\begin{aligned} h_{i,j} &= \langle\phi_i| - \frac{1}{2}\nabla^2 + V_{eff}\,|\phi_j\rangle - \langle\tilde{\phi}_i| - \frac{1}{2}\nabla^2 + \tilde{V}_{eff}\,|\tilde{\phi}_j\rangle\,, \\ o_{i,j} &= \langle\phi_i|\phi_j\rangle - \langle\tilde{\phi}_i|\tilde{\phi}_j\rangle\,, \end{aligned} \tag{3.100}$$

and are evaluated for each atom on radial grids with spherical harmonics

3.3.5 Numerical atomic orbitals

In the previous subsections we have discussed how the Kohn-Sham equations can be solved using plane waves as a basis set. Another approach for the construction of the basis set is implemented in SIESTA and is based on localized atomic functions, particularly numerical atom-centred orbitals (NAOs). The atomic orbitals, $\phi_{\mathrm{I}nlm}(\mathbf{r})$, are the products of the radial function, $\phi_{\mathrm{I}nl}(\mathbf{r}_{\mathrm{I}})$, and the spherical harmonic, $Y_{lm}(\hat{\mathbf{r}}_{\mathrm{I}})$, centred at the site I at the position $\mathbf{R}_{\mathrm{I}}$

$$\phi_{\mathrm{I}nlm}(\mathbf{r}) = \phi_{\mathrm{I}nl}(r_{\mathrm{I}})Y_{lm}(\hat{\mathbf{r}}_{\mathrm{I}}), \tag{3.101}$$

where $\mathbf{r}_\mathrm{I} = \mathbf{r} - \mathbf{R}_\mathrm{I}$, n is the number of orbital and (l, m) label the angular momentum. The spherical harmonics reflect the symmetry of each orbital and are fixed analytical functions. The radial term is flexible and can be adapted for each system and each atomic species. One can also model the radial part analytically, using Slater or Gaussian orbitals. The NAOs are implemented in the SIESTA code which we used also for electronic transport. There can be several orbitals n with the same angular numbers, (l, m), but with different radial dependence, which are labelled '$multiple - \zeta$' basis. The radial functions are determined by a cubic spline interpolation from a values given on the fine radial mesh. Each radial function vanishes above some cutoff radius, r_c, defined for each function. Up to r_c the shape of the function is completely free and can be defined by the user. In the following, the implementation of NAO's within SIESTA will be described.

In the case of a minimal single-ζ basis set (one radial function per angular momentum) the most convenient and efficient method of construction is by finding the eigenfunctions of the isolated (pseudo-) atom confined within the spherical potential well[42,43] where the radius of the confining potential can be different for each orbital. However, in order to obtain a basis in which the effect of the confinement is similar for all the orbitals it is better to define a common energy shift $\delta\epsilon_l$ for all atoms and angular momentum. Hence, the radial functions $\phi_l(\mathbf{r})$ are numerical eigenfunctions of the atomic pseudopotential $V_l(r)$ for an energy $\epsilon_l + \delta\epsilon_l$

$$\left(-\frac{1}{2r}\frac{d^2}{dr^2}r + \frac{l(l+1)}{2r^2} + V_l(r)\right)\phi_l(r) = (\epsilon_l + \delta\epsilon_l)\,\phi_l(r), \tag{3.102}$$

with $\phi_l(\mathbf{r}_c) = 0$ (the indexes I and n were omitted for simplicity). The energy shift $\delta\epsilon_l$ is chosen to ensure that the first node of $\phi_l(\mathbf{r})$ occurs at the desired cutoff radius r_c. The $\delta\epsilon_l$ is defined by parameter PAO.EnergyShift (see below).

For generating multiple ζ basis, the method based on split-valence idea adjusted to the NAOs[41,42] is implemented. A numerical function $\phi_l^{2\zeta}(r)$ that reproduces the tail of the first $\phi_l^{1\zeta}(r)$ function outside radius $r_m < r_c$ is added. The $\phi_l^{2\zeta}(r)$ orbital continues smoothly towards the origin as $r^l(a_l - b_l r^2)$, thus

$$\phi_l^{2\zeta}(r) = \begin{cases} r^l(a_l - b_l r^2) & \text{if } r < r_m \\ \phi_l^{1\zeta}(r) & \text{if } r \geqslant r_m \end{cases}$$

with parameters a_l and b_l ensuring the continuity and the differentiability at r_m. These orbitals therefore combine the decay of the atomic eigenfunctions with a smooth behaviour inside r_m. Each step of constructing the basis set in SIESTA is schematically presented in Fig. 3.11. In order to improve the accuracy of the calculations and account for the deformation induced by bond formation one can add additional polarization orbitals with angular momentum $(l + 1)$.

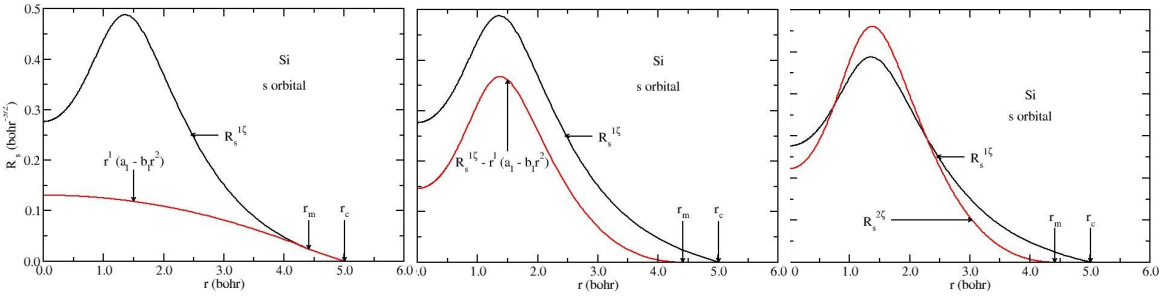

Figure 3.11: Generations of multiple-ζ basis in SIESTA with split valence method for Si. Left: we start from the 1-ζ function, defined inside radius r_c, we want to supplement. We define second radius r_m after which the 2-ζ reproduces the tail of the 1-ζ and continues smoothly towards the origin as $r^l(a_l - b_l r^2)$. Middle: We can define the function which is the difference between 1-ζ and the smooth function $r^l(a_l - b_l r^2)$. The same Hilbert space can be expanded but with the advantage that now 2-ζ vanishes at r_m. Right: Finally, the 2-ζ is normalized. The r_m is controlled by PAO.SplitNorm parameter. Figure adapted from Ref. 41.

Electron Hamiltonian

SIESTA combines numerical atomic orbitals with the NCPP method. The core electrons are replaced by norm-conserving pseudopotential in fully non-local Kleinman-Bylander form. Hence, the Kohn-Sham Hamiltonian can be written in the form

$$\hat{H} = \hat{T} + \sum_{\mathrm{I}} V_{\mathrm{I}}^{loc}(\mathbf{r}) + \sum_{\mathrm{I}} V_{\mathrm{I}}^{\mathrm{KB}}(\mathbf{r}) + V_{\mathrm{H}}(\mathbf{r}) + V_{xc}(\mathbf{r}), \tag{3.103}$$

where $\hat{T}$ is the kinetic energy operator, $V_{\mathrm{H}}(\mathbf{r})$ and $V_{xc}(\mathbf{r})$ are the Hartree and exchange-correlation potentials. The $V_{\mathrm{I}}^{loc}(\mathbf{r})$ and $\sum_{\mathrm{I}} V_{\mathrm{I}}^{\mathrm{KB}}(\mathbf{r})$ are the local and nonlocal (KB) parts of pseudopotential of atom I.

Before going further, the Hamiltonian can be first transformed in a way to eliminate the long range part of local potential V_{I}^{loc} centred at ion I. The long range part can be screened by the potential V_{I}^{atom} created by the atomic electron density n_{I}^{atom} which is calculated based on basis wave functions of the valence electrons. The screened neutral atom I is then represented by the potential V_{I}^{NA} of the form

$$V_{\mathrm{I}}^{NA} = V_{\mathrm{I}}^{loc} + V_{\mathrm{I}}^{atom}. \tag{3.104}$$

Moreover, since basis functions are zero beyond some cutoff radius r_c, also the V_{I}^{NA} is zero in the region beyond r_c. If we define the difference between the self-consistent electron density and the sum of the atomic densities such that

$$\delta n(\mathbf{r}) = n(\mathbf{r}) - \sum_{\mathrm{I}} n_{\mathrm{I}}^{atom}(\mathbf{r}). \tag{3.105}$$

The $\delta n(\mathbf{r})$ represents the electronic density modifications due to creation of chemical bonds and the charge transfer between atoms. The $\delta n(\mathbf{r})$ creates the electrostatic potential $\delta V_{\mathrm{H}}(\mathbf{r})$ which allows to reformulate the initial Hamiltonian as

$$\hat{H} = \hat{T} + \sum_{\mathrm{I}} V_{\mathrm{I}}^{\mathrm{KB}}(\mathbf{r}) \sum_{\mathrm{I}} V_{\mathrm{I}}^{NA}(\mathbf{r}) + \delta V_{\mathrm{H}}(\mathbf{r}) + V_{xc}(\mathbf{r}). \tag{3.106}$$

As a consequence all the potentials in the above Hamiltonian are short-range ones. The matrix elements of the first two terms include two-centre integrals which are evaluated in reciprocal space and interpolated for various interatomic distances. The remaining terms are calculated on a three dimensional real-space grid[42] and the fineness of this grid is controlled by a 'grid cutoff' parameter. The potentials $V_{\mathrm{I}}^{NA}(\mathbf{r})$ are tabulated as a function of the distance to atoms I and simply interpolated at any desired grid point. The last two terms require the calculation of the electron density on the grid.

Definition of basis set

The main advantage of the NAO's is their efficiency since the number of basis functions is usually quite small.[43] However, the price to pay is the lack of systematic for convergence. In contrast to plane wave methods there is no unique way for increasing the basis set size, also the rate of convergence depends on the way the basis is enlarged. Below, are the main parameters which define the basis set with their default values indicated.

Basis size:	PAO.BasisSize	DZP
Range of first-zeta:	PAO.EnergyShift	0.02 Ry
Second-zeta:	PAO.BasisType	Split
Range of second-zeta:	PAO.SplitNorm	0.15

One can also specify explicitly the basis set with the required orbitals and cutoff values for each of them in the block %block PAO.Basis. A basis constructed for valence states of oxygen atom in our calculations is presented below as an example.

```
%block PAO.Basis                    # Define Basis set
  O        2                        # Species label, number of l-shells
  n = 2   0    2                   # n, l, Nzeta
        6.0   0.0                   # rc (first-zeta), rm (second zeta)
        1.0   1.0                   # scaling factors
  n = 2   1    2                   # n, l, Nzeta
        6.0   0.0                   # rc (first-zeta), rm (second zeta)
        1.0   1.0                   # scaling factors
%endblock PAO.Basis
```

Here, n and l denote the principal and the angular quantum numbers. The value of r_m is not specified so it is calculated from PAO.SplitNorm. Similarly, if r_c is not defined it is obtained based on PAO.EnergyShift value. Analogically, basis for valence states of Mg and Fe were constructed. Split-valence bases for Mg and O of double-ζ type for s and p orbitals with the cutoff radii of 6.0 a.u. were constructed. For Fe, double-ζ for $4s$ and single-ζ for $4p$ and $3d$ orbitals with cutoff radii 5.6 a.u. for $4s$ and $4p$ and 5.2 a.u. for $3d$ orbitals were used. The cutoff radii of the second-ζ is determined based on the split norm parameter equal 0.2 Ry. The electronic temperature is set to 300 K (smearing parameter). A mesh cutoff defining the real-space grid for calculating the potential and the electron density was set to 600 Ry. These parameters are based

on previous theoretical studies concerning transport through similar Fe/V/MgO/Fe junction.[152] Because of lack of systematic convergence of the basis set we decided to start with the basis that was already tested. Nonetheless, we have tried to test also other types of basis and the examples of DOSs for Fe are shown in Fig. 3.12. On the right, we compare basis sets that were used in two different articles. The first one was already described by Feng *et. al.*[152] and the second one basis by Garcia-Suarez *et al.*[153] with the configuration of DZP-SZ-DZ for $4s$, $4p$ and $3d$ orbitals respectively and $r_c = 6$ a.u. for each orbital. The r_m is calculated from split norm parameter set to 0.39 Ry. As it can be seen, the basis used in both articles gave practically the same shape of DOS which is comparable with Fig. 3.2. However, when we switch to DZ and DZP basis (right panel), generated automatically by SIESTA with split norm 0.39 Ry and energy shift 0.2 Ry, the difference is significant. When we compared the resulting basis set parameters it turned out that for automatically generated basis set the cutoff radius for the orbitals is smaller namely 4.3 a.u. for the $4s$ orbital and 2.4 a.u. for the $3d$ orbital. This example demonstrates how changes in initial parameters can modify the results. For a better comparison all plots were shifted to a common zero energy Fermi level.

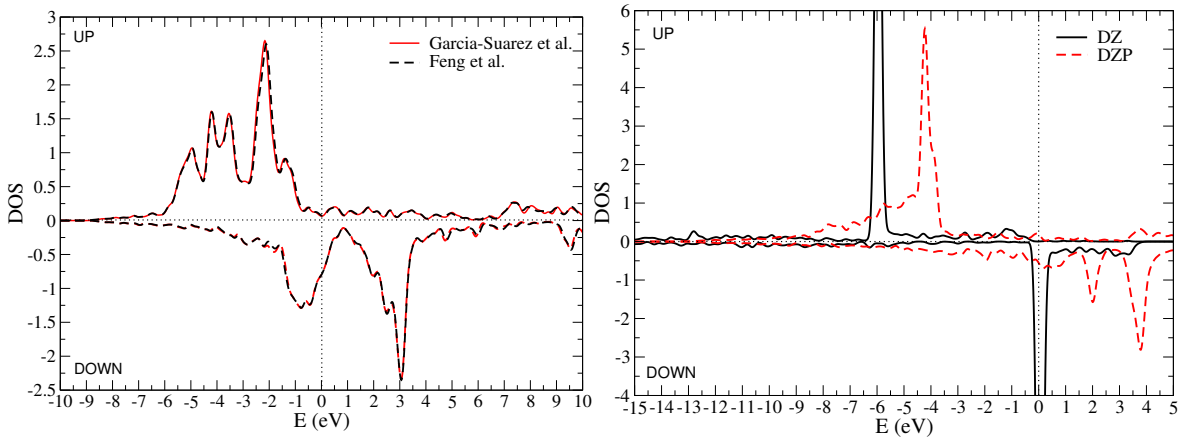

Figure 3.12: Comparison of basis sets generated with SIESTA for Fe. Left panel: basis taken from Garcia-Suarez *et al.*[153] with DZP-SZ-DZ for $4s$, $4p$ and $3d$ orbitals, respectively and $r_c = 6$ a.u. for each orbital, and *Feng et al.*[152] with the configuration DZ-SZ-SZ for $4s$, $4p$ and $3d$ orbitals, respectively and $r_c = 5.6$ a.u. for $4s$ and $4p$ orbitals and 5.2 a.u. for $3d$. Right panel: DZ and DZP basis generated automatically in SIESTA with only $4s$ and $3d$ states included. Lattice constant of Fe $a_{\mathrm{Fe}} = 2.86$ Å is used.

It is important to stress that the SIESTA basis set is not complete and we cannot describe all the highest states well enough as with a plane wave basis. Of course, one can increase the number of orbitals, use multiple-ζ or add polarization orbitals, but this increases time of the calculations and does not necessarily guarantee a better convergence. Especially, as in our work, if we go from bulk MgO and Fe, for which the tests were done, to much bigger junctions with many atoms per supercell. Therefore, some choices have to be made. We want to calculate afterwords the electric transport through Fe/MgO/Fe junctions and what matters for us is that the DOS is reproduced accurately especially at the vicinity of the Fermi level.

The basis set is not the only factor which influences the convergence of the calculations. Other important parameters are: a scheme used for mixing the density from one iteration to another, the proportion between old and new density which are mixed, the smearing parameter (in SIESTA referred as electronic temperature) and k-point mesh type which can be either Γ centered or not. Again, there is no systematic way to choose combination of these parameters to improve the convergence. Thus, one has to try to adjust them for the system at hand. In our case, these parameters were tested on ideal Fe(7ML)/MgO(5ML)/Fe(6ML) junctions with the lateral size equal to MgO lattice constant $a_{\mathrm{MgO}} = 4.242$ Å. In structures like this the additional difficulty is that different types of materials are involved, namely an insulator and a ferromagnetic metal, for which requirements concerning the choice of k-point grid, smearing and mixing parameters are different. Therefore, after some tests, we used in transport calculations Pulay mixing scheme where the new density is mixed with the old one after 8 iterations and a mixing weight of 0.05. The choice of the k-point grid will be discussed in the part concerning the electronic transport since the electrodes and scattering region have to be tested separately.

3.3.6 Summary

In conclusion, in this chapter the DFT method for solving the many-body electron problem was presented. The mathematical basics of DFT are given by Hohenberg-Kohn theorems and the practical implementation is based on the Kohn-Sham equations. The crucial step in defying the Kohn-Sham equations is the assumption that the interacting system can be mapped on the noninteracting one with the same density. As a result, the equation to solve, is the one-electron Schrödinger-like equation with an effective potential incorporating all the interactions in the system. However, the DFT formalism still needs some approximations and choices to be made before solving the Kohn-Sham equations. These are summarized at the schema below.

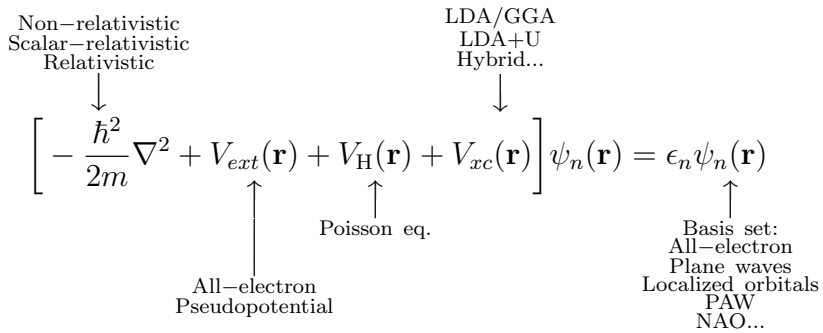

The practical solution of the many-body problem, even after a series of approximations, is not an easy task. Nonetheless, due to efficient algorithms, massive parallelization and use of the supercomputers, DFT calculations can be performed for systems of hundreds of atoms with great accuracy. Within the work presented in this thesis the results were obtained using three different codes, VASP[37,38] implementing the PAW method, Quantum-Espresso (QE)[39,40] using a plane wave basis set with the pseudopotential (NCPP, USPP) or the PAW method and less extensively the SIESTA package[41–43] which combines the NAO basis with the NCPP.

4 Ballistic transport

In this chapter the basic principles of quantum transport in nano-devices will be explained. Classically, transport phenomena obeys Ohm's law where a current is a linear function of the applied voltage. However, when the size of the device becomes smaller and it is comparable to the electron wavelength quantum effects begin to manifest. The most crucial factor which defines the electric conductance is related to the scattering properties of a device. Landauer was the first to develop a formalism connecting the device scattering properties to the conductance. Here, the main aspects of his derivation and the extension of the formalism by Büttiker will be described. These formulas are further implemented in two codes that are used in this thesis, the PWcond and the TranSIESTA. In both codes, the current through the device is evaluated within Landauer-Büttiker formalism by using different techniques to calculate the transmission. In PWcond a flux of electrons is injected onto the scattering region of a device, and a probability for each state to be either transmitted or reflected is evaluated. In TranSIESTA a different philosophy is adapted namely one can consider explicitly the system with open boundary conditions, and treat the non-equilibrium conditions caused by the applied voltage using the Keldysh formalism with the non-equilibrium Green function. Both of these approaches will be described in the following sections.

4.1 Landauer-Büttiker formalism

The electronic transport in a macroscopic conductor respects Ohm's law where the conductance G can be calculated knowing the material's conductivity σ and geometry as

$$G = \sigma \frac{A}{L}, \tag{4.1}$$

where A is the cross section and L the length of the conductor. This relation is valid only if the transport regime is *diffusive*, i.e. the dimensions of a metallic sample are

larger than the electron mean free path l_m and the electron motion can be compared to a random walk. When the size of a metallic contact is decreased and becomes comparable or smaller than the electron mean free path, $L < l_m$, the electronic transport turns into the *ballistic* regime. When the contact cross-section approaches the size of an atom we enter in the quantum transport regime. For example, for metallic contacts at the nanometer scale the quantum mechanical nature of charge carriers has to be included to obtain reliable predictions about the conductance.

Landauer was the first to give a description of the electronic transport in the ballistic quantum regime.[44,45] He linked the conductance of a nanocontact to the transmission probability of an electron at the Fermi level to traverse a device. He considered however only one propagating state. An extension of the theory to multiplechannel was made by Buttiker and the theory is called now as the Landauer-Buttiker. In this approach a nanocontact is modelled as a scattering region with metallic leads connected on each side to infinite electrodes which serve as reservoirs of electrons (Fig. 4.1). Each of the electrodes has a well defined chemical potential denoted as μ_{L} and μ_{R} for the left and the right electrode respectively. Inside the leads, the electrons can be described as propagating Bloch waves along the longitudinal direction, while in the perpendicular directions due to lateral confinement their momentum is quantized. As a consequence, when a small bias is applied between the reservoirs, the current is driven by a finite number of left- and right moving modes. The number of modes allowed by the lateral confinement depends on the size of the metallic leads in the transverse directions, i.e. in the limit of an infinitesimal cross section, only one transverse mode would be allowed and there will be only one channel available for charge transport.

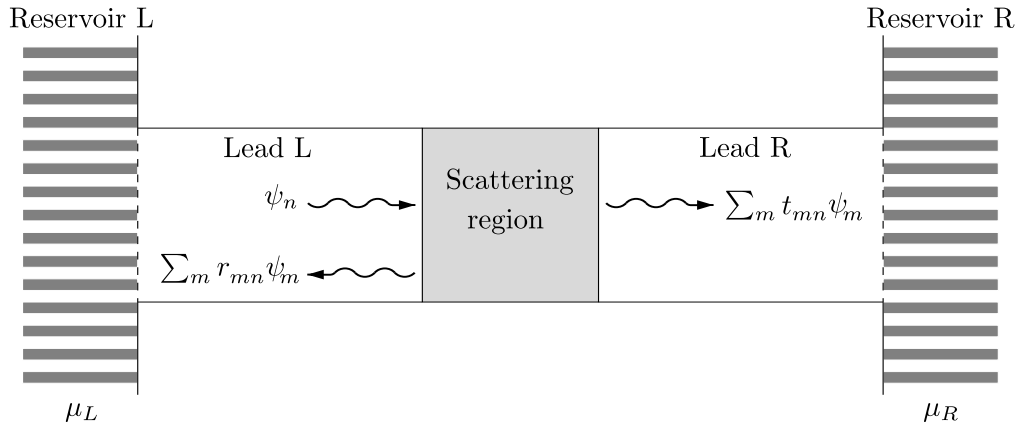

Figure 4.1: Representation of a model conductor for ballistic transport calculations within the Landauer-Buttiker formalism. A scattering region with two leads is attached to the electrons reservoirs characterized by two chemical potentials, μ_{L} and μ_{R}. An incoming wave ψ_n can be transmitted into wave ψ_m of the Lead R with a probability t_{mn} and reflected into state ψ_m of the Lead L with a probability r_{mn}. Adapted from Ref. 154.

To derive the Landauer-Büttiker formula for the conductance some assumptions have to be made: 1) the two reservoirs inject uncorrelated electrons into the device region at their own chemical potentials, 2) the difference of the chemical potential of the left μ_{L} and right μ_{R} leads is such that $\mu_{\mathrm{L}} - \mu_{\mathrm{R}} \to 0$, i.e. we are working in the

limit of the linear response, 3) the outgoing electrons can be injected into the reservoirs without any additional back-scattering, thus the reservoirs act as perfect absorbers for electrons. Landauer originally considered the transport of only one Bloch state coming form the electron reservoir. Hence, the current, for the two spin directions, emitted by the left reservoir in the energy range between two chemical potentials ($\mu_{\mathrm{L}} - \mu_{\mathrm{R}}$) is

$$I = \frac{ev_k}{L}\left(\frac{dn}{dE}\right)(\mu_{\mathrm{L}} - \mu_{\mathrm{R}}), \tag{4.2}$$

where $v_k = \frac{1}{\hbar}\frac{\partial E_k}{\partial k}$ is the group velocity, and $\frac{dn}{dE}$ is the DOS for the carriers with positive velocity ($+k$). The DOS can be rewritten in terms of v_k as

$$\frac{dn}{dE} = \frac{\partial n}{\partial k}\frac{\partial k}{\partial E_k} = \frac{L}{hv_k}, \tag{4.3}$$

and therefore the current becomes

$$I = \frac{e}{h}(\mu_{\mathrm{L}} - \mu_{\mathrm{R}}). \tag{4.4}$$

Next, we can define the voltage across the sample as $eV = \mu_{\mathrm{L}} - \mu_{\mathrm{R}}$ so the conductance is written as

$$G = \frac{I}{V} = \frac{2e^2}{h} = G_0, \tag{4.5}$$

where the factor 2 takes into account the spin and G_0 is the so called the *quantum of conductance*. This formula shows that even in the case of a perfect conductor with reflection-less electrodes there is a finite resistance which for a single-mode conductor is equal to $G_0^{-1} = 12.9\ \mathrm{k\Omega}$.[46] Moreover, since this result arises due to cancellation between group velocity and the DOS one can expect the conductance quantum to be independent on the DOS or the band dispersion of the propagating electron, i.e. both s and d electrons can give the same contribution to the current regardless of their own dispersion.

$$f_{\mathrm{L}}(E - \mu_{\mathrm{L}}) = \left[e^{(E-\mu_{\mathrm{L}})/k_BT} + 1\right]^{-1}, \tag{4.6}$$

and the right reservoir with probability

$$f_{\mathrm{R}}(E - \mu_{\mathrm{R}}) = \left[e^{(E-\mu_{\mathrm{R}})/k_BT} + 1\right]^{-1}. \tag{4.7}$$

The net current flowing from the left electrode to the right electrode is now

$$I = \frac{2e}{h}\int \left(f_{\mathrm{L}}(E - \mu_{\mathrm{L}}) - f_{\mathrm{R}}(E - \mu_{\mathrm{R}})\right) dE. \tag{4.8}$$

If the reservoirs have the same chemical potentials, $\mu_{\mathrm{L}} = \mu_{\mathrm{R}} = E_{\mathrm{F}}$, the current vanishes because the electronic distribution in both reservoirs becomes equal to the Fermi distribution function f_0 for the system at equilibrium

$$f_0(E - E_{\mathrm{F}}) = \left[e^{(E-E_{\mathrm{F}})/k_BT} + 1\right]^{-1}. \tag{4.9}$$

In the *linear regime*, when a small bias $\delta V = (\mu_{\mathrm{L}} - \mu_{\mathrm{R}})/e$ is applied, the resulting current δI is proportional to δV and the ballistic conductance becomes

$$G = \frac{\delta I}{\delta V} = \frac{2e^2}{h} \int \left(-\frac{\partial f_0}{\partial E} \right) dE, \tag{4.10}$$

where

$$-\frac{\partial f_0}{\partial E} \cong \frac{f_{\mathrm{L}}(E - \mu_{\mathrm{L}}) - f_{\mathrm{R}}(E - \mu_{\mathrm{R}})}{\mu_{\mathrm{L}} - \mu_{\mathrm{R}}}, \tag{4.11}$$

is the derivative of the equilibrium Fermi distribution function. In the limit of low temperatures f_0 and its first derivative can be approximated with

$$f_0 \approx -\theta(E_{\mathrm{F}} - E), \qquad -\frac{\partial f_0}{\partial E} \approx \delta(E_{\mathrm{F}} - E), \tag{4.12}$$

where θ is the step function and δ the Dirac distribution, and therefore the conductance will be given by eq. 4.5.

Because in the central region the electrons can be scattered we can introduce a probability T(E) for an electron with energy E for being transmitted into the lead at the opposite side and a probability R(E) for being reflected, such that T(E) + R(E) = 1. Therefore, the formula for the current in eq. 4.8 can be generalized to[46]

$$I = \frac{2e}{h} \int T(E) \left(f_{\mathrm{L}}(E - \mu_{\mathrm{L}}) - f_{\mathrm{R}}(E - \mu_{\mathrm{R}}) \right) dE. \tag{4.13}$$

The difference $\mu_{\mathrm{L}} - \mu_{\mathrm{R}}$ between the left and right chemical potentials was assumed to be small enough so that the energy dependence of T and R within this energy range can be neglected and the conductance can be evaluated just at the Fermi energy as

$$G = \frac{2e^2}{h} T(E_{\mathrm{F}}). \tag{4.14}$$

The above formula shows that, within the linear regime, the conductance can be obtained by evaluating the transmission coefficient at the Fermi energy. In the limiting case, for single-mode ideal conductor, the mode is perfectly transmitted and $T(E_{\mathrm{F}}) = 1$ which gives the quantum of conductance G_0.

The more general formalism, extended to multiple mode transmission was proposed by Büttkier.[47] Here, each mode can be partially reflected and partially transmitted into itself or into other modes (Fig. 4.1). Let's assume that for a given energy we have M_{L} modes active in the left lead and M_{R} modes active in the right lead. An incoming wave from the left n-th channel has a probability T_{mn} of being transmitted into the m-th channel on the other side of the scatterer and R_{mn} of being reflected to the m-th channel on the same side of the scatterer. The analogue quantities for states coming from the right electrode can be also defined and are denoted by primes. The amplitudes of incoming and outgoing modes are connected by the so-called *scattering matrix* $\mathbf{S}$ of the form

$$\mathbf{S} = \begin{bmatrix} [\mathbf{s}_{11}] & [\mathbf{s}_{12}] \\ [\mathbf{s}_{21}] & [\mathbf{s}_{22}] \end{bmatrix} = \begin{bmatrix} [\mathbf{r}] & [\mathbf{t}'] \\ [\mathbf{t}] & [\mathbf{r}'] \end{bmatrix}.$$

To illustrate how this matrix is constructed let's consider an example where we have three propagating modes in total as schematically presented in Fig. 4.2. The coefficients

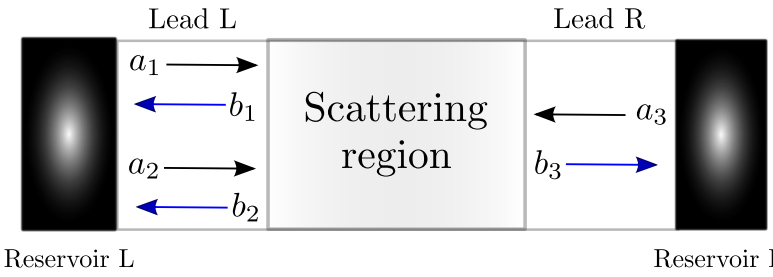

Figure 4.2: A device preserving coherent transport and characterized by a scattering matrix at each energy. The scattering matrix relates the incoming mode amplitudes a to the outgoing mode amplitudes b.

a_1, a_2, a_3 correspond to the amplitudes of incoming waves while b_1, b_2, b_3 correspond to the outgoing or reflected waves. Therefore, the incoming and the outgoing waves are connected by the relation

$$\begin{bmatrix} b_1 \\ b_2 \\ b_3 \end{bmatrix} = \begin{bmatrix} s_{11} & s_{12} & s_{13} \\ s_{21} & s_{22} & s_{23} \\ s_{31} & s_{32} & s_{33} \end{bmatrix} \begin{bmatrix} a_1 \\ a_2 \\ a_3 \end{bmatrix} = \begin{bmatrix} r_{11} & r_{12} & t'_{13} \\ r_{21} & r_{22} & t'_{23} \\ t_{31} & t_{32} & r'_{33} \end{bmatrix} \begin{bmatrix} a_1 \\ a_2 \\ a_3 \end{bmatrix}.$$

The size of the S-matrix is defined by the number of propagating modes available for a given energy. If we denote the total number of propagating modes as M_{T} then it will be equal simply to $M_{\mathrm{T}} = M_{\mathrm{L}} + M_{\mathrm{R}}$, and the size of the **S**-matrix is $M_{\mathrm{T}} \times M_{\mathrm{T}}$. The transmission probability of an incoming mode n to the mode m $T_{m\leftarrow n}$ is obtained by taking the squared magnitude of the corresponding element of the **S**-matrix

$$T_{m\leftarrow n} = |s_{m\leftarrow n}|^2 \tag{4.15}$$

The total transmission of electrons from the left electrode to the right one is then evaluated as

$$\overline{T}_{R\leftarrow L} = \sum_{m\in R,\ n\in L} T_{m\leftarrow n}, \tag{4.16}$$

and analogically, the transmission from the right electrode to the left is given by

$$\overline{T}_{L\leftarrow R} = \sum_{n\in L,\ m\in R} T_{n\leftarrow m}. \tag{4.17}$$

The arrows in the subscripts are here just to indicate that the direction of propagation is backwards from the second script to the first one. These arrows will be skipped for simplicity.

An important property of the **S**-matrix is that it has to be unitary in order to ensure current conservation and the following relation between the matrix blocks **r** and **t** holds

$$\mathbf{r}^\dagger\mathbf{r} + \mathbf{t}^\dagger\mathbf{t} = \mathbf{I}, \tag{4.18}$$

as well as analogous expressions for blocks $\mathbf{r}'$ and $\mathbf{t}'$. A proof of this can be found in Ref. 46 (sec. 3.1) and will not be reproduced here. The unitary of the **S**-matrix also

implies that in terms of the matrix elements we have

$$\sum_{m=1}^{M_{\mathrm{T}}} |s_{mn}|^2 = 1 = \sum_{m=1}^{M_{\mathrm{T}}} |s_{nm}|^2. \tag{4.19}$$

The first relation is obvious since it represents the sum of the transmission probabilities for a given incoming mode n over all possible output modes m. This sum must be equal one since the current must be conserved so an incoming electron must to go somewhere. The second relation is not that obvious because we sum the transmission probabilities over all possible input for a fixed output state. Nonetheless, both results follow the unitarity of the **S**-matrix which is necessary for current conservation.

The total conductance, from the left to the right electrode generalized to multi-channel situation, is now written as

$$G = \frac{2e^2}{h} \sum_m T_{mn} = \frac{2e^2}{h} \sum_m |t_{mn}|^2 = \frac{2e^2}{h} Tr[tt^\dagger]. \tag{4.20}$$

What is important to be noticed is, to ensure unitarity of the **S**-matrix and validity of above formula for the conductance, the scattering matrix elements s_{mn} have to be defined as the ratio between normalized amplitudes, i.e. for modes carrying unitary current. The way of calculating the **S**-matrix and the normalized coefficient as it is implemented in PWcond will be presented in the next subsection.

4.2 Ballistic transport calculations in PWCOND

In this part the method implemented in PWcond and which we used to compute the scattering matrix will be presented. The coefficients of the **S**-matrix can be evaluated by solving the scattering problem where the electron transport is assumed to occur in an open quantum system containing a scattering region connected on both sides to semi-infinite electrodes. The electrodes have a perfect periodic crystalline structure while the scattering region can contain any kind of defects and all the reflection and transmission processes take place inside it. The solution method is based on the solution of the Kohn-Sham equations with USPP and a plane wave basis set as developed in the work of Smogunov *et al.*[40] Originally, the NCPP were used as proposed by Choi and Ihm,[155] however as describe before NCPP are less suitable for describing localized d valence electrons.

The Bloch scattering state Ψ for the whole system, including the leads and the scattering region, is a solution of the Kohn-Sham equations of the form

$$\left[-\nabla^2 + V_{eff} + \widehat{V}_{\mathrm{NL}}\right] |\Psi\rangle = E\widehat{S} |\Psi\rangle \,, \tag{4.21}$$

where V_{eff} is an effective local potential and $\widehat{V}_{\mathrm{NL}}$ denotes the non-local part of USPP

$$\widehat{V}_{\mathrm{NL}} = \sum_{I,mn} D^{\mathrm{I}}_{mn} |\beta^{\mathrm{I}}_m\rangle \langle\beta^{\mathrm{I}}_n| \,. \tag{4.22}$$

We can rewrite eq. 4.21 in more suitable form, without the overlap operator on the right hand side, as

$$\left[-\nabla^2 + V_{eff} + \widehat{V}'_{\mathrm{NL}}\right] |\Psi\rangle = E\,|\Psi\rangle\,, \tag{4.23}$$

where D^{I}_{mn} is replaced by $\tilde{D}^{\mathrm{I}}_{mn} = D^{\mathrm{I}}_{mn} - Eq^{\mathrm{I}}_{mn}$ and $\widehat{V}'_{\mathrm{NL}}$ is written as before but using new coefficients.

We assume that the electron transport is along the z direction and the scattering region is restricted to the region $0 < z < L$ and is connected to the semi-infinite left at $z < 0$ and right lead at $z > L$. The effective potential V_{eff}, the screened USPP coefficients D^{I}_{mn} and the q^{I}_{mn} are obtained in the previous self-consistent calculations where the supercell includes the scattering region with part of the leads on both sides. In the xy plane the supercell is repeated periodically, thus in this plane the electronic states can be written in the usual Bloch form

$$\Psi(\mathbf{r}_\perp + \mathbf{R}_\perp, z) = e^{i\mathbf{k}_\perp \mathbf{R}_\perp}\Psi(\mathbf{r}_\perp, z), \tag{4.24}$$

where $\mathbf{r}_\perp = (x, y)$ and $\mathbf{R}_\perp = n_1\mathbf{a}_1 + n_2\mathbf{a}_2$. Noticing that for a particular energy E, different $\mathbf{k}_\perp$ are independent, any scattering state can be classified according to the value of $\mathbf{k}_\perp$ and expanded in x and y directions using plane waves as

$$\Psi_{\mathbf{k}_\perp}(\mathbf{r}_\perp, z) = \sum_{\mathbf{G}_\perp} \Psi_{\mathbf{k}_\perp}(\mathbf{G}_\perp, z) e^{i(\mathbf{G}_\perp + \mathbf{k}_\perp)\cdot\mathbf{r}_\perp}. \tag{4.25}$$

The sum over $\mathbf{G}_\perp$ includes all the plane waves in the expansion and defines the 2D basis set with N_{2D} elements.

The vectors $\mathbf{R}$ of the direct lattice can be separated in the component of the perpendicular 2D-lattice $\mathbf{R}_\perp$ and part denoting the position of nucleus I within the supercell $\mathbf{R}_{\mathrm{I}}$ as $\mathbf{R} = \mathbf{R}_\perp + \mathbf{R}_{\mathrm{I}}$. Then, the non-local part of the potential can be expressed as

$$\widehat{V}_{\mathrm{NL}}\,|\Psi_{\mathbf{k}_\perp}\rangle = \sum_{\mathrm{I},mn} \tilde{D}^{\mathrm{I}}_{mn}\,\langle\beta^{\mathrm{I}}_n|\Psi_{\mathbf{k}_\perp}\rangle \left(\sum_{\mathbf{R}_\perp} e^{i\mathbf{k}_\perp\cdot\mathbf{R}_\perp}\beta^{\mathrm{I}}_m(\mathbf{r} - \mathbf{R}_\perp - \mathbf{R}_{\mathrm{I}})\right), \tag{4.26}$$

since the following relation holds

$$\langle\beta^{\mathrm{I}}_n|\Psi_{\mathbf{k}_\perp}\rangle = e^{i\mathbf{k}_\perp\cdot\mathbf{R}_\perp}\,\langle\beta^{\mathrm{I}}_n|\Psi_{\mathbf{k}_\perp}\rangle\,, \tag{4.27}$$

and the coefficients $\tilde{D}^{\mathrm{I}}_{mn}$ are independent of $\mathbf{R}_\perp$. For simplicity we can make the following definitions

$$\begin{aligned} P_{\mathrm{I}m}(\mathbf{r}) &\equiv \sum_{\mathbf{R}_\perp} e^{i\mathbf{k}_\perp\cdot\mathbf{R}_\perp}\beta^{\mathrm{I}}_m(\mathbf{r} - \mathbf{R}_\perp - \mathbf{R}_{\mathrm{I}}), \\ C^{\mathbf{k}_\perp}_{\mathrm{I}m} &\equiv \sum_n \tilde{D}^{\mathrm{I}}_{mn}\,\langle\beta^{\mathrm{I}}_n|\Psi_{\mathbf{k}_\perp}\rangle\,, \end{aligned} \tag{4.28}$$

and state that for the transport calculations the energy is a fixed input parameter. The Kohn-Sham equations can then be rewritten as

$$\left[-\nabla^2 + V_{eff} - E\right]|\Psi_{\mathbf{k}_\perp}\rangle + \sum_{\mathrm{I}m} P_{\mathrm{I}m}C^{\mathbf{k}_\perp}_{\mathrm{I}m} = 0, \tag{4.29}$$

where the sum over Im includes projectors associated to the atomic centers inside the supercell.

The above equation has to be satisfied by the scattering wave function for the whole system. Now, for a given $\mathbf{k}_\perp$-point the scattering state with energy E, that originates from a right-moving Bloch state ψ_k, incoming from $z = -\infty$ is expressed as

$$\Psi_{\mathbf{k}_\perp} = \begin{cases} \psi_k + \sum_{k' \in L} r_{k'k}\psi_{k'}, & z \leq 0 \\ \sum_n c_n \phi_n(\mathbf{r}) + \sum_{\mathrm{I}m} c_{\mathrm{I}m}\phi_{\mathrm{I}m}(\mathbf{r}), & 0 \leq z \leq L \\ \sum_{k' \in R} t_{k'k}\psi_{k'}, & z \geq L \end{cases}$$

where the sum over $k' \in L$ ($k' \in R$) includes all Bloch waves $\psi_{k'}$ propagating or decaying to the left (right) in the left (right) lead. These propagating and decaying Bloch states create the complex band structure of a solid.

The procedure of solving equation 4.29 and determining the scattering wave function $\Psi_{\mathbf{k}_\perp}$ is then performed separately for the electrodes and the scattering region and the complete solution is constructed by matching wave functions at the interfaces between the central region and the electrodes.

The electrons move ballistically in the self-consisted potential, obtained from ground state DFT calculations for the scattering region, where reflection and transmission are restricted only to the scattering region. Periodic boundary conditions are applied in the x and y directions and electrons wave function in this plane have a Bloch form and can be classified with $k_\perp$ index. Different $k_\perp$ do not mix and can be treated separately.

Electrode region

Within the leads, the scattering states have the usual Bloch form in the xy plane, where the periodicity is present (eq. 4.24) while along the z axis, without translational symmetry, they satisfy the condition

$$\psi_k(\mathbf{r}_\perp, z + d) = e^{ikd}\psi_k(\mathbf{r}_\perp, z), \tag{4.30}$$

with k being in general a complex number and d the length of the electrode unit cell in the z direction of the corresponding bulk crystal. The wave functions ψ_k with $\mathrm{Im}k = 0$ and $\mathrm{Im}k \neq 0$ correspond to propagating and decaying states, respectively.

The ψ_k can be obtained from the general solution of eq. 4.29 inside a unit cell of the leads, i.e. $z_0 < z < z_0 + L$, and written as a linear combination of two kinds of terms

$$\psi_k(\mathbf{r}) = \sum_n c_{n,k}\phi_n(\mathbf{r}) + \sum_{\mathrm{I}m} c_{\mathrm{I}m,k}\phi_{\mathrm{I}m}(\mathbf{r}). \tag{4.31}$$

The first term on the right hand side includes ϕ_n, which are linearly independent solutions of the homogenous equation associated to eq. 4.29 of the form

$$\left[-\nabla^2 + V_{eff}(\mathbf{r}) - E\right]|\phi_n\rangle = 0, \tag{4.32}$$

and the second term contain the $\phi_{\mathrm{I}m}$ which are particular solutions of the inhomogeneous equation

$$\left[-\nabla^2 + V_{eff}(\mathbf{r}) - E\right]|\phi_{\mathrm{I}m}\rangle + P_{\mathrm{I}m} = 0. \tag{4.33}$$

Both ϕ_n and $\phi_{\mathrm{I}m}$ are periodic in the xy plane and the summation over Im in eq. 4.31 is over all the projectors in the unit cell of the lead.

The function 4.31 is a solution of eq. 4.29 if the coefficients $c_{Im,k}$ are equal

$$c_{\mathrm{I}m,k} = \sum_n \tilde{D}^{\mathrm{I}}_{mn} \langle \beta^{\mathrm{I}}_n | \psi_k \rangle \,. \tag{4.34}$$

Furthermore, the allowed values of k at a given energy E are found by imposing the condition in eq. 4.30 along z to the ψ_k and its z-derivative

$$\psi_k(\mathbf{r}_\perp, z+d) = e^{i\mathbf{k}_k d}\psi_k(\mathbf{r}_\perp, z), \tag{4.35}$$

$$\psi_k^{'}(\mathbf{r}_\perp, z+d) = e^{i\mathbf{k}_k d}\psi_k^{'}(\mathbf{r}_\perp, z_0). \tag{4.36}$$

Inserting eq. 4.31 into eqs. 4.34-4.36 leads to a generalized eigenvalue problem

$$AX = e^{ikd}BX, \tag{4.37}$$

where A and B are two general complex matrices. The above equation is solved to evaluate a complex band structure and generalized Bloch state ψ_k at a given energy E and $\mathbf{k}_\perp$. The size of the matrices A and B is equal to $N_{2D} \times N_{2D}$. The obtained eigenstates vectors $X = \{c_{n,k}, c_{\mathrm{I}m,k}\}$, which contain the coefficients required to calculate the scattering state ψ_k as defined in eq. 4.31.

Scattering region and wave function matching

Analogically, the scattering state $\Psi_{\mathbf{k}_\perp}$ within the central region, $0 < z < L$ can be written as

$$\Psi_{\mathbf{k}_\perp}(\mathbf{r}) = \sum_n c_n \phi_n(\mathbf{r}) + \sum_{\mathrm{I}m} c_{\mathrm{I}m}\phi_{\mathrm{I}m}(\mathbf{r}), \tag{4.38}$$

where $\phi_n(\mathbf{r})$ and $\phi_{\mathrm{I}m}(\mathbf{r})$ are solutions of eq. 4.32 and 4.33, respectively, restricted to the scattering region. The coefficients $c_{\mathrm{I}m}$ are then given by

$$c_{\mathrm{I}m} = \sum_n \tilde{D}^{\mathrm{I}}_{mn} \langle \beta^{\mathrm{I}}_n | \Psi_{\mathbf{k}_\perp} \rangle \,. \tag{4.39}$$

Moreover, the coefficients corresponding to the nonlocal spheres intersecting the boundaries of the scattering region and shared with the electrodes, have also to satisfy for the spheres intersecting the plane $z = 0$

$$c_{\mathrm{I}m,k} + \sum_\beta r_{k'k} c_{\mathrm{I}m,k'} = \sum_n \tilde{D}^{\mathrm{I}}_{mn} \langle \beta^{\mathrm{I}}_n | \Psi_k \rangle = c_{\mathrm{I}m}, \tag{4.40}$$

and for sphere intersecting the plane $z = L$

$$\sum_{k'} t_{k'k} c_{\mathrm{I}m,k'} = \sum_n \tilde{D}^{\mathrm{I}}_{mn} \langle \beta^{\mathrm{I}}_n | \Psi_k \rangle = c_{\mathrm{I}m}. \tag{4.41}$$

The last three equations, in addition to the standard matching conditions for the wave function and its derivative at the boundary planes, give a set of linear algebraic equations which are solved to obtain the unknown coefficients $\{c_n, c_{\mathrm{I}m}, r_{k'k}, t_{k'k}\}$.

Conductance calculations

The last step is to evaluate the scattering matrix and the conductance. In order to fulfil the unitary condition in eq. 4.18, the $t_{kk'}$ coefficients have to be normalized as $t'_{kk'} = \sqrt{I_k/I_{k'}}t_{kk'}$, where I_k is the current carried by the propagating Bloch state ψ_k. The expression for a current flowing through a plane S perpendicular to the z axis and located at z_0 written using the USPP approach is

$$I_k^0 = 2Im\left[\int_S d\mathbf{r}_\perp \psi_k^*(\mathbf{r}_\perp, z_0)\frac{\partial\psi_k(\mathbf{r}_\perp, z)}{\partial z}\bigg|_{z=z_0}\right]. \tag{4.42}$$

The above formula is valid only if the plane does not cross any nonlocal atomic sphere. A more general formula, valid for any z_0 is then given as

$$I_k = I_k^0 - 2Im\left[\sum_{I,mn}\tilde{D}^{\mathrm{I}}_{mn}\langle\beta^{\mathrm{I}}_n|\psi_k\rangle\int_{-\infty}^{z_0}dz\int_S d\mathbf{r}_\perp\beta^{\mathrm{I}}_m(\mathbf{r}-\mathbf{R}_{\mathrm{I}})\psi_k^*(\mathbf{r})\right]. \tag{4.43}$$

Having the current one can define the normalized coefficients and build the $t^\dagger t$ matrix which is used to get the ballistic conductance of the system through the equation

$$G = G_0 T = \sum_{k'k}|T_{k'k}|^2 = Tr[\mathbf{T}^\dagger\mathbf{T}], \tag{4.44}$$

where T is the matrix of normalized transmission amplitudes $T_{k'k} = \sqrt{I_{k'}/I_k}\cdot t_{k'k}$

An important point to notice is that the above formula assumes that the current operator is diagonal in the basis of Bloch states. However, this is not always the case. A mixing between states might occur if there are degenerate states with the same k in z direction, e.g. states coming from atomic p_x, p_y or d_{xz},d_{yz} levels if the system has an axial symmetry around z axis. As a consequence, before calculating the conductance, the Bloch states have to be orthogonalized with respect to the current operator as

$$\begin{aligned} I_{kl} = I_{kl}^0 + i\sum_{I,mn}\tilde{D}^{\mathrm{I}}_{mn}\times\Big[&\langle\beta^{\mathrm{I}}_n|\psi_l\rangle\int_{-\infty}^{z_0}dz\int_S d\mathbf{r}_\perp\beta^{\mathrm{I}}_m(\mathbf{r}-\mathbf{R}_{\mathrm{I}})\psi_k^*(\mathbf{r}) - \\ &\langle\beta^{\mathrm{I}}_n|\psi_k\rangle\int_{-\infty}^{z_0}dz\int_S d\mathbf{r}_\perp\beta^{\mathrm{I}}_m(\mathbf{r}-\mathbf{R}_{\mathrm{I}})\psi_l^*(\mathbf{r})\Big], \end{aligned} \tag{4.45}$$

where

$$I_{kl}^0 = -i\int_S d\mathbf{r}_\perp\left[\psi_k^*(\mathbf{r}_\perp, z_0)\frac{\partial\psi_l(\mathbf{r}_\perp, z)}{\partial z}\bigg|_{z=z_0} - \frac{\partial\psi_k(\mathbf{r}_\perp, z)}{\partial z}\bigg|_{z=z_0}\psi_l(\mathbf{r}_\perp, z_0)\right]. \tag{4.46}$$

To summarized, the ballistic conductance is evaluated in three steps:

1. The supercell DFT electronic structure calculations are performed with plane wave PWscf code to obtain the self-consistent potential V_{eff} and the screened coefficients D^{I}_{mn}. In the case of spin polarized calculations both values will depend on the spin of the electron.

2. Complex band structure of the infinite electrodes is evaluated and propagating Bloch states are orthogonalized with respect to the current operator using Eq. 4.45.

3. The transmission coefficients t_{mn} are calculated for each rightward propagating state ψ_k of the left electrode and then the total transmission T is obtained.

Test case - Al monoatomic wire

Before calculating the transmission for Fe/MgO/Fe junctions we wanted to make sure that the PWCOND compilation we are using is correct and program works properly. Thus, we have performed simple test calculations with examples provided with the QE distribution and compared our results with the reference data. We present here a case of a monoatomic Al nanowire without and with H atom adsorbed as shown in Fig. 4.3. The scheme indicates also a division of the simulation cell into the bulk-like part of the electrode used for the complex band calculations (unit cell) and the scattering region.

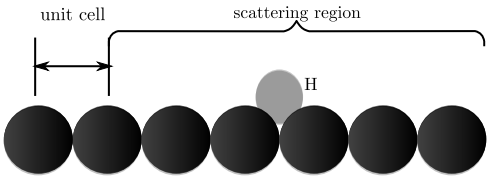

Figure 4.3: Scheme of an Al wire with H impurity. Unit cell denotes the part used in complex band structure lead calculations. The scattering region contains part with the impurity and also part of the leads.

In Fig. 4.4 we compare our results for Al wires with the reference data. The left panel compares the complex band structures for the monoatomic Al wire obtained with the unit cell defined in Fig. 4.3. The right panel shows the transmission as a function of energy for an ideal Al wire and a wire with H as an impurity. We don't want to discuss any physical properties of such wires or make any interpretation of the results. What is important for us in this example is that our results match exactly the reference ones and that PWCOND works properly. We can now proceed with the calculations of Fe/MgO/Fe junctions.

Convergence parameters

In order to calculate the transmission as implemented in the PWCOND one has to define the scattering region and the bulk-like electrodes. The definition of the bulk-like electrode part is easy since one has to use the smallest possible unit cell corresponding to the crystal structure of the electrode that matches the scattering region. In our case with Fe electrodes, which were rotated to fit the MgO structure, we have 4 atoms of Fe in the unit cell which give two layers of Fe along the z direction as shown in Fig. 4.5. In the scattering region we can vary the number of MgO layers without any particular restrictions, except maybe the computational cost. But we should also include a part

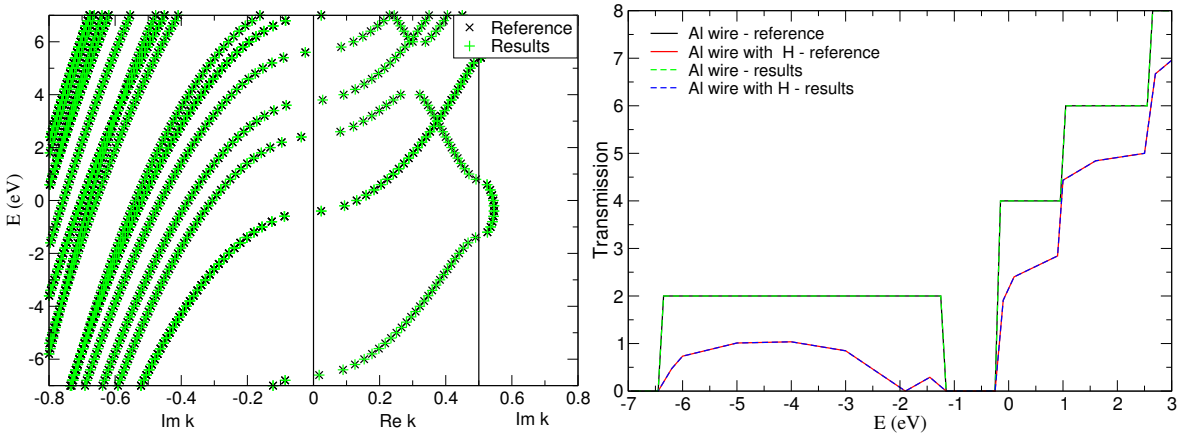

Figure 4.4: Test case of Al wire with and witouth H impurity. The plots compare our with the reference data.

of the leads on each side of the MgO spacer. The question is how many electrode layer should be in the scattering region? To answer this we have studied the changes of the electrostatic potential in the scattering region. To guarantee that the electron wave function changes smoothly at the interface between the electrode and the scattering region, the part of the leads in the scattering region has to be big enough so that the changes induced in the electrostatic potential due to interaction with MgO are screened within the scattering region. If not, we will have an artificial potential that scatters the incoming electrons and might affect the results.

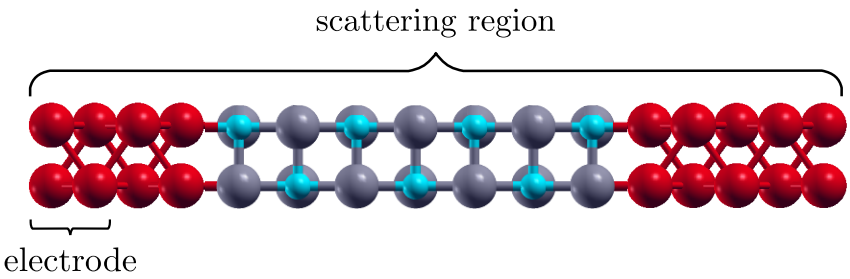

Figure 4.5: Geometry of Fe/MgO/Fe junction used in our work. The scattering region consists of varying number of MgO layers attached always to 4 and 5 ML of Fe on the left and on the right side, respectively. In the electrode bulk calculations we used unit cell with 2 Fe layers along the z direction.

In Fig. 4.6 we compare the total electrostatic potential for the scattering region with 4 and 5 ML of Fe on each side of MgO (see Fig. 4.5) with the total potential of the bulk electrode. We can clearly noticed changes in the Fe potential at the interface induced by MgO. From the 2nd-3rd ML of Fe the bulk electrostatic potential is restored. In order to guarantee also a proper geometry matching of the scattering region and the electrodes, we ended up wit 4 ML of Fe on the left side of MgO and 5 ML of Fe on the right side. For the defect calculations we just doubled the lateral size of the junctions. When the antiparallel alignment of the electrodes was considered the size of the junction also along the z direction was doubled such that the composition of the supercell was Fe(P)/MgO/Fe(AP)/MgO/F(P). That was necessary to avoid direct

interactions between parallel and anitparralel electrode alignment when the periodic boundary conditions are applied.

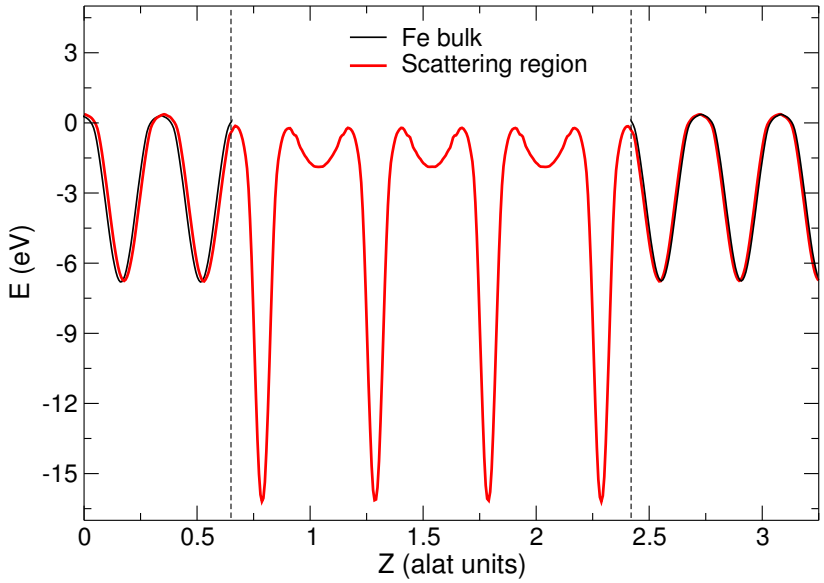

Figure 4.6: Comparison of the total electrostatic potential of bulk Fe and that of the scattering region. Dashed lines indicate the two interfaces between Fe and MgO in the scattering region.

One more important factor is the convergence of the 2D basis set used in the calculations. There two parameters controlling the basis set: (i) *ewind* which defines the energy window for reducing the 2D plane wave basis set in the transverse XY plane, and (ii) *epsproj* which is a threshold for the 2D basis set reduction. The default values for the two are $ewind = 1Ry$ and $epsproj = 0.001$. Generally, the larger *ewind* and the smaller *epsproj* the higher the accuracy of the calculations. At the same time, with increasing accuracy the computational cost increases and one has to find a compromise between these factors. One more parameter to take into account is *nz1* which defines the number of subslabs in the slab for the numerical calculation of various integrals. Again, the bigger *nz1* the higher accuracy, and the default vale is *nz1=11*. All these parameters were tested by calculating the complex band structure of bulk Fe and MgO. Fig. 4.7 presents changes of the real and the complex bands with values of *ewind*, *esproj* and $nz1$ as indicated. The difference in the band structure can be noticed between the $ewind = 1$, $esproj = 3$, $nz1 = 5$ and $ewind = 3$, $esproj = 5$, $nz1 = 11$. Further increase of these parameters does not change any more the band structures for both Fe and MgO. Therefore, we have used $ewind = 3$, $esproj = 5$, $nz1 = 11$ in further calculations.

The transmission was evaluated and plotted as a function of k-points in the 2D BZ. Therefore, the k-point mesh has also to be converged. We have tested meshes of 20×20, 30×30, 50×50 and 80×80 k-points. We decided to keep the 50×50 mesh since the last two meshes gave well defined shapes of transmission curves and considering computational cost the variety of structures we believe it is the best choice.

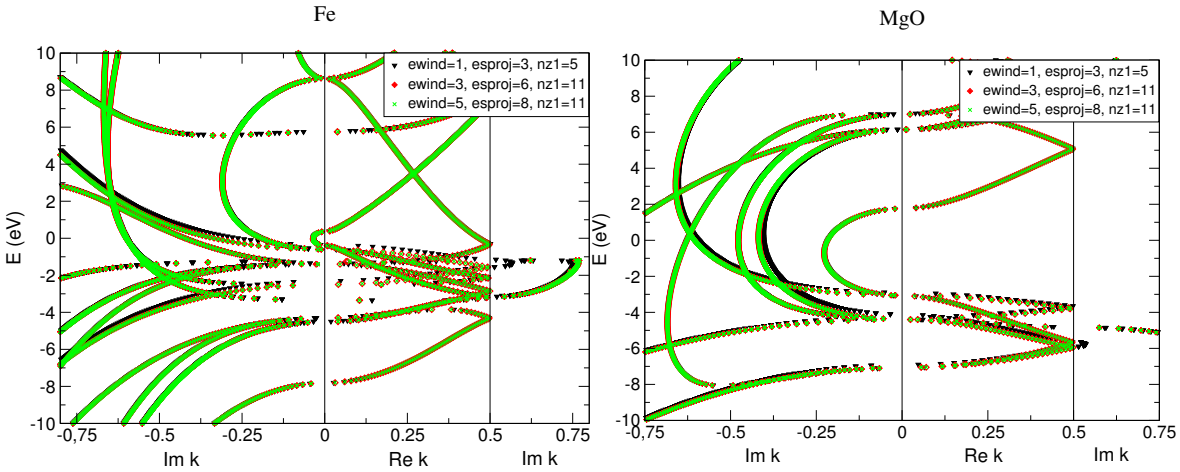

Figure 4.7: Comparison of complex band structure for Fe (left) and MgO (right) for different choices of *ewind*, *esproj* and $nz1$ parameters. The results are well converged with values $ewind = 3$, $esproj = 5$, $nz1 = 11$ which were used in further calculations.

4.3 Ballistic transport calculation in TranSIESTA

An alternative method for calculating the conductance using the Landauer-Büttiker formalism is based on Keldysh formalism in conjunction with the non-equilibrium Green function technique. The starting point is again dividing the system into the central region coupled on the left and on the right to semi-infinite metallic leads. This time however, instead of diagonalizing the Hamiltonian matrix to obtain the scattering states, one uses the non-equilibrium Green function to evaluate the current through a device. In the case of non-interacting systems and coherent transport regime the so called single-particle Green function can be used. In this part the basic concepts needed for understanding the Green function technique will be given and the manner it is used for calculating the transmission. The full derivation of Landauer-Büttiker formula within the Green function framework can be found elsewhere.[156,157] Here, only the final expressions for calculating the current within the Green function technique will be given.

4.3.1 Single particle Green function

The single-particle Green function, $\mathbf{G}^0(\epsilon)$, for a system of non-interacting particles is defined as a solution of the Schrödinger equation in the form

$$[\epsilon \pm i\eta - \mathbf{H}]\,\mathbf{G}^0(E) = \mathbf{I}, \tag{4.47}$$

where η an infinitesimal number such that $\eta \to 0^+$ and the Green function is simply obtained by the matrix inversion

$$\mathbf{G}^0(\epsilon) = \frac{1}{(\epsilon \pm i\eta)\mathbf{I} - \mathbf{H}}. \tag{4.48}$$

It is clear that η is added in order to avoid singularities in the denominator when the energy ϵ coincide with the eigenvalue ϵ_n of the Hamiltonian. We can distinguish now

two types of Green functions: the *retarded* Green function defined as

$$\mathbf{G}^{0,R}(\epsilon) = \lim_{\eta \to 0^+} G^0(\epsilon + i\eta - H)^{-1}, \tag{4.49}$$

and *advanced* Green function

$$\mathbf{G}^{0,A}(\epsilon) = \lim_{\eta \to 0^+} G^0(\epsilon - i\eta - H)^{-1}. \tag{4.50}$$

In the following we will use only the retarded Green function $\mathbf{G}^R$ where the superscript will be skipped for simplicity.

To illustrate how the Green function is constructed we can consider a simple two-level system without interactions described by the Hamiltonian

$$H = \begin{pmatrix} \epsilon_1 & 0 \\ 0 & \epsilon_2 \end{pmatrix},$$

for which the corresponding Green function is easily found to be

$$\mathbf{G}^0(\epsilon) = \frac{1}{(\epsilon + i\eta - \epsilon_1)(\epsilon + i\eta - \epsilon_2)} \begin{pmatrix} \epsilon + i\eta - \epsilon_2 & 0 \\ 0 & \epsilon + i\eta - \epsilon_1 \end{pmatrix}.$$

Consequently, the $\mathbf{G}^0(\epsilon)$ function has to obey the same boundary conditions as the eigenfunctions ψ_n of the Hamiltonian. If we consider a system with periodic boundary conditions, as before in DFT method, the Hamiltonian eigenvalues are $\mathbf{k}$-point dependent and now also the Green function has dependence on $\mathbf{k}$. Hence, the $\mathbf{G}^0_\mathbf{k}$ can be rewritten in terms of $\psi_{n\mathbf{k}}$

$$\mathbf{G}^0_\mathbf{k}(\epsilon) = \sum_n \frac{|\psi_{n\mathbf{k}}\rangle \langle \psi_{n\mathbf{k}}|}{\epsilon + i\eta - \epsilon_{n\mathbf{k}}}. \tag{4.51}$$

It is instructive to split the Green function into the real and imaginary part

$$\begin{aligned} \mathrm{Re}\mathbf{G}^0_\mathbf{k}(\epsilon) &= \sum_n \frac{|\psi_{n\mathbf{k}}|^2 \mathcal{L}_{n\mathbf{k}}(\epsilon)(\epsilon - \epsilon_{n\mathbf{k}})}{\eta}, \\ \mathrm{Im}\mathbf{G}^0_\mathbf{k}(\epsilon) &= -\sum_n |\psi_{n\mathbf{k}}|^2 \mathcal{L}_{n\mathbf{k}}(\epsilon), \\ \mathcal{L}_{n\mathbf{k}}(\epsilon) &\equiv \frac{\eta}{(\epsilon - \epsilon_{n\mathbf{k}})^2 + \eta^2}, \end{aligned} \tag{4.52}$$

where for $\eta \to 0^+$ a Lorentzian function $\mathcal{L}_{n\mathbf{k}}(\epsilon)$ is infinitely narrow δ-like function with an area of π and full with at half maximum 2η.

Once the Green function for a system at hand is calculated we have access to its physical properties, such as the density of states (DOS), which is given now by

$$\mathrm{DOS}(\epsilon) = \frac{-1}{\pi} \mathrm{Tr}\left[\mathrm{Im}\mathbf{G}^0_\mathbf{k}(\epsilon)\right], \tag{4.53}$$

and the projected density of states (LDOS)

$$\mathrm{LDOS}(\epsilon) = \frac{-1}{\pi} \mathrm{Im}\mathbf{G}^0_{\mathbf{k}\{ii\}}(\epsilon), \tag{4.54}$$

at a local site i.

The greatest advantage of the Green function formalism is that one can obtain the physical properties of any system without explicitly calculating its eigenvectors and hence avoiding the diagonalization of the Hamiltonian matrix. Naively, one would expect that the Green functions are not suitable for periodic systems since now to calculate the DOS a double integral, over E and $\mathbf{k}$, is required instead of an integral just over $\mathbf{k}$. However, the Green function technique posses other methods to overcome such difficulties, in particular the *self energy* term which is introduced to describe the coupling of the system with the external environment. The concept of the self energy and its importance in the conductance calculation is described in the following.

4.3.2 System with interactions

Let's now consider a situation where we introduce a perturbation $\mathbf{V}$ to the single particle Green function and defined the perturbed Green function $\mathbf{G}$ as

$$[(\epsilon + i\eta)\mathbf{I} - \mathbf{H} - \mathbf{V}]\,\mathbf{G} = \mathbf{I}. \tag{4.55}$$

By rearranging the above equation and using Eq. 4.47 we get

$$\begin{aligned} [(\epsilon + i\eta)\mathbf{I} - \mathbf{H}]\,\mathbf{G} &= \mathbf{I} + \mathbf{V}\mathbf{G} \\ \mathbf{G} &= \mathbf{G}^0 + \mathbf{G}^0\mathbf{V}\mathbf{G}, \end{aligned} \tag{4.56}$$

which is known as the *Dyson* equation. The perturbation $\mathbf{V}$ can be of any kind, i.e. local impurity, neighbouring cell, infinite bulk etc. To understand the usefulness of this construction let's consider once more two level system but this time with interactions between the states, which are treated as a perturbation, hence the corresponding operators are

$$\mathbf{H} = \begin{pmatrix} \epsilon_1 & 0 \\ 0 & \epsilon_2 \end{pmatrix}, \qquad \mathbf{V} = \begin{pmatrix} 0 & t \\ t & 0 \end{pmatrix}.$$

We can start with the perturbation of $\mathbf{H}_{11}$ due to the neighbouring site $\mathbf{H}_{22}$ and write it as

$$\mathbf{G}_{11} = \mathbf{G}^0_{11} + \mathbf{G}^0_{11}\mathbf{V}_{12}\mathbf{G}_{21} \tag{4.57}$$

and from the matrix product in Eq. 4.56 we can write $\mathbf{G}_{21} = \mathbf{G}^0_{22}\mathbf{V}_{21}\mathbf{G}_{11}$ and insert

$$\begin{aligned} \mathbf{G}_{11} &= \mathbf{G}^0_{11} + \mathbf{G}^0_{11}\mathbf{V}_{12}\mathbf{G}^0_{22}\mathbf{V}_{21}\mathbf{G}_{11}, \\ \mathbf{G}_{11} &= \left[\epsilon + i\eta - \epsilon_1 - \mathbf{V}_{12}\mathbf{G}^0_{22}\mathbf{V}_{21}\right]^{-1}, \\ \mathbf{G}_{11} &\equiv \left[\epsilon + i\eta - \epsilon - \Sigma(E)\right]^{-1}, \end{aligned} \tag{4.58}$$

where $\Sigma(E) = \mathbf{V}_{12}\mathbf{G}^0_{22}\mathbf{V}_{21}$ is the so called self-energy term with en energy dependence due to $\mathbf{G}_{22}$. The self energy can be understood in terms of two aspects, 1) the eigenstate energies are re-normalized due to an external perturbation and, 2) the energy levels are broadened due to the coupling with an external perturbation and have therefore a finite life time.[156]

The above procedure can be extended to more complex systems, like in our case to junction coupled to the electrodes. Again we divide the system into a central part,

containing the spacer and a part of the leads, connected on both sides to the semi-infinite electrodes (see Fig. 4.1). We assume here that the central region is big enough and there is no interaction between electrodes whatsoever. The full Hamiltonian of the considered structure is a block matrix in the form

$$\mathbf{H} = \begin{pmatrix} \mathbf{H}_{\mathrm{L}} & \mathbf{V}_{\mathrm{LC}} & 0 \\ \mathbf{V}_{\mathrm{CL}} & \mathbf{H}_{\mathrm{C}} & \mathbf{V}_{\mathrm{CR}} \\ 0 & \mathbf{V}_{\mathrm{RC}} & \mathbf{H}_{\mathrm{R}} \end{pmatrix}$$

where $\mathbf{H}_{\mathrm{L}}$ and $\mathbf{H}_{\mathrm{R}}$ describe respectively the left and right electrodes, $\mathbf{H}_{\mathrm{C}}$ the central region, $\mathbf{V}_{\mathrm{CL}}(\mathbf{V}_{\mathrm{CR}})$ the coupling between the central region and left (right) electrode. The Hamiltonian should be Hermitian so that the following relations hold: $V_{\mathrm{CL}} = V_{\mathrm{LC}}^{\dagger}$ and $V_{\mathrm{CR}} = V_{\mathrm{RC}}^{\dagger}$. The Eq. 4.55 can be rewritten as

$$\begin{pmatrix} E - \mathbf{H}_{\mathrm{L}} & -\mathbf{V}_{\mathrm{LC}} & 0 \\ -\mathbf{V}_{\mathrm{LC}}^{\dagger} & E - \mathbf{H}_{\mathrm{C}} & -\mathbf{V}_{\mathrm{RC}}^{\dagger} \\ 0 & -\mathbf{V}_{\mathrm{RC}} & E - \mathbf{H}_{\mathrm{R}} \end{pmatrix} \begin{pmatrix} \mathbf{G}_{\mathrm{L}}^{0} & \mathbf{G}_{\mathrm{LC}} & 0 \\ \mathbf{G}_{\mathrm{CL}} & \mathbf{G}_{\mathrm{C}}^{0} & \mathbf{G}_{\mathrm{CR}} \\ 0 & \mathbf{G}_{\mathrm{RC}} & \mathbf{G}_{\mathrm{R}}^{0} \end{pmatrix} = \mathbf{I}$$

where $\mathbf{E} = (\epsilon + i\eta)\mathbf{I}$. In a more general situation, if we use atomic orbitals as a basis set and assume that the basis functions are not orthogonal an overlap matrix $\mathbf{S}$ should be introduced instead of $\mathbf{I}$. Nonetheless, we can proceed using only $\mathbf{I}$ without any loss of generality. The goal now is to find the system Green function $\mathbf{G}_{\mathrm{C}}$ which will define all quantities of interest. From the matrix equation 4.3.2 we have

$$\begin{aligned} (\mathbf{E} - \mathbf{H}_{\mathrm{L}})\mathbf{G}_{\mathrm{LC}} - \mathbf{V}_{\mathrm{LC}}\mathbf{G}_{\mathrm{C}}^{0} &= 0, \\ -\mathbf{V}_{\mathrm{LC}}^{\dagger}\mathbf{G}_{\mathrm{LC}} + (\mathbf{E} - \mathbf{H}_{\mathrm{C}})\mathbf{G}_{\mathrm{C}}^{0} - \mathbf{V}_{\mathrm{RC}}^{\dagger}\mathbf{G}_{\mathrm{RC}} &= \mathbf{I}, \\ -\mathbf{V}_{\mathrm{RC}}\mathbf{G}_{\mathrm{C}}^{0} + (\mathbf{E} - \mathbf{H}_{\mathrm{R}})\mathbf{G}_{\mathrm{RC}} &= 0. \end{aligned} \tag{4.59}$$

From the first and the third equations one obtains

$$\begin{aligned} \mathbf{G}_{\mathrm{LC}} &= (\mathbf{E} - \mathbf{H}_{\mathrm{L}})^{-1}\mathbf{V}_{\mathrm{LC}}\mathbf{G}_{\mathrm{C}}^{0}, \\ \mathbf{G}_{\mathrm{RC}} &= (\mathbf{E} - \mathbf{H}_{\mathrm{R}})^{-1}\mathbf{V}_{\mathrm{RC}}\mathbf{G}_{\mathrm{C}}^{0}, \end{aligned} \tag{4.60}$$

and by substituting it into the second equation we get

$$\mathbf{G}_{\mathrm{C}}^{0} = \left[\mathbf{E} - \mathbf{H}_{\mathrm{C}}^{0} - \Sigma_{\mathrm{L}}(E) - \Sigma_{\mathrm{R}}(E)\right]^{-1}, \tag{4.61}$$

where again Σ denotes the self-energy term describing the coupling between the central region and the left (right) electrodes. The self-energy terms are expressed as

$$\begin{aligned} \Sigma_{\mathrm{L}}(E) &= (\mathbf{E} - \mathbf{V}_{\mathrm{LC}}^{\dagger})\frac{1}{(\mathbf{E} - \mathbf{H}_{\mathrm{L}})}(\mathbf{E} - \mathbf{V}_{\mathrm{LC}}), \\ \Sigma_{\mathrm{R}}(E) &= (\mathbf{E} - \mathbf{V}_{\mathrm{RC}}^{\dagger})\frac{1}{(\mathbf{E} - \mathbf{H}_{\mathrm{R}})}(\mathbf{E} - \mathbf{V}_{\mathrm{RC}}). \end{aligned} \tag{4.62}$$

An important feature of the Green function method is that the solution of a system under an external perturbation requires only the self-energy of the perturbation. As it was mentioned the self energy can be interpreted as a broadening of the energy levels due to the coupling with the external perturbation, or as the discussed case, with the

leads. This is schematically presented in Fig. 4.8. If the central region is isolated the eigenstates of $\mathbf{H}_{\mathrm{C}}$ are well defined energy spectrum of the Hamiltonian and an electron at a particular energy state has a finite probability to tunnel to the left and the right electrodes. If however, the coupling between the electrodes and the central region is included, the discrete states of the isolated sample broaden into resonances and their energy is shifted or renormalized. At the same time an electron acquires a finite lifetime to scatter from the central region into the electrodes.

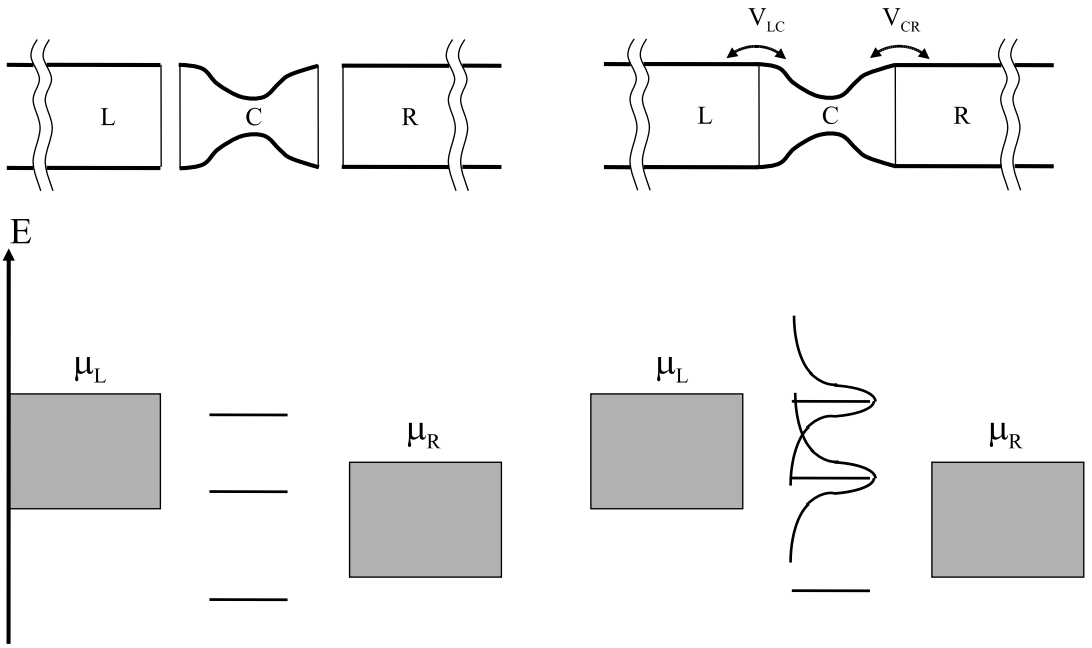

Figure 4.8: Schematic representation of the self energy concept which incorporates effect of coupling of a device region to the semi-infinite electrodes. If the central region is isolated from the external perturbations the energy levels are well defined sharp states (left panel). However, when the central region is coupled to two semi-infinite electrodes (right panel), its energy states are renormalized and broaden due to the presence of the electrodes. Taken from Ref. 157.

It is important to remind that $\Sigma_{L/R}(E)$ is not a Hermitian operator and so the eigenvalues of $H+\Sigma$ are in general complex numbers. The anti-hermitian part of $\Sigma_{L/R}$ is defined as

$$\Gamma = i[\Sigma_{\mathrm{L/R}}(E) - \Sigma^{+}_{\mathrm{L/R}}(E)] \tag{4.63}$$

and can be interpreted as the broadening of the electron level due to presence of the electrodes as explained before.

It might seem that the evaluation of the self-energies of the electrodes would involve inverting an infinite matrix $\mathbf{H}_{\mathrm{L/R}}$. One can notice however that the interaction between the electrodes and the central region is actually restricted to the few layers close to the interface. Therefore, in practice only the so called *surface Green function* of the lead has to be evaluated. To do so the electrode is divided into *principal layers* such

that the size of each one should be large enough to prevent interactions between not neighbouring ones. In the TranSIESTA implementation, which involves NAO basis set, the size of the principal layer of the electrode depends on the largest cutoff radius for the numerical functions of the basis set. The self-energy is then calculated iteratively using the method proposed by Sancho *et al.*[158]

The Green function technique, applied to the calculation of the conductance, transforms the original problem of the spacer and the electrodes into the problem of the central region 'open' to the electrodes via the self-energies.[157] The self-energies take care of the scattering due to the presence of the electrodes. It is in some sense equivalent to the single-particle scattering problem discussed before using Landauer-Büttiker formula.

Conductance calculations in TranSIESTA

TranSIESTA combines the non-equilibrium Green functions with the localized atomic orbitals as a basis set. The Hamiltonian matrices for the left $\mathbf{H}_{\mathrm{L}}$ and the right $\mathbf{H}_{\mathrm{R}}$ leads and the corresponding self-energies, $\Sigma_{\mathrm{L/R}}$, are obtained from two separate calculations for the bulk systems where periodic boundary conditions with Bloch's theorem in all directions are used. From these calculations the self-energies are calculated by representing the electrodes by two semi-infinite layers.[159,160] The remaining parts of the Hamiltonian, $\mathbf{V}_{\mathrm{LC}}, \mathbf{V}_{\mathrm{RC}}$ and $\mathbf{H}_{\mathrm{C}}$ depend on the non-equilibrium density and are evaluated using a self-consistent procedure.

The derivation of the non-equilibrium density matrix and the Landauer-Büttiker formula within the Green function technique will not be described here and can be found for example in Refs. 156, 157. We will recall only the final formulas and stress out the points important in practical calculations using the TranSIESTA code. The following expressions resulting from the Green function technique are the most relevant formulas for the calculations of the current, and it is useful to summarize them here:

$$\begin{aligned} \mathbf{G}_{\mathbf{k}}(z) &= \frac{1}{z\mathbf{S}_{\mathbf{k}} - \mathbf{H}_{\mathbf{k}} - \Sigma_{\mathrm{L},\mathbf{k}}(z) - \Sigma_{\mathrm{L},\mathbf{k}}(z)}, \\ \Gamma_{j,\mathbf{k}}(z) &= i[\Sigma_{j,\mathbf{k}(z)} - \Sigma^{\dagger}_{j,\mathbf{k}}(z)]/2, \\ f_j &= \frac{1}{1+\exp[(\epsilon-\mu_j)/k_BT]}, \end{aligned} \tag{4.64}$$

where $j = \{L, R\}$ and $z = \epsilon + i\eta$. Here, the overlap matrix $\mathbf{S}$ appears due to the non-orthogonality of the basis functions.

The non-equilibrium density matrix in the general non-equilibrium Green function formalism involves integration over k-space and energy space and is given by

$$\rho = \frac{1}{\pi}\int\int_{-\infty,BZ}^{\infty} d\epsilon d\mathbf{k}\mathbf{G}_{\mathbf{k}}(z)\left[\Gamma_{\mathrm{L},\mathbf{k}}(z)f_{\mathrm{L}}(\epsilon) + \Gamma_{\mathrm{R},\mathbf{k}}(z)f_{\mathrm{R}}(\epsilon)\right]\mathbf{G}^{\dagger}_{\mathbf{k}}(z). \tag{4.65}$$

Then, this density is split naturally into a left and a right part as

$$\begin{aligned}\rho_{\mathrm{L}} &= \frac{i}{\pi}\int\int d\epsilon d\mathbf{k}\left[\mathbf{G}_{\mathbf{k}}(z)-\mathbf{G}_{\mathbf{k}}(z)\right]f_{\mathrm{L}}(\epsilon)+\frac{1}{\pi}\int\int d\epsilon d\mathbf{k}\mathbf{G}_{\mathbf{k}}(z)\Gamma_{\mathrm{R},\mathbf{k}}(\epsilon)\mathbf{G}^{\dagger}_{\mathbf{k}}(z)\left[f_{\mathrm{R}}(\epsilon)-f_{\mathrm{L}}(\epsilon)\right],\\ \rho_{\mathrm{R}} &= \frac{i}{\pi}\int\int d\epsilon d\mathbf{k}\left[\mathbf{G}_{\mathbf{k}}(z)-\mathbf{G}_{\mathbf{k}}(z)\right]f_{\mathrm{R}}(\epsilon)+\frac{1}{\pi}\int\int d\epsilon d\mathbf{k}\mathbf{G}_{\mathbf{k}}(z)\Gamma_{\mathrm{L},\mathbf{k}}(\epsilon)\mathbf{G}^{\dagger}_{\mathbf{k}}(z)\left[f_{\mathrm{L}}(\epsilon)-f_{\mathrm{R}}(\epsilon)\right].\end{aligned} \tag{4.66}$$

We omitted the integral boundaries for simplicity. These formulas can be separated in the equilibrium $\rho_{j,eq}$ and non-equilibrium $\Delta_{j,neq}$ terms as

$$\begin{aligned}\rho_{j,eq} &= \frac{i}{\pi}\int\int d\epsilon d\mathbf{k}\left[\mathbf{G}_{\mathbf{k}}(z)-\mathbf{G}^{\dagger}_{\mathbf{k}}(z)\right]f_j(\epsilon),\\ \Delta_{j,neq} &= \frac{1}{\pi}\int\int d\epsilon d\mathbf{k}\mathbf{G}_{\mathbf{k}}(z)\Gamma_{j'\neq j,\mathbf{k}}\mathbf{G}^{\dagger}_{\mathbf{k}}(z)\left[f_{j'}(\epsilon)-f_j(\epsilon)\right].\end{aligned} \tag{4.67}$$

The precision of the results depends on how well these terms are computed.

First, one can consider the integral over k-points. As already explained the integral has to be replaced by the weighted sum over k-point grid and one should converge the k-sampling. In the implementation of SIESTA/TranSIESTA only the inversion symmetry is used to reduce the number of k-points in the BZ. In principle, the k-point sampling should be converged using the standard SIESTA method and next the same mesh should be used in TranSIESTA run. There is one important difference between the two, namely the k-point sampling along the transport direction z in TranSIESTA calculation is always set to 1. This is due to the fact that periodic boundary conditions are only applied in the xy plane, while along the z axis we have open boundary conditions in order to apply a voltage across the structure. In the case of the electrode, however, we need k-point sampling in all three directions since periodic boundary conditions are applied along three directions. The electronic states of the electrode are obtained from the usual bulk calculations. The k-point grid in the lateral direction should match the one used for the central region while along the z-axis the required mesh should be much bigger, at least around 80-100 points. This is because the $\mathbf{H}_{\mathrm{L}}$ and $\mathbf{H}_{\mathrm{R}}$ are calculated under periodic boundary conditions while $\mathbf{H}_{\mathrm{C}}$ is evaluated with open boundary conditions using the self-energies from $\mathbf{H}_{\mathrm{L}}$ and $\mathbf{H}_{\mathrm{R}}$, respectively. It is clear that the k-point grids should match in the xy plane for both parts. On the other hand, along the z direction, the self-energy calculation effectively corresponds to an infinite number of k-points, hence a lot of points should be used for the electrode calculation to make sure that the electronic structures of the electrodes and the central region match. Especially important is the Fermi level which has to be closely matched between the electrode and the scattering region. A discrepancy in Fermi level lead to slow or bad convergence or even inaccurate results since artificial scattering can be introduced by the Fermi level mismatch.

The integration over the energy is slightly more complicated and is performed differently for the equilibrium and the non-equilibrium parts of the density. The equilibrium part, $\rho_{eq,\mathbf{k}}$, is evaluated using a complex contour method based on the residu theorem.[46,161] The poles of the retarded Green function lie on the real axis (energy

eigenvalues) and on the imaginary axis (the Fermi function poles) and the function is analytical otherwise. The contour in the complex plane, as shown in Fig. 4.9, begins with the line segment L, followed by the circle segment C, and running along the real axis from $(EB + i\delta)$ to $(\infty + i\delta)$, where EB has to be below the bottom of the valence-band edge and encloses only the poles of $f(z)$ located at $z_\nu = i(2\nu+1)kT$. The contour

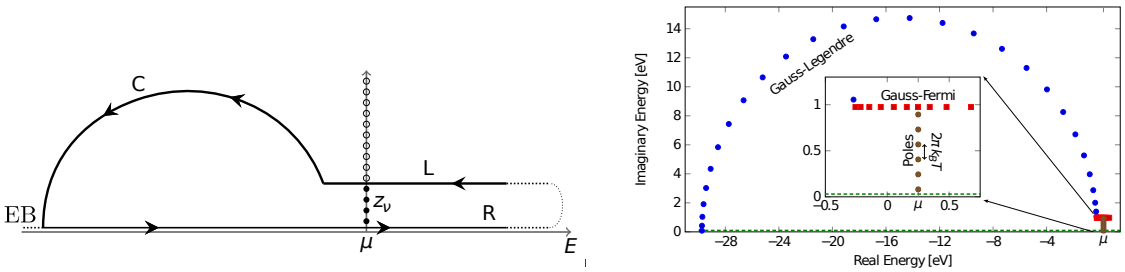

Figure 4.9: The closed contour in the complex plane defined to evaluate the equilibrium density matrix part. Taken from Ref. 159.

integral can be calculated numerically for a given temperature by defining the number of Fermi poles to enclose, which ensures that the complex contour stays away from the real axis. Since the Green function will be smooth sufficiently away from the real axis, the contour integral can be evaluated using a Gaussian quadrature as schematically shown in the right panel of Fig. 4.9.

The non-equilibrium part $\Delta_{j,neq}$ is more difficult to calculate since it is not an analytical function. Therefore it is evaluated using a fine grained numerical integration. Since this part depends on the difference between the occupation function of the two electrodes, the energy for which the integration is performed is confined to the bias window with respect to different Fermi distributions.

Once the non-equilibrium density matrix is evaluated the utility TBtrans can be used to calculate the transport properties based on the TranSIESTA output files. The current is then given in the Green function formalism by

$$I(V) = G_0 \int\int d\epsilon d\mathbf{k} \mathrm{Tr}\left[\Gamma_{\mathrm{L},\mathbf{k}} \mathbf{G}^\dagger_{\mathbf{k}}(z) \Gamma_{\mathrm{R},\mathbf{k}} \mathbf{G}_{\mathbf{k}}(z)\right] (f_{\mathrm{L}}(\epsilon) - f_{\mathrm{R}}(\epsilon)). \tag{4.68}$$

The transmission amplitude matrix $\mathbf{t}$ of an electron going from left to right is now given by

$$\mathbf{t}(\epsilon) = [\Gamma_{\mathrm{R}}(\epsilon)]^{1/2} \mathbf{G}(\epsilon) [\Gamma_{\mathrm{L}}(\epsilon)]^{1/2}, \tag{4.69}$$

and hence the expression 4.68 is equivalent to the Landauer-Büttiker formula for the conductance

$$G(V) = \frac{G_0}{V} \int d\epsilon [f_{\mathrm{L}}(\epsilon) - f_{\mathrm{R}}(\epsilon)] Tr[\mathbf{t}^\dagger \mathbf{t}](\epsilon). \tag{4.70}$$

Comments on convergence

The main reason why we used TranSIESTA is the fact that it actually allows to apply different bias on each electrode. In PWcond one can change the energy at which transmission is evaluated, nonetheless this energy is the same for both leads. This means that the same states are available for the tunnelling in both electrodes (assuming electrodes are of the same material). In a real MTJs the measured TMR depends on the applied bias. Increasing the voltage changes the sates in the emitting and collecting electrodes that participate in the tunnelling process and in turn that affects the TMR. In experiments performed in our institute by the group of Dr Bowen the voltages used for MTJ based on MgO are reaching up to 1-2 eV (this value actually depends on the temperature of measurements and also the method of junction preparation and is strongly dependent on a device). Therefore, we would like to verify how oxygen vacancies can affect the voltage dependent transmission and make contact to experiment.

We started with the same geometry of Fe/MgO/Fe in the scattering region as in the PWcond calculations and fixed the number of MgO layers to 5. The way we constructed the basis set in the SIESTA/TranSIESTA codes was already explained in sec. 4.3.2. The principal layer composed of 4 ML of Fe was sufficient to restrict interaction between them to the first neighbours. As we checked, the 4×4 k-point mesh in the xy plane is enough for the convergence of DOS. As already explained, in the scattering region the k-point sampling along the z direction is set to one while for the electrode calculations we set this value to 100. We used the default values controlling the convergence of the Green function calculations, changing only the value of applied voltage.
We also varied the position of F/M centers within the MgO layers, shifting the defect from the middle MgO layer to the one at the interface. However, we were not able to converge all the structures. As mentioned before, the convergence in SIESTA/TranSIESTA is more tricky than in codes based on plane waves and it is not easy to improve it. Additional difficulties arise due to the applied bias and the non-equilibrium conditions. In principle, one should start with zero-bias calculations and then slowly increase the voltage. For better convergence it is advised to use as a starting point the density matrix evaluated for the closest value of the voltage. With this procedure, we were able to reach 0.6 eV for ideal junctions, 0.4 eV when the defect was in the middle layer and only 0.2 eV when the defect was placed in the 2nd MgO ML from the interface. The structures with the vacancies in the interfacial layer did not converge even in the case of zero-bias calculations. Changing the basis set, density mixing parameters or increasing the k-point sampling did not solve the problem. One of the possible reasons is that the size of the electrode included in the scattering region is not sufficient when we introduce defects in the MgO. The encountered problems need further investigations and should be solved in the future work. The results obtained with TranSIESTA and discussed in the next part are therefore only preliminary and not yet conclusive.

Part III

Results and discussion

5

Electronic properties of oxygen vacancies in magnetic Fe(FeCo)/MgO junctions

In this chapter we will present results concerning the electronic properties of single and double oxygen vacancies in MgO. First, we will consider oxygen vacancies in a bulk MgO and discuss their impact on the electronic structure of MgO. Next, we will present more realistic structures with Fe(FeCo) electrodes attached. We will show that the M center energy level does not depend on the geometrical position or the orientation of the defect plane with respect to the electrodes. In the last part, we will describe briefly how based on complex band structure calculations the attenuation coefficient of the wave function in MgO changes when the defects are present. All the calculations were performed by means of the VASP package using the PAW method and the GGA functional, unless stated otherwise.

5.1 F/M-MgO structural properties

Bulk MgO is an ionic crystal with rock salt structure in which each Mg and O atoms are six-fold coordinated. During the crystal formation, 2 electrons from Mg $3s^2$ valence shell are transferred to the O $2p^4$ valence shell making the valence band of mainly oxygen $2p$ character, and the lowest empty conduction band of magnesium s-d character.

To simulate oxygen vacancies in MgO we used supercells of 64 atoms of a simple cubic structure. For all calculations the experimental lattice constant of MgO of 4.212 Å was adopted. The F/M centers are created by removing one/two neutral oxygen atoms from the supercell. The structure relaxation revealed that in the case of F center the atoms surrounding the vacancy are shifted symmetrically away from the defect creating an octahedral environment around the cavity. All the atoms are pushed away from the vacancy and the displacements are schematically shown in Fig. 5.1. The change of Mg-O distance along the each axis is only about 0.0077 Å. In the case of the

M center the situation is slightly more complicated. An M center is constituted of two neighbouring oxygen vacancies and the displacement of the surrounding atoms are not all the same any more (see Fig. 5.1).

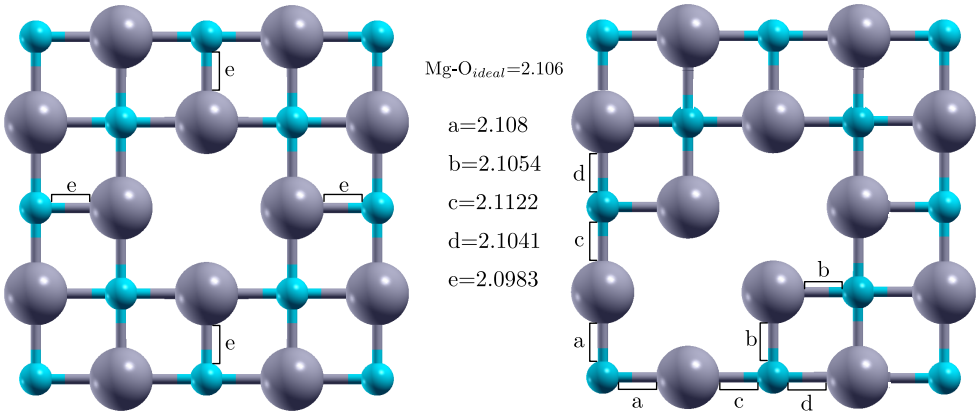

Figure 5.1: Schematic representation of atom relaxation around defect sites for F (left) and M (right) ceners. Changes of the Mg-O distance for each structure are indicated in the panels. Note that for F centers all atoms shift the same manner.

To verify the influence of atomic relaxation on electronic structure of F- and M-MgO we show in Fig. 5.2 the total density of sates before and after relaxation imposed on the DOS of ideal MgO. We notice that upon removal of neutral oxygen atoms, states disappear in the valence band, and the electrons left by each missing oxygen ion are accommodated in quantum states with energy levels in the bulk band gap. We will refer to these levels as *ground state* levels. Moreover, some changes are seen close to the conduction band minimum and we call them the corresponding *excited states* of the defect. What is important is that the atomic displacements due to atomic relaxations do not affect the position of the defect levels and as such can be neglected. This can be understood considering that electrons remaining after the oxygen removal are localized around the vacancy site and mimic the electron distribution of the missing O^{2-} ion. Therefore, the positions of the lattice around the vacancy do not change significantly. The change of the total energy upon atomic relaxation is also negligibly small (see Tab. 5.1).

As it was already mentioned before, oxygen vacancies can also appear in charged state with one (F^{+}) or two (F^{+2}) electrons removed. In a such a situation the lattice distortion around the defect will be more pronounced since the positively charged center will attract more O^{-2} ions and will repel Mg^{+2} ions. This was shown in the work of Ertekin *et al.*[110] where they found that the Mg-Mg distance increases from 0.11 Å to 0.19 Å in the case of singly and doubly charged F center, respectively, and is one order of magnitude bigger than for the neutral vacancy. Similar results were also obtained in the work of Rinke *et al.*[109] As a consequence the defect level positions can change and the charged and neutral states can be distinguished in experiments. The scenario including charged defects, however, will not be considered in this thesis.

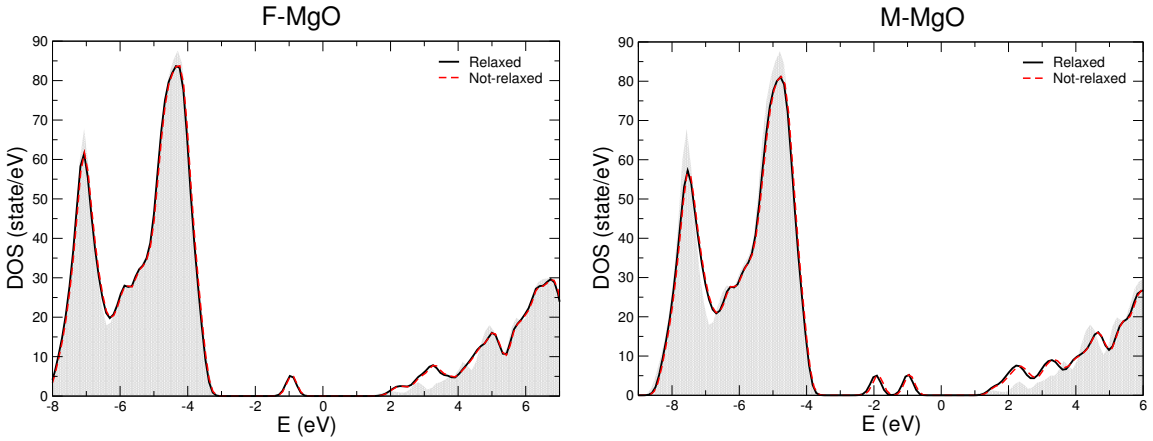

Figure 5.2: DOS for F-MgO (left) and M-MgO (right) for the unrelaxed and relaxed structures imposed on DOS for an ideal MgO (shaded area). Atomic relaxation does not affect the defect position.

5.2 Defect formation energy

A formation energy E_f of the point defects X is defined as[162]

$$E_f[X] = E_{tot}[X] - E_{tot}[bulk] - \sum_i n_i \mu_i, \tag{5.1}$$

where $E_{tot}[X]$ is the total energy of a supercell with a defect X, and $E_{tot}[bulk]$ is the total energy for the ideal structure using the same supercell. The number n_i corresponds to the number of atoms of type i which are added ($n_i > 0$) or removed ($n_i < 0$) from the supercell, and μ_i denotes the chemical potential of a particular species. In the case of oxygen vacancies in the MgO the chemical potential represents the energy of the reservoir with which atoms are exchanged, here it stands for the energy of O_2 reservoir. The formation energies for F, M and two separate F centers are summarized in Tab. 5.1.

Table 5.1: Total energies and formation energies for F and M centers and two F separated F centers (2×F) in one supercell.

Defect	Total energy before relaxation	Total energy after relaxation	Defect formation energy
F	-369.288	-369.292	7.315
2×F	-357.577	-357.585	14.647
M	-357.690	-357.701	14.531

The formation energy of an M center is higher than that of a F center which agrees with previous theoretical calculations of Ref. 27. However, what is interesting, is that the formation energy of two separated F centers is about 0.12 eV higher than that of a paired F-centers constituting an M center. This indicates that the creation of an M center should be more favourable than two separate F centers in the same

structure. Indeed, experiment showed that by changing the annealing temperature of MgO samples pairing of F centers can be enhanced.[163] In fact, different barrier heights in MgO-based junctions annealed at 200°C and 300°C were measured and associated with single or double oxygen vacancies. These barrier heights were evaluated using an $\hat{I}$ method (read as "*I-hat*"). The $\hat{I}$ allows the determination of the effective barrier heights from the experimental I-V characteristic curve and it is instructive to briefly describe it here. In principle, one measures two current-voltage characteristics at two different temperatures, such that $T_1 < T_2$, and then computes the changes in the current based on the following formula

$$\hat{I}(T_1; T_2; V) = \left(\frac{I(T_2; V)}{I(T_1; V)} - 1 \right) \times 100. \tag{5.2}$$

The maximum values in the resulting $\hat{I}$ curves are due to reaching a tunnelling barrier height associated with defects. Moreover, different vacancy levels can be activated at different temperatures and so different characteristics can be obtained for one junction as a function of a temperature.

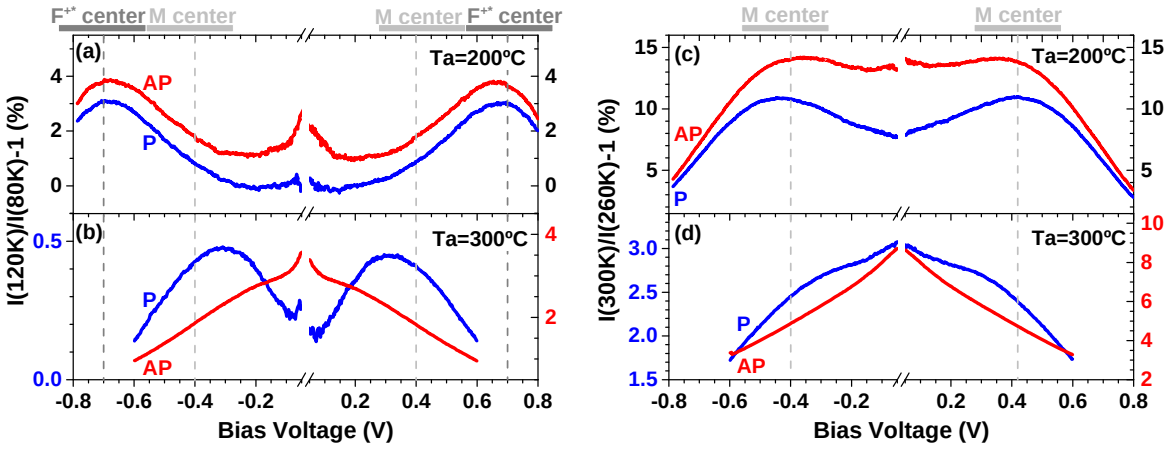

Figure 5.3: Changes of I_P and I_{AP} due to increasing temperature by 40 K within the (a,b) $80 < T < 250$ K and (b,d) 250 K$< T$ temperature ranges for which charged F centers and M centers respectively determine[?] the MTJ's effective tunnel barrier height. Panels (a,c) and (b,d) respectively present data for MTJs annealed at T_a =200°C and T_a =300°C. Annealing at T_a =300°C reduces the ratio of F to M centers, such that the F-center tunnel barrier no longer appears, while the M-center tunnel barrier appears only in the MTJ's P state. Taken from Ref. 163.

Fig. 5.3 shows I-V curves obtained based on the $\hat{I}$ method. If we compare now panel (a) and (b) in Fig. 5.3, corresponding to annealing temperature T_a of 200°C and 300°C respectively, we clearly see the vanishing of the peak located around -0.7 eV and an appearing one at -0.4 eV. The peak at -0.7 eV is associated with F-center state and that at 0.4 eV with the paired oxygen vacancies. The right panels show curves for the same junctions but obtained for different temperature range. In principle, we consider the 80$< T <$250 K (panels a,b) range for which the effective tunnel barrier height can be defined by the charged single oxygen vacancy's excited state (denoted F^{+*}); and the

250 K$< T$ range (panels c,d) for which it is the M center's ground state. Comparing the datasets of panels (a,c), we can identify a 0.7 eV barrier height within $80 < T < 250$ K due to the F^{+*} state, and a 0.45 eV barrier height within 250 K $< T$ due the M_2 state, in both P and AP magnetic configurations. In contrast, MTJs annealed at T_a =300°C do not exhibit any more a signature of the F^{+*}-mediated barrier height state within the 80$< T <$250 K range (Fig. 5.3 b). Instead, we observe only a weak signature of a M_2-mediated barrier height. This signature, which sustains for 250 K$< T$ (Fig. 5.3 d), is present in the MTJ's P state but not the AP state. This means that the enhanced spintronic response of our MTJs with T_a =300°C compared to those with T_a =200°C is in part due to a Δ_1 tunnelling transmission channel in the MTJ's P state that is driven by the M_2-defined barrier height per our theory.

5.3 Electronic properties of M-MgO

The band structure of the M-MgO was calculated for supercells of 64 and 216 atoms in order to eliminate possible periodic image interactions between vacancies. The removal of two oxygen atoms from the 64 and 216 atom supercells resulted in vacancy concentrations of 6.25% and 1.85%, respectively. Figure 5.4 depict the corresponding band structures. As seen also in Fig. 5.1, the double oxygen vacancy results in the creation of two occupied energy levels below E_F. In the case of 216 atom supercell these levels exhibit no energy dispersion which means that the defects are well separated from each other and there is no artificial interaction between them. It also shows that the defects are localized in space and not interact much with the surrounding environment. In the case of 64 atom supercell a small dispersion of the defect levels can be noticed near the Γ point and is attributed to the interaction between periodic images of vacancies. Nonetheless, this dispersion did not change significantly the level positions and as such it can be neglected. This is important considering the computational cost and gives reasonable limits for the supercell size, especially for junctions with antiparallel configuration of the magnetization of the electrodes.

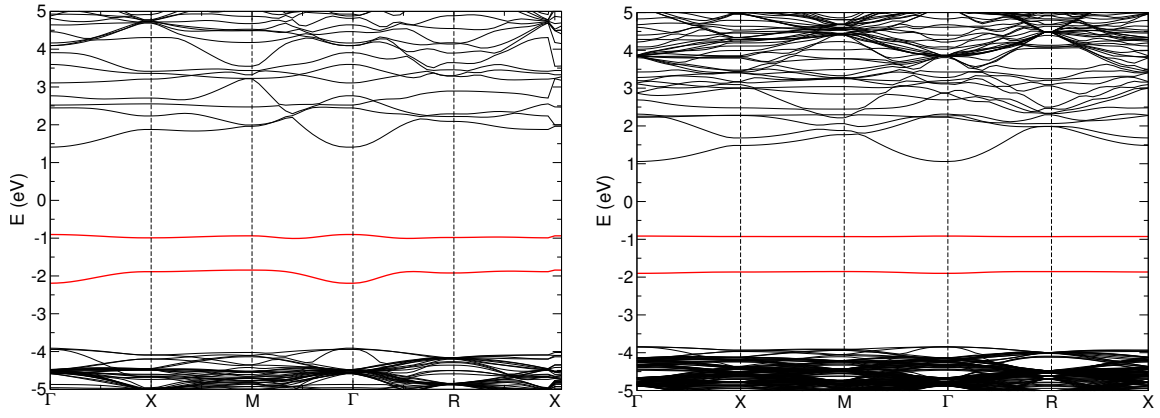

Figure 5.4: Band structure for M-MgO for supercell containing 62 (left) and 214 (right) atoms respectively. The defect levels are present in the band gap.

To understand the nature of the M-center levels we have computed the orbital projected band structure, the so called *fat bands*, and the orbital projected DOS for M-MgO as shown in Fig. 5.5. As explained before, the valence states of MgO are mostly of O p character while the conduction bands are made of Mg mixture of s and p-like states. The defect levels show mostly contributions form p-like orbitals with a smaller part coming from s-like states. By projecting the DOS on Mg and O sites separately we found that for the most part the M-levels are created by Op orbitals hybridizing with s and p states coming from Mg. The contribution of d-like states is much smaller and can be neglected.

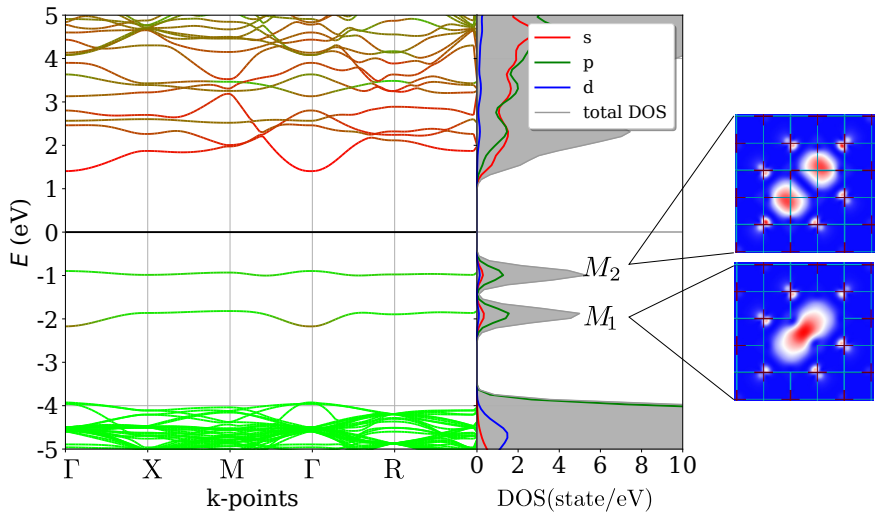

Figure 5.5: Band structure and orbital projected DOS for M-MgO. Insets show the electron distribution for each of the ground state energy levels of the M center.

Similar results were obtained when we investigated the electronic distribution around the vacancy sites for an energy range containing the ground state levels of M-center and the corresponding excited states in the conduction band region. Figure 5.6 presents the spatial distribution of the electron density for both the ground (panels a/c) and excited (panels b/d) states of M-MgO. In panels a/b(c/d), a 214-atom(62-atom) supercell were used. We observe how the neighbouring oxygen vacancies hybridize to create an M center. As expected from the band structure plots, the electrons remaining after oxygen removal are localized on the vacancy sites and the electrons are distributed among the vacancies. Since the M center's excited state lies within the conduction band states, a nonzero electron density is present on atoms far from the defect. The electron density plots also reveal a hybridization between both the ground and excited M center levels and the nearest oxygen ions showing that indeed the deflect level should be mostly due to Op orbitals. The spatial electron density of the M center is fully isolated from that of image M centers for the 214-atom supercell calculation. Thus, the lateral extent of the M center spans 1 ML on either side of the oxygen vacancy sites that define the M center. On the other hand, spatial overlap develops between the electron density of M centers in the 62-atom supercell calculation. This means that M centers separated by 2 ML of MgO will experience electronic interactions. Furthermore, we note the presence of a very minor DOS on MgO planes 2 and 3 when M centers are separated

by 4 atomic planes. This leads us to conclude on a separation between interacting M centers of up to 3 ML which will be important when we will consider MgO incorporated in the MTJ. The electron distribution indicates also that the ground states of M center reflect mostly s-like distribution, while the excited states are of p-like character.

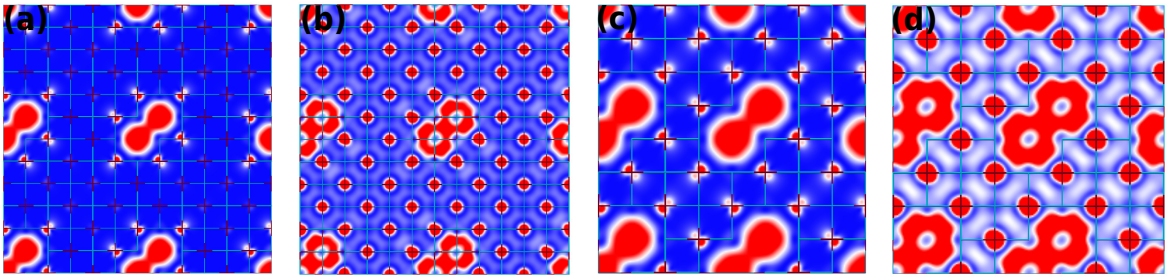

Figure 5.6: Spatial maps of the electron density in the xy plane, and within the energy range containing the M_1 and M_2 states (panels a/c) and M_1^* and M_2^* states (panels b/d), for a 214-atom supercell (panels a/b) and a 62-atom supercell (panels c/d). Periodic images are also shown.

Moreover, we are plotting as insets in Fig. 5.5 the electron distribution for each of the M centers ground stares separately. It is clear that the electron distribution for M_1 state resembles a bonding-like state and M_2 an antibonding behaviour. As in the case of bond formation between atoms, coupling between two F centers causes creation of bonding state with lower energy and antibonding state with higher energy with respect to the original F-state. Indeed, as it will be shown in the following sections of this chapter the F center peak is positioned always in between two M-center ground states. As a consequence the barrier height created by F-center will always be higher than the one associated with an M_2 state.

5.3.1 Band unfolding

The use of supercells is necessary in the simulation of defects to assure they are well separated from each other and their properties are well described. However, as was explained before the band number increases with the number of atoms in the supercell making hard to evaluate the M-center influence on the MgO band structure itself. Hence, to reveal how the presence of defects will influence the band symmetries of MgO, we unfolded the band structure of the supercell onto the Brillouin zone of the fcc primitive cell as explained in the methodology part.

In Figure 5.7, we compare the unfolded band structure along the $K-\Gamma-X$ direction of the supercell with (right panel) and without the M center (left panel). The color scale indicates the probability of preserving the Bloch character (symmetry) of the original bands. The unfolded bands of M-MgO show that the defect states slightly affect the lowest conduction band of MgO (blurring of the bands in the Figure) which is also consistent with the DOS shown in Fig. 5.1. However, despite the blurring, the energy dispersion in the BZ is very close to that of bulk MgO. This shows that the symmetry of the bulk MgO is only marginally altered by the M centers.

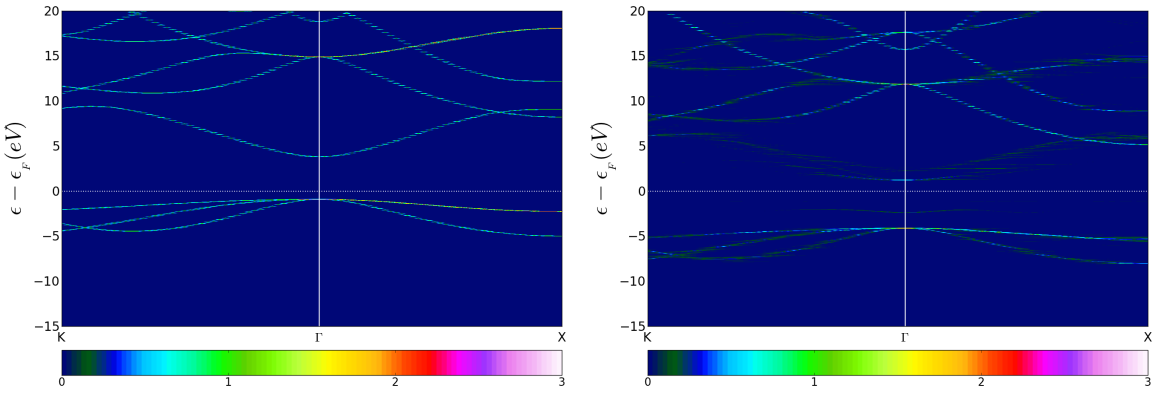

Figure 5.7: Band structure of supercells of MgO (left) and M-MgO (right), for 64 and 62 atoms, respectively, unfolded onto a primitive cell of MgO. The Fermi level is at the zero of the energy scale.

5.3.2 Hybrid calculations

The choice of the GGA functional, as it was explained in the methodology chapter, impairs a semi-quantitative assignment of the position of the M center's localized states in the MgO band gap. To correct this, we used a hybrid HSE03 functional that mixes the non-local Fock exchange with that of DFT in a certain proportion (see subsection 3.2.5 for more details).

Figure 5.8 presents the results of GGA and HSE03 bulk calculations for both M-MgO and F-MgO, with $E_F \equiv 0$. For both F-MgO and M-MgO, compared to the GGA results, the hybrid functional causes a shifting of the valence and the conduction bands towards lower and higher energies, respectively. The hybrid functional, due to the inclusion of a portion of the exact Fock exchange which is orbital dependent, increases the localization reducing the self interaction error appearing in LDA/GGA. This fact has almost no influence on the F state position since it is a single localized level. However, in the case of an M center, where two additional energy levels are created in the MgO band gap, the difference can be noticed and we see a shifting of the M_1 state further away from the M_2 level. The difference of the position of the GGA M_1 and the HSE03 is about 0.27 eV.

Nonetheless, aside from the shift in the M_1 energy position, we otherwise obtain a similar energy dependence of the DOS. This shows that less intensive GGA-based calculations already yield a qualitatively correct picture of the electronic properties of oxygen vacancies in MgO. It is worth noticing that the defect levels are placed near the middle of the MgO band gap irrespective of the functional used.

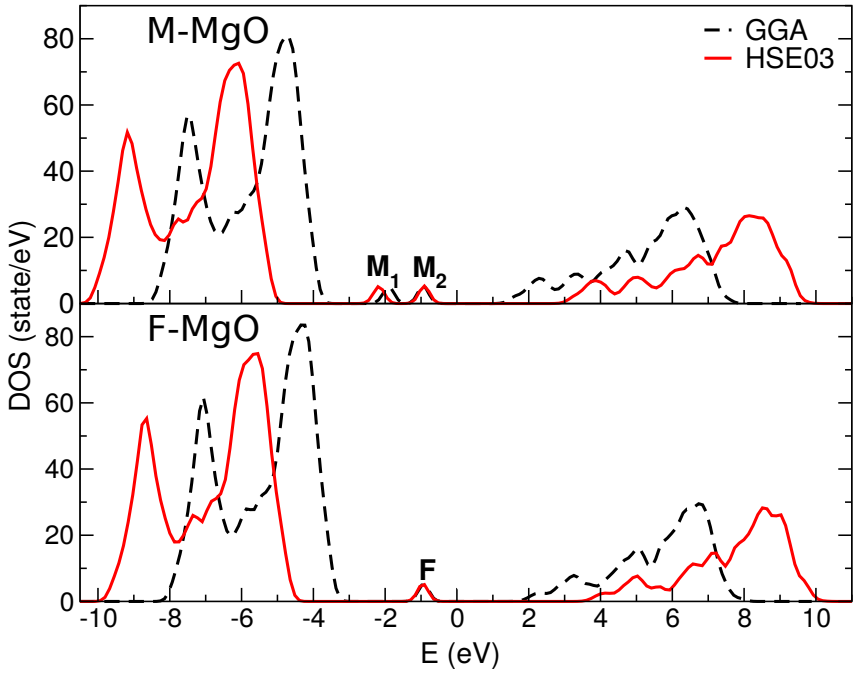

Figure 5.8: GGA and HSE03 calculated DOS for bulk M-MgO (top panel) and F-MgO (bottom panel).

5.4 Thin films of MgO

We considered so far the F/M center within the bulk MgO material. The electron distribution plots revealed the hybridization between the M center levels and the closest oxygen atoms hence the lateral extend of the M-defect in the plane of defect reaches up to 4 ML. The question to answer now is how much MgO must surround the M center so as to screen its electronic properties against disruptions to the MgO environment? Disruptions to these electronic properties can be due to the presence of a metal, vacuum, or another dielectric.

Let us first consider the case of an MgO surface. We used a slab with 7 ML of MgO in the z direction and we doubled the lattice parameter of MgO along the x and y directions. In order to ensure no interactions between periodic images along the z direction, we inserted 15 Å of vacuum. We did not relax the atoms here since we found that the structural relaxation does not significantly influence defect level positions.

Fig. 5.9 shows the layer projected DOS of the 7 ML-MgO slab in contact with vacuum imposed on the DOS of a bulk MgO (shaded area). The band gap of MgO decreases when approaching the surface due to the downward shift of the conduction bands. This is due to the removal of the periodicity in the z direction which weakens the ionic potential with respect to its bulk value and causes dangling bonds at the MgO surface layer and hence the creation of surface states. Since the surface states are localized close to the interface and decay inside the material, they are restricted basically to the first two layers of MgO the closest to the interface and the bulk band gap is restored from the third layer of MgO.

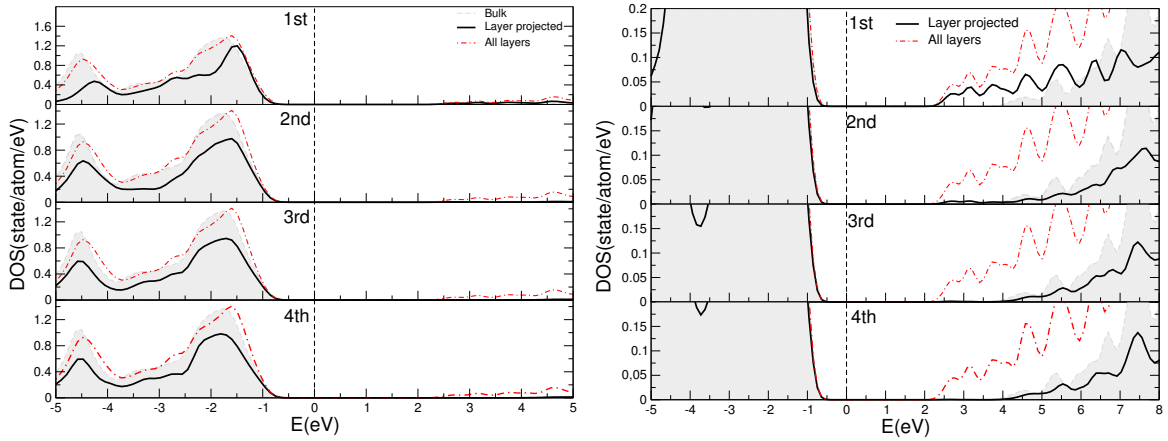

Figure 5.9: Layer projected DOS for MgO(7ML) thin film along the (001) direction in contact with vacuum. The 1st layer is at the surface one and the 4th one in the middle of the MgO film.

Next, we examined the 7 ML slab with a generated M-center. The M center was placed in the xy plane parallel to the interface and was moved from the 1st layer, which is in contact with the vacuum, down to the 4th layer of MgO. Fig. 5.10 presents the resulting layer projected DOS for M-MgO/vacuum system. As it can be seen, the M center affects the two proximal MgO layers indicating the hybridization with the closest neighbours which agrees with the electron distribution plots discussed earlier. Therefore, the effective extent of the M center along the direction perpendicular to the defect plane is estimated to 3 ML. Consequently, we see from Fig. 5.10 that placing the M center 3 ML away from the MgO surface layer, i.e. on the 4th layer, is sufficient to preserve the M center properties (M_1 and M_2 peak positions, no additional density near or between these peaks is coming from the surface states). This is also the case when the M center is placed on the 3rd or 2nd layer from the surface. However, when the M center is placed on the 1st layer, the peak positions change. This surface M center likely exhibits modified properties compared to the case of a deeper positioning within MgO, as expected from the literature.[112,164]

The work of Pacchioni and Freund[164] showed that for different concentrations of oxygen vacancies at the surface of MgO and especially for the case of one or two vacancies the atoms displacements even on the surface can be neglected.

To confirm the GGA results on ultrathin MgO films, we performed hybrid HSE03 calculations with an MgO slab placing the M center in the middle layer (Fig. 5.11). As in the case of bulk MgO (see Fig. 5.8) the hybrid functional shifts the valence and conduction bands towards lower and higher energies, respectively. At the interface layer, this shift is asymmetric and from the third layer is 1.5 eV symmetric shift as for the bulk. This asymmetric shift at the interface is due to surface conduction states that reduce the band gap. In addition, the M levels are slightly shifted towards lower energies compared to the GGA results. The GGA and HSE03 differences in peak positions with respect to the Fermi level are about 0.21 eV and 0.49 eV for the M_2 and M_1 levels respectively. The shift of the M_2 level was not observed in calculations concerning bulk material and here it is caused by the influence of the surface.

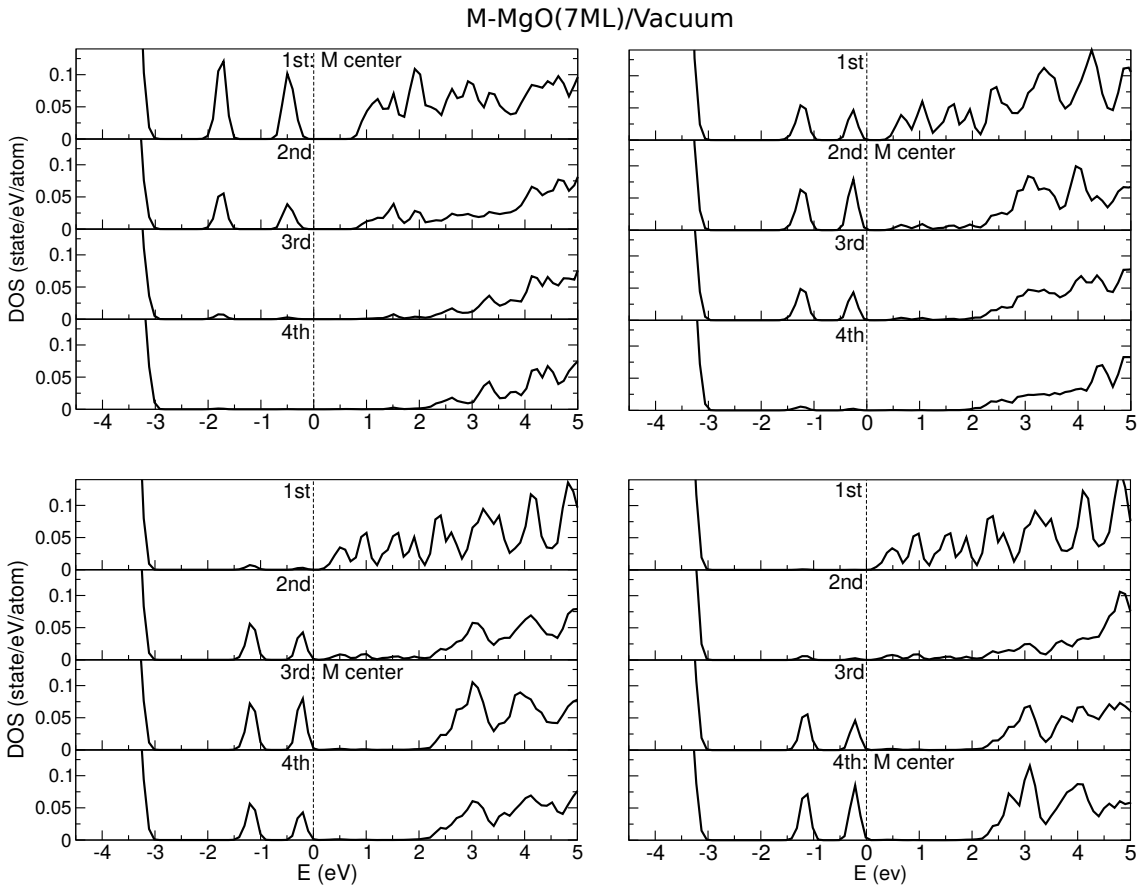

Figure 5.10: Layer-projected DOS for M-MgO/vacuum system along the (001) direction with the M center located in different layers.

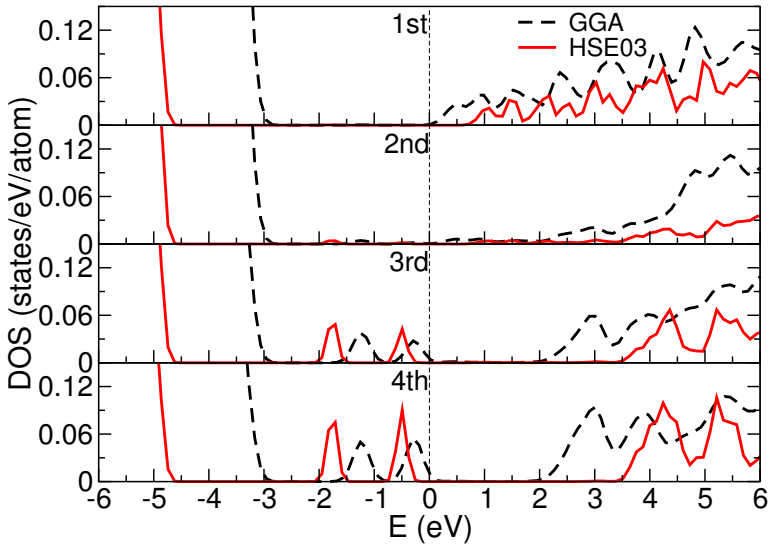

Figure 5.11: GGA and HSE03 calculated layer-projected DOS for 7 MgO layers containing an M center within the middle, layer.

When we compare the layer projected DOS of MgO slab with and without the M center we notice a downward shift of the valence bands when the defect is present. This actually shows that defects define the position of the Fermi level of the M-MgO slab. In the case of an interface with an electrode it is more complicated since one has to include additional states induced by the electrode itself. This is discussed in the next part.

5.5 Fe/MgO junctions

To find the proper position of the defect levels with respect to the Fermi level the ferromagnetic electrodes have to be attached. The electrodes will define the common Fermi level for the whole structure. At the metal/insulator interface we should expect the electron transfer between the two materials in order to attain the equilibrium and common chemical potential for the whole structure.[73,165] As a result, MIGS will be created in the band gap of MgO which will actually peg the Fermi level position for the junction and establish the defect position accordingly.

The geometry of the MgO/Fe supercell was based on the experimental results namely the Fe cell is rotated by a 45° with respect to MgO to match the lattice constants of both materials and avoid strains in the structure, thus $a_{\mathrm{MgO}} = \sqrt{2}a_{\mathrm{Fe}}$ (see sec. 1.2.1). Oxygen atoms are placed on top of Fe atoms and the Fe-O distance at the interface is fixed to 2.17 Å following previous theoretical predictions.[28,83] However, it is important to notice that the distance measured experimentally is varying from 2 Å[166,167] up to 2.2 Å.[15] Due to differences in the experimental values we decided to used the Fe-O separation obtained theoretically for the relaxed interfaces. We fixed the lattice constant of the MgO ($a_{\mathrm{MgO}} = 4.21$ Å) and adjusted the electrodes lattice to it ($a_{\mathrm{Fe/FeCo}} = a_{\mathrm{MgO}}/\sqrt{2}$). This choice reflects the experimental evidence[49] that the annealing of FeCoB/MgO-based MTJs leads to a recrystallization of the electrode/barrier interfaces so as to adopt the MgO lattice constant. The lattice constant of the electrode was increased to match that of MgO in the xy plane. The lattice parameter along the z axis is rescaled accordingly. The structure of the junction and relevant parameters are indicated in Fig. 5.12.

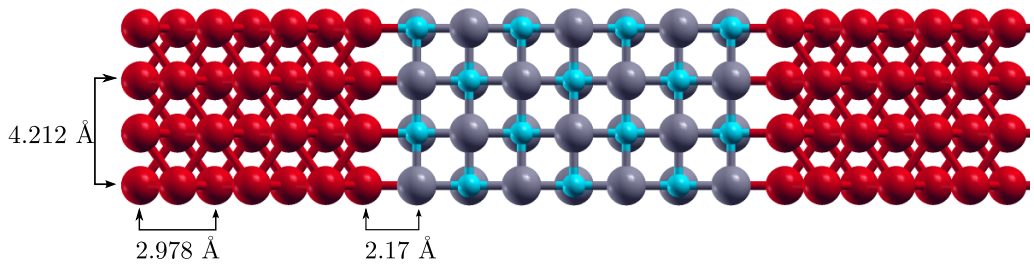

Figure 5.12: Schematic representation of Fe/MgO junction with lattice parameters indicated. Red atoms are Fe, blue O and grey Mg. The lattice constant of Fe is changed from nominal value of $a_{Fe} = 2.87$ Å to 2.978 Å.

To show the changes in the electronic structure of Fe due to different lattice constants, we compare in Fig. 5.13 the DOS of Fe for both iron lattice parameters. As

it can be seen, the change of the lattice constant preserves the shape of the DOS but causes a small shift of both spin densities. As such, the spin up density at the Fermi level is decreased with respect to the original Fe DOS while the spin down DOS is increased. The magnetic moment found for Fe is equal to 2.246 μ_B and changes to 2.630 μ_B when the MgO lattice constant is used. Nonetheless, as we check for the M-MgO(5ML)/Fe junction this does not influence the defect level position afterwords. Therefore, meaningful predictions can be done based on the actual structure.

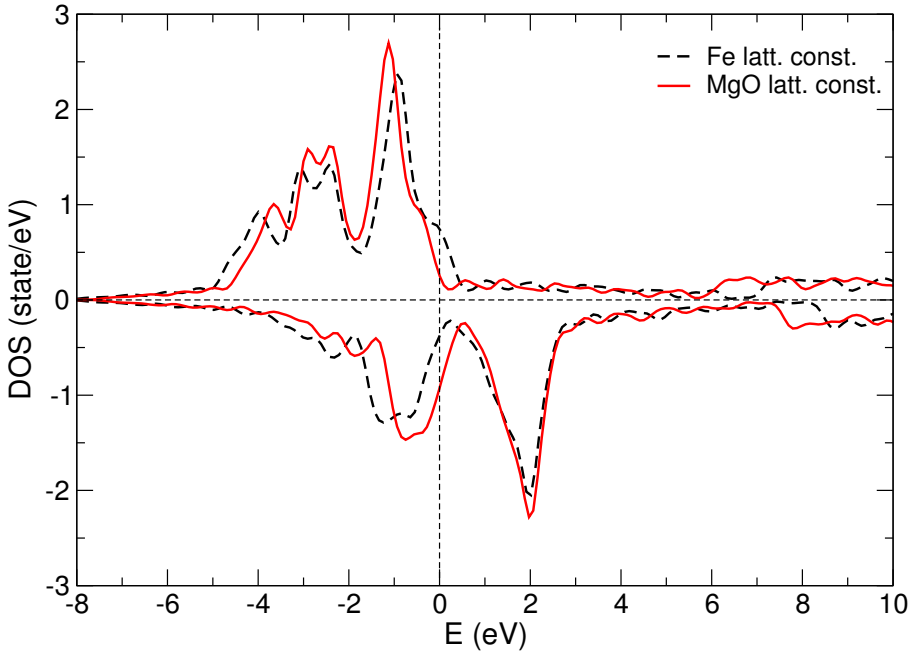

Figure 5.13: DOS for Fe with the bulk lattice constant $a_{\mathrm{Fe}} = 2.87$ Å compared to a Fe with lattice constant adjusted to that of MgO such that $a'_{\mathrm{Fe}} = a_{\mathrm{Mg}}/\sqrt{2} = 2.978\mathring{A}$.

The ideal junction structure had the lateral size of 4.212 Å, corresponding to one unit cell. We used 7 ML of Fe as an electrode and varied the number of MgO layers from 3 to 7 ML. As discussed, since the effective size of the M center extends up to 3-4 ML, in the case of 3 ML MgO spacer the defect contributions interfered with the states coming from the electrodes and these structures will not be presented. For spacers with 5 ML and 7 ML the results are similar concerning the defect level positions and the interaction between the defect and the electrode and we will therefore discuss only the case of 7 ML in more detail.

5.5.1 Ideal Fe/MgO junction

The most crucial parameter defining the value of the transmission is the hybridization at the interface between the electrode and the spacer. Therefore, we studied changes induced by defects in the layer projected DOS of our junctions. First, we will discuss interfacial hybridization in the ideal junction and then we will switch to MgO-spacers with defects.

We analyzed the projected DOS on Mg and O for each layer of the MgO spacer (see Fig. 5.14). The 1st layer is the one in contact with Fe and the 4th ML is in the

middle of the MgO spacer. Due to the contact with the metallic electrodes, MIGS appear in the MgO band gap and decay with the number of MgO layers. As a result the band gap of MgO disappears at the interface because of states coming from Fe. From the third layer the band gap of a bulk MgO is restored as in the case of thin film calculations. The difference with respect to the interface with vacuum is that the ferromagnetic electrode induces spin polarization at MgO layers and the difference in the DOS of spin up and down electrons can be clearly seen. Moreover, the DOS in the band gap at the first MgO layer is more pronounced for the oxygen states indicating that the hybridization at the interface is mostly due to Fe-O interaction and Mg is hardly involved.

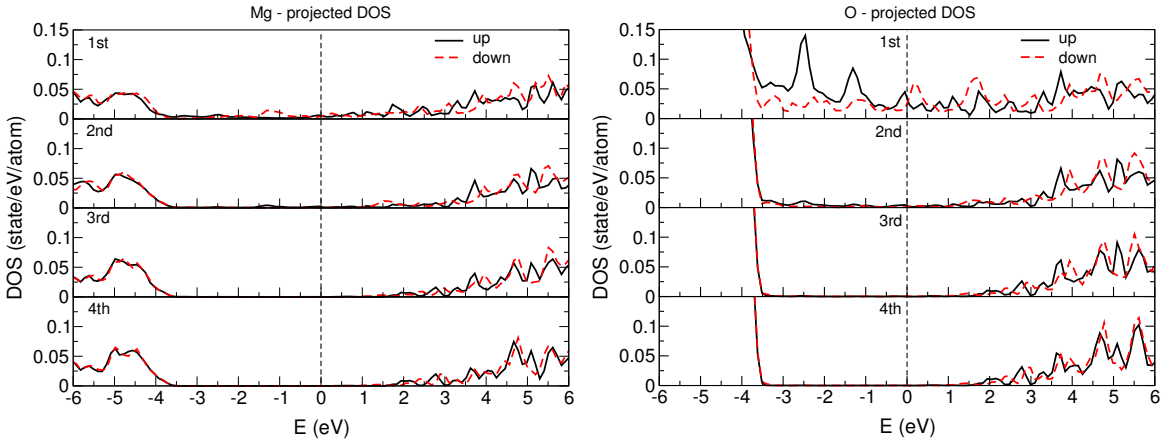

Figure 5.14: MgO-layer and atom projected DOS for the ideal MgO(7ML)/Fe(7ML) junction. The 1st layer is the one at the interface with the electrode and 4th is the middle one.

To understand the interface, we also plot the layer projected DOS for Fe electrode (Fig. 5.15). The 1st layer is always the one at the interface. We can clearly see the modifications at the interfacial Fe layer with respect to the middle layers and additional splitting and shift of states for both spin populations not present in the bulk. As a consequence, the DOS for the majority electrons is reduced at the vicinity of the Fermi energy whereas for the minority electrons the Fermi level falls near a sharp peak in the DOS.

To better understand the nature of hybridization at the interface, we show in Fig. 5.16 the orbital and atom projected DOS for the atoms at the interface. In the case of Fe the most pronounced peaks are due to d orbitals. The DOS associated with s and p states is much smaller. The peaks of the d states, for both majority and minority electrons in Fe, coincide in energy with p states of O atoms which is an indication of strong hybridization. We verified that that the hybridization occurs between Fe d_{yz} and O p_y at about -2.5 eV and Fe d_{z^2} and O p_z between peak at -1.5 eV for the majority spins. For the minority electrons the hybridization occurs above the Fermi level as seen in Fig. 5.16. The interaction between O and Fe explains the split of the DOS of Fe.

During the junction formation the electrons are rearranged between the Fe and MgO layers in order to correctly offset the bands of MgO relative to these of Fe. This

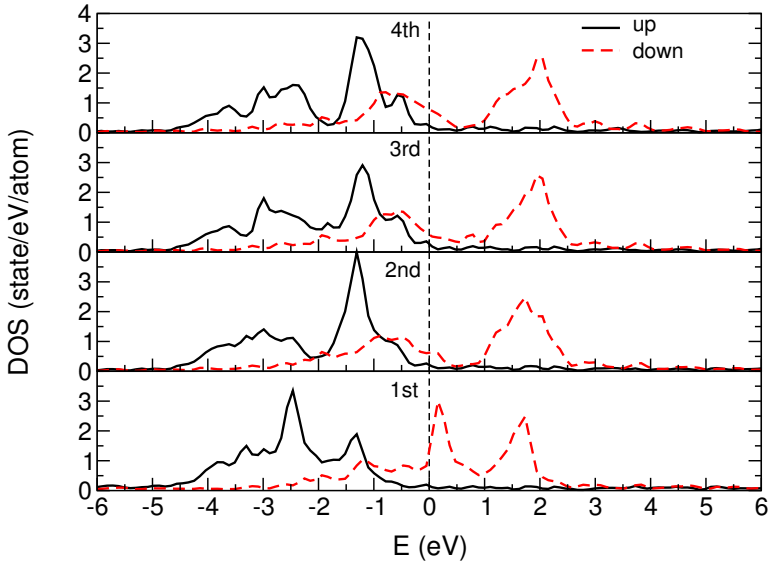

Figure 5.15: Layer projected DOS for Fe electrode.

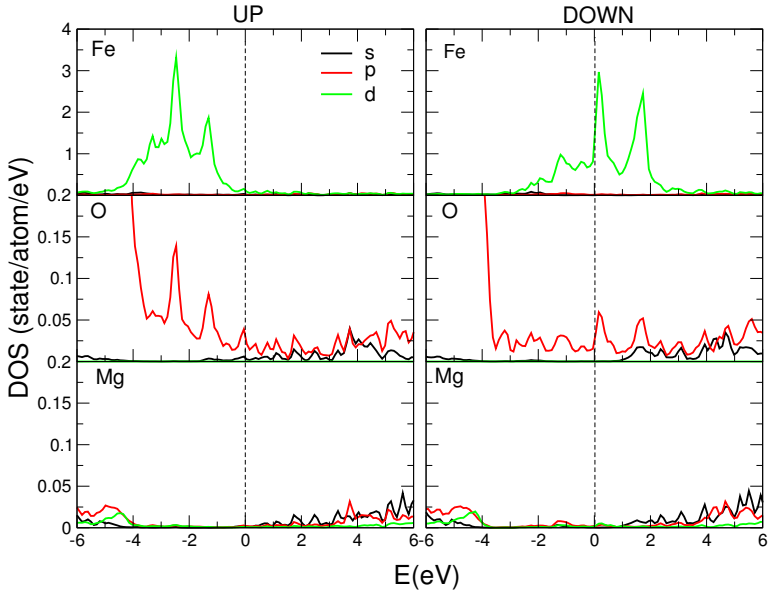

Figure 5.16: Layer and orbital projected DOS for Fe, Mg and O at the interface.

electron rearrangement at the interface was determined using Bader analysis.[168,169] Fig. 5.17 presents the results for Fe/MgO junction where Q denotes the change in the average electrons for a particular layer with respect to the corresponding bulk value. Bader analysis demonstrates that due to the electron transfer, the interfacial Fe looses electrons and the second Fe layer gains a significant amount of electrons, whereas MgO is loosing electrons to Fe. Similar results using GGA were obtained in the paper of Feng *et al.*[152] They have also pointed out the importance of the interface relaxation on the resulting electron transfer as well as the choice of the exchange-correlation functional.

The electron transfer is also reflected in the change of magnetic moments of Fe, Mg and O atoms at the interface. These are summarized in table 5.2. The magnetic moment

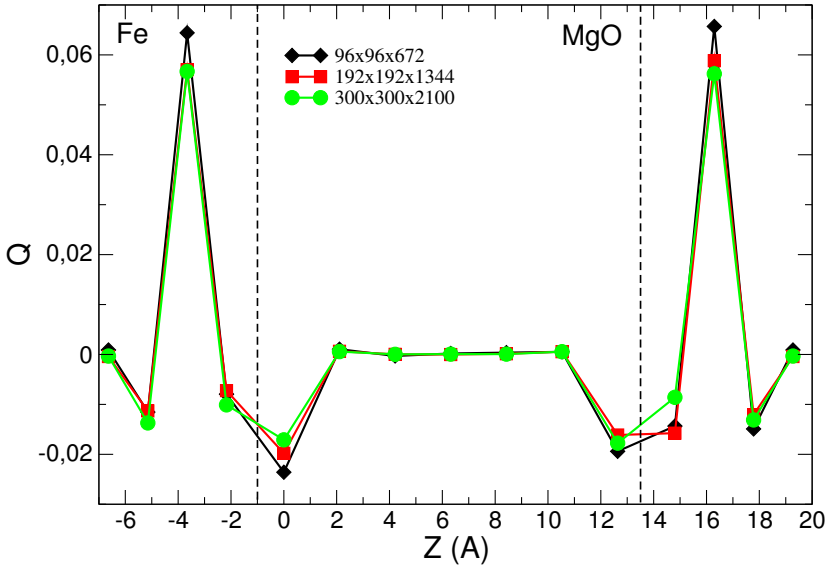

Figure 5.17: Bader analysis for ideal Fe(7ML)/MgO(7ML) junction. Q denotes the change in the average electrons for a particular layer with respect to the bulk value. Three different real space grids $96 \times 96 \times 672$, $192 \times 192 \times 1344$ and $300 \times 300 \times 2100$, are used to monitor the convergence of the electron transfer.

of Fe changes from 2.637 μ_B in the middle layer to value of 2.944 μ_B at the interfacial layer. In addition, induced magnetic moment of 0.031 μ_B appears on the O atoms at the interface and its bigger than one induced at Mg.

Table 5.2: The magnetic moment at atoms in an ideal Fe/MgO junction. The values are given in units of μ_B.

ML	Fe	Mg	O
4th	2.637	0.0	0.0
3rd	2.653	0.0	0.0
2nd	2.637	0.002	0.02
1st	2.944	-0.008	0.031

5.5.2 M-MgO/Fe junction

To study defects within the MgO spacer the lateral size of the simulation cell was doubled, i.e. increased to 8.424 Å, which corresponds with the size of a 64 atom cell used in bulk calculations. We can therefore expect small interactions between periodic images of the defect sites in the lateral directions. Nonetheless, this fact should not affect significantly the results as discussed before and the computational cost is reasonable.

Fig. 5.18 presents the DOS projected on MgO layers with M center shifted within the layers as indicated in the plots. The M_2 state is found at -0.7 eV below the Fermi level while the M_1 is at -1.7 eV. The F center level is placed at -1.2 eV below Fermi (plot not shown here). As expected the barrier height associated with the F center is in between barriers created by the M_2 and M_1 states. As before we can see that the vacancy affects also the closest MgO layers which leads to effective defect extend up to 3 ML of MgO along the direction perpendicular to the M-center plane.

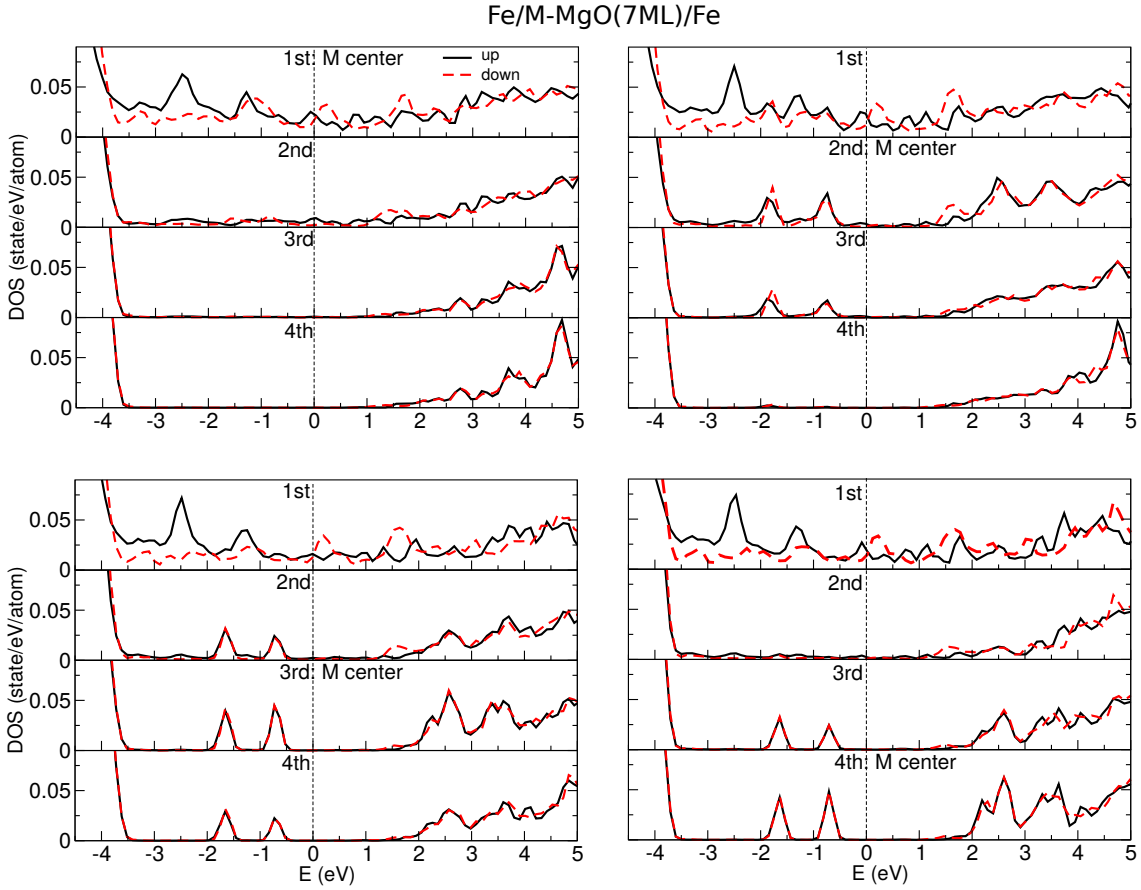

Figure 5.18: Spin-polarized layer-projected DOS for Fe/M-MgO/Fe system with the M center placed in different layers.

What is also important when we shift the M center within the MgO is that the defect energy level remains practically unchanged. Clearly if the defect is closer to the interface this might affect the hybridization between the two types of materials which

in turn influences the position of the Fermi level. In practice however, the differences in the Fermi level position for these structures is about 0.09 eV and can be neglected.

Figure 5.18 also shows that, as in the case of an ideal junction, the presence of the ferromagnetic electrode induces spin polarization on the MgO layers and the impact of reducing the distance between the M center and the Fe/MgO interface. While the energy splitting between the M_1 and the M_2 states remain when the M center is moved from MgO ML 4 to ML 3, this is no longer the case when the M center is on MgO ML 2. In latter case, the two M levels are connected. When the M center is placed at the interface, its on-site DOS is washed out, as is that on the neighbouring MgO ML 2. Moreover, induced spin polarization at the M-center is present when the defect is in the 1st or 2nd ML.

To determine the changes in the interfacial hybridization induced by the M center, we compare in Fig. 5.19 the layer projected DOS for each atomic species at the interface. The Fe DOS is only slightly affected upon shifting the M center to the interfacial ML which infers that the most important impact comes from the interaction with the MgO layers at the interface. Bigger changes can be noticed in the cases of Mg and O projected DOS which explains the before-mentioned induced spin polarization at the vacancy site due to the interaction of the M center and Fe at the interface.

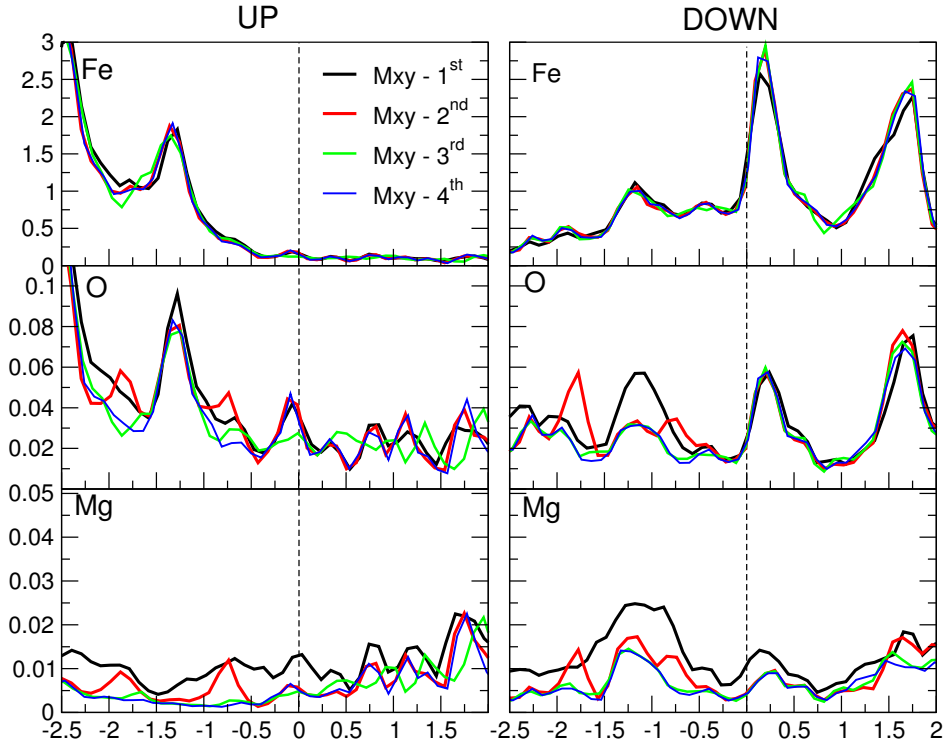

Figure 5.19: Spin-polarized layer-projected DOS for Fe/M-MgO/Fe system with the M center placed in different layers.

For the moment we have considered only the situation where the M center is in the plane parallel to the interfaces. We found that the effective size of the M center in the direction perpendicular to the interface reaches up to 3 ML of MgO. But we can also rotate the M center such that it will be almost aligned along the z direction and occupying two neighbouring MgO layers and having an effective size of 4 ML.

Regardless of the orientation of the defect plane the level position of the M center remains practically unchanged and similar results for the DOS where also obtained (not shown). Even though the changes in the DOS upon shifting or rotating the M center within the MgO spacer are not significant, these changes will have huge impact on the transmission as it will be shown in the next chapter.

5.6 FeCo/MgO junction

We have already discussed the importance of the electrode in the spin polarized tunnelling thought the MTJ, and highlighted that the highest TMR values were obtained for FeCoB/MgO MTJ. This was attributed to the fact that Co is fully spin polarized in contrast to Fe (see discussion in Sec. 1.3.3).

The real electrodes are alloys which are annealed in order to restore the crystalline structure but the exact arrangement of Fe and Co atoms is not really known. Moreover, the role of boron or its influence on the electronic structure of FeCo electrode is not clear. Therefore in our work we decided to consider a simplified scenario where the FeCo electrode has the same structure as that of Fe (see Fig. 5.12). Due to the two-atom unit cell, calculations using FeCo electrode resulted in a Co/MgO interface. Nonetheless, even the simplified structure can give us some insights about the impact of the type of electrode on the defect levels and on the transport properties.

5.6.1 Ideal FeCo/MgO junction

As before we have started with the analysis of the layer projected DOS for the ideal FeCo/MgO junction. The results for MgO layer and atom projected DOS are similar to the case of Fe/MgO MTJ (Fig. 5.12), namely the hybridization at the interface is mostly due to Co-O interactions and the spin polarization is induced at the MgO. To not repeat similar plots we will not reproduce it here but in Appendix B.

What is interesting in the case of FeCo/MgO junction is that the valence band (VB) maximum of MgO is higher in energy by about 0.5 eV compared to that of Fe/MgO. To understand this behaviour we have performed once more a Bader analysis to check how the electrons are rearranged at FeCo interface (Fig. 5.20). As explained, due to the simplified structure of FeCo alloy, the resulting electrode has alternating Fe and Co layers, with Co at the interfacial layer. In contrast to Fe/MgO interface, the first layer of Co gains more electrons coming form MgO while the second layer of Fe looses electrons. In general Fe loses electrons in favour of Co.

Different electron rearrangements also influence the magnetic moments of the electrode and that of MgO. The magnetic moment of Co is modified from bulk value of 1.909 μ_B to 1.777 μ_B due to the composition of the electrode and Fe-Co. Moreover, the change of the magnetic moment between middle and interfacial electrode layers is much bigger in the case of the Fe electrode, and also the magnetic moments induced on Mg and O atoms are bigger for Fe/MgO junction.

The difference in the interaction of Fe and FeCo with MgO can be explained by the fact that Co has one electron more than Fe and consequently it has a different work function. Indeed the work function of Fe is 4.6 eV and that of Co is 5 eV. As a result,

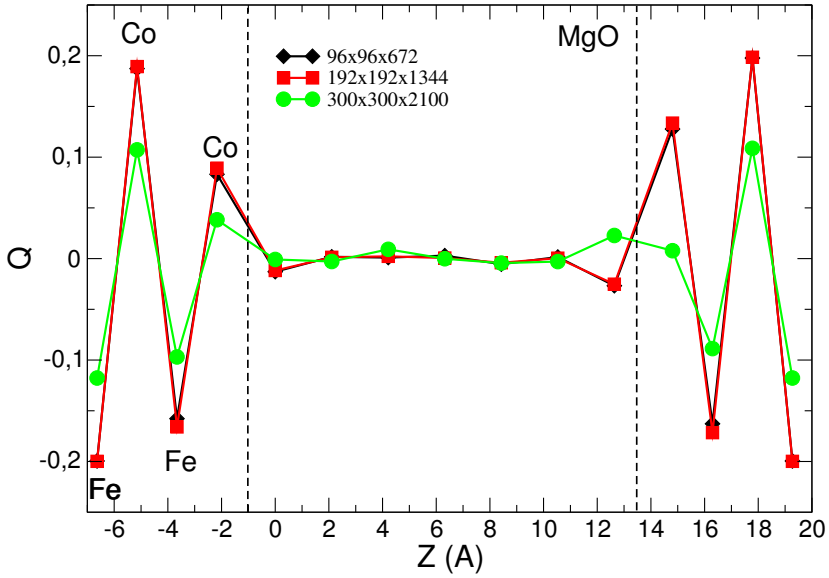

Figure 5.20: Bader analysis evaluated in the same manner as in Fig. 5.17 but for an ideal FeCo(7ML)/MgO(7ML) junction.

Table 5.3: The magnetic moment at atoms in an ideal FeCo/MgO junction. The values are given in units of μ_B.

ML	Fe/Co	Mg	O
4th	2.907	0.00	0.00
3rd	1.777	0.00	0.00
2nd	2.880	0.001	0.01
1st	1.744	-0.006	0.014

Fe will 'attract' more electrons coming from MgO and MgO lowers its potential to keep its electronic structure unchanged. Another way of understanding this difference at the interface is to consider the Wannier wave function emanating from MgO. Because Co has one electron more than Fe it will repel stronger incoming electrons and as a result the MgO Wannier wave function will penetrate less in Co than in Fe.

To understand the hybridization at the interface, we analyzed the orbital and atom projected DOS for interfacial atoms (see Fig 5.21). We observe that the Op peaks coincide in energy with those of Co d orbitals for the majority and the minority spin electrons, indicating a hybridization between the two types of orbitals.

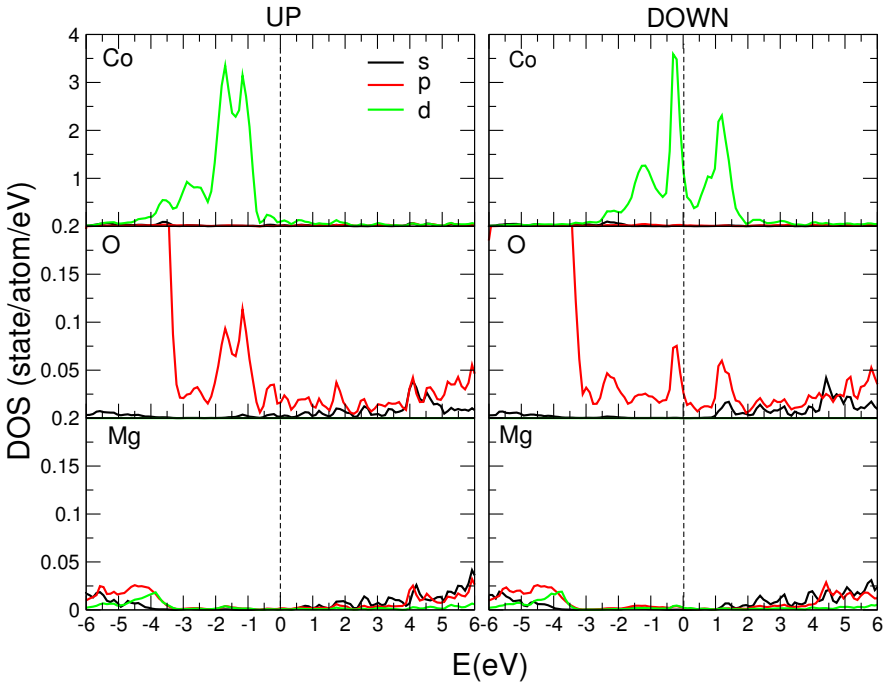

Figure 5.21: Layer and orbital projected DOS for the atoms at the FeCo/MgO interface.

5.6.2 M-MgO/FeCo junction

We also examined the M-center defect level position within FeCo/M-MgO MTJ in similar fashion as for Fe/MgO. To not repeat the whole analysis we will present here only the case where the M center is in the middle layer of the MgO spacer. As it was seen for Fe/MgO, systems shifting and rotating the M center does not influence the energy position of the defect levels and repeating similar detail analysis will not bring us different physics.

Fig. 5.22 presents the layer projected DOS for the MgO spacer. The M center peak position is this time closer to the Fermi level than that of Fe/M-MgO. The M_2 state is now at -0.2 eV while M_1 state shifts to -1.2 eV. The F center, not shown here, is at -0.7 eV below the Fermi level, i.e., in between the M center states as for Fe/M-MgO. The shift of all defect states is by 0.5 eV towards higher energies. The same band structure shift was also observed in case of an ideal FeCo/MgO junction. Therefore, it is not only the defect positions that are shifting upon the change of the electrode but the whole band structure of MgO which is rigidly shifted due to different electron rearrangement at the interfaces. The separation between the MgO valence band and the F/M center levels is actually the same regardless of the electrode type.

We studied also junctions with a pure Co electrode and an alloy FeCo electrode with 50% mixture of Fe and 50% of Co at the interface. We found that pure Fe and Co at the interface define the lower and upper limits for defect level position. Any mixing of Fe and Co at the interfacial electrode layer will shift the vacancy position accordingly between these two limits.

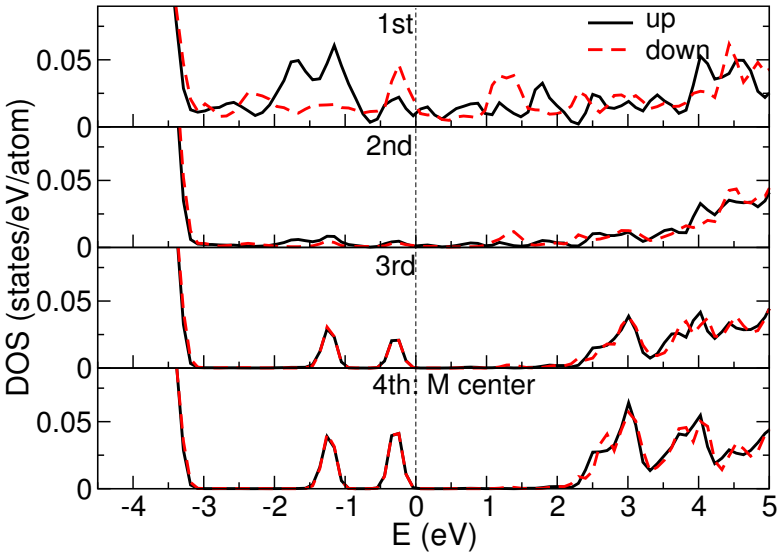

Figure 5.22: Layer projected DOS for M-MgO/FeCo MTJ with the M center located in the 4th ML.

5.7 Chain of vacancies

For the moment we only discussed a single F and an M-center type oxygen vacancies. However, it is interesting to know what will happen if we include more oxygen vacancies in one junction? A scenario with randomly distributed defects were considered already by Ke *et al.*[100] (see sec. 2.4.1). One more interesting possibility arises due to a chain of vacancies, i.e. one oxygen vacancy, i.e. F center, appears in each layer of MgO through the whole MgO spacer. One can imagine that such chain is a channel that connects the two ferromagnetic electrodes and forms what is called a hotspot.

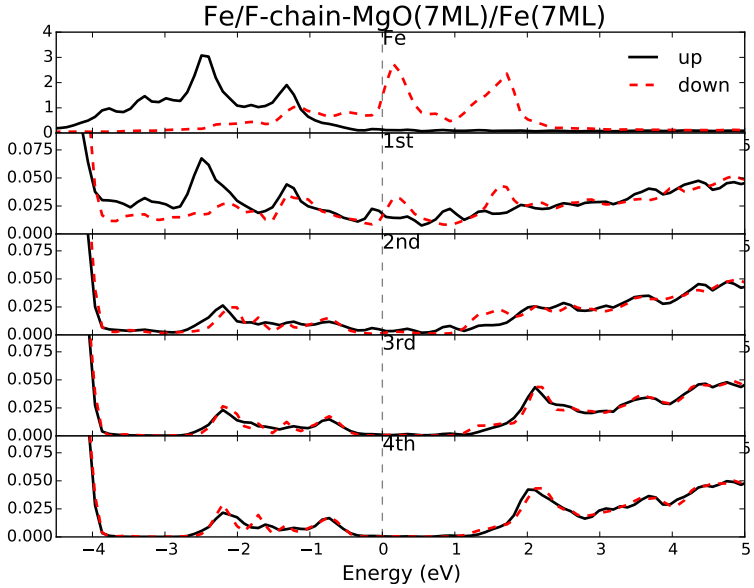

Figure 5.23: Layer and atom projected DOS for MgO/Fe MTJ with a F center chain along the whole MgO spacer.

We decided to explore this scenario and see whether it will bring any new physics. Fig. 5.23 shows the layer projected DOS for a chain of F centers. What is interesting is that we notice a broad band of defect levels at the vicinity of the Fermi level. In fact, there is still some DOS up to the 3rd MgO layer. If we switch to FeCo electrodes or reduce number of MgO layers we can generate non-zero DOS at the Fermi level going through the whole structure.

5.8 Complex band structure of defects in MgO

As it was explained in Sec. 1.2.4, during electron transport thorough a MTJ, electrons coming from a ferromagnetic electrode will couple to the decaying states in an insulator band gap. At a given energy and $\mathbf{k}_{\parallel}$ point the propagating states have to couple to decaying ones with the same symmetry. Then, the attenuation coefficient of the electron wave function will be also symmetry dependent. The properties of these evanescent states can be evaluated based on the complex band structure (CBS) of the insulating spacer, i.e. dispersion relation of the form $E(k_z)$ with $k_z = q + i\kappa$. Therefore, before going into more intensive transport calculations involving F and M centers, one can try to make some predictions based on the CBS of MgO and verify the changes induced by the defects to the attenuation coefficient κ. The CBS calculations of F/M-MgO were performed employing the PWCOND module.[40,155] We used a 64 atom supercell and the CBS was evaluated along Γ-X high symmetry direction in the BZ. The resulting CBS plot was quite complicated due to band folding. Therefore, as done by *Velev et al.*[28] regarding the F-type MgO CBS, we extracted only the data corresponding to Δ_1 symmetry channel. Moreover, when the defects were introduced, some loops were connecting the defect level with the conduction band states at X point in the BZ. These loops were reflected back to the Γ for better visualization and comparison.

We present in Fig. 5.24 the CBS of M-MgO for a M center lying in a plane that is either orthogonal to (panel a), or contains (panel b), the [001] direction of transmission, which we labelled as z. The intersection of these loops with the Fermi level determines the coefficient $\kappa = |Im\ k|$ of exponentially decaying transmission along z for the electrons at the Fermi level that tunnel across the barrier. Here, the Fermi level of the FeCo/MgO/FeCo system was used, and the complex loop for ideal MgO is shown for comparison (blue dashed line). We also show the results for a F center in MgO (panel (c)). When the M center is oriented perpendicular to z, we find that $\kappa_{\mathrm{M-MgO}} \simeq \kappa_{\mathrm{MgO}}$. In contrast, we find that $\kappa_{\mathrm{M-MgO}} < \kappa_{\mathrm{MgO}}$ when the M center is partly along z. This means here that the important Δ_1 tunnelling transmission, at zero-to-low applied bias voltage across a M-type MTJ, of electrons with respect to the M_2 state, is comparable to that of an ideal MTJ, and can even be enhanced when M center is partly aligned along the transport direction.

These predictions, however, should be treated with caution. First of all, we consider here only Δ_1 channel completely neglecting other symmetries. One has to remember that the resulting transmission is a sum of all spin and symmetry channels and the possible enhancement of transmission when the M center is partially along the z direction might not be that straightforward as expected from CBS since we cannot say how κ values are changed for other channels. Second, the κ is defined at point of

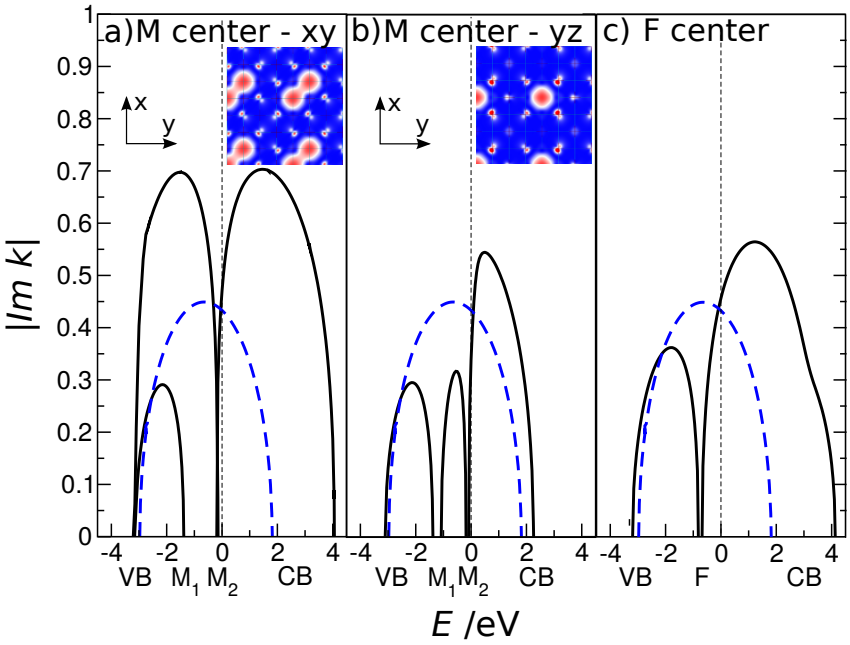

Figure 5.24: Attenuation coefficient of the tunnelling electron wave function across the MgO band gap of the Δ_1 channel for M-MgO for a M center in (a) the xy plane and (b) the yz plane. The corresponding cases of bulk MgO (dashed blue line) and of F-MgO in panel (c), are shown for comparison. The Fermi energy is that of a FeCo/MgO/FeCo heterostructure. The energy positions of the valence band (VB) and conduction band (CB) edges, and of the F, M_1 and M_2 states are denoted. The electron density plots of the antibonding M_2 state within panels (a) and (b) depict the M center's geometry relative to the direction z of the tunnelling transmission.

intersection of the Fermi level and the complex loop. Here, the Fermi level was taken from FeCo/MgO calculations. But, as was mentioned the position of the Fermi level is very sensitive to the variations of the interfacial distance. We did not include any relaxation at the interface which would probably affect the Fermi level. As it can be seen in Fig. 5.24 even small changes to the position of the Fermi level can change significantly the resulting value of κ, especially when the defects are considered. Even if we adapt the Fermi level from Fe/MgO calulation it would be 0.5 eV higher than for the FeCo/MgO and value of κ would increase for all defected structures. Third, the CBS is evaluated assuming periodic boundary conditions and infinite bulk structure of MgO. However, in a real junction the size of the MgO spacer is limited and the Bloch theorem might not be properly applied. One would need to add vacuum in the simulation cell to get more realistic band structure. In such case however, the complex band structure becomes more difficult to interpret since, as shown for thin films, the band gap of MgO changes when approaching the surface.

5.9 Summary

In this chapter we analyzed the ground state electronic properties of M centers embedded either in MgO bulk or MgO spacer in the Fe(FeCo)/MgO MTJs. We showed that the creation of an M center leads to the appearance of two occupied energy levels within the MgO band gap denoted as M_1 and M_2. The M center is created by the interaction of the two F centers therefore the M-state levels mimic the bonding (M_1) and antibonding (M_2) atomic-like states and the barrier height associated with the M_2 state will be always smaller than the one associated with the F center. Moreover, the M center also affects the closest oxygen atoms which leads to its effective size of 4 ML in the defect plane and 3 ML in the perpendicular direction. This fact restrict the size of the MgO spacer which can be used in order to preserve the properties of the M centers to at least 5 ML.

By attaching ferromagnetic electrodes we were able to establish the defect level position with respect to the common Fermi level and compare the calculated values with experimental data. We have found the energy range for the M_2 state from -0.7 eV up to -0.2 eV below the Fermi level when we switch from Fe to FeCo electrode. The M_1 state is found 1 eV lower in energy in both cases. The F center, as expected, is placed in between the M center states and is at -1.2 eV and -0.7 eV for Fe and FeCo electrodes respectively. The change of the defect level position upon changing the electrode is due to different electron transfer at the interfaces for each system. In fact, the whole band structure of MgO is shifted while the distance between the defect level and the MgO valence band remains the same. As we verified, shifting the M center within the MgO layers or changing its orientation does not influence significantly the corresponding energy level positions. Therefore, we can associate the measured barrier heights of $\approx$0.4 eV with the presence of paired oxygen vacancies.

It is however important to notice that when the defect is approaching the interface the associated DOS of the electrode is not much affected. But, as we will see in the next chapter, changing the position of the defect with respect to the interface impacts significantly the resulting transmission. The complex band structure considerations suggest also that the orientation of the M center with respect to the transport direction is important. As such, if the M center is partially along the transport direction, i.e. in a plane perpendicular to the interfaces, the attenuation coefficient for the Δ_1 channel is expected to be smaller than for the M center in a plane parallel to the interfaces and the resulting transmission should be enhanced. All these points will be addressed in the next chapter where the transmission is discussed.

6 Transmission through the Fe/MgO/Fe junction

In this chapter we will discuss the transmission calculations for Fe/MgO/Fe junctions with various types of oxygen vacancies in the MgO spacer. The calculations were performed using both PWcond and TranSIESTA, which implement the Landauer-Büttiker formula for evaluating the conductance. The PWcond was used for most whereas the TranSIESTA was used only when a finite voltage is applied. We will discuss the changes in the transmission due to variation of the MgO thickness and the defect position with respect to the electrode. We will also show that the orientation of the M center with respect to the transport direction is important as suggested by the CBS calculations. In the last part, we will briefly present the results obtained with the TranSIESTA code when a finite voltage is applied. The latter are preliminary and are not yet conclusive. They will be discussed as a perspective of this work.

6.1 Ideal MgO-based junctions

We started with the calculations of junctions with the ideal MgO structure to have a reference point when the defects are introduced. The number of the MgO layers was varied and we will first focus on structures with 5 MgO ML spacer. The results found for the 7 ML spacer are similar and will be only briefly discussed. All the presented data concern the conductance calculated at the Fermi level unless stated otherwise in the text.

Fig. 6.1 presents the transmission in the two dimensional Brillouin Zone (2D BZ) for the parallel electrode magnetization for the spin up and the spin down electron channels (the left and the middle panels) and the corresponding transmission for the antiparallel configuration (the right panel). In agreement with previous theoretical predictions discussed in the Chapter 2, we found the majority electron transmission

centered around the Γ point which is dominated by the Δ_1 symmetry. The transmission for the minority channel occurs basically at the edges of the 2D BZ and is much smaller than for the majority channel. The transmission in the AP configuration is a mixture of features seen in both spin channels. By summing the transmission over the BZ

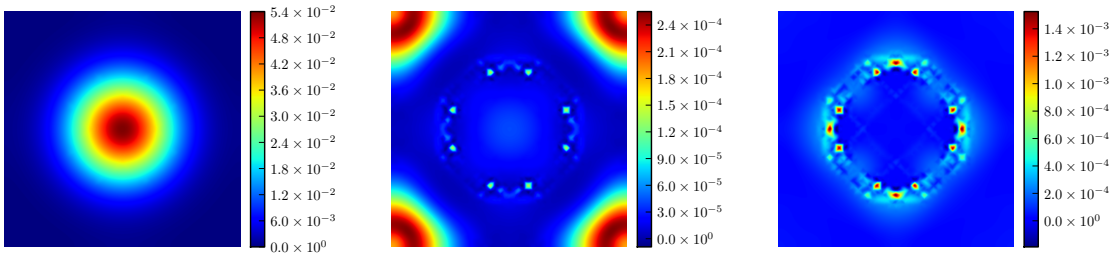

Figure 6.1: Transmission in the two dimensional Brillouin zone (2D BZ) for ideal Fe/MgO(5ML)/Fe junction. The panels correspond respectively to the transmission in the P configuration for the spin up and the spin down channels and the transmission in the AP configuration. All other transmission figures are arranged in the same manner.

and multiplying by G_0 for each channel we obtained the conductance and the resulting TMR. In Tab. 6.1 we summarized the results for junctions with 5 and 7 ML of MgO. As expected, the value of the transmission decays exponentially with the thickness of the MgO spacer and hence drops by at least one order of magnitude when we go from 5 to 7 ML of MgO. At the same time the TMR increases with the number of the MgO layers. This reflects the spin filtering effect discussed in detail in Chapter 1. In particular, along the transport direction at the Fermi level of Fe, states with different symmetries for the spin up and the spin down electrons exist and give rise to high TMR values found for Fe/MgO/Fe crystalline junctions. The Δ_5 and $\Delta_{2'}$ symmetry channels appear for both spin populations and contribute to the conductance in P and AP configurations. The Δ_1 symmetry is present only for the majority electron population and dominates the transmission in the P configuration. Each of these symmetry channels has a different attenuation rate in the barrier region such that $\kappa_{\Delta_1} < \kappa_{\Delta_5} < \kappa_{\Delta_{2/2'}}$. When the MgO thickness is increased the contributions to the conductance from strongly attenuated Δ_5 and $\Delta_{2'}$ channels become smaller. This leads to bigger overall difference in the transmission between the P and the AP configurations and causes the increase of the TMR. According to literature,[50] the TMR value should continue to grow up to 13 ML of MgO where we expect that the Δ_1 will be dominating the transmission. After exceeding this thickness the TMR will also start to decrease due to exponential decay of the tunnelling current.

Table 6.1: The calculated total transmission and resulting TMR for ideal Fe/MgO/Fe junction with 5 and 7 ML of MgO.

	P-UP	P-DOWN	AP	TMR [%]
5 ML	$7.90{\cdot}10^{-3}$	$4.57{\cdot}10^{-5}$	$9.99{\cdot}10^{-5}$	7850
7 ML	$5.33{\cdot}10^{-4}$	$2.93{\cdot}10^{-7}$	$4.26{\cdot}10^{-6}$	12402

6.2 F/M center in the middle layer of MgO

In the next step of our studies, we generated oxygen vacancies in the middle layer of the MgO spacer. The M center was placed in a plane parallel to the interfaces. Fig. 6.2(c) and 6.3(c) show the corresponding 2D BZ transmission for F and M centers, respectively. The transmission distribution for the spin down electrons is almost unaffected by the presence of the vacancies. We observed only an increase in the transmission amplitude with respect to the ideal case. More significant changes are noted in the spin up channel where a clear distinction between the F and the M defects can be made. It seems that F center scatters the propagating electrons to states with higher **k**-vector values. As a result, the transmission has a minimum at the Γ point and occurs mostly along k_x and k_y lines having a maximum at the edges of the 2D BZ. The electrons are scattered symmetrically in each direction due to spherical symmetry of a single oxygen vacancy. However, for the spin up transmission with M center, it becomes broadened in the 2D BZ but sill with maximum values mostly centered around the Γ point. It clearly suggest that, in contrast to the F center, the coherent transport can be still possible when M center exists in the MgO spacer. Even so, the total transmission in the spin up channel is reduced with respect to the ideal junction (Tab. 6.2). It is however counter intuitive that the total transmission for the spin down channel and the AP configuration are enhanced when we introduce the F and M vacancies. Furthermore, the transmission distribution in the AP configuration changes significantly compared to Fig. 6.1. The drop of the TMR when the defects are present is evident but reaches higher values for the M center rather than for the F center. We found similar trends also for the 7 ML spacer for which the total transmission is shown in Tab. 6.2. Again, if we increase the number of MgO layers the TMR also increases regardless of the type of defects. The transmission results obtain for the structures with oxygen vacancies

Table 6.2: Total transmission and resulting TMR for Fe/F-MgO/Fe and Fe/M-MgO/Fe junctions with 5 and 7ML of MgO. The F/M center is always in the middle layer.

	P-UP	P-DOWN	AP	TMR [%]
F (5ML)	$7.21{\cdot}10^{-4}$	$6.31{\cdot}10^{-5}$	$3.20{\cdot}10^{-4}$	145
M (5ML)	$1.71{\cdot}10^{-3}$	$1.47{\cdot}10^{-4}$	$4.48{\cdot}10^{-4}$	315
F (7ML)	$1.19{\cdot}10^{-5}$	$6.21{\cdot}10^{-7}$	$3.08{\cdot}10^{-6}$	304
M (7ML)	$6.19{\cdot}10^{-5}$	$6.87{\cdot}10^{-7}$	$3.63{\cdot}10^{-6}$	1624

can explain the experimental results of high TMR in the junctions with the 0.4 eV barrier height due to paired oxygen vacancies. It also confirms the initial assumption that coherent transport can be preserved when an M center is present.

Note that, the defect level positions discussed in the previous chapter were evaluated using the VASP code with the PAW basis set. Here, we switched to a plane wave basis set in conjunction with the USPP. We checked that the shape of the layer projected DOS is practically the same but we noticed asmall shift of about 0.15 eV, of the F and M_1 states towards lower energies. Therefore, we have examined also the transmission in the energy window ±0.1 eV around the Fermi level to verify how this shift can influence

the conductance. In the case of the spin up transmission the 2D BZ distribution and the amplitude of the transmission is practically the same for all structures. However, some changes were observed in the spin down transmission. This is caused probably by the interfacial resonant states (IRS) which have stronger contribution for the spin down transmission. As we will show in the part concerning the TranSIESTA calculations, the spin down channel is also more affected by the changes in bias voltage than the spin up channel. Nonetheless, this fact should not influence the generality of the presented results since the contributions from the spin down channel to the G_{P} are much smaller than from the spin up electrons.

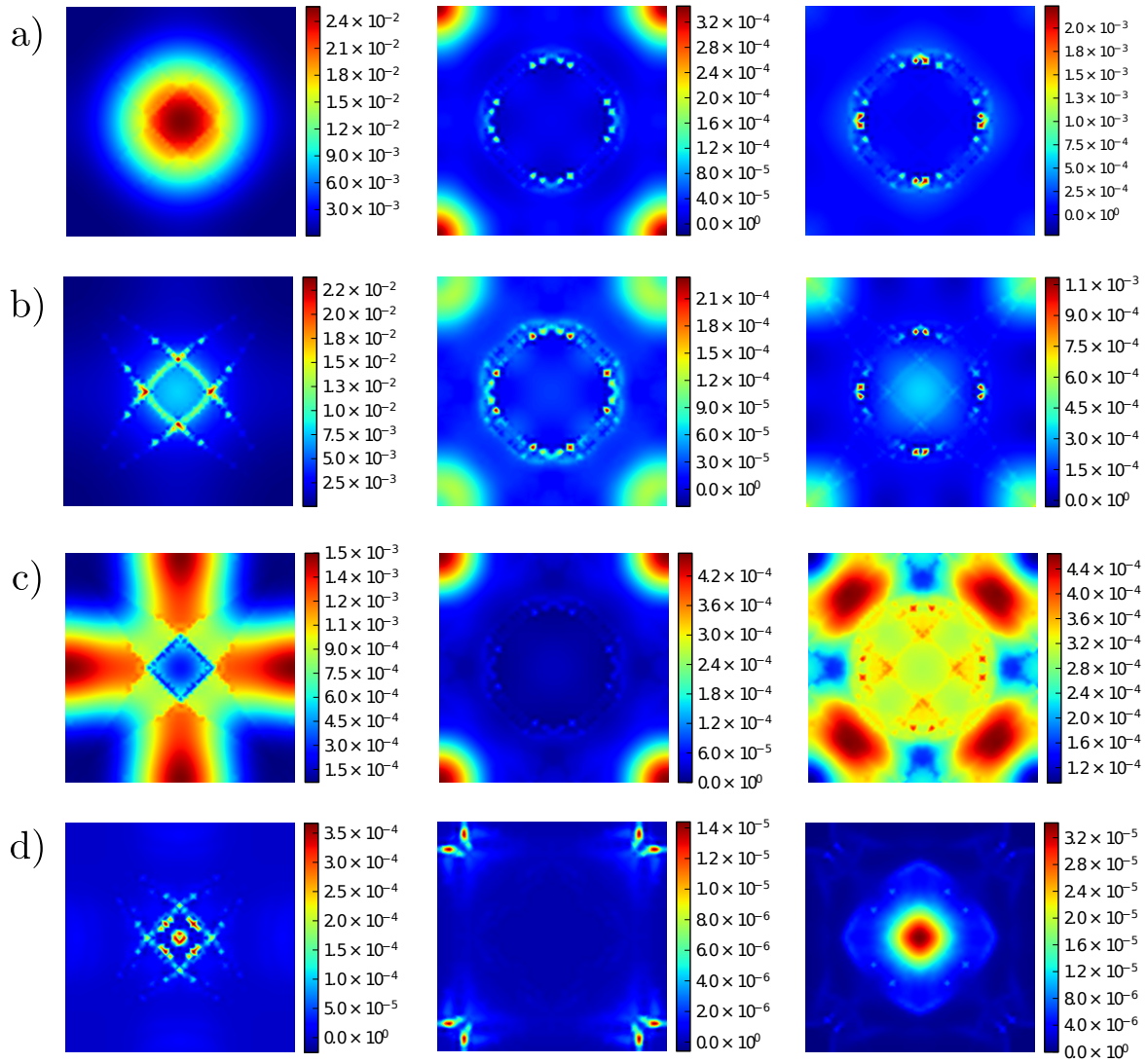

Figure 6.2: Transmission in the 2D BZ for Fe/F-MgO/Fe junction with F center in a) first ML, b) second ML, c) third ML and d) fourth ML. From the left panels correspond to the transmission of spin up and spin down channels in P configuration, and the last the AP configuration. Note that panels a-c are for F-MgO with 5 ML spacer whereas panel d is for 7 ML spacer.

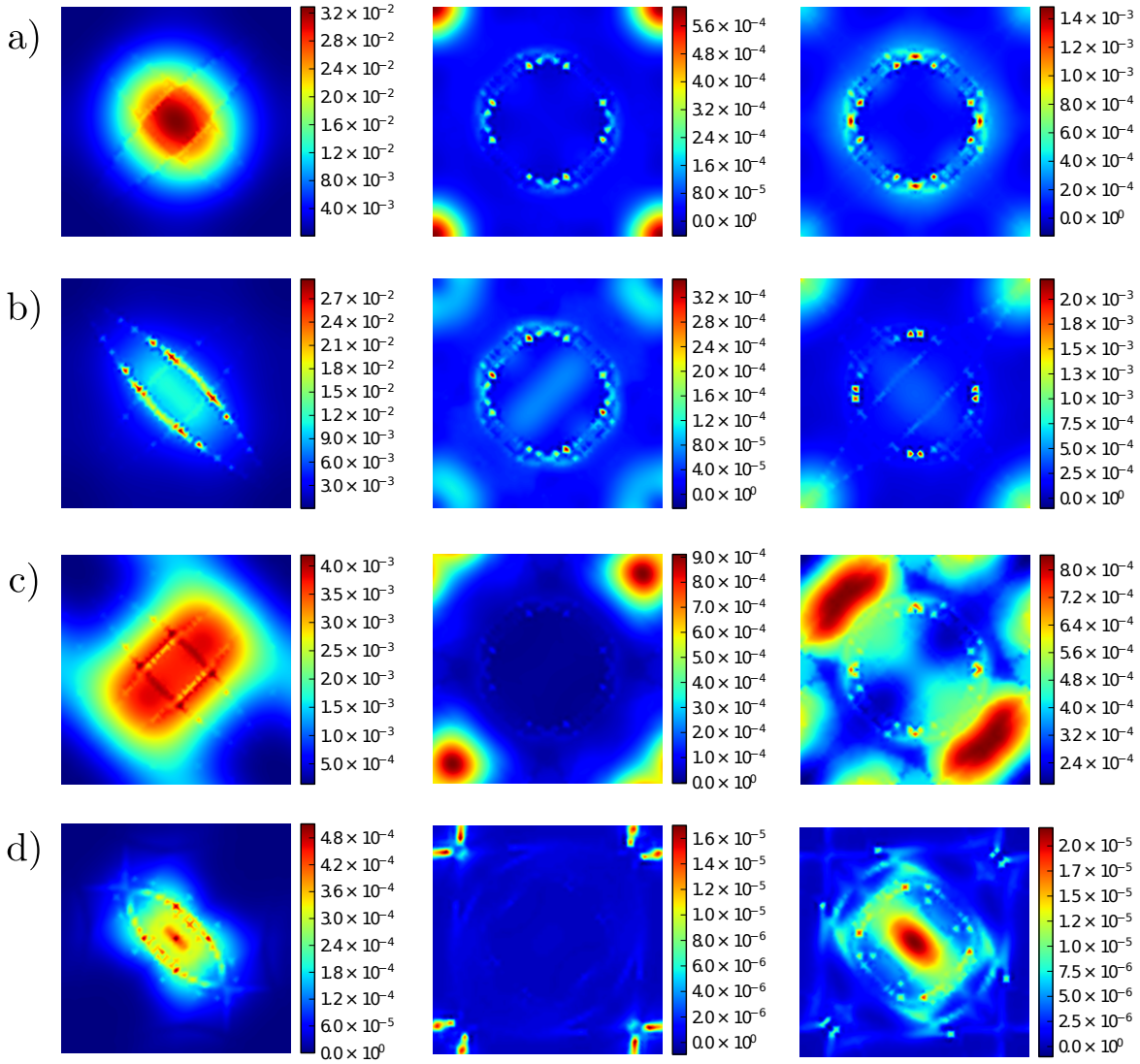

Figure 6.3: Transmission in the 2D BZ for Fe/M-MgO/Fe junction arranged in the same manner as Fig. 6.2 but for M center.

6.3 Effect of shifting the vacancy on the transmission

We wanted to verify whether the modifications to the transmission induced by the F and M centers are sensible to their position in the junction and hence to the surrounding environment. To do so, we varied the position and the orientation of F/M vacancies in MgO as discussed in the previous chapter. Even though, we did not observe any significant change in the layer projected DOS when the vacancy was approaching the interface, the transmission, was found to significantly depend on the defect position.

Figures 6.2(a) and 6.3(a) show the 2D BZ transmission with vacancies generated in the interfacial MgO layer. Note that, the M center is always in the plane parallel to the interfaces. Interestingly, we found that the transmission distribution is almost the same as for the ideal junction with the peaks amplitude very close to the ideal case

(see Fig. 6.1). The calculated TMR reached about 4261% and 3911% for the F and M center respectively, and they are of the same order of magnitude as for the ideal junction.

More surprisingly, when we placed vacancies on the second layer from the interface the transmission decreases and we observed some new sharp spikes in the spin up channel (Figs. 6.2(b) and 6.3(b)). The spin down and the AP transmission distributions are only slightly affected. Again, there is no clear distinction between the F and M center influence.

To understand this behaviour we compare these result with the case of the 7 ML MgO spacer where the vacancy is in the middle layer and is symmetrically screened from the ferromagnetic electrodes by three MgO layers on each side. The resulting transmission for F and M center is plotted in Figs. 6.2(d) and 6.3(d), respectively. Once more we witness the appearance of additional features coming from sharp spikes surrounding the middle peak. Some changes are also noticeable in the spin down and the AP transmission, but these changes are due to symmetry filtering effects discussed before. We might try to explain this oscillatory-like behaviour considering the geometrical position of the vacancy with respect to the Fe atoms. In Fig. 6.4 we show schematic cross section through the Fe/MgO/Fe junction. We can distinguish two situations: (i) in the 1^{st} oxygen atoms/vacancies are directly on top of Fe atoms, (ii) in the 2^{nd} the distance between the Fe and O/vacancy is increased and the Fe-vacancy interaction is screened by Mg atoms. Apparently, if the Fe-vacancy interaction is screened by Mg atoms we obtain additional sharp features not seen when the vacancy is in the same line as the interfacial Fe atom (1^{st} case). The layer alternation also causes rotation of the M center in the xy plane when we go from one layer to the next one and explains the observed rotation in the transmission amplitude in the 2D BZ (compare for example panel (c) and (d) in Fig. 6.3).

Figure 6.4: Schematic cross section through the Fe/MgO/Fe structure. We can distinguish two cases: 1^{st} when the vacancy is generated in the line on top of interfacial Fe atom and 2^{nd} when the distance between the Fe and vacancy is increased and interaction between the two is screened by Mg atoms.

We analyzed also in more detail the orbital projected DOS at the interface. This time we considered only one of the Fe atoms directly on top of the vacancy/oxygen. Here, we will focus on the M center, the results for F center are similar. In Fig. 6.5 we compare the changes in the d-orbital DOS for Fe when the M center approaches the interface. The shaded area corresponds to the ideal junction. As before, the M center on 3rd or 4th ML does not influence the interfacial Fe atoms. Even if the M center is present on the 2nd ML we do not observe a significant d-DOS variations. However, at the interfacial layer when the M center is in direct proximity to the Fe atom the d-DOS changes. To find out what is the nature of this change we examined the d-orbital DOS projected on each angular momentum component (Fig. 6.6). We examine two cases, the first with Fe on top of the M center and the second with Fe on top of

O with the M center in the middle of the spacer (4th layer). In the previous chapter, we showed that the peaks due to d_{z^2} and $d_{yz/xz}$ for both spin populations, coincide in energy with O-p states indicating hybridization between the two atoms. When we introduce the vacancy we observe a pronounced modifications for the d_{z^2} orbital. One has to remember that the M center is not a vacuum region but contains localized electrons which now interact directly with the electrode. The d_{z^2} is strongly reduced due to this interaction for the spin up electrons and it is shifted in energy for the spin down electron population. Some changes are also visible for the d_{yz} and d_{xz} orbitals. Moreover, the differences in the spin down electron population at the Fermi level are noticeable. We studied also k-resolved DOS near the Fermi level for the interfacial Fe layer. Nonetheless, the changes were not significant when the vacancy was closer to the interface. We noticed mostly the variations in k-distribution for d_{z^2} state as also indicated by the plots presented here. For simplicity we will not show the data here.

The behaviour we found for vacancies generated at the interfacial MgO layer can be interpreted as a reduction of the effective MgO thickness and thus of the barrier for electron tunnelling when vacancies are present at the interface.[50]

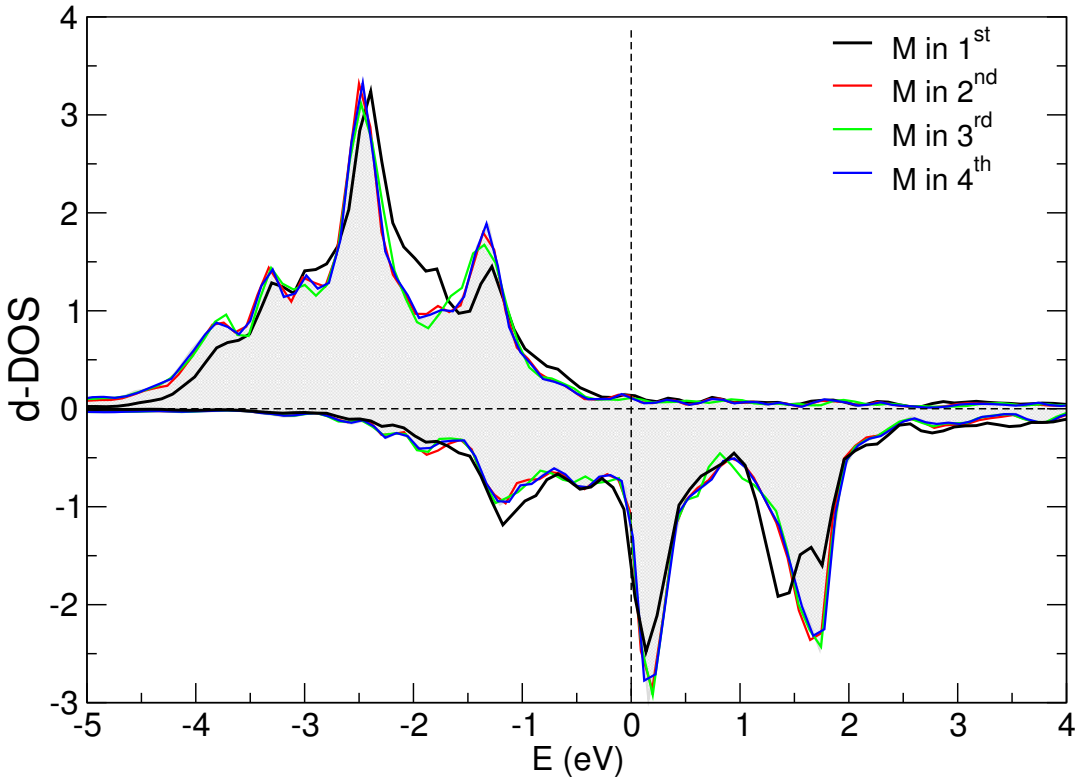

Figure 6.5: The d-projected DOS for Fe atom at the interface on top of the vacancy line. The M center is shifted from the 1st to the 4th MgO layer.

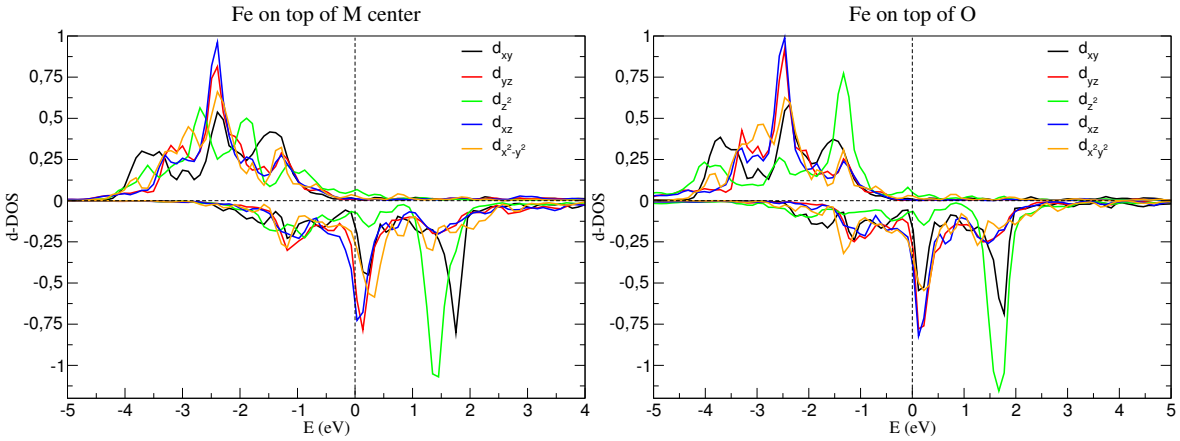

Figure 6.6: The d-DOS projected on each angular momentum component for the same Fe atom when the M center is in the interfacial layer (left) and when it is in the 4th layer (right).

6.4 Rotating the M center

One more interesting scenario we took into account was rotating the M center plane. The results we discussed so far were about the M center placed in a MgO plane parallel to the interfaces. As it was already mentioned in the previous chapter, since the M center extends over few layers it can be rotated with respect to the transport direction. The CBS calculations indicated that if the M center is partially along the transport direction the attenuation coefficient for the Δ_1 can be even smaller or comparable to the ideal case. Therefore, we wanted to verify if this will be reflected in the actual transmission. To be consistent, we studied a symmetric structure of the junction so that we had an even number of MgO layers with the M center generated in the two middle layers. We started with MgO spacer of 4 ML but this was not enough to properly screen the M center form the influence of the electrodes and also there was apparently an interaction between the electrodes themselves because the transmission was similar to that for 3 ML. Therefore we increased the spacer thickness to 6 ML with the M center spanned between the third and the fourth planes. We had to also increase the number of electrode layers included in the scattering region to assure proper geometrical matching at the interfaces.

Fig. 6.7 presents the transmission for both spin channels in the P configuration and the corresponding AP one. The spin down transmission is also practically unaffected by the defect, as well as the AP transmission. The spin up transmission is even more concentrated around the Γ point than before. The TMR value reached 1423%, as high as the F/M center in the interfacial layer. In fact, if we compare the spin up transmission in Fig. 6.7 and 6.3(c) we conclude that the shape of the transmission reflects in some sense the symmetry/orientation of the M center. We tried to schematically illustrate in Fig. 6.8 the landscape seen by propagating electron when it approaches the M center with different orientation with respect to the transport direction (along the z axis). When the M center is generated in the same xy plane. i.e. parallel to the interfaces (left panel), vacancies are along the diagonal, the electron wave function encounters simultaneously the two oxygen vacancies. This also explains the elongation of the transmission peak along the diagonal of the plane in Fig. 6.3(c). On the

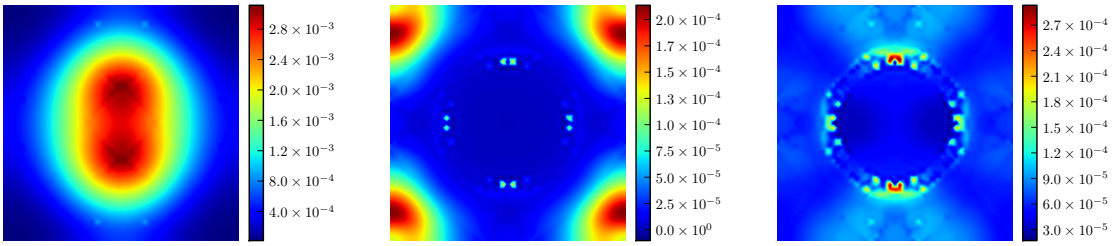

Figure 6.7: Transmission in the 2D BZ for Fe/M-MgO/Fe junction with 6 ML MgO spacer and the M center spanned between 3rd ant 4th ML in the yz plane.

other hand, when the M center is partially along the transport direction, i.e. in the yz plane where the two oxygen vacancies are in consecutive xy planes (right panel), the propagating electron reaches first one oxygen vacancy and then the other. As a result, the transmission is now along the k_y direction in the BZ (Fig. 6.7). The transmission peaks have the same intensity because we considered symmetrical MgO spacer such that electrons propagating from the left and the right electrodes see the same potential landscape. We did not check for the changes in the transmission due to the shifting of the vacancy but we can assume the relative intensity of the peaks can vary.

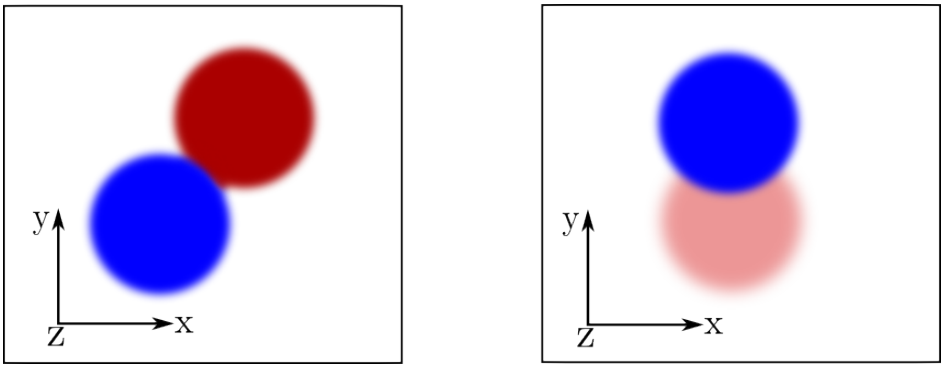

Figure 6.8: Schematic representation of the orientation of the M center with respect to the z axis transport direction. The blue and red balls represent the oxygen vacancies, different colors are introduce just for a better visualization. Note that when the M center is partially along the z axis the two oxygen vacancies are in consecutive xy planes, this is illustrated by blurring the red ball (right panel).

Due to the different orientation of the M center, the character of the propagating wave function can also be affected since the wave function has to be continuous through the whole junction. Therefore, we should be able to observe modifications induced by the vacancy, even away from the defect, reflected in the 2D BZ DOS. We compare the k-resolved DOS for the d-orbitals of the interfacial Fe layer when the M center is in xy plane (Fig. 6.9(a)) and in the yz plane (Fig. 6.9(b)). Clearly the k-resolved DOS distribution varies for the two geometries. The most important contributions to the LDOS are coming from d_{z^2} orbitals (note the different scale for each orbital), the $d_{x^2-y^2}$ and d_{xy} are quite significant while the d_{zx} and d_{zy} are of minor importance. The M center affects basically the k-DOS distribution with respect to the ideal junction, not really the intensity of the DOS. For the spin down electrons, contrary to the spin

up populations, the most important are the contributions from d_{zx} and d_{zy} orbitals. Next, equally significant are the $d_{x^2-y^2}$ and the d_{xy} orbitals while the d_{z^2} are the least involved. Again, the M center causes changes in the k-DOS distribution rather that the DOS intensities. These different orbital contributions in the spin up and the spin down channels agree with the electron symmetries expected to exist at the Fermi level in Fe along the Γ-H direction and explain the high values of the calculated TMR. It is important to recall that the spin up channel includes mostly $\Delta_1(d_{z^2})$ symmetry and some contributions from $\Delta_{2'}(d_{x^2-y^2}, d_{xy})$ and $\Delta_5(d_{zx}, d_{zy})$ symmetries while the spin down channel is composed mostly of electrons with Δ_5 symmetry and less contributions are due to $\Delta_{2'}$ and Δ_1 symmetries. This analysis also shows that the DOS at the vicinity of the Fermi level is not much affected by the presence of defect except at the interface.

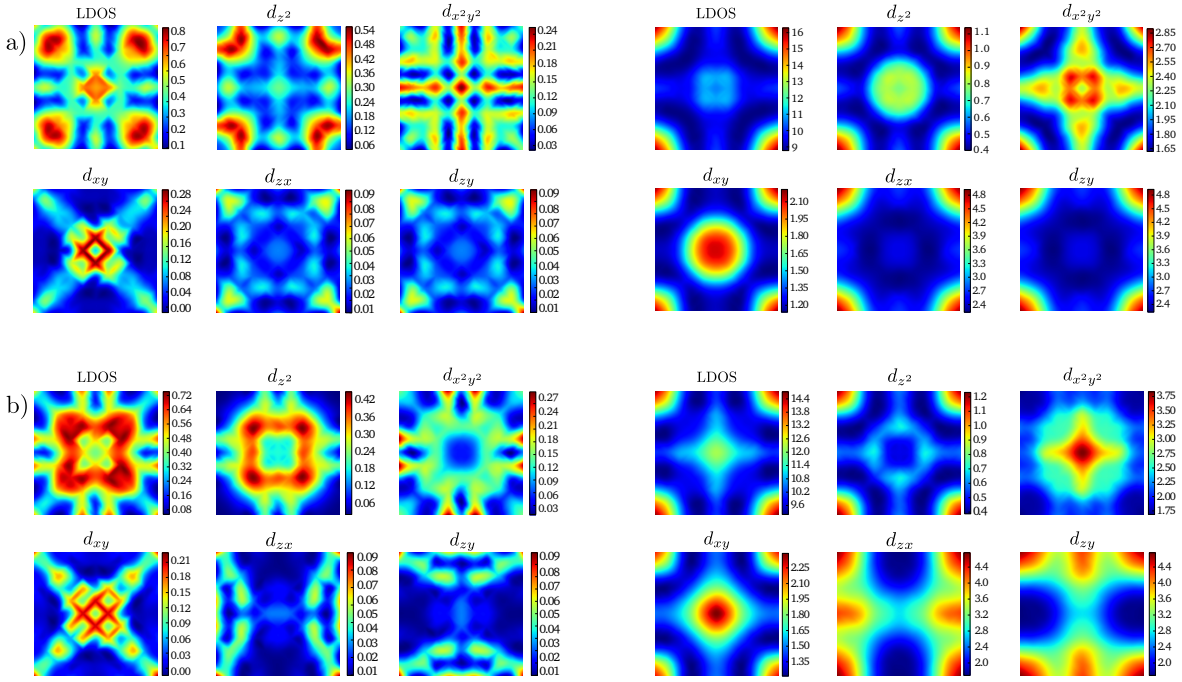

Figure 6.9: k-resolved DOS for d orbitals of interfacial Fe layer at the vicinity of Fermi level a) with M center in the xy plane parallel to the interface with M center in the 4th layer of MgO(5ML) spacer, and b) in the plane perpendicular to the interface, i.e. in yz plane with M center spanned between 3rd and 4th MgO(6ML) spacer. The left panels are for spin up and the right for spin down electron populations.

Note that we did not observe strong changes in the k-resolved DOS of Fe interfacial layer near the Fermi level induced by F and M center in the xy plane compared to the ideal case. In some sense this contradicts the situation discussed here. Before, we found mostly an alternation in the k-DOS distribution in the plane of the F/M vacancy and its closest neighbours while Fe sites where slightly affected only when the vacancies were present at the interface. Here, however, when we rotate the M center the modifications of the Fe 2D BZ DOS between the two situations are quite obvious. One of possible reasons for this discrepancies might be due to different number of MgO layers used, i.e. 5 ML for M in xy plane and 6 ML for the M in yz plane. In other words, the character of the propagating wave function might be influenced by either

the odd or the even number of MgO/Fe ML in the structure. Yet, we did not study in more details the junctions with an even number of MgO layers, especially the ideal case to refer to. At this point it is hard to say if the observed variations in the k-resolved DOS are due to the M center orientation or rather to the odd or even number of MgO layers. It is definitely an interesting direction to follow for further investigations.

6.5 Summary of PWCOND results

In this part we discussed the transmission at the Fermi level for Fe/MgO/Fe junctions in the ideal case and with various oxygen vacancies in the MgO spacer. As expected, we obtained an exponential decay of the total transmission with the MgO thickness an increase in the TMR due to symmetry filtering effects. The introduction of a single oxygen vacancy causes stronger scattering of the electron wave function compared to the double vacancy. This proves that the partially coherent transport remain possible if M centers are present and explains the high TMR values measured for junctions with barriers of 0.4 eV.
Moreover, we found that the position of the vacancy with respect to the electrode is quite important. If the F/M center are present at the interface the 2D BZ transmission distribution is practically the same as for an ideal junction with small modifications in the peak intensities. There is no clear distinction between the two types of defects in this case. The resulting TMR is around 4000% for two vacancy species and can be interpreted as due to the decrease of the effective barrier thickness for the electron tunnelling. Since the electrons remain on the vacancy sites, the hybridization with the Fe atoms changes slightly symmetries at the Fermi level and thus explains the decrease of the TMR compared to the ideal junction. We showed that shifting the F/M center position with respect to the interface can lead to oscillatory-like behaviour and give additional sharp spikes in the spin up transmission if the defects are placed on even MgO layers.

We studied also the changes induced by rotating the M center plane with respect to the transport direction. We observed that the 2D BZ transmission distribution is correlated with the orientation of the M center and the potential landscape felt by the propagating electron due to the presence of the vacancy. We did not study yet the possible modifications of the transmission and k-resolved DOS due to shifting towards the interface of the M center generated in the yz plane. It is also not clear what is the connection between the k-resolved DOS and the odd-even number of MgO layers. This study will be carried out in the near future.

We mentioned in the previous chapter that changing electrode from Fe to Co affects the defect level position. Therefore, we also performed calculations with Co and FeCo electrode and MgO spacer of 5ML to determine the change in the transmission. We did not present these results here since we found similar trends concerning the influence of F and M centers. Also, because experiments with pure Co electrodes or FeCo alloys with only Co at the interfaces are not actually performed. These results were used to determine how the properties of F/M centers depend on the electrode type. As for the Fe electrode, we found that the spin up transmission is affected the most by the presence of vacancies while the spin down transmission distribution does not change

much. The transmission intensity in the spin up channel is always higher in presence of M center rather than F center. Surprisingly, the shift of the defect level with respect to Fe electrodes does not affect much the transmission in the P configuration for M center. More changes were noticed for the F center where we found higher transmission amplitude around the Γ point with respect to the Fe/F-MgO/Fe system. Nonetheless, the scattering to states with higher **k**-vector values was still present leading to lowering of the transmission compared to that of the M center. Also when approaching the F/M vacancies towards FeCo interface we obtained a similar behaviour as for the Fe/MgO/Fe junctions. Therefore, we claim that the properties of F and M centers are quite robust and are not changed much by the different types of electrodes. The most important factors are still the position of the defect with respect to the interface and the orientation of the M center with respect to the transport direction.

6.6 Calculated conductance with TranSIESTA

Our aim was to investigate the behaviour of the transmission across Fe/MgO(5ML)/Fe MTJ, with oxygen vacancies within the MgO spacer, when the voltage is applied. These calculations were done at the end of this thesis and the results presented here are therefore only preliminary and indicative. We started with the same configuration for the scattering region as previously to be able to compare the outcome of both codes. Due to problems with convergence of some structures (see sec. 4.3.2) we will focus here only on the ideal junction and ones with F/M center generated in the middle layer of MgO. We have not yet included the AP magnetization alignment of the electrodes and the presented data correspond only to the P configuration.

Fig. 6.10 shows the 2D BZ transmission at zero bias through the ideal junction for the spin up and the spin down electron channels. The shape of the transmission distribution for the spin up electrons is practically the same as the one found in the previous calculations (see Fig. 6.1). The only difference is the increase of the transmission amplitude which is about one order of magnitude higher than before. On the other hand, the differences in the spin down transmission distribution are much more significant. Here, contrary to the spin up case, the transmission amplitude is decreased with respect to the previous findings. The transmission in the minority electron channel depends significantly on the IRS and one should investigate the DOS of the interfacial Fe layer to revel weather these states are present or not. Unfortunately, it turned out that the size of the electrode we included in the scattering region might not be sufficient for the TranSIESTA calculations.

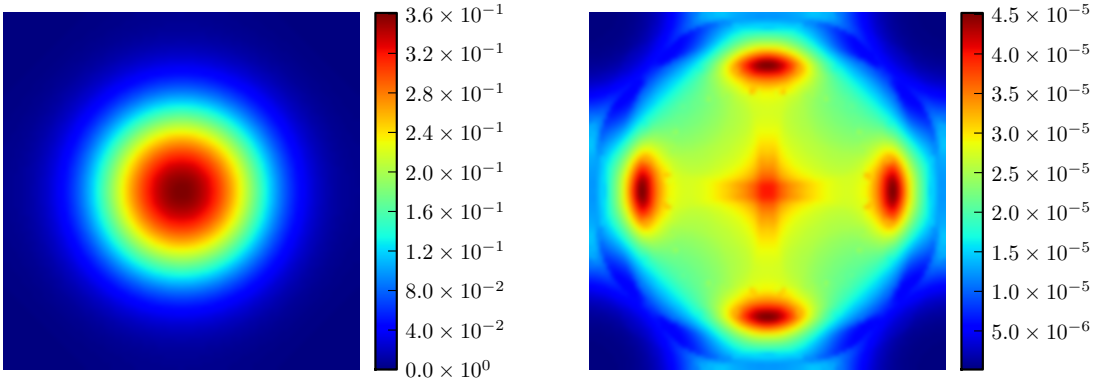

Figure 6.10: k-resolved transmission at 0 V for ideal Fe/MgO/Fe junction evaluated using TranSIESTA.

Therefore, we decided to consider a simplified scenario where we investigate the DOS for Fe with the lattice parameter of MgO, i.e. $a_{\mathrm{Fe}} = a_{\mathrm{MgO}}/\sqrt{2}$, obtained within SIESTA and Quantum Espresso and compared to that obtained with VASP (see Fig. 6.11). For TranSIESTA we compare two basis sets namely the one used in our calculations (solid red line) and the basis set of used by Garcia-Suarez *et al.*[153] (blue dashed line; see sec. 3.3.5 for details). All the curves where shifted to the common Fermi level which is at the zero energy. Clearly, the DOSs evaluated with two codes are shifted with respect to each other. We compared two basis set of SIESTA used before in the literature and

both give the same shift namely the spin up density is moved towards lower energies while the spin down density towards higher energies. The QE DOS is in good agreement with that computed using VASP. The different prediction of the DOS between QE and SIESTA can affect the transmission afterwords and explain discrepancies we observed in the transmission from the PWCOND and the TranSIESTA. In this point however we cannot state what is the cause of the shifting the DOS. Note that the basis sets used in the literature, and then adapted by us, were optimized for Fe structure with lattice constant $a_{\mathrm{Fe}} = 2.866\mathring{A}$ whereas we adjusted the lattice parameter of Fe to that of MgO. It is possible that with change in the lattice parameter these basis sets no longer describe correctly some states. Nonetheless, these predictions show direction in which we can look for a reason of the discrepancies between the two codes and these will be investigated in our future work.

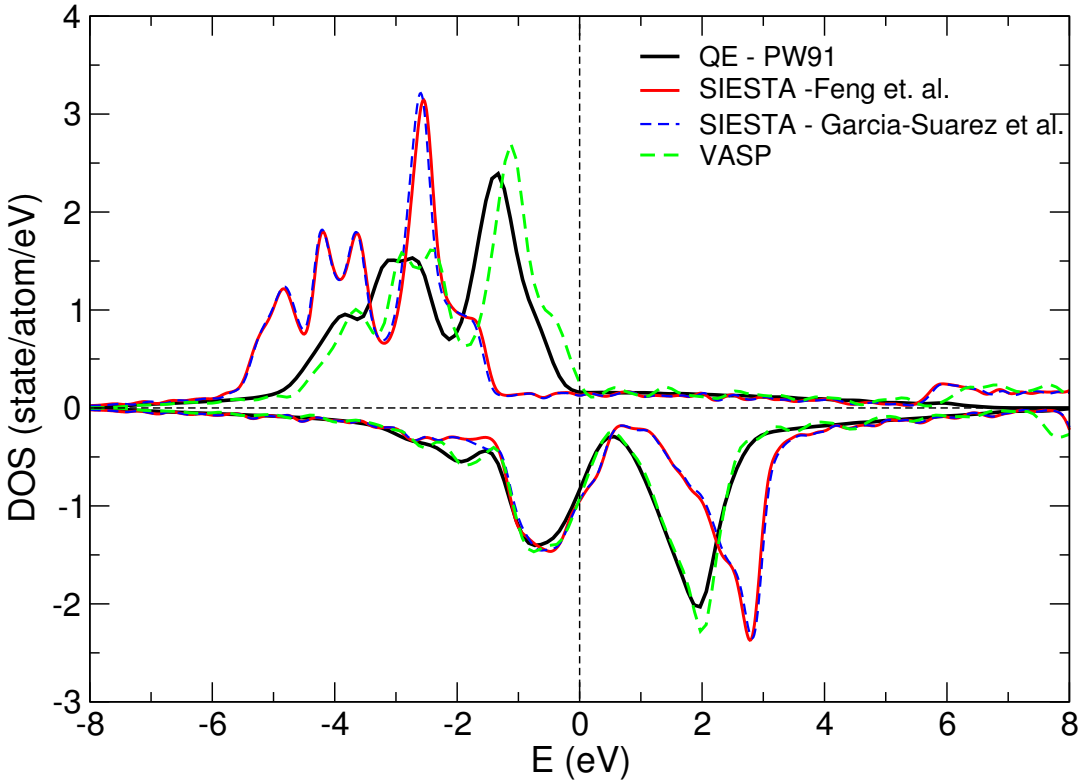

Figure 6.11: Comparison of the DOS for Fe with lattice constant $a_{\mathrm{Fe}} = a_{\mathrm{MgO}}/\sqrt{2}$ obtained from QE, SIESTA, and VASP. For SIESTA we compare also two basis sets, the one used in our calculations (red line) adapted from *Feng et al.*[152] and the basis set used in work of Garcia-Suarez *et al.*[153] (blue dashed line) for similar MTJ.

Despite difficulties in the interpretation of the TranSIESTA output we proceeded with the calculations involving F and M centers. Figs. 6.12 and 6.13 present the transmission for the zero bias for the F and M-type vacancies, respectively. We find similar trends in the transmission amplitude as for the ideal junction, namely the transmission in the spin up channel is increased while in the spin down channel is decreased with respect to the PWCOND results. The transmission distribution for the minority electrons again differs from the previous findings while we can still notice similarities for the majority electrons. In the case of the F center, the maximum of the

transmission is again away from the Γ point. For the M center we can claim that the transmission is mostly centered around the Γ point. The two round bumps present in Fig. 6.13, corresponding to the maximum transmission amplitude, are separated due to the projection of the data on the 2D BZ. If we plot it as a 3D surface (not shown here) we can still observe that the transmission is high in the region between the two peaks. Since TranSIESTA uses localized atomic orbitals the interatomic region might not be that well describe as in the case of plane wave basis set and not all contributions to the transmission might be properly described. What is interesting, in both codes is that vacancies affect more the transmission in the spin up electron channel while the spin down transmission is more sensitive to changes in the energy at which the conductance is evaluated.

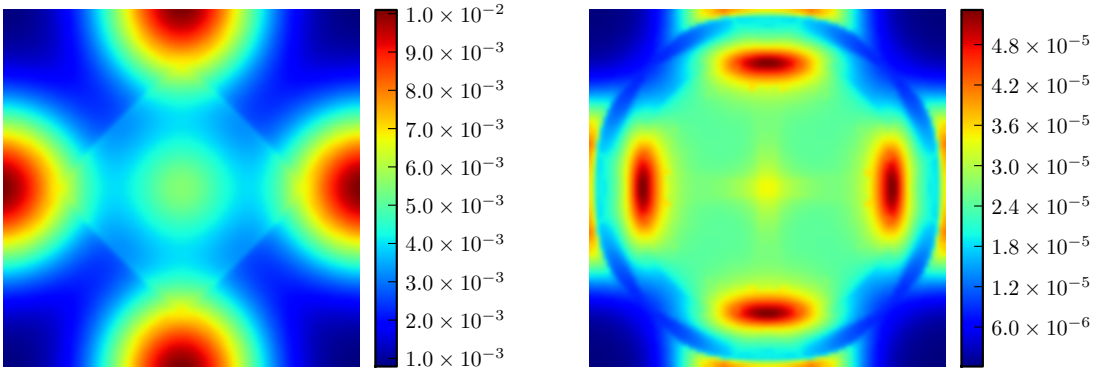

Figure 6.12: 2D BZ transmission at 0 V for Fe/F-MgO/Fe junction evaluated using TranSIESTA.

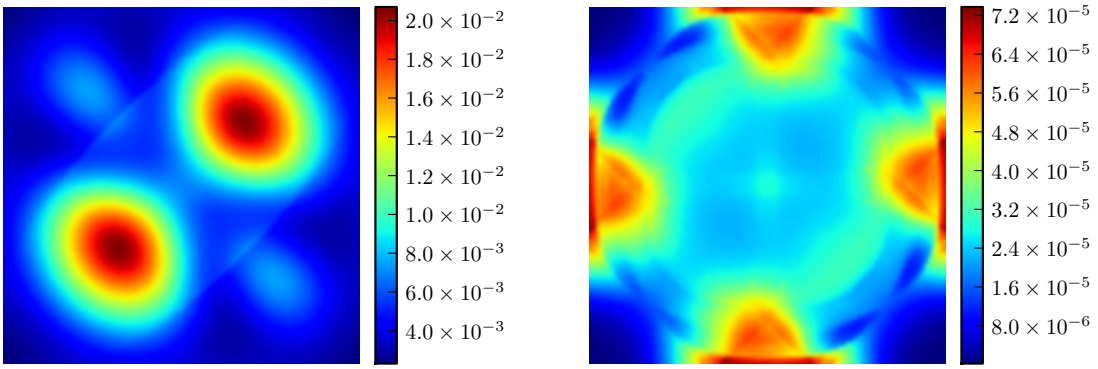

Figure 6.13: 2D BZ transmission at 0 V for Fe/M-MgO/Fe junction evaluated using TranSIESTA.

As stated at the beginning, our goal was to investigate a bias dependent properties of the oxygen vacancies and these results will be discussed now. We studied the changes in the transmission and the electric current up to 0.4 eV. Beyond this value, the calculations of the density matrix for the defect structures did not converge properly. Fig. 6.14 plots the changes in the transmission as a function of the energy

and applied voltage. We compare separately the changes for the spin up and the spin down channels. Interestingly, we notice a peak in the transmission for the M-MgO/Fe around -1.25 eV which indicates the resonant condition with the defect level. In the corresponding case of the F center it seems that the defect level is located at about -2 eV (we can notice only the initial increase in the transmission around this value). We find that the transmission for the spin up channel is not affected much by the applied bias. Bigger changes occur in the spin down channel. Therefore, we compared also the 2D BZ transmission for different bias values and indeed we observed more pronounced variations in the spin down transmission (plots not shown). These drastic changes in the minority spin channel are most probably due to reaching the interfacial resonant states discussed before.

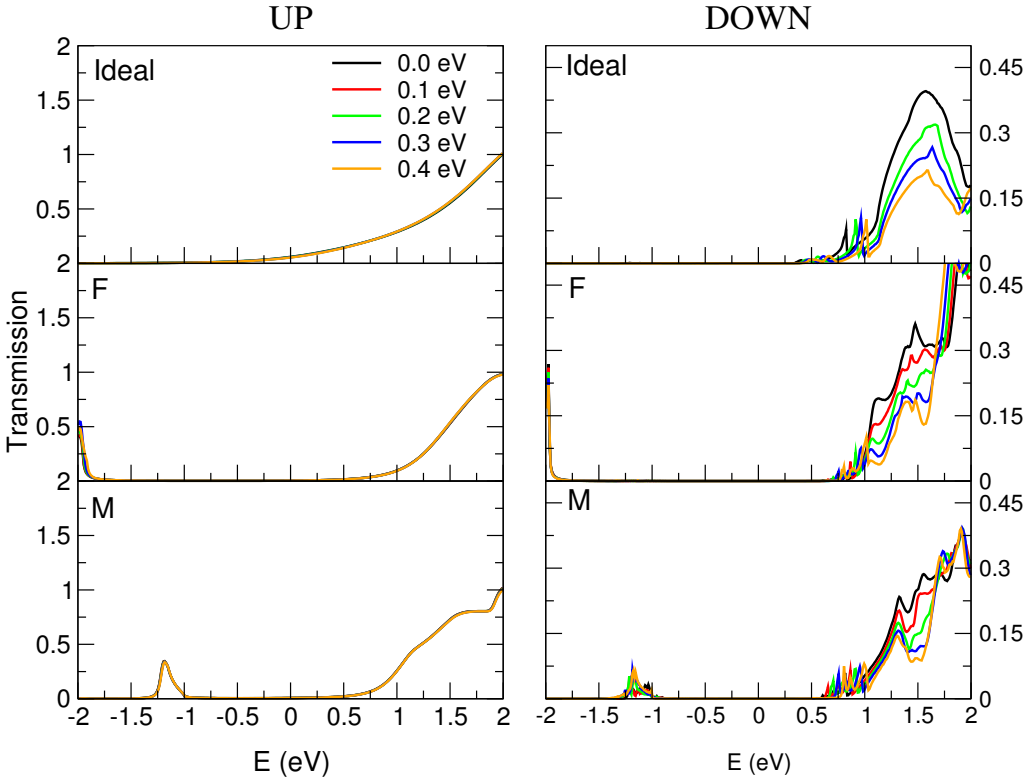

Figure 6.14: Averaged transmission as a function of energy and applied bias for the spin up and the spin down channels.

Finally, we plot in Fig. 6.15 the current-voltage characteristic for the considered junctions. Notably, the highest value of current in the spin up case is predicted for the ideal junction. When the defects are introduced the spin up current drops significantly. Nonetheless, it can be noticed that the current is higher for the M-MgO rather than the F-MgO junctions. The contributions to the current due to tunnelling of the spin down electrons are much smaller than these from spin up electrons. Interestingly, here the current increases when the defect are present. This might indicate that new channels for conduction in the spin down channel become open when the vacancies are introduced.

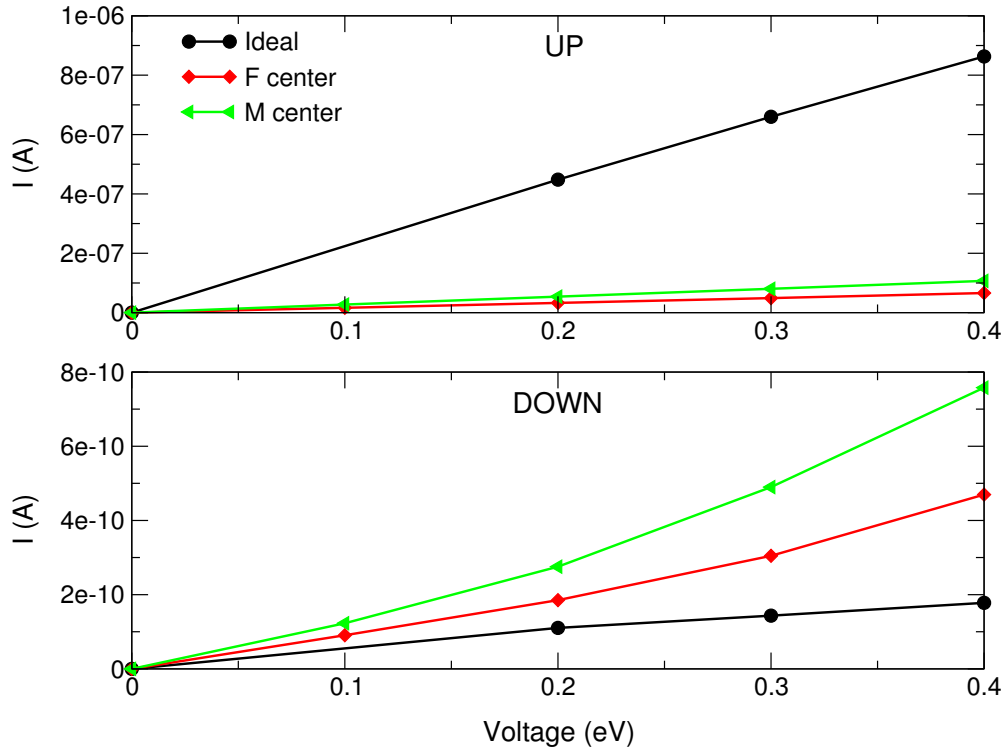

Figure 6.15: Current voltage characteristic of ideal, F-MgO and M-MgO-based MTJs.

Summary

In this part, we compared the transmission evaluated at the Fermi level with two different codes, PWCOND and TranSIESTA. Both codes give similar predictions of a F and M center properties. The transmission in the spin up channel, is centered mostly around the Γ point when a M center is present and is scattered away from the Γ when a F center is introduced. For the spin down electrons the differences in transmission between the two codes are more pronounced. Nonetheless, in both cases we do not observe drastic changes in the spin down transmission distribution when the defects are present. We can actually say that oxygen vacancies affect mostly the spin up electron channel leaving the spin down practically unchanged. On the other hand, the transmission for the minority electrons varies much more than the majority one when the bias voltage is applied. This is most probably due to IRS which are addressed when the bias is changed.

The differences between the codes are mostly due to different basis sets used. In the case of the localized orbitals the interatomic regions might not be that well described as in with the plane wave basis set. Moreover, as indicated by studies of Fe DOS, some states can be shifted in energy when the localized basis set is used and hence do not appear any more at the Fermi level and are neglected in the transmission. The results obtained with TranSIESTA have to be treated with care due to the problems with convergence and the definition of the scattering region and the basis set. As already discussed, this might introduce some additional scattering of the propagating electron wave function and affects the results. The encountered issues regarding the TranSIESTA calculations are left as a perspective work.

7

Probing a device's active atoms using synchrotron radiation

The usual experimental techniques of material science focus either on investigating the physical properties of materials or a response of a device under external stimuli. The last few years brought an intensification of the combined material and device studies, in the so-called *in operando* approach where the objective is to corrolate the device performance to its physical properties.[51–54] This novel study was used for MgO-based magnetic tunnel junction where the junction during magnetotransport measurements was illuminated by soft x-ray radiation. Such a procedure allowed to asses the contributions of the photoelectron emanating from the $1s$ state of oxygen to the electronic transport. These novel experiments were performed at synchrotron facility SOLEIL by experimentalists from IPCMS and were interpreted using our theoretical calculations.[55]

In this part we will explain briefly the principles and purpose of the x-ray absorption experiments and how they can be combined with simultaneous magnetoransport measurements. Then, we will discuss our transport calculations in order to better understand those experiments.

7.1 X-ray absorption spectroscopy

X-ray absorption spectroscopy (XAS) is a technique widely used for structural characterization of a material. The photoelectric absorption occurs if the photon energy is comparable to the binding energy of an electron in an atomic shell, i.e. the energy is in a range 0.1-100 keV.[170] The photon energy is transferred to a core electron which is either ejected from the atom or promoted to an empty state above the Fermi level. Since the absorption process is from a core initial state with a well defined angular momentum, the quantum mechanical selection rules select the symmetry of the final state in the continuum. Therefore, a particular absorption edge can be distinguished

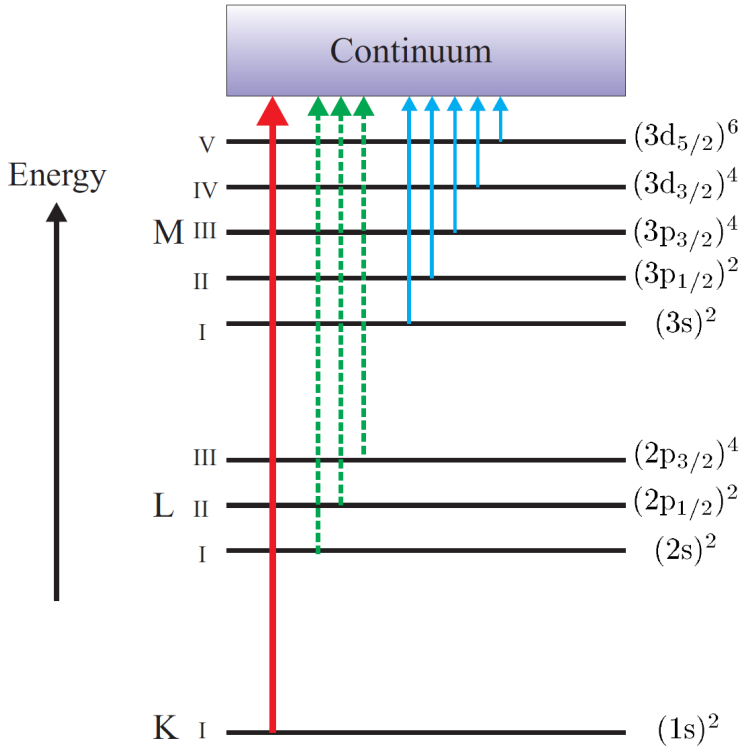

Figure 7.1: A schematic illustration of the photoelectric absorption on a given atomic shell giving rise to K, L, M absorption edges in the x-ray absorption spectra. The shells are labelled as $(nl_j)^{2j+1}$ where n, l and j are principal, orbital and total angular momentum quantum numbers respectively. Taken from 170.

and is labelled as K, L_1, L_2, L_3, M_1, M_2,, etc., and corresponds to the absorption of a photon by a core electron from the $1s$, $2s$, $2p_{1/2}$, $2p_{3/2}, 3s$, $3p_{1/2}$ shell (Fig. 7.1). For example, the most intense feature of K-edge is due to core transitions from $1s$ to p-like final states. After the electron excitation the hole generated in the core shell will be filled by another electron.

The absorption edges are unique for each element and by tuning the energy of the x-ray photons the core level excitations are initiated for a specific atomic species and core orbital within the sample. This makes x-ray absorption a powerful tool giving an insight into material's electronic structure and its environment. One can yield the information about the quantity of atoms, their charge state, chemical environment and the resulting electronic/magnetic properties. This combined with a high brilliance of a synchrotron facility allows to resolve a minute populations of atoms, even if they are buried within the complex multilayer structure of a device.[55]

7.2 Combined XAS and magnetotransport measurement

The combination of an operating device, so as its state is alternated, with simultaneous photoexcitation of the specific species by x-rays, can provide an insight on the

proportion of the atoms which actually contribute to define the device state. In the case of MgO-based MTJs the XAS studies were focused only on the atoms involved in the operation by measuring their magnetotransport properties as they absorb x-rays.

The stacks with composition: glass//Ta(5)/Co(10)/IrMn(7.5)/FeCoB(4)/MgO(2.5)/ FeCoB(2.5)/Ta(1)/Pt(1) (all numbers in nanometers) were fabricated and post-annealed to crystallizes the MTJ interfaces. The SiO_2 was used to insulate the bottom and top electrodes of the device. As explained before, the key role for the performance of the MTJs is played by the spin- and symmetry-polarized density of electronic states created at the interface between the ferromagnetic electrode and the tunnel barrier. Here, one of the crucial factors is the Fe-O bonding and the studies were focused on the K-edge of oxygen. Since oxygen is present not only in the MgO spacer but also in the SiO_2 all these different contributions should be reflected in the measured spectra (see Fig. 7.3 (d)). Therefore, in the first step, the spectra of the non-processed glass//Ta(5)/Co(10)/IrMn(7.5)/FeCoB(4)/MgO(2.5)/ stack, either annealed or not, were measured and used as a reference spectra for MgO. A glass//SiO_2(150) samples were used to obtain the reference data for the SiO_2 that encapsulated the device.

Fig. 7.2 shows the XAS spectra at the O K-edge of the referential stacks for MTJs. The energy range $537 < E(eV) < 541$ is the so called pre-edge region, preceding the O K-edge maximum absorption at 543.5 eV, and giving information about the oxygen sites chemical environment. The pre-peaks observed for the non-annealed samples were qualitatively identified as the spin- and symmetry-polarized bands of Fe oxides, with a 1.4 eV crystal-field splitting between Δ_1 and Δ_5 states and a 3.6 eV spin-splitting between spin $\uparrow$ and $\downarrow$ states (see Ref.55 and references therein). The sample annealing leads to a strong decrease of the Fe oxide peaks spectral intensity. This reduction of the interfacial Fe oxides indicated by the XAS studies can be one of the reasons why annealing increases the TMR. The disappearance of the FeO_x $\Delta_1^{\downarrow}$ peak, inferring reduced Fe-O bonds across the interface, implies the closing of a tunnelling transmission channel that would otherwise decrease TMR.[16] It is worth to remind that the Fe-O bonds we referring to, are in the plane parallel to the interface.

The direct linking of the XAS studies to the magnetotransport is not easy. The XAS data do not resolve whether the observed Fe oxides may still take part in magnetotransport and one can only state that they are reduced upon annealing. Moreover, the structural defects in the tunnel barrier, like oxygen vacancies, can lead to an effective reduction of the barrier spatial extent and energy height. These form the so-called "hotspots" which tunnel almost all the tunneling current.[171,172] Therefore their combined electronic properties shall drive the overall MTJ performance (see Fig. 7.3 (c)). Additionally, the MTJ encapsulation by the dielectric SiO_2 layer (Fig. 7.3 (d)) can in principle alter the MTJ pillar periphery chemistry and in turn impact also TMR.

Nonetheless, we try to compare the XAS spectra with magnetoresistane measurements as shown in Fig. 7.4. The electronic transport across the MTJ was measured while sweeping the photon energy. As already explained, due to the symmetry filtering mechanism across Fe/MgO/Fe junctions the resistance R changes upon switching from a parallel to antiparalell alignment of the electrode magnetization and defines the TMR. The dominant transmission in P and AP channels is governed by the electrons with Δ_1 and Δ_5 symmetries, respectively. Panels (b) and (c) correspond to resulting $R(E)$

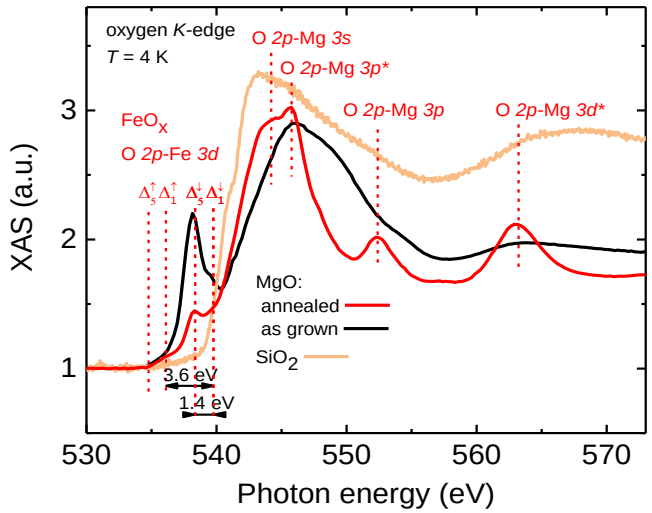

Figure 7.2: The referential XAS spectra of MgO and SiO_2. X-ray absorption spectra measured for the annealed and non-annealed CoFeB/MgO, and glass/SiO_2 non-processed stacks. The peak assignment reflects the allowed transitions from oxygen $1s$ core to the final state indicated in red. Taken from Ref. 55.

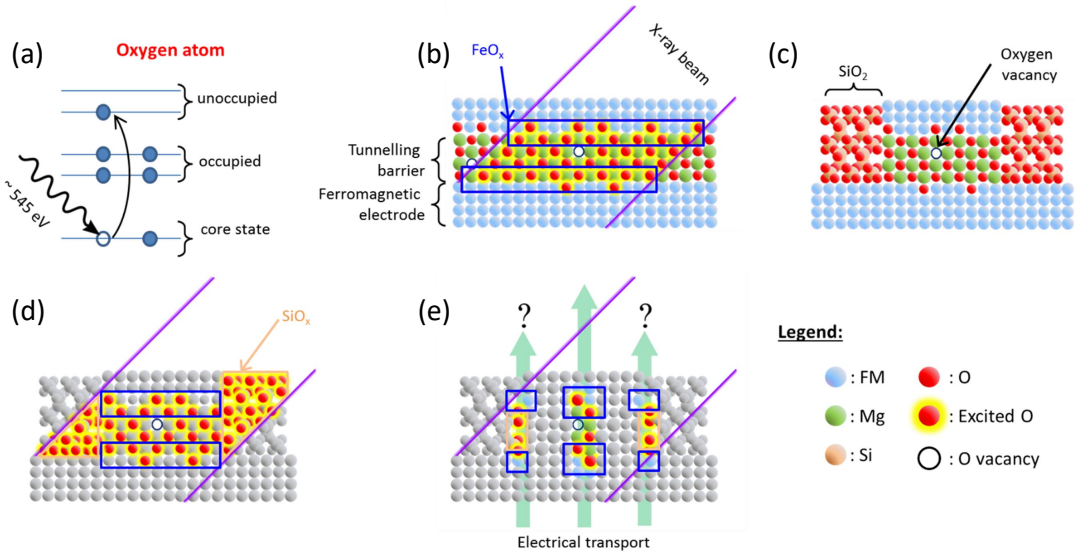

Figure 7.3: Probing a device's active atoms with combined XAS and magnetotransport measurements. (a) The photons with the energy adjusted to O K-edge allow to probe (excite) the selected atomic species. (b) MgO tunnel barrier sandwiched by two ferromagnetic electrodes. The x-rays excite all the oxygen sites in the system. Blue rectangles indicate the regions of possible appearance of the interfacial oxides. (c) The pillar of a single MTJ encapsulated by SiO_2. The localized structural defects, *e.g.*, oxygen vacancy, may funnel all the tunneling current. (d) Illustration of the XAS measurement which probes all the oxygen sites within the system. (e) Principle of combined XAS and electric measurement revealing the information about only those oxygen sites which contribute to the transport. Taken from Ref. 55.

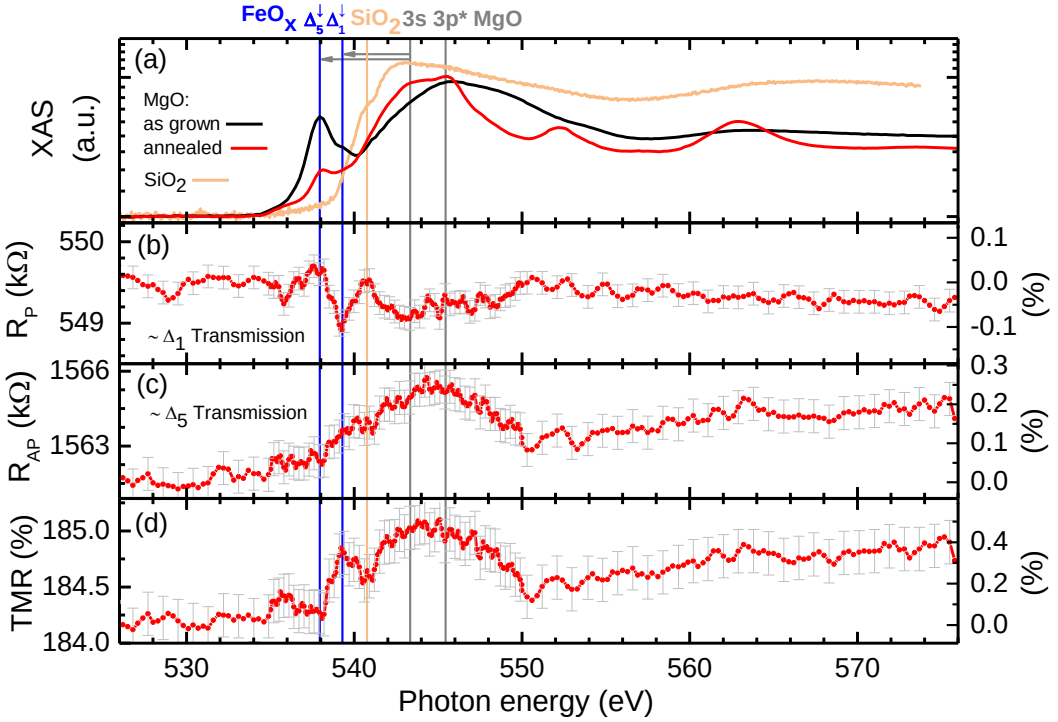

Figure 7.4: Combined XAS and magnetoresistance measurements of MgO-based MTJ. (a) The XAS spectra acquired with linear vertical polarized photons at the reference stacks of annealed and non-annealed MgO, and encapsulating SiO_2. Note a decreasing intensity of the Fe oxide peaks upon annealing. The photon energy dependence of the MTJ resistance in P (b) and AP (c) states with resulting TMR ratio (d) were recorded at $T = 20\,\mathrm{K}$ and low bias voltage $V = \pm 10\,\mathrm{mV}$. The right hand scale reflects the deviation from the baseline established at the pre-edge region. Taken from Ref. 55.

dependence at $T = 20\,\mathrm{K}$ upon reaching the O K-edge for a 10 mV applied voltage in the parallel (R_P) and anti-parallel (R_AP) configurations of the electrode magnetization.

We consider first the pre-edge energy region, $537 < E(eV) < 541$. We noticed that R_P exhibits a small but clear minimum at 539.3 eV when the $\Delta_1^\downarrow$ state of the interfacial Fe oxide is addressed. This shows that the Fe-O bonds are present and play a role in the transport despite that XAS measurements indicated decrease of these bonds upon annealing. One can explain this minima in R_P by considering an additional electron in the "excited" state that appears due to x-ray absorption and enhances the electrical transport across the otherwise insulating Fe oxide, causing the resistance to decrease. This effect is present only in R_P since, as mentioned, the Δ_1 transmission channel dominates the solid-state tunnelling across MgO in the P state. On the other hand, R_AP is not affected by the photoexcitation of the Fe oxide spin-down states ($\Delta_5^\downarrow$) because the corresponding spin-up states are fully occupied, that is there are no available states in the counter electrode (we are assuming here that both interfaces are oxidized). We do not observe any strong correlation between the XAS of the encapsulating SiO_2 and the magnetotransport for R_P and R_AP which indicates that the excitation of the Si-O states do not influence the device performance. Therefore, the MTJ pillar periphery plays a secondary role in the device's operation.

We can discuss now the junction's performance alteration upon reaching the maximum of the oxygen K-edge. While sweeping the photon energy across the K-edge region (535 eV – 545 eV) R_{P} stays mostly unaffected, that is decreases by 0.1% while R_{AP} increases by 0.25%. The resulting TMR ratio, reaching $\sim 180\%$ in used MTJs at $T = 20\,\mathrm{K}$, increases by $\sim 0.5\%$.

7.3 Theoretical investigations

To understand this behaviour we performed theoretical calculations where we investigated the changes in complex band structure of MgO under the x-ray excitation and then the transmission through Fe/MgO/Fe with the "excited" oxygen atom. To do so, we used the so-called $Z + 1$ approach.[56–58] This approximation can be used for simulating the electronic structure of an atom upon absorption of an x-ray photon in which an additional electron is placed in the conduction band. This mimics the x-ray excited state but does not include the core hole created after the electron removal. In practice, all that means that we replaced oxygen in MgO by fluorine which has one electron more than oxygen. Therefore, we are getting an "excited" electron in the conduction band. To validate this approach, we calculated the XAS of MgO and MgF with the VASP package using the PBE functional. The XAS is calculated based on the electric dipole approximation and does not include core hole effects. The simulation cell of both materials had a bcc structure with two atoms per unit cell. The resulting spectra are presented in Fig. 7.5. To match the experimental spectrum with the theoretical one, the theoretical curves were energy-shifted and a step function was added. We find a good agreement regarding the energy separation between the peaks C, D, E, and F between the experimental and the theoretical spectra. The edge shapes imply that replacing oxygen sites with fluorine keeps a similar set of allowed dipole transitions and suggest that the assumed approximation gives a reasonable outcome.

We have then calculated the DOS for MgO but this time including the core hole in the 1s state oxygen (denoted as "Oh"). This was done with the QE package by choosing special pseudopotential for the oxygen atom that includes the core hole, from the QE pseudopotential library. We compare the total DOS (Fig. 7.6 (a)) for MgOh and MgF conduction bands, i.e. the final states for an excited electron, and acknowledge their similar shapes. This is further confirmed by the p-projected DOS (Fig. 7.6 (b)) for fluorine and oxygen atoms including the core hole. These results imply that "MgF" can be used as an approximation of the x-ray photoexcited MgO with a core hole and hence the $Z + 1$ approach can be employed to calculated the CBS for "excited" MgO. Moreover, by using the $Z + 1$ approximation rather than explicit pseudopotential with core hole, we get an excited electron in the conduction band. Note that the DOS of MgF and MgO without the core hole are substantially different (Fig. 7.6 (a)).

Validating the used method, we then calculated the CBS for "MgF". In principle, one should consider a supercell containing only one "excited" atom since the x-ray do not excite all oxygen atoms at once but only small part of them. However, due to band folding it is practically impossible to extract the information only about Δ_5 complex loop. Moreover, as we checked, one excited atom in a supercell (64 MgO atoms with one

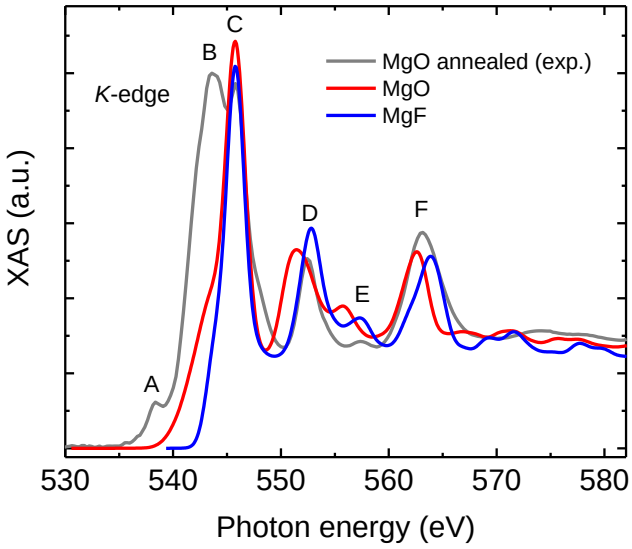

Figure 7.5: Theoretical XAS spectra of MgO and MgF. The result of calculation for the K-edge shape of the oxygen (fluorine) within MgO (MgF). The spectra are energy-shifted and compared to the experimental data acquired on annealed CoFeB/MgO stack. The peaks C, D, E, and F are in agreement with the experimental data. The substitution of oxygen with fluorine preserves the same set of allowed dipolar transitions. Taken from Ref. 55.

oxygen atom replaced by fluorine) results only in minor changes in the resulting CBS (not shown here). Therefore, we assumed the limiting case with the maximum possible impact of the x-ray absorption on the Δ_1 and Δ_5 transmission channels, where all of the oxygen atoms are excited. Note that this picture is closer to the scenario where the tunnelling current is tunnelled through the "hotspots". Due to simplification we made we could use a tetragonal cell with only 4 atoms. The CBS loops were evaluated along $\Gamma - X$ high symmetry direction of the BZ. We extracted only the data corresponding to the Δ_1 and Δ_5 symmetry channels as presented in Fig. 7.7 where the "MgF" complex loops are denoted as the "excited MgO". The Fermi level was set to the mid gap of MgO.

As already explained, the intersection point of the complex loop and Fermi level is related to the attenuation coefficients κ_1 and κ_5 of the electrons with symmetry Δ_1 and Δ_5 respectively. When we compare loops for MgO and its "excite" counterpart we can notice that around the Fermi level the κ_1 coefficient, governing the transmission in the P state, increases very moderately while we witness a notable increase of the κ_5 rate, which dominates the transmission in the MTJ AP state. If we simply assume R (R_o) to be the MTJ resistance with (without) the x-ray photoelectron the attenuation can be expressed as $R = R_\mathrm{o} e^{-\kappa d}$, where d is the barrier thickness. Then, the absolute changes $d\kappa_1 = -0.05$ and $d\kappa_5 = -0.15$ in the tunnelling attenuation lead to a three times smaller impact on R_P compared to R_AP. This supports the experimental observations of an increase in R_AP and a much lower impact on R_P. Nonetheless, the CBS calculations correspond to the extreme case and the direction of the experimentally observed phenomena and not model the real system, so it can be considered as giving a qualitative trend comparable with the experiment.

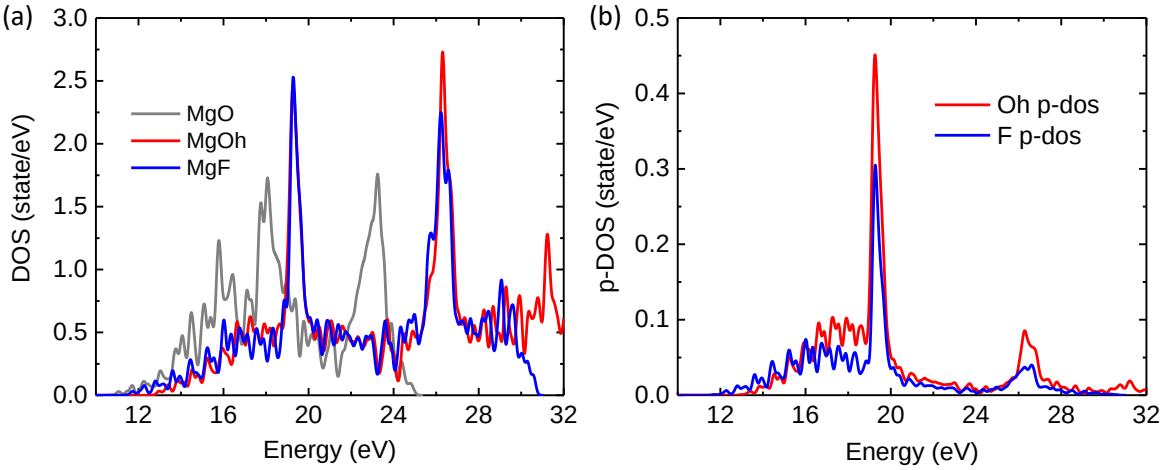

Figure 7.6: DOS for MgO and MgF ground state density of states. Only the conduction bands are shown. Panel (a) corresponds to the total and (b) to p-projected DOS of MgF, MgO, and MgOh with "Oh" denoting the inclusion of the core hole. Taken from Ref. 55.

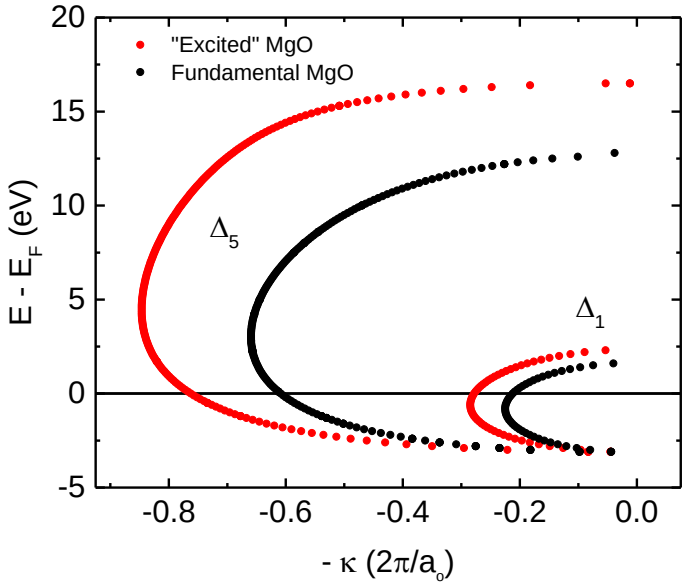

Figure 7.7: Complex band structure calculation of MgO. Result of the $Z+1$ simulation described in text. The complex loops length for the Δ_1 and Δ_5 electronic symmetry reflects the alteration of the tunneling current attenuation coefficients κ_1 and κ_5 upon absorption of the x-ray photon by the oxygen site. This confirms the minor (sizeable) variation of the R_{P} (R_{AP}), governed by Δ_1 (Δ_5) transmission channel, upon reaching the oxygen K-edge witnessed in the experiment. Taken from Ref. 55.

Therefore, to simulate more realistic scenario we considered the transmission through Fe/MgO(5ML)/Fe junction with one fluorine atom replacing oxygen in the middle layer of MgO. We did include any additional oxidization at the interface. The resulting 2D BZ transmission is plotted in Fig. 7.8. Indeed, we noticed an increase in the spin up channel transmission with respect to the not excited MgO (see Fig.6.1). Moreover, the transmission is more broadened in the BZ, but always centered around the Γ point.

The total transmission, summed over all points in the BZ, for the spin up channel increases from $7.9 \cdot 10^{-3}$ to $1.85 \cdot 10^{-1}$. The change in the total transmission for the spin down channel is from $4.57 \cdot 10^{-5}$ for normal MgO to $4.842 \cdot 10^{-4}$ for "excited MgO". Clearly, the spin up channel, dominated by Δ_1 contributions is more affected than the spin down channel, where the Δ_5 symmetry dominates. This in turn agrees with CBS predictions for "excited MgO" and the experiment.

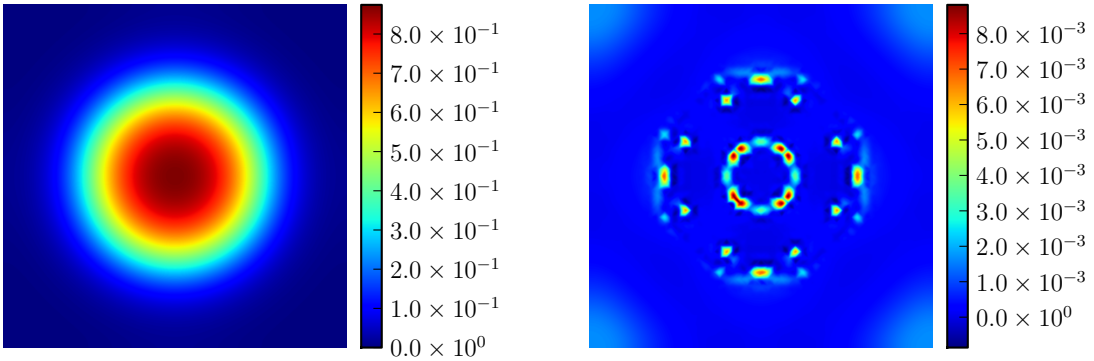

Figure 7.8: Transmission in 2D BZ for Fe/MgO/Fe with one fluorine atom placed in the middle layer of MgO to mimic the "excited" oxygen state after x-ray absorption. Left panel shows spin up channel and the right spin down channel for parallel magnetic configuration of the electrodes.

7.4 Summary

We presented how the x-ray spectroscopy can be combined with the electric transport measurements in order to obtain a device-driven atomic selectivity and probe only these atoms which are involved in transport mechanism. These novel technique can provide more comprehensive understanding of how a complete device operates and how a small subset of atoms contributes to its performance. Thanks to experiments involving MgO-based MTJs we can get insight into the nature of transport mechanism and factors influencing the resulting TMR.

This is also challenging from the theoretical point of view since we are trying to simulate an operating device with excited atoms. This goes far beyond a 'simple' ground state DFT calculations and more appropriate would be to use time-dependent DFT formalism. Nonetheless, by making reasonable approximations we can gain some understanding using the ground state theory.

8

General conclusions and perspectives

At the beginning of this thesis manuscripts we highlighted the importance of MTJ technologies and their broad applications. We emphasized the role played by defects in such junctions and motivated the importance of understanding the origin and the properties of structural imperfections in real devices. After reviewing the state of the art concerning the investigations of different defect species we pointed out the particular role of oxygen vacancies within the MgO spacer. We also motivated the interesting aspect of paired oxygen vacancies forming M centers. This thesis was dedicated to gain a deeper understanding of the electronic properties of these M centers and their effect on the transmission and justify the assumption of their superior usefulness over single oxygen vacancies. We used highly advanced density functional theory formalism to carry out the calculations.

Technological processes are inseparably linked to creation of various kinds of defects in MgO-based MTJ and despite the continuous development of preparation methods, which allowed to achieve TMR values over 1000% at low temperatures and around 600% at RT, its hardly possible to avoid all of the structural imperfection. Instead we can try to make use of them and as we showed throughout this thesis double oxygen vacancies can give a promising perspective for spintronic applications. As we found, the barrier heights corresponding to M centers are always smaller than the barriers associated with F centers. This is due to a process of M center creation during which two F centers hybridize and give rise to two M center energy levels, located in the MgO band gap, that mimic the bonding and antibonding like states. The antibonding level of an M center is always higher in energy than the F center level and therefore it creates lower barrier heights for electron tunnelling than the F center.

When we incorporated F and M centers in Fe(FeCo)/MgO junctions we found a drop of TMR of about one order of magnitude with respect to the ideal junctions which can explain the aforementioned discrepancies between the theoretically predicted TMR and experimental values. Moreover, we observed that defects have larger impact on

the spin up channel transmission, where the dominant role is played by electrons with Δ_1 symmetry, and left the corresponding spin down channel, dominated by Δ_5 electrons, almost unaffected. The F center caused strong scattering of the propagating electron wave function to the states with higher **k**-vector values which decreases the conductance in the spin up channel for the P configuration. Interestingly, due to the spherical symmetry of the F center, this scattering was also symmetric and the maximum amplitudes of the transmission where found along k_x and k_y axis in the 2D BZ. In contrast, in the presence of the M center the transmission spectrum was broadened in the 2D BZ but still mostly centered around the Γ point and therefore partially preserving the coherent transmission. Consequently, we were always obtaining higher values of TMR in presence of M centers rather than F centers. As we verified, the properties of F and M centers are robust with respect to a change of the electrode. We observe that the defect level position is shifted, up to 0.5 eV, when we switched from Fe to Co(FeCo) electrodes. However, this fact did not change significantly the impact of the oxygen vacancies on the the transmission and again we found a lower transmission for F-MgO spacer compare to that of M-MgO. What is interesting, in recent experiments conducted at IPCMS, is a shifting of the defect levels position upon changing from symmetric FeCoB/MgO/FeCoB junctions to asymmetric FeCoB/MgO/FeB structures, was actually observed (results about to be published). As we predicted, all the levels were rigidly moved but their relative positions did not change.

The most crucial factor affecting the properties of F an M centers is their position with respect to the interface. Placing vacancies at the interfacial MgO layer resulted in practically the same shape of the transmission distribution and its amplitude as for ideal junctions. In this situation, there is no clear distinction between the F and M centers and the resulting TMR reached about 4261% and 3911% respectively. In this case, the system can be interpreted as an MTJ with reduced effective barrier thickness for the propagating electrons. When we shifted vacancies further from the interface the transmission dropped drastically but it was larger in the presence of an M center than a F center.

The overall picture shows that, if we cannot avoid oxygen vacancies within the MgO spacer, it is better to have M centers than F centers. Our calculations also demonstrated that the formation of double oxygen vacancy is more energetically favourable than two separate single vacancies in the same structure. Moreover, experimental results showed that we can actually control the type of oxygen vacancies within the sample by proper choice of the preparation conditions. For instance, the increase of the annealing temperature up to 300°C can trigger the grouping of oxygen vacancies into bigger clusters. Although, we will not get rid of all F centers, we might decrease considerably their relative population with respect to that of M centers.

We believe that our theoretical studies gave a better insight into the defect-induced transmission through MgO-based magnetic tunnel junctions and helped in resolving the origin of measured low barrier heights which can be now associated with paired oxygen vacancies. We also explained how we can control the oxygen vacancy type in a sample and what are the crucial factors defining their properties. We hope that this work will initiate in future theoretical and experimental efforts directed towards possible technological applications.

Nonetheless, there are still remaining open questions and room for improvement. For instance, an interesting behaviour was found when we compared the k-resolved d - DOS for the interfacial Fe layer near the Fermi level for the two M center orientations. The two distributions were quite different and it is not likely that it completely was due to the M center orientation. Especially, that when we shifted the vacancy towards the interface the corresponding changes in the k-DOS distribution were minor. Initially, we associated this behaviour to the difference in the total number of MgO layers used, odd versus even. We did not study in more detail structures with an even number of MgO layers but this point is definitely interesting to explore in the future. Besides, the transmission calculations for various bias voltages should be also continued in a further work since these kind of simulations are closer to the real situation. We should also solve the encountered problems with TranSIESTA and compare the results to these obtained with PWcond, which is itself interesting, and makes the transport calculations more reliable. We also did not include charged oxygen vacancies which can appear in MgO spacer. This would improve the understanding of the barrier heights measured in MgO-based junction and complete the picture of defect levels created by various oxygen vacancies.

In the last chapter of this thesis we described a combined XAS and magneto-transport measurements performed on MgO-based junctions. The aim was to find the modification in the tunnelling current induced by the electrons knocked out from the core states by x-ray absorption. To simulate transport in such complex conditions we used $Z + 1$ approximation so that we replaced one oxygen atom in the MgO by a fluorine atom. We found that by including an additional electron in the conduction band the transmission in the spin up channel is enhanced while the spin down transmission is much less affected. This actually was proved experimentally by finding that the resistance in parallel magnetic configuration decreases for the x-ray energy necessary to eject an electron from the $1s$ core level of oxygen. These studies demonstrate how challenging are *in operando* measurements from experimental and theoretical point of view and that these two approaches have to be combined in order to understand the underlying physics. Even based on ground state calculations we can gain some insight into processes occurring in an operating devise. Further developing of such techniques, both experimentally and theoretically, would have a great impact not only in the field of spintronics but also on technology.

Appendices

A

Generation of USPP

The generation of the USPP starts by solving self-consistently Kohn-Sham equation for a given atomic species, resulting in the screened all electron potential, V_{AE}, as in the case of NCPP. A set of reference energies, ϵ_l, is chosen for each angular momentum and the radial Schrödinger equation with V_{AE} is solved within r_c at each ϵ_l giving regular solutions, ψ_n (n denotes set of quantum numbers $\{lm\}$). Next steps are as follow:

1. A smooth local potential $V_{loc}(\mathbf{r})$ is generated which matches the all-electron potential after specified cut-off radius r_L, $V_{loc}(\mathbf{r}) = V_{AE}(\mathbf{r})$ for $r > r_L$.

2. Similarly a smooth pseudo wave function $|\tilde{\psi}_n\rangle$ is determined, with constrain that it matches the all-electron wave function, $\psi_n(\mathbf{r})$ at $r \geq r_{c,n}$.

3. A set of new orbital functions, $|\chi_n\rangle$, which vanish at $r > r_{c,n}$ is constructed such that:
$$|\chi_n\rangle = (\epsilon_n - T - V_{loc})\,|\tilde{\psi}_n\rangle\,. \tag{A.1}$$
Also the projectors $|\beta_n\rangle$ necessary for the definition of the nonlocal part of the potential are determined
$$|\beta_n\rangle = \sum_m (B^{-1})_{nm}\,|\chi_m\rangle\,, \tag{A.2}$$
where $|\beta_n\rangle$ satisfy the relation $\langle\beta_n|\tilde{\psi}_m\rangle = \delta_{nm}$ and B_{nm} is an auxiliary matrix of inner products
$$B_{nm} = \langle\tilde{\psi}_n|\chi_m\rangle \tag{A.3}$$

4. To compensate the difference between pseudo and all-electron density a set of augmentation functions Q_{nm} is defined as
$$Q_{nm}(r) = \psi_n^*(\mathbf{r})\psi_m(\mathbf{r}) - \tilde{\psi}_n^*(\mathbf{r})\tilde{\psi}_m(\mathbf{r}), \tag{A.4}$$

and the related augmentation charges

$$q_{nm} = \langle \psi_n | \psi_m \rangle_R - \langle \tilde{\psi}_n | \tilde{\psi}_m \rangle_R \,, \tag{A.5}$$

where subscript R denotes the cutoff radius which is slightly larger than the maximum of the $r_{c,n}$ and r_L (the so called diagnostic radius).

5. D_{nm} is defined as $D_{nm} = B_{nm} + \epsilon_m q_{nm}$ which in turn determines the non-local potential as

$$V_{NL} = \sum_{nm} D_{nm} \left| \beta_n \right\rangle \left\langle \beta_m \right| . \tag{A.6}$$

With all above definitions the pseudowave functions $|\tilde{\psi}_n\rangle$ obey the secular equation

$$H \left| \tilde{\psi}_n \right\rangle = \epsilon_n S \left| \tilde{\psi}_n \right\rangle , \tag{A.7}$$

with Hamiltonian

$$H = T + V_{loc} + \sum_{nm} D_{nm} \left| \beta_n \right\rangle \left\langle \beta_m \right| , \tag{A.8}$$

and overlap matrix

$$S = 1 + \sum_{nm} q_{nm} \left| \beta_n \right\rangle \left\langle \beta_m \right| . \tag{A.9}$$

Thus, the pseudo-wave function that obeys the same equation as the all-electron wave function is found. In the last step, once the D_{nm} are obtained the local part and the nonlocal coefficients of the bare pseudopotential are evaluated by a descreening procedure

$$V_{loc}^{ion} = V_{loc} - V_H - V_{xc}, \tag{A.10}$$

$$D_{nm}^{(0)} = D_{nm} - \int dr V_{loc}(\mathbf{r}) n(\mathbf{r}). \tag{A.11}$$

The pseudo-potential is finally given by

$$\tilde{V} = V_{loc}^{ion} + \sum_{nm} D_{nm}^{(0)} \left| \beta_n \right\rangle \left\langle \beta_m \right| , \tag{A.12}$$

$$n(\mathbf{r}) = \sum_i \left[|\tilde{\psi}_i(\mathbf{r})|^2 + \sum_{nm,I} Q_{nm}^I(\mathbf{r}) \left\langle \tilde{\psi}_i(\mathbf{r}) | \beta_n^I \right\rangle \left\langle \beta_m^I | \tilde{\psi}_i(\mathbf{r}) \right\rangle \right] \tag{A.13}$$

B

FeCo/MgO ideal junction

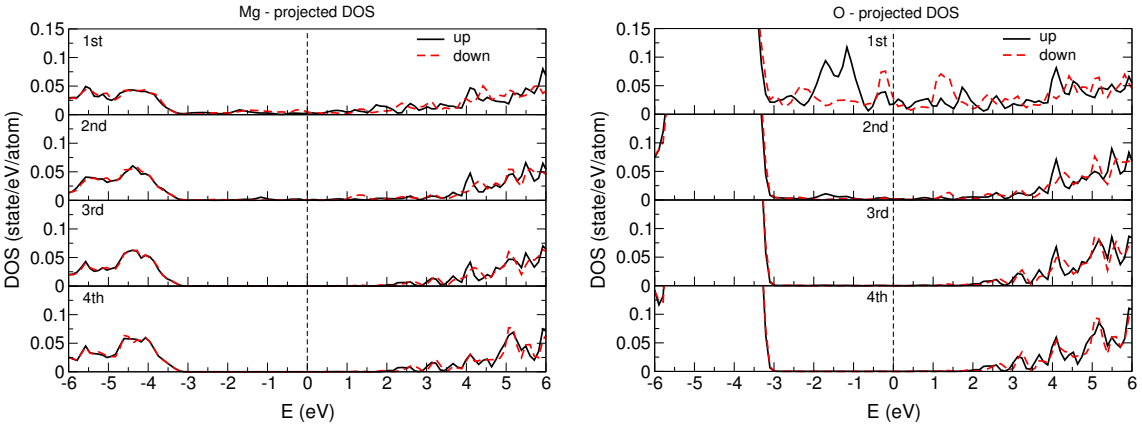

Figure B.1: MgO-layer and atom projected DOS for the ideal MgO(7ML)/FeCo(7ML) junction. The 1st layer is the one at the interface with the electrode and 4th is the middle one.

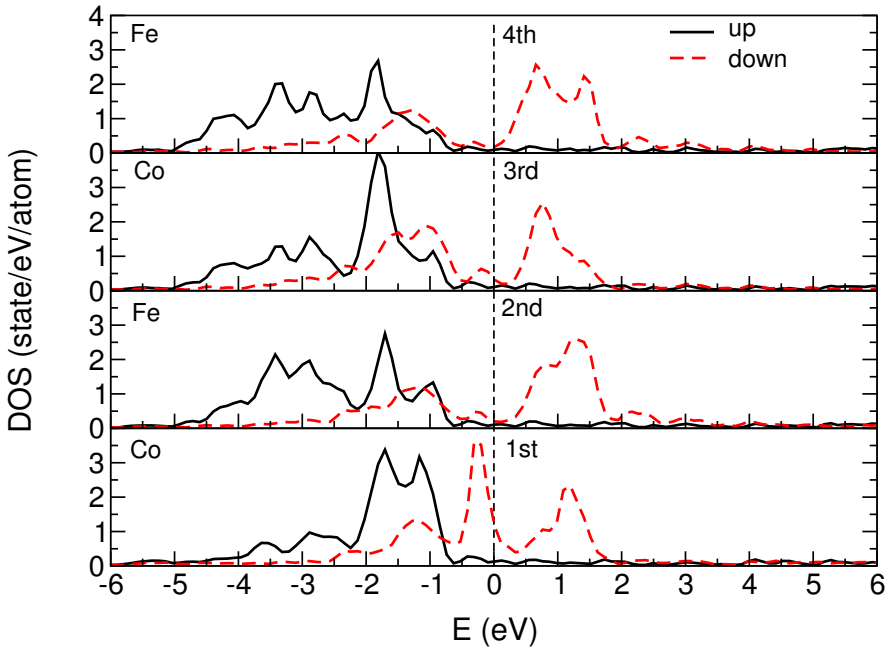

Figure B.2: Layer projected DOS for FeCo electrode. The electrode is made of alternating Fe and Co layers with Co at the interface.

Bibliography

[1] I. Žutić, J. Fabian, and S. Das Sarma. Spintronics: Fundamentals and applications. *Reviews of Modern Physics*, 76(2): 323–410, 2004.

[2] A. Makarov, T. Windbacher, V. Sverdlov, and S. Selberherr. CMOS-compatible spintronic devices: a review. *Semiconductor Science and Technology*, 31(11): 113006, 2016.

[3] J. W. Lu, E. Chen, M. Kabir, M. R. Stan, and S. A. Wolf. Spintronics technology: past, present and future. *International Materials Reviews*, 61(7): 456–472, 2016.

[4] S. Peng, Y. Zhang, M. Wang, Y. Zhang, and W. Zhao. Magnetic Tunnel Junctions for Spintronics: Principles and Applications. In: *Wiley Encyclopedia of Electrical and Electronics Engineering*, vol. 1936, pp. 1–16. John Wiley & Sons, Inc., Hoboken, NJ, USA, 2014.

[5] M. N. Baibich, J. M. Broto, A. Fert, F. N. Van Dau, F. Petroff, P. Etienne, G. Creuzet, A. Friederich, and J. Chazelas. Giant Magnetoresistance of (001)Fe/(001)Cr Magnetic Superlattices. *Physical Review Letters*, 61: 2472–2475, 1988.

[6] G. Binasch, P. Grünberg, F. Saurenbach, and W. Zinn. Enhanced magnetoresistance in layered magnetic structures with antiferromagnetic interlayer exchange. *Physical Review B*, 39: 4828–4830, 1989.

[7] M. Julliere. Tunneling between ferromagnetic films. *Physics Letters A*, 54(3): 225–226, 1975.

[8] J. M. MacLaren, X.-G. Zhang, W. H. Butler, and X. Wang. Layer KKR approach to Bloch-wave transmission and reflection: Application to spin-dependent tunneling. *Physical Review B*, 59: 5470–5478, 1999.

[9] J. Mathon and A.Umerski. Theory of tunneling magnetoresistance of an epitaxial Fe/MgO/Fe(001) junction. *Physical Review B*, 63: 220403(R), 2001.

[10] W. H. Butler, X. G. Zhang, S. Vutukuri, M. Chshiev, and T. C. Schulthess. Theory of tunneling magnetoresistance for epitaxial systems. *IEEE Transactions on Magnetics*, 41(10): 2645–2648, 2005.

[11] W. H. Butler. Tunneling magnetoresistance from a symmetry filtering effect. *Science and Technology of Advanced Materials*, 9(1): 014106, 2008.

[12] X.-G. Zhang and W. H. Butler. Band structure, evanescent states, and transport in spin tunnel junctions. *Journal of Physics: Condensed Matter*, 15(41): R1603–R1639, 2003.

[13] W. H. Butler, X.-G. Zhang, T. C. Schulthess, and J. M. MacLaren. Reduction of electron tunneling current due to lateral variation of the wave function. *Physical Review B*, 63: 092402, 2001.

[14] S. Ikeda, J. Hayakawa, Y. Ashizawa, Y. M. Lee, K. Miura, H. Hasegawa, M. Tsunoda, F. Matsukura, and H. Ohno. Tunnel magnetoresistance of 604% at 300K by suppression of Ta diffusion in CoFeB/MgO/CoFeB pseudo-spin-valves annealed at high temperature. *Applied Physics Letters*, 93(8): 082508, 2008.

[15] H. L. Meyerheim, R. Popescu, J. Kirschner, N. Jedrecy, M. Sauvage-Simkin, B. Heinrich, and R. Pinchaux. Geometrical and compositional structure at metal-oxide interfaces: MgO on Fe(001). *Physical Rreview Letters*, 87 7: 076102, 2001.

[16] Effects of the iron-oxide layer in Fe-FeO-MgO-Fe tunneling junctions. *Physical Review B*, 68(9): 6–9, 2003.

[17] F. Bonell, S. Andrieu, A. M. Bataille, C. Tiusan, and G. Lengaigne. Consequences of interfacial Fe-O bonding and disorder in epitaxial Fe/MgO/Fe(001) magnetic tunnel junctions. *Physical Review B*, 79(22): 224405, 2009.

[18] M. Mizuguchi, Y. Suzuki, T. Nagahama, and S. Yuasa. In situ scanning tunneling microscopy observations of polycrystalline MgO(001) tunneling barriers grown on amorphous CoFeB electrode. *Applied Physics Letters*, 91(1): 012507, 2007.

[19] J. J. Bean, M. Saito, S. Fukami, H. Sato, S. Ikeda, H. Ohno, Y. Ikuhara, and K. P. McKenna. Atomic structure and electronic properties of MgO grain boundaries in tunnelling magnetoresistive devices. *Scientific Reports*, 7(1): 45594, 2017.

[20] T. Miyajima, T. Ibusuki, S. Umehara, M. Sato, S. Eguchi, M. Tsukada, and Y. Kataoka. Transmission electron microscopy study on the crystallization and boron distribution of CoFeB/MgO/CoFeB magnetic tunnel junctions with various capping layers. *Applied Physics Letters*, 94(12): 122501, 2009.

[21] X. Kozina, S. Ouardi, B. Balke, G. Stryganyuk, G. H. Fecher, C. Felser, S. Ikeda, H. Ohno, and E. Ikenaga. A nondestructive analysis of the B diffusion in Ta–CoFeB–MgO–CoFeB–Ta magnetic tunnel junctions by hard x-ray photoemission. *Applied Physics Letters*, 96(7): 072105, 2010.

[22] S. Pinitsoontorn, A. Cerezo, A. K. Petford-Long, D. Mauri, L. Folks, and M. J. Carey. Three-dimensional atom probe investigation of boron distribution in CoFeB/MgO/CoFeB magnetic tunnel junctions. *Applied Physics Letters*, 93(7): 071901, 2008.

[23] A. K. Rumaiz, C. Jaye, J. C. Woicik, W. Wang, D. A. Fischer, J. Jordan-Sweet, and C. L. Chien. Boron migration due to annealing in CoFeB/MgO/CoFeB interfaces: A combined hard x-ray photoelectron spectroscopy and x-ray absorption studies. *Applied Physics Letters*, 99(22): 222502, 2011.

[24] H. Kurt, K. Rode, K. Oguz, M. Boese, C. C. Faulkner, and J. M. D. Coey. Boron diffusion in magnetic tunnel junctions with MgO (001) barriers and CoFeB electrodes. *Applied Physics Letters*, 96(26): 262501, 2010.

[25] S. Mukherjee, R. Knut, S. M. Mohseni, T. N. Anh Nguyen, S. Chung, Q. Tuan Le, J. Åkerman, J. Persson, A. Sahoo, A. Hazarika, B. Pal, S. Thiess, M. Gorgoi, P. S. Anil Kumar, W. Drube, O. Karis, and D. D. Sarma. Role of boron diffusion in CoFeB/MgO magnetic tunnel junctions. *Physical Review B*, 91: 085311, 2015.

[26] Z. Wang, M. Saito, K. P. McKenna, S. Fukami, H. Sato, S. Ikeda, H. Ohno, and Y. Ikuhara. Atomic-Scale Structure and Local Chemistry of CoFeB–MgO Magnetic Tunnel Junctions. *Nano Letters*, 16(3): 1530–1536, 2016.

[27] A. Gibson, R. Haydo, and J. P. LaFemina. Stability of vacancy defects in MgO: The role of charge neutrality. *Physical Review B.*, 50(4): 2582–2592, 1994.

[28] J. P. Velev, K. D. Belashchenko, S. S. Jaswal, and E. Y. Tsymbal. Effect of oxygen vacancies on spin-dependent tunneling in Fe/MgO/Fe magnetic tunnel junction. *Applied Physics Letters*, 90: 072502, 2007.

[29] J. P. Velve, M. Y. Zhuravlev, K. D. Belashchenko, S. S. Jaswal, E. Y. Tsymbal, T. Katayama, and S. Yuasa. Defect-Mediated properties of magnetic tunnel junction. *IEEE Transactions on Magnetics*, 43(6): 2770–2775, 2007.

[30] F. Schleicher, U. Halisdemir, D. Lacour, M. Gallart, S. Boukari, G. Schmerber, V. Davesne, P. Panissod, D. Halley, H. Majjad, Y. Henry, B. Leconte, A. Boulard, D. Spor, N. Beyer, C. Kieber, E. Sternitzky, O. Cregut, M. Ziegler, F. Montaigne, E. Beaurepaire, P. Gilliot, M. Hehn, and M. Bowen. Localized states in advanced dielectrics from the vantage of spin- and symmetry polarized tunneling across MgO. *Nature Communications*, 5: 4547, 2014.

[31] G. Miao, Y. Park, J. Moodera, M. Seibt, G. Eilers, and M. Münzenberg. Disturbance of Tunneling Coherence by Oxygen Vacancy in Epitaxial Fe/MgO/Fe Magnetic Tunnel Junctions. *Physical Review Letters*, 100(24): 246803, 2008.

[32] S. Yuasa, T. Nagahama, A. Fukushima, Y. Suzuki, and K. Ando. Giant room-temperature magnetoresistance in single-crystal Fe/MgO/Fe magnetic tunnel junctions. *Nature Materials*, 3(12): 868–871, 2004.

[33] S. S. P. Parkin, C. Kaiser, A. Panchula, P. M. Rice, B. Hughes, M. Samant, and S.-H. Yang. Giant tunnelling magnetoresistance at room temperature with MgO (100) tunnel barriers. *Nature Materials*, (3): 862–867, 2004.

[34] K. P. McKenna and J. Blumberger. Crossover from incoherent to coherent electron tunneling between defects in MgO. *Physical Review B*, 86(24): 245110, 2012.

[35] P. Hohenberg and W. Kohn. Inhomogeneous Electron Gas. *Physical Review*, 136(3B): B864–B871, 1964.

[36] W. Kohn and L. J. Sham. Self-Consistent Equations Including Exchange and Correlation Effects. *Physical Review*, 140(4A): A1133–A1138, 1965.

[37] G. Kresse and J. Furthmüller. Efficient iterative schemes for ab initio total-energy calculations using a plane-wave basis set. *Physical Review B*, 54(16): 11169, 1996.

[38] G. Kresse and D. Joubert. From ultrasoft pseudopotentials to the projector augmentedwave method. *Physical Review B*, 59(3): 1758, 1999.

[39] P. Giannozzi, S. Baroni, N. Bonini, M. Calandra, R. Car, C. Cavazzoni, D. Ceresoli, G. L. Chiarotti, M. Cococcioni, I. Dabo, A. D. Corso, S. de Gironcoli, S. Fabris, G. Fratesi, R. Gebauer, U. Gerstmann, C. Gougoussis, A. Kokalj, M. Lazzeri, L. Martin-Samos, N. Marzari, F. Mauri, R. Mazzarello, S. Paolini, A. Pasquarello, L. Paulatto, C. Sbraccia, S. Scandolo, G. Sclauzero, A. P. Seitsonen, A. Smogunov, P. Umari, and R. M. Wentzcovitch. QUANTUM ESPRESSO: a modular and open-source software project for quantum simulations of materials. *Journal of Physics: Condensed Matter*, 21(39): 395502, 2009.

[40] A. Smogunov, A. D. Corso, and E. Tosatti. Ballistic conductance of magnetic Co and Ni nanowires with uultrasoft pseudo-potentials. *Physical Review B*, 70(4): 045417, 2004.

[41] E. Artacho, D. Sánchez-Portal, P. Ordejón, A. García, and J. M. Soler. Linear-Scaling ab-initio Calculations for Large and Complex Systems. *Physica Status Solidi (b)*, 215(1): 809–817, 1999.

[42] J. M. Soler, E. Artacho, J. D. Gale, A. García, J. Junquera, P. Ordejón, and D. Sánchez-Portal. The SIESTA method for ab initio order- N materials simulation. *Journal of Physics: Condensed Matter*, 14(11): 2745, 2002.

[43] J. Junquera, O. Paz, D. Sánchez-Portal, and E. Artacho. Numerical atomic orbitals for linear-scaling calculations. *Physical Review B*, 64: 235111, 2001.

[44] R. Landauer. Electrical resistance of disordered one-dimensional lattices. *The Philosophical Magazine: A Journal of Theoretical Experimental and Applied Physics*, 21(172): 863–867, 1970.

[45] R. Landauer. Electrical transport in open and closed systems. *Zeitschrift für Physik B Condensed Matter*, 68(2): 217–228, 1987.

[46] S. Datta. *Electronic trasnport in mesoscopic systems*. Cambridg University Press, 1995.

[47] M. Büttiker, Y. Imry, R. Landauer, and S. Pinhas. Generalized many-channel conductance formula with application to small rings. *Physical Review B*, 31(10): 6207–6215, 1985.

[48] Y. Uenaka and T. Uchino. Photoexcitation, trapping, and recombination process of the F-type centers in lasing MgO microcrystals. *Physical Review B*, 83(19): 195108, 2011.

[49] J. Hayakawa, S. Ikeda, F. Matsukura, H. Takahashi, and H. Ohno. Dependence of giant tunnel magnetoresistance of sputtered CoFeB/MgO/CoFeB magnetic tunnel junctions on MgO barrier thickness and annealing temperature. *Japanese Journal of Applied Physics*, 44(4L): L587, 2005.

[50] Y. Ke, K. Xia, and H. Guo. Oxygen-Vacancy-Induced Diffusive Scattering in Fe/MgO/Fe Magnetic Tunnel Junctions. *Physical Review Letters*, 105(23): 236801, 2010.

[51] X. Liu, W. Yang, and Z. Liu. Recent progress on synchrotron-based in-situ soft X-ray spectroscopy for energy materials. *Advanced Materials*, 26(46): 7710–7729, 2014.

[52] N. Barrett, D. M. Gottlob, C. Mathieu, C. Lubin, J. Passicousset, O. Renault, and E. Martinez. Operando x-ray photoelectron emission microscopy for studying forward and reverse biased silicon p-n junctions. *Review of Scientific Instruments*, 87(5), 2016.

[53] A. Gurlo and R. Riedel. In Situ and Operando Spectroscopy for Assessing Mechanisms of Gas Sensing. *Angewandte Chemie International Edition*, 46(21): 3826–3848, 2007.

[54] L. Joly, B. Muller, E. Sternitzky, J.-G. Faullumel, A. Boulard, E. Otero, F. Choueikani, J.-P. Kappler, M. Studniarek, M. Bowen, and P. Ohresser. Versatile variable temperature insert at the DEIMOS beamline for in situ electrical transport measurements. *Journal of Synchrotron Radiation*, 23(3): 652–657, 2016.

[55] M. Studniarek, U. Halisdemir, F. Schleicher, B. Taudul, E. Urbain, S. Boukari, M. Hervé, C.-H. Lambert, A. Hamadeh, S. Petit-Watelot, O. Zill, D. Lacour, L. Joly, F. Scheurer, G. Schmerber, V. Da Costa, A. Dixit, P. A. Guitard, M. Acosta, F. Leduc, F. Choueikani, E. Otero, W. Wulfhekel, F. Montaigne, E. N. Monteblanco, J. Arabski, P. Ohresser, E. Beaurepaire, W. Weber, M. Alouani, M. Hehn, and M. Bowen. Probing a Device's Active Atoms. *Advanced Materials*, 29(19), 2017. 1606578.

[56] B.-K. Teo and P. A. Lee. Ab initio calculations of amplitude and phase functions for extended x-ray absorption fine structure spectroscopy. *Journal of the American Chemical Society*, 101(11): 2815–2832, 1979.

[57] P. A. Lee and G. Beni. New method for the calculation of atomic phase shifts: Application to extended x-ray absorption fine structure (EXAFS) in molecules and crystals. *Physical Review B*, 15(6): 2862–2883, 1977.

[58] J. Mustre de Leon, J. J. Rehr, S. I. Zabinsky, and R. C. Albers. Ab initio curved-wave x-ray-absorption fine structure. *Physical Review B*, 44(9): 4146–4156, 1991.

[59] K. Nagasaka. CPP-GMR technology for magnetic read heads of future high-density recording systems. *Journal of Magnetism and Magnetic Materials*, 321(6): 508–511, 2009.

[60] J. Daughton. GMR applications. *Journal of Magnetism and Magnetic Materials*, 192(2): 334–342, 1999.

[61] I. Ennen, D. Kappe, T. Rempel, C. Glenske, and A. Hütten. Giant Magnetoresistance: Basic Concepts, Microstructure, Magnetic Interactions and Applications. *Sensors*, 16(6): 904, 2016.

[62] D. Rifai, A. N. Abdalla, K. Ali, and R. Razali. Giant magnetoresistance sensors: A review on structures and non-destructive eddy current testing applications. *Sensors (Switzerland)*, 16(3), 2016.

[63] G. A. Prinz. Magnetoelectronics. *Science*, 282(5394): 1660–1663, 1998.

[64] J. S. Moodera, L. R. Kinder, T. M. Wong, and R. Meservey. Large Magnetoresistance at Room Temperature in Ferromagnetic Thin Film Tunnel Junctions. *Physical Review Letters*, 74: 3273–3276, 1995.

[65] D. Wang, C. Nordman, J. M. Daughton, Z. Qian, and J. Fink. 70% TMR at room temperature for SDT sandwich junctions with CoFeB as free and reference Layers. *IEEE Transactions on Magnetics*, 40(4): 2269–2271, 2004.

[66] A. D. Kent and D. C. Worledge. A new spin on magnetic memories. *Nature Nanotechnology*, 10(3): 187–191, 2015.

[67] C. Chappert, A. Fert, and F. N. V. Dau. The emergence of spin electronics in data storage. *Nature Materials*, 6: 813–823, 2007.

[68] S. Ikeda, J. Hayakawa, Y. M. Lee, F. Matsukura, Y. Ohno, T. Hanyu, and H. Ohno. Magnetic tunnel junctions for spintronic memories and beyond. *IEEE Transactions on Electron Devices*, 54: 991–999, 2007.

[69] C. Kittel. *Introduction to Solid State Physics*. John Wiley & Sons, Inc., New York, 6th ed., 1986.

[70] J. M. D. Coey and S. Sanvito. Magnetic semiconductors and half-metals. *Journal of Physics D: Applied Physics*, 37(7): 988–993, 2004.

[71] R. Meservey, P. M. Tedrow, and P. Fulde. Magnetic Field Splitting of the Quasiparticle States in Superconducting Aluminum Films. *Physical Review Letters*, 25(18): 1270–1272, 1970.

[72] S. Parkin, X. Jiang, C. Kaiser, A. Panchula, K. Roche, and M. Samant. Magnetically engineered spintronic sensors and memory. *Proceedings of the IEEE*, 91(5): 661–680, 2003.

[73] N. Ashcroft and N. Mermin. *Solid State Physics*. Saunders College, Philadelphia, 1976.

[74] M. Beth Stearns. Simple explanation of tunneling spin-polarization of Fe, Co, Ni and its alloys. *Journal of Magnetism and Magnetic Materials*, 5(2): 167–171, 1977.

[75] J. C. Slonczewski. Conductance and exchange coupling of two ferromagnets separated by a tunneling barrier. *Physical Review B*, 39(10): 6995–7002, 1989.

[76] Y. Qi, D. Y. Xing, and J. Dong. Relation between Julliere and Slonczewski models of tunneling magnetoresistance. *Physical Review B*, 58: 2783–2787, 1998.

[77] S. Yuasa and D. D.Djayaprawira. Giant tunnel magnetoresistance in magnetic tunnel junctions with a crystalline MgO(001) barrier. *Journal of Physics D: Applied Physics*, 40(21): R337, 2007.

[78] C. Tiusan, F. Greullet, M. Hehn, F. Montaigne, S. Andrieu, and A. Schuhl. Spin tunnelling phenomena in single-crystal magnetic tunnel junction systems. *Journal of Physics: Condensed Matter*, 19: 165201, 2007.

[79] V. Heine. Theory of Surface States. *Physical Review*, 138: A1689–A1696, 1965.

[80] N. P. Ph. Mavropoulos and P. H. Dederichs. Complex Band Strucutre and Tunneling through Ferromagnet/InsulatorFerromagnet Junctions. *Physical Review Letters*, 85(5): 1088–1091, 2000.

[81] Y.-C. Chang. Complex band structures of zinc-blende materials. *Physical Review B*, 25: 605–619, 1982.

[82] P. H. Dederichs, P. Mavropoulosa, O. Wunnickea, N. Papanikolaoua, V. Bellinia, R. Zellera, V. Drchalb, and J. Kudrnovskýb. Importance of complex band structure and resonant states for tunneling. *Journal of Magnetism and Magnetic Materials*, 240: 108–113, 2002.

[83] W. H. Butler, X.-G. Zhang, T. Schulthess, and J. M. MacLaren. Spin-dependent tunneling conductance of Fe-MgO-Fe sandwiches. *Physical Review B*, 63: 054416, 2001.

[84] K. D. Belashchenko, J. Velev, and E. Y. Tsymbal. Effect of interface states on spin-dependent tunneling in Fe/MgO/Fe tunnel junctions. *Physical Review B*, 72: 140404, 2005.

[85] X.-G. Zhang and W. H. Butler. Large magnetoresistance in bcc Co/MgO/Co and FeCo/MgO/FeCo tunnel junctions. *Physical Review B*, 70(17): 172407, 2004.

[86] S. Yuasa, A. Fukushima, H. Kubota, Y. Suzuki, and K. Ando. Giant tunneling magnetoresistance up to 410% at room temperature in fully epitaxial Co/MgO/Co magnetic tunnel junctions with bcc Co(001) electrodes. *Applied Physics Letters*, 89(4): 042505, 2006.

[87] M. Bowen, V. Cros, F. Petroff, A. Fert, C. Martínez Boubeta, J. L. Costa-Krämer, J. V. Anguita, A. Cebollada, F. Briones, J. M. de Teresa, L. Morellón, M. R. Ibarra, F. Güell, F. Peiró, and A. Cornet. Large magnetoresistance in Fe/MgO/FeCo(001) epitaxial tunnel junctions on GaAs(001). *Applied Physics Letters*, 79(11): 1655, 2001.

[88] J. Faure-Vincent, C. Tiusan, E. Jouguelet, F. Canet, M. Sajieddine, C. Bellouard, E. Popova, M. Hehn, F. Montaigne, and A. Schuhl. High tunnel magnetoresistance in epitaxial Fe/MgO/Fe tunnel junctions. *Applied Physics Letters*, 82(25): 4507–4509, 2003.

[89] F. Bonell, T. Hauet, S. Andrieu, F. Bertran, P. Le Fèvre, L. Calmels, A. Tejeda, F. Montaigne, B. Warot-Fonrose, B. Belhadji, A. Nicolaou, and A. Taleb-Ibrahimi. Spin-Polarized Electron Tunneling in bcc FeCo/MgO/FeCo(001) Magnetic Tunnel Junctions. *Physical Review Letters*, 108: 176602, 2012.

[90] D. D. Djayaprawira, K. Tsunekawa, M. Nagai, H. Maehara, S. Yamagata, N. Watanabe, S. Yuasa, Y. Suzuki, and K. Ando. 230% room-temperature magnetoresistance in CoFeB/MgO/CoFeB magnetic tunnel junctions. *Applied Physics Letters*, 86(9): 092502, 2005.

[91] Y. M. Lee, J. Hayakawa, S. Ikeda, F. Matsukura, and H. Ohno. Effect of electrode composition on the tunnel magnetoresistance of pseudo-spin-valve magnetic tunnel junction with a MgO tunnel barrier. *Applied Physics Letters*, 90(21): 212507, 2007.

[92] S. S. Mukherjee, D. MacMahon, F. Bai, C.-L. Lee, and S. K. Kurinec. Study of boron diffusion in MgO in CoFeB|MgO film stacks using parallel electron energy loss spectroscopy. *Applied Physics Letters*, 94(8): 082110, 2009.

[93] Y. Han, J. Han, H. J. Choi, H.-J. Shin, and J. Hong. Effect of Diffused B During Annealing on the Electronic Structure of the MgO Barrier in CoFeB/MgO/CoFeB Magnetic Tunnel Junctions. *Applied Physics Express*, 5(3): 033001, 2012.

[94] V. Harnchana, A. T. Hindmarch, M. C. Sarahan, C. H. Marrows, A. P. Brown, and R. M. D. Brydson. Evidence for boron diffusion into sub-stoichiometric MgO (001) barriers in CoFeB/MgO-based magnetic tunnel junctions. *Journal of Applied Physics*, 113(16): 163502, 2013.

[95] J. D. Burton, S. S. Jaswal, E. Y. Tsymbal, O. N. Mryasov, and O. G. Heinonen. Atomic and electronic structure of the CoFeB/MgO interface from first principles. *Applied Physics Letters*, 89(14): 142507, 2006.

[96] Z. Bai, L. Shen, Q. Wu, M. Zeng, J.-S. Wang, G. Han, and Y. P. Feng. Boron diffusion induced symmetry reduction and scattering in CoFeB/MgO/CoFeB magnetic tunnel junctions. *Physical Review B*, 87: 014114, 2013.

[97] G. H. Rosenblatt, M. W. Rowe, G. P. Williams, R. T. Williams, and Y. Chen. Luminescence of F and F^+ centers in magnesium oxide. *Physical Review B*, 39(14): 10309–10318, 1989.

[98] S. Mitani, T. Moriyama, and K. Takanashi. Fe/MgO/FeCo(100) epitaxial magnetic tunnel junctions prepared by using in situ plasma oxidation. *Journal of Applied Physics*, 93(10): 8041–8043, 2003.

[99] A. Popov, E. Kotomin, and J. Maier. Basic properties of the F-type centers in halides, oxides and perovskites. *Nuclear Instruments and Methods in Physics Research Section B: Beam Interactions with Materials and Atoms*, 268(19): 3084 – 3089, 2010.

[100] Y. Ke, K. Xia, and H. Guo. Disorder Scattering in Magnetic Tunnel Junctions: Theory of Nonequilibrium Vertex Correction. *Physical Review Letters*, 100(16): 166805, 2008.

[101] N. Pathak, P. S. Ghosh, S. K. Gupta, R. M. Kadam, and A. Arya. Defects induced changes in the electronic structures of MgO and their correlation with the optical properties: a special case of electron-hole recombination from the conduction band. *RSC Advances*, 6: 96398–96415, 2016.

[102] M. L. Bortz, R. H. French, D. J. Jones, R. V. Kasowski, and F. S. Ohuchi. Temperature dependence of the electronic structure of oxides: MgO, $MgAl_2O_4$ and Al_2O_3. *Physica Scripta*, 41(4): 537, 1990.

[103] L. A. Kappers, R. L. Kroes, and E. B. Hensley. F^+ and F'centers in magnesium oxide. *Physical Review B*, 1: 4151–4157, 1970.

[104] Y. Chen, R. T. Williams, and W. A. Sibley. Defect Cluster Centers in MgO. *Physical Review*, 182: 960–964, 1969.

[105] Y. Chen, R. Gonzalez, O. E. Schow, and G. P. Summers. Charge and mass transfer involving hydrogen in MgO crystals thermochemically reduced at high temperatures. *Physical Review B*, 27: 1276–1282, 1983.

[106] Y. Chen, J. L. Kolopus, and W. A. Sibley. Luminescence of the F^+ Center in MgO. *Physical Review*, 186: 865–870, 1969.

[107] G. P. Summers, T. M. Wilson, B. T. Jeffries, H. T. Tohver, Y. Chen, and M. M. Abraham. Luminescence from oxygen vacancies in MgO crystals thermochemically reduced at high temperatures. *Physical Review B*, 27: 1283–1291, 1983.

[108] R. González, M. A. Monge, J. E. M. n. Santiuste, R. Pareja, Y. Chen, E. Kotomin, M. M. Kukla, and A. I. Popov. Photoconversion of F-type centers in

thermochemically reduced MgO single crystals. *Physical Review B*, 59: 4786–4790, 1999.

[109] P. Rinke, A. Schleife, E. Kioupakis, A. Janotti, C. Rödl, F. Bechstedt, M. Scheffler, and C. G. Van de Walle. First-Principles Optical Spectra for F Centers in MgO. *Physical Review Letters*, 108: 126404, 2012.

[110] E. Ertekin, L. K. Wagner, and J. C. Grossman. Point-defect optical transitions and thermal ionization energies from quantum Monte Carlo methods: Application to the F-center defect in MgO. *Physical Review B*, 87: 155210, 2013.

[111] D. Domínguez-Ariza, C. Sousa, F. Illas, D. Ricci, and G. Pacchioni. Ground- and excited-state properties of M-center oxygen vacancy aggregates in the bulk and surface of MgO. *Physical Review B*, 68(5): 054101, 2003.

[112] F. Finocchi, J. Goniakowski, and C. Noguera. Interaction between oxygen vacancies on MgO(100). *Physical Review B*, 59: 5178–5188, 1999.

[113] D. O'Connell, B. Henderson, and J. Bolton. Uniaxial stress and polarisation studies of F_2 centre luminescence in MgO. *Solid State Communications*, 38(4): 283 – 285, 1981.

[114] J. Bolton, B. Henderson, and D. O'Connell. Photoluminescence of F_2^{+2} centres in additively coloured magnesium oxide. 38: 287–290, 1981.

[115] M. A. Monge, A. I. Popov, C. Ballesteros, R. González, Y. Chen, and E. A. Kotomin. Formation of anion-vacancy clusters and nanocavities in thermochemically reduced MgO single crystals. *Physical Review B*, 62: 9299–9304, 2000.

[116] M. Born and R. Oppenheimer. Zur Quantentheorie der Molekeln. *Annalen der Physik*, 389(20): 457–484, 1927.

[117] D. R. Hartree. The Wave Mechanics of an Atom with a Non-Coulomb Central Field. Part I. Theory and Methods. *Mathematical Proceedings of the Cambridge Philosophical Society*, 24(1): 89–110, 1928.

[118] J. C. Slater. Note on Hartree's Method. *Physical Review*, 35: 210–211, 1930.

[119] V. Fock. Näherungsmethode zur Lösung des quantenmechanischen Mehrkörperproblems. *Zeitschrift für Physik*, 61(1): 126–148, 1930.

[120] P. Hohenberg, W. Kohn, and L. Sham. The Beginnings and Some Thoughts on the Future. In: *Advances in Quantum Chemistry*, vol. 21, pp. 7–26. 1990.

[121] R. Stowasser and R. Hoffmann. What Do the Kohn-Sham Orbitals and Eigenvalues Mean? *Journal of the American Chemical Society*, 121(14): 3414–3420, 1999.

[122] K. Capelle. A bird's-eye view of density-functional theory. *Brazilian Journal of Physics*, 36: 1318 – 1343, 2006.

[123] D. M. Ceperley and B. J. Alder. Ground State of the Electron Gas by a Stochastic Method. *Physical Review Letters*, 45(7): 566–569, 1980.

[124] J. P. Perdew and A. Zunger. Self-interaction correction to density-functional approximations for many-electron systems. *Physical Review B*, 23(10): 5048–5079, 1981.

[125] J. P. Perdew and Y. Wang. Accurate and simple analytic representation of the electron-gas correlation energy. *Physical Review B*, 45(23): 13244–13249, 1992.

[126] R. M. Martin. *Electronic structure*. Cambridg University Press, 2004.

[127] J. P. Perdew and K. Burke. Comparison shopping for a gradient-corrected density functional. *International Journal of Quantum Chemistry*, 57(3): 309–319, 1996.

[128] A. D. Becke. Density-functional exchange-energy approximation with correct asymptotic behavior. *Physical Review A*, 38: 3098–3100, 1988.

[129] C. Lee, W. Yang, and R. G. Parr. Development of the Colle-Salvetti correlation-energy formula into a functional of the electron density. *Physical Review B*, 37: 785–789, 1988.

[130] J. P. Perdew and Y. Wang. Accurate and simple analytic representation of the electron-gas correlation energy. *Physical Review B*, 45: 13244–13249, 1992.

[131] J. P. Perdew, K. Burke, and M. Ernzerhof. Generalized Gradient Approximation Made Simple. *Physical Review Letters*, 77(18): 3865–3868, 1996.

[132] A. I. Liechtenstein, V. I. Anisimov, and J. Zaanen. Density-functional theory and strong interactions: Orbital ordering in Mott-Hubbard insulators. *Physical Review B*, 52: R5467–R5470, 1995.

[133] V. I. Anisimov, F. Aryasetiawan, and A. I. Lichtenstein. First-principles calculations of the electronic structure and spectra of strongly correlated systems: the LDA + U method. *Journal of Physics: Condensed Matter*, 9(4): 767, 1997.

[134] A. Georges, G. Kotliar, W. Krauth, and M. J. Rozenberg. Dynamical mean-field theory of strongly correlated fermion systems and the limit of infinite dimensions. *Reviews of Modern Physics*, 68: 13–125, 1996.

[135] G. Kotliar, S. Y. Savrasov, K. Haule, V. S. Oudovenko, O. Parcollet, and C. A. Marianetti. Electronic structure calculations with dynamical mean-field theory. *Reviews of Modern Physics*, 78: 865–951, 2006.

[136] J. P. Perdew, M. Ernzerhof, and K. Burke. Rationale for mixing exact exchange with density functional approximations. *The Journal of Chemical Physics*, 105(22): 9982–9985, 1996.

[137] J. Heyd, G. E. Scuseria, and M. Ernzerhof. Hybrid functionals based on a screened Coulomb potential. *The Journal of Chemical Physics*, 118(18): 8207–8215, 2003.

[138] J. Paier, M. Marsman, K. Hummer, G. Kresse, I. C. Gerber, and J. G. Ángyán. Screened hybrid density functionals applied to solids. *The Journal of Chemical Physics*, 124(15): 154709, 2006.

[139] J. Paier, R. Hirschl, M. Marsman, and G. Kresse. The Perdew–Burke–Ernzerhof exchange-correlation functional applied to the G2-1 test set using a plane-wave basis set. *The Journal of Chemical Physics*, 122(23): 234102, 2005.

[140] J. Hafner. Ab-initio simulations of materials using VASP: Density-functional theory and beyond. *Journal of Computational Chemistry*, 29(13): 2044–2078, 2008.

[141] J. Kohanoff. *Electronic Structure Calculations for Solids and Molecules: Theory and Computational Methods*. Cambridge University Press, 2006.

[142] P. V. C. Medeiros, S. Stafström, , and J. Björk. Effects of extrinsic and intrinsic perturbations on the electronic structure of graphene: Retaining an effective primitive cell band structure by band unfolding. *Physical Review B*, 89(4): 041407(R), 2014.

[143] P. V. C. Medeiros, S. S. Tsirkin, S. Stafström, and J. Björk. Unfolding spinor wave functions and expectation values of general operators: Introducing the unfolding-density operator. *Physical Review B*, 91(4): 041116(R), 2015.

[144] H. J. Monkhorst and J. D. Pack. Special points for Brillouin-zone integrations. *Physical Review B*, 13: 5188–5192, 1976.

[145] P. E. Blöchl, O. Jepsen, and O. K. Andersen. Improved tetrahedron method for Brillouin-zone integrations. *Physical Review B*, 49: 16223–16233, 1994.

[146] D. R. Hamann, M. Schlüter, and C. Chiang. Norm-Conserving Pseudopotentials. *Physical Review Letters*, 43: 1494–1497, 1979.

[147] D. Vanderbilt. Soft self-consistent pseudopotentials in a generalized eigenvalue formalism. *Physical Review B*, 41(11): 7892–7895, 1990.

[148] N. Troullier and J. L. Martins. Efficient pseudopotentials for plane-wave calculations. II. Operators for fast iterative diagonalization. *Physical Review B*, 43(11): 8861–8869, 1991.

[149] L. Kleinman and D. M. Bylander. Efficacious Form for Model Pseudopotentials. *Physical Review Letters*, 48: 1425–1428, 1982.

[150] L. N. David J. Singh. *Planewaves, Pseudopotentials and the LAPW Method*. Springer US, 2006.

[151] P. E. Blöchl. Projector augmented-wave method. *Physical Review B*, 50(24): 17953–17979, 1994.

[152] X. Feng, O. Bengone, M. Alouani, I. Rungger, and S. Sanvito. Interface and transport properties of Fe/V/MgO/Fe and Fe/V/Fe/MgO/Fe magnetic tunneling junctions. *Physical Review B*, 79(21): 214432, 2009.

[153] V. M. García-Suárez, C. M. Newman, C. J. Lambert, J. M. Pruneda, and J. Ferrer. Optimized basis sets for the collinear and non-collinear phases of iron. *Journal of Physics: Condensed Matter*, 16(30): 5453–5459, 2004.

[154] G. Sclauzero Andrea Dal Corso. *Modeling CO adsorption on Pt and Au monatomic chains and nanocontacts*. Ph.D. thesis, SISSA, the International School for Advanced Studies, 2010.

[155] H. J. Choi and J. Ihm. Ab initio pseudopotential method for the calculation of conductance in quantum wires. *Physical Review B*, 59(3): 2267, 1999.

[156] S. Datta. *Quantum Transport : Atom to Transistor*. Cambridg University Press, 2005.

[157] M. D. Ventra. *Electrical transport in nanoscale systems*. Cambridg University Press, 2008.

[158] M. P. L. Sancho, J. M. L. Sancho, J. M. L. Sancho, and J. Rubio. Highly convergent schemes for the calculation of bulk and surface Green functions. *Journal of Physics F: Metal Physics*, 15(4): 851–858, 1985.

[159] M. Brandbyge, J.-L. Mozos, P. Ordejón, J. Taylor, and K. Stokbro. Density-functional method for nonequilibrium electron transport. *Physical Review B*, 65(16): 165401, 2002.

[160] N. R. B. Papior. *Computational Tools and Studies of Graphene Nanostructures*. Ph.D. thesis, DTU Nanotech.

[161] E. N. Economou. *Green's Functions in Quantum Physics*, *Springer Series in Solid-State Sciences*, vol. 7. Springer Berlin Heidelberg, 2006.

[162] C. Freysoldt, B. Grabowski, T. Hickel, J. Neugebauer, G. Kresse, A. Janotti, and C. G. Van de Walle. First-principles calculations for point defects in solids. *Reviews of Modern Physics*, 86: 253–305, 2014.

[163] B. Taudul, E. N. Monteblanco, U. Halisdemir, D. Lacour, F. Schleicher, F. Montaigne, E. Beaurepaire, S. Boukari, M. Hehn, M. Alouani, and M. Bowen. Tunneling Spintronics across MgO Driven by Double Oxygen Vacancies. *Advanced Electronic Materials*, 3(7), 2017.

[164] G. Pacchioni and H. Freund. Electron Transfer at Oxide Surfaces. The MgO Paradigm: from Defects to Ultrathin Films. *Chemical Reviews*, 113(6): 4035–4072, 2013.

[165] C. G. Van de Walle and R. M. Martin. Theoretical study of band offsets at semiconductor interfaces. *Physical Review B*, 35(15): 8154–8165, 1987.

[166] T. Urano and T. Kanaji. Atomic and Electronic Structure of Ultrathin Iron Film on MgO(001) Surface. *Journal of the Physical Society of Japan*, 1988.

[167] W. Wulfhekel, M. Klaua, D. Ullmann, F. Zavaliche, J. Kirschner, R. Urban, T. Monchesky, and B. Heinrich. Single-crystal magnetotunnel junctions. *Applied Physics Letters*, 78(4): 509–511, 2001.

[168] W. Tang, E. Sanville, and G. Henkelman. A grid-based Bader analysis algorithm without lattice bias. *Journal of Physics: Condensed Matter*, 21(8): 084204, 2009.

[169] M. Yu and D. R. Trinkle. Accurate and efficient algorithm for Bader charge integration. *The Journal of Chemical Physics*, 134(6): 064111, 2011.

[170] P. Willmott. *An Introduction to Synchrotron Radiation: Techniques and Applications*. A John Wiley & Sons, Ltd., Publication, 2011.

[171] V. Da Costa, C. Tiusan, T. Dimopoulos, and K. Ounadjela. Tunneling Phenomena as a Probe to Investigate Atomic Scale Fluctuations in Metal/Oxide/Metal Magnetic Tunnel Junctions. *Physical Review Letters*, 85(4): 876–879, 2000.

[172] D. J. Kim, W. S. Choi, F. Schleicher, R. H. Shin, S. Boukari, V. Davesne, C. Kieber, J. Arabski, G. Schmerber, E. Beaurepaire, W. Jo, and M. Bowen. Control of defect-mediated tunneling barrier heights in ultrathin MgO films. *Applied Physics Letters*, 97(26): 263502, 2010.

Beata TAUDUL

Effet de la symétrie des lacunes d'oxygéné dans MgO sur le transport électronique polarise en spin

Résumé

En spintronique, l'étude des hétérostructures multicouches composées d'une électrode ferromagnétique et d'une couche isolante mince, c'est-à-dire des jonctions tunnel magnétiques (JTM), est particulièrement importante. Le système canonique est le Fe/MgO/Fe où les hautes valeurs du rapport de la magnétoresistance tunnel (TMR) ont été mesurées. Le facteur crucial définissant la performance de la jonction est l'imperfection structurelle dans un dispositif réel. Dans notre travail, nous nous sommes concentrés sur des lacunes d'oxygène dans MgO. Au moyen de la théorie de la fonctionnelle de densité, nous avons étudié les propriétés électroniques de l'état fondamental des lacunes d'oxygène simples et doubles dans MgO massif, appelées respectivement centres F et M. Nous avons ensuite étudié l'impact de ces lacunes sur le transport balistique dans les jonctions magnétiques. Nous avons démontré le rôle supérieur joué par les centres M et nous avons prouvé qu'un transport cohérent, préservant le spin et la symétrie des électrons, est possible en présence de centres M.

Mots clés : spintronique, jonction tunnel magnétique, magnétorésistance tunnel, lacunes d'oxygène, théorie fonctionnelle de la densité, transport balistique

Résumé en anglais

In sprintronics, the study of multilayer heterostructures composed of a ferromagnetic electrodes and a thin insulating layer, i.e. magnetic tunnel junctions (MTJs), is of special importance. The canonical systems are MTJs made of Fe/MgO/Fe where hight tunneling mangetoresistance ratio (TMR) values were measured. The crucial factor defining the junction performance is the structural imperfection appearing in a real devices. In our work we focused in particular on oxygen vacancies in MgO. By means of density functional theory we studied ground state electronic properties of single and double oxygen vacancies, referred as F and M centers, respectively, in bulk MgO. We then switched to full junctions where we investigated the impact of vacancies on the ballistic transport. We demonstrated that M centers played a superior role and proved that coherent transport, preserving electrons spin and symmetry, is possible in presence of paired vacancies.

Keywords : spintronics , magnetic tunnel junction, tunnel magnetoresistance, oxygen vacancies, density functionl theory, ballistic transport